

A Thesis Submitted for the Degree of PhD at the University of Warwick

Permanent WRAP URL:

<http://wrap.warwick.ac.uk/110843/>

Copyright and reuse:

This thesis is made available online and is protected by original copyright.

Please scroll down to view the document itself.

Please refer to the repository record for this item for information to help you to cite it.

Our policy information is available from the repository home page.

For more information, please contact the WRAP Team at: wrap@warwick.ac.uk

**HIGH RESOLUTION, HIGH SENSITIVITY TANDEM
MASS SPECTROMETRY OF MACROMOLECULES
USING TIME-OF-FLIGHT TECHNIQUES.**

Emmanuel N. Raptakis

Submitted for the qualification of Doctor of Philosophy.

University of Warwick.

Department of Chemistry

July 1996

Table of Contents.

Title page.....	i
Table of Contents	ii
List of Figures	vii
Acknowledgments.....	xiv
Declaration	xv
Abbreviations	xvi
Abstract.....	xxiii

1. Chapter One	1
1.1 Evolution of mass spectrometry and its applications	1
1.1.1 The dawn of mass spectrometry.....	1
1.1.2 Mass analysers.....	3
1.1.2.1 Sector mass analysers.	3
1.1.2.2 Time-of-flight mass spectrometry.....	7
1.1.2.2.1 Linear time-of-flight mass spectrometers.....	7
1.1.2.2.2 Historical overview.....	9
1.1.2.3 Ion reflectron in time-of-flight mass spectrometry.....	15
1.1.2.3.1.1 Single stage reflectrons.	15
1.1.2.3.1.2 Double stage reflectrons.....	19
1.1.2.3.1.3 Quadratic field reflectrons.....	24
1.1.3 Ionisation techniques.....	32
1.1.3.1 Historical overview	32
1.1.3.2 Liquid - secondary ions mass spectrometry (L-SIMS).	34

1.1.3.3 Laser desorption.....	36
1.1.3.4 Matrix assisted laser desorption and ionisation (MALDI).....	37
1.1.3.4.1 Matrices in MALDI.....	41
1.1.3.4.2 MALDI and time-of-flight mass spectrometry	43
1.1.3.5 Electrospray ionisation.....	47
1.1.4 Ion detectors.	49
1.2 Tandem mass spectrometry.	52
1.2.1 Instrumentation in tandem mass spectrometry.....	55
1.2.2 Collision-induced dissociation.	59
1.2.3 Post-source decay.	66
1.3 Mass spectrometry in biological analysis.	68
1.3.1 Biological macromolecules.	68
1.3.2 Peptides and proteins sequencing.....	70
1.3.2.1 Standard techniques.	70
1.3.2.2 Pure mass spectrometric techniques.	71
2. Chapter Two.....	76
2.1 Introduction.....	76
2.2 Instrumentation.	76
2.2.1 The vacuum chamber.	76
2.2.2 The ion source.	80
2.2.2.1 The wobble probe.	83
2.2.2.2 Acceleration and ion collimation region.....	86
2.2.2.3 Ion trajectory simulations.	89
2.2.2.4 Design and construction.....	95
2.2.3 The laser system and beam delivery optics.	98
2.2.3.1 The excimer and dye lasers.	98
2.2.3.2 The optical components.	100
2.2.4 The ion detector.....	101
2.3 Experimental.	101
2.4 Results and discussion.	105

3. Chapter Three.	110
3.1 Introduction.....	110
3.2 The CONCEPT 4-sector double focusing tandem mass spectrometer. .	111
3.3 The MALDI source.....	113
3.3.1 The nitrogen laser.....	113
3.3.2 The optical components.....	114
3.3.3 Ion optics.	118
3.3.4 The electrostatic analyser.	120
3.3.5 The magnetic analyser.....	120
3.3.6 The array detector.....	122
3.4 Experimental results and discussion.	124
4. Chapter Four.	130
4.1 Introduction	130
4.2 The double-focusing mass spectrometer as the first stage of a tandem mass spectrometer.....	135
4.2.1 Time and spatial aberrations in the two sectors.	135
4.2.2 The ion buncher.....	140
4.2.3 Time-of-flight aberrations on electrostatic lenses.....	146
4.3 The quadratic-field mirror as the second stage of a tandem mass spectrometer.....	150
4.3.1 Theoretical considerations on resolution in an ideal-focusing mirror.	150
4.3.1.1 Fundamental limitations on mass resolution.	151
4.3.1.1.1 Length of field-free region.....	151
4.3.1.1.2 Limitations inherent to the fragmentation process	156
4.3.1.1.2.1 Velocity spread caused by collision-induced dissociation	156
4.3.1.1.2.2 Limits to mass resolution due to the length of the collision cell.	158
4.3.1.1.3 Metastable decay	161
4.3.1.2 Comparison with the orthogonal scheme.....	164
4.3.2 Theoretical considerations on ion transmission.	167

4.3.2.1 Ion transmission in the quadratic field.....	167
4.3.2.2 Limits to transmission due to angular scattering	173
4.3.3 Beam deflector design.	174
5. Chapter Five.....	177
5.1 Overview.....	177
5.2 Ion production and transmission in the double-focusing analyser.....	179
5.2.1 Design and construction of a MALDI ion source for the Concept double-focusing mass spectrometer.....	179
5.2.1.1 Ion source employing quadrupole doublet.....	186
5.2.1.1.1 The extraction and collimation regions	189
5.2.1.1.2 The quadrupole doublet	192
5.2.1.2 Ion source employing electrostatic lenses.....	197
5.2.2 The parallel time-of-flight analyser and intermediate detection system.....	202
5.3 Construction of the time-of-flight mirror of the Mag-TOF tandem mass spectrometer.....	204
5.3.1 Introduction and vacuum system.....	204
5.3.2 The ion buncher and delivery ion optics.	206
5.3.3 The collision cell, post-accelerating region and z-deflector.....	214
5.3.4 Design and construction of the quadratic field mirror.....	218
5.3.4.1 Multi-electrode system for sustaining the quadratic field.	218
5.3.4.2 Long-range field sag and its correction.....	221
5.3.4.3 Short-range perturbations.....	223
5.3.4.4 Perturbations on the field boundaries	225
5.3.4.4.1 The front boundary of the ion mirror.....	225
5.3.4.4.2 The end-electrode of the ion mirror.	227
5.3.5 Practical design considerations.	227
5.4 Control and acquisition system.....	233
5.5 Results and discussion.	237
5.5.1 Transmission optimization and alignment experiments.....	237

5.5.2 Experiments with the MALDI ion source	238
5.5.3 Tandem mass spectrometry experiments with peptides.	241
5.6 Conclusions.....	245
6. Appendix I.....	251
References	253

List of Figures

Figure 1. The diagram shows the operating principle of a "velocity focusing" mass spectrograph similar to the one designed by Aston (see text).....	6
Figure 2. Schematic of the Willey-MacLaren time-of-flight mass spectrometer.....	11
Figure 3. Schematic of a plasma desorption mass spectrometer.....	14
Figure 4. Schematic diagram showing the flight path of an ion in a single-stage reflectron time-of-flight analyser.....	17
Figure 5. Schematic of a time-of-flight mass spectrometer with a double stage ion reflectron.	21
Figure 6. Ion flight times as a function of energy in a time-of-flight mass analyser with a double-stage reflectron [].	23
Figure 7. Potential distribution in quadratic fields along the ion optical axis x_0 is the initial coordinate (starting point) of an ion. $2a-x_0$ is the coordinate of ideal time focusing.....	25
Figure 8. Schematic of the quadratic ion mirror time-of-flight instrument introduced by Yoshida [37].....	28
Figure 9. Assembly drawing of a time-of-flight instrument incorporating a quadratic ion mirror. The quadratic potential distribution is created by pure geometry field-sustaining electrodes.....	31
Figure 10. Schematic of the VMAS time-of-flight mass spectrometer.....	33
Figure 11. Schematic diagram of an L-SIMS ion source.....	35
Figure 12. Positive ions MALDI spectra at 266 nm of bovine insulin with sinapinic acid as matrix at various laser fluences. The energy of the laser pulses is measured using a calibrated photodiode system [].	40
Figure 13. Chemical compositions of some of the most widely used matrices in MALDI mass spectrometry.....	45
Figure 14. An electron multiplier optimised for time-of-flight use. The first dynode is perpendicular to the ion path to eliminate time-spread.....	50
Figure 15. Schematic of the KRATOS 4-sector tandem mass spectrometer. .	54
Figure 16. Schematic of a triple-quadrupole tandem mass spectrometer.....	56

Figure 17. Definition of the impact angle, ϕ	63
Figure 18. Nomenclature scheme for the labeling of peptide fragments.	74
Figure 19. Photograph and schematic diagram of the large scale time-of-flight mass spectrometer.	78
Figure 20. Mechanical drawing and photograph of the wobble probe.....	84
Figure 21. SIMION ion trajectory simulations illustrating the effect of an accelerating and a decelerating "Einzel" lens on the same diverging ion beam. The two lenses have identical geometry. The decelerating lens can achieve the same focusing conditions as the accelerating, for lower values of potential.	88
Figure 22. The ion source model as implemented in the SIMION software. ..	90
Figure 23. A micro-lens created in the vicinity of the hole on the accelerating electrode, may over-focus ions coming out of the sample surface for certain electrode geometries and positions of the sample probe.....	92
Figure 24. SIMION simulations of ion trajectories in the chosen geometry for the ion source of the large-scale time-of-flight mass spectrometer. (a) accelerating lens, (b) decelerating lens.	94
Figure 25. Assembly drawing of the ion source of the large-scale time-of-flight mass spectrometer.	96
Figure 26. Time-of-flight mass spectrum of CsI clusters received in the large scale TOF mass spectrometer. The resolution of this spectrum is 400 FWHM, although resolution of 700 has been observed for single shot experiments.	103
Figure 27. a) MALDI mass spectrum of mixture of bombesin and bovine insulin with sinapinic acid matrix, received in the large scale time-of-flight mass spectrometer. b) MALDI mass spectrum of bombesin with 4-hydroxy α -cyanocynamic acid matrix, demonstrating matrix-adduct peaks.....	106
Figure 28. Polymer samples analysed using the large scale time-of-flight mass spectrometer, with DHB matrix . a) PMMA 583 average mass with Li	

and Cs adducts, b) PEG 1500 average mass with Na and Cl adducts and c) polystyrene 5000 average weight with Ag ⁺ adducts.	108
Figure 29 Schematic diagram of the ion optical configuration of the Kratos Concept IHH four-sector tandem mass spectrometer.	112
Figure 30. Photograph of the optical bench for the nitrogen laser and close-up photograph of optical components of the MALDI source of the second double-focusing mass analyser of the four-sector mass spectrometer. A metal-sheet cover was made to enclose stray laser radiation.....	115
Figure 31. Three-dimensional schematic drawing of the in-vacuum mirror mount/tube.	117
Figure 32. Schematic of the ion optics of the collision cell exit of the KRATOS Concept IHH four-sector tandem mass spectrometer.	119
Figure 33. Photograph of the second mass analyser of the KRATOS Concept IHH four-sector tandem mass spectrometer. The detector assembly of the instrument is designed to allow quick substitution of the point detector with an array detector, allowing simultaneous detection of ions with masses within approximately 4% of the mass range.....	123
Figure 34. Mass spectra received with the MALDI ion source in the collision cell area of the KRATOS Concept IHH tandem mass spectrometer. a) LHRH with resolution 1000 (FWHM); b)bombesin with resolution 3500 (FWHM).....	125
Figure 35. Medium resolution mass spectrum of polystyrene (PS1680) with Ag ⁺ adduct.	127
Figure 36. a) A "snapshot" of the 1625 Da mass ion peak of polystyrene with Ag ⁺ adduct is shown. The magnet is kept static and signal of ions of the chosen mass range is integrated with the array detector. b) theoretical isotopic distribution of the 1625 Da mass ion peak of polystyrene with Ag ⁺ adduct.	128
Figure 37 Schematic of a Nier-Johnson double-focusing mass spectrometer, demonstrating the geometric parameters of the sectors and the initial	

parameters of the beam, as well as the parameters describing the final ion packet.	137
Figure 38. a) Illustration of the time-focusing action of the ion buncher. b) Schematic of the ion buncher.	141
Figure 39. Schematic of an electrostatic lens.	148
Figure 40. Deviation of TOF (relative to TOF of ions with energy qV_f as a function of the ratio of energy qe_f to maximum ion energy qV_p , for different L_d/L_p values and $V_f = 0.7 V_p$	153
Figure 41. Deviation of TOF (relative to TOF of ions with energy qV_f as a function of the ratio of energy qe_f to maximum ion energy qV_p , for different L_d/L_p values and $V_f = 0.7 V_p$ at acceleration gaps L_a/L_p : (a) $L_a/L_p = 0.01$; (b) $L_a/L_p = 0.02$	155
Figure 42. TOF for different fragment ions as a function of decay time inside the quadratic field, in units of precursor ion TOF. $L_d = L_a = 0$. The decay time is given relative to the flight time of the precursor ion through the mirror.	163
Figure 43. Comparison of resolution for the longitudinal and the orthogonal scheme for ideal TOF analysers and 20 mm collision cell length: a) collision gas He, b) collision gas Xe.	166
Figure 44. A two-dimensional representation of the parabolic potential of Eq. 4-58. The third dimension (z) is field-free.	169
Figure 45. Schematic of the MS2 region of the Mag-TOF tandem mass spectrometer prototype.	172
Figure 46. Photograph of the Mag-TOF prototype tandem mass spectrometer.	178
Figure 47. Photograph of the wobble-probe of the MALDI source of the Mag-TOF prototype tandem mass spectrometer.	181
Figure 48. Schematic of the optical path of the laser beam of the Mag-TOF prototype tandem mass spectrometer.	183
Figure 49. A SIMION model of the extraction and collimation region of the MALDI ion source incorporating a quadrupole doublet.	188

Figure 50. Ion trajectory simulations performed with the SIMION software for two different ion energies: a) initial energy 10 eV; b) initial energy 20 eV.	190
Figure 51. Schematic diagram of the quadrupole doublet.	193
Figure 52. Photograph of the ion optical components of the MALDI source assembly, including the conical extraction electrodes and the quadrupole doublet. The ion source cradle is not shown.	195
Figure 53. Ion trajectory simulations of the focusing and collimation characteristics of the MALDI ion source in two planes: a)y-plane, b)z-plane	199
Figure 54. a) Photograph of the MALDI ion source assembly. b) Mechanical drawing of the planar-symmetry focusing and collimating ion optics.	201
Figure 55. Schematic of the MS2 region of the Mag-TOF prototype tandem mass spectrometer.	207
Figure 56. Experimental results illustrating the time-focusing action of the ion buncher. The FWHM of the unbunched and bunched peaks were 50 and 5 ns respectively.	209
Figure 57. SIMION ion trajectory simulations of various components of the interfacing ion optics region of between the double focusing mass spectrometer and the quadratic ion mirror.	211
Figure 58. Photograph of the two different-design collision cells of the Mag-TOF prototype tandem mass spectrometer.	213
Figure 59. Photograph of the region before the quadratic mirror, including the differentially-pumped chamber. A number of ion optical elements can be seen including one of the y-lenses and the z-deflector, as well as the ion detector.	215
Figure 60. SIMION simulation of ion trajectories in the post-accelerating region.	217
Figure 61. Simulation of field sustaining system on the side of a mirror with planar hyperbolic field (see text for notation): a) cross-section of the	

mirror; b) SIMION illustration of the potential distribution inside the mirror.....	220
Figure 62. Dependence of Fourier coefficients B_n on the number of harmonics n , when the total number of electrodes, $N=20$	224
Figure 63. Simulation of field sustaining system on the flange of a mirror with planar hyperbolic field: a) cross section of the mirror; b) SIMION illustration of the potential distribution inside the mirror.	226
Figure 64. Photograph of the MS2 of the Mag-TOF prototype tandem mass spectrometer. The electrode boards seen on the top of the vacuum chamber were the exact negative image of the actual electrodes of the ion mirror.	229
Figure 65. Photograph of the MS2 region of the Mag-TOF prototype tandem mass spectrometer, illustrating ion optics, the collision-cell differentially-pumped chamber, the ion mirror and the resistor chain.	231
Figure 66. Photograph of the pyramid-shape capacity coupled detector anode of the Mag-TOF prototype tandem mass spectrometer.	234
Figure 67. Schematic of the control and acquisition system of the Mag-TOF prototype tandem mass spectrometer.	235
Figure 68. Tandem mass spectrum of Cs_4I_3 . The resolution achieved for the parent and fragment ions demonstrates the proof of the concept of the Mag-TOF prototype tandem mass spectrometer.	239
Figure 69. The first tandem mass spectrum of renin substrate tetradecapeptide received with the Mag-TOF prototype tandem mass spectrometer...	243
Figure 70. Tandem mass spectrum of bombesin achieved with the Mag-TOF prototype tandem mass spectrometer.	244
Figure 71. Tandem mass spectra of substance P received with the Mag-TOF prototype tandem mass spectrometer. The amount of sample use has been 1 picomole and 500 femtomole for the upper and lower spectrum respectively.	246

Figure 72. Tandem mass spectra of renin substrate tetradecapeptide received with the Mag-TOF prototype tandem mass spectrometer. The amount of sample used was 1 picomole.....247

Acknowledgments.

I would like to thank my academic supervisor Professor Peter Derrick, for giving me the chance to be involved in such a stimulating project and acquire a wide variety of experiences and knowledge through his guidance and assistance during the course of this work.

I would like to thank Alex Colburn, for his valuable help in solving numerous experimental problems during this work, as well as for his support and friendship.

I particularly like to thank my dear friend and colleague, Dr. Alexander Makarov whose invaluable support and friendship was critical to the success of this work.

Dr. Anastasios Giannakopoulos, Dr. Ulla Andersen, Dr. Mike Belov, Dr. David Reynolds, Dr. Richard Gallagher, Dr. Elaine Scrivener, Dr. Dominic Chan, Dr. Desmond Yau, Anne-Mette Hoberg, Jonathan Haywood, Dr. Helen Cooper have been good friends and colleagues throughout this work, stimulating helpful discussion and offering their practical aid.

Thanks to Harry Willes and the other members of the mechanical and electronics workshop of the Department of Chemistry for their rapid and efficient respond to the many technical challenges that were tackled during this work.

Thanks to Steve Davis and Andy Hoffman of HD Technologies as well as Jonathan Bradford, Barry Wright, Bob Lawther and David Denne of Kratos Analytical for their help in solving practical problems during the project.

I would like to acknowledge the financial support of British Petroleum for the first year and the European Commission for the next two years of this work.

Finally, I would like to thank my family for their unlimited support and particularly my fiancée Patrizia Schmid for her unconditional love and devotion that inspired me and helped me go through with this work.

Declaration

I hereby declare that this thesis is my own work and that, to the best of my knowledge and belief, it contains no material previously published or written by another person, nor material which to a substantial extent has been accepted for the award of any other degree or diploma of a university or any other institute of higher learning, except where due acknowledgment is made in the text. I particularly acknowledge the major contribution of Dr. Alexander Makarov in the theoretical analysis presented in chapters 4 and 5 of this work.

Emmanuel Nikolaos Raptakis

Abbreviations

	differentiation in time
Δ	initial coordinate spread
τ	rise-time of the push-out high-voltage pulse of the ion buncher
σ	cross section
θ	scattering angles of the parent ions
φ	collision angle
v	velocity of an ion
δ	velocity spread
θ	incident angle of the ion beam to the field region of an ion mirror
α	angular spread in all directions
ω_c	cyclotron frequency of the ion in a Fourier transform/ion cyclotron resonance mass spectrometer
ψ_e	angles of the electric sector
ΔH	total dispersion at the detector in the z -direction of the beam for ion masses from 0 to m_p
ψ_m	angles of the magnetic sector
Δt	time-length of the peak at a specified height
ΔU	change of potential energy
ΔV_0	energy spread
Δv_y	changes in the orthogonal component of the initial velocity
Δ_x, Δ_y	maximum spreads of velocities within the precursor ion beam following collision
Δx_{ab}	overall displacement of the ion relative to the mean ion due to aberrations from all initial parameters other than energy spread (in the ion buncher region)
$\Delta y_0'$	change of inclination due to focusing in an Einzel lens
a	coordinate of the point of potential minimum of a quadratic field

ADC	analogue-to-digital converter
A_n	Fourier coefficients
B	magnetic field induction
B	magnetic sector
B_n	corrected Fourier coefficients
C	Celsius
CAD	collisionally activated decomposition
CID	collision-induced dissociation
d	gap of a parallel-plate deflector
d	length of acceleration region
Da	Daltons
d_B	length of the first region of a double stage ion mirror
DFMS	double-focusing mass spectrometer
DHB	2,5-dihydroxybenzoic acid
d_R	length of the second region of a double stage ion mirror
e	electron charge
E	electrostatic field
E	electrostatic analyser
E_{CM}	center-of-mass collision energy
E_k	kinetic energy of an ion leaving the ion source
eV	electron volts
f	focal length of an Einzel lens
FAB	fast atom bombardment
FD	field desorption
FT-ICR	Fourier transform/ion cyclotron resonance mass spectrometer
FWHM	full width at half maximum
H	width of the quadratic ion mirror
h	length of the collision cell
I	attenuated parent beam current
I_0	parent ion current without collision gas
IR	infrared

K	relative energy spread
keV	kilo electron volts
l	length of a parallel-plate deflector
L	length of field-free region
L-SIMS	liquid secondary-ions mass spectrometry
L_{Σ}	effective path length
L_{1e}	length of the first field-free regions for the electric sector
L_{2m}	length of the second field-free region for the magnetic sector
L_a	length of the post-acceleration region
L_d	length of a field-free region preceding a quadratic mirror
L_e	effective path length in the orthogonal scheme time-of-flight analyser
L_m	quadratic ion-mirror length
L_p	depth of penetration in a quadratic mirror
M	molar
M	magnification of the electric sector
m	mass of an ion
m	meter
$m/\Delta m$	definition of mass resolution
m_s	mass of the particular atom of the large molecule that takes part in the collision
Mag-TOF	magnetic sector/time-of-flight prototype tandem mass spectrometer
MALDI	matrix-assisted laser desorption/ionisation
m_f	fragment ion mass
m_g	mass of the collision gas
m_{ion}	mass of the large ion that collides with a collision gas atom
m_p	precursor ion mass
MS-1	first mass analyser of a tandem mass spectrometer
MS-2	second mass analyser of a tandem mass spectrometer
n	target gas number density

PEEK	polyetheretherketone
Q	internal energy taken up by the ion during a collision
q	number of charges of an ion
Q	quadrupole analyser
$q\epsilon$	ion energy spread
$q\epsilon_f$	variable corresponding to the fragment ion energy
qV_f	fragment ion energy
qW	kinetic energy release in the center-of-mass coordinate system
r	radius of ion trajectory in a homogeneous magnetic field
R	mass resolution
RRKM	Rice-Ramsperger-Kassel-Marcus
R_1	inner radius of the ESA plates
R_2	outer radius of the ESA plates
r_e	radius of the electric sector
r_m	of the magnetic sector
T	total flight-time of an ion to the point of time-focus of the ion buncher
t	time
T_t	time aberration coefficient due to rise-time of the push-out high-voltage pulse of the ion buncher
T_e	time aberration coefficients due to energy spread
T_{ab}	time aberration coefficient due to all parameters other than r and ϵ
t_0	time when an ion intercepts the exit slit of the ion buncher
T_0	Mean flight-time
T_d	time-of-flight of an ion to the buncher region
TDC	time-to-digital converter
T_f	time-of-flight in the quadratic field
t_i	initial time deviation
TOF	time-of-flight
T_{ss}	time when an ion passes through the source slit

U	ion energy after the ion source
U_0	mean energy of the ions
U_{acc}	accelerating potential in the large-scale TOF MS ion source
U_B	potential difference of the first region of a double stage ion mirror
U_d	voltage across a parallel-plate deflector
U_{lens}	Einzel lens potential in the large-scale TOF MS ion source
u_m	potential on m^{th} electrode of the quadratic ion mirror
U_m	maximum voltage applied to the end of the quadratic ion-mirror
U_{ort}	push-out potential in an orthogonal-scheme DFMS-TOF tandem mass spectrometer
U_R	potential difference of the second region of a double stage ion mirror
U_i	overall acceleration potential in the orthogonal scheme
UV	ultraviolet
V_0	accelerating potential of an ion source
V_a	post-accelerating potential
V_k	maximum value of the push-out voltage of the ion buncher
v_y	orthogonal component of the initial velocity
ω	frequency of oscillations in a quadratic field
x_c	coefficient of chromatic aberration
x_a	angular aberration coefficient
x_e	energy spread aberration coefficients
x_0	coordinate of the mean ion of the packet at the moment $t=T_d$
x_y	starting y -coordinate aberration coefficients
Y	root mean square value of the arrival coordinate of the ion beam in the y direction
y_0	initial y -coordinate
y_0'	initial inclination of the trajectory to the direction x ($dy/dx _{t=0}$)
y_k	arrival coordinate on the detector of the quadratic ion-mirror
y_m	maximum value of a uniform distribution

z_m'

tilt angle of the quadratic ion mirror

Z_{\max}

coordinate at the detector of the maximum deflection of the parent ion

Abstract

The first of the three parts of this study involves the construction of a large scale time-of-flight mass spectrometer. A large aluminium-alloy vacuum chamber was designed and manufactured. Ion trajectory modelling was carried out for defining the optimum ion optical configuration of the matrix-assisted laser desorption/ionisation (MALDI) ion source that was designed and constructed. A floating ion detector assembly was designed and installed. MALDI mass spectrometry experiments were performed with biomolecules and polymer samples.

The second part of this work involves the design and construction of a MALDI ion source in the collision cell area of a four-sector tandem mass spectrometer. The apparatus makes use of an array detector installed as the detector of the second double-focusing mass analyser of this instrument. High resolution and sensitivity mass spectra of high mass biomolecules and polymer samples were acquired. Resolution in excess of 3500 full-width at half maximum (FWHM) has been observed.

The third part of this work describes the theoretical considerations, the design the construction and the performance of a prototype magnetic sector/time-of-flight tandem mass spectrometer with an ideal time-focusing ion mirror as the second mass analyser (Mag-TOF). The method followed in order to overcome the inherent incompatibilities of the two mass-analysis stages is discussed. The theoretical description of the ideal time-focusing reflectron is presented, together with analysis of the time-aberrations of the delivery ion optics and the TOF part of the instrument, and their influence to resolution and sensitivity. Initial experiments have been performed to prove the feasibility of the operational principle of this prototype instrument. High resolution (approximately 3000, FWHM) tandem mass spectra of peptides are presented. The instrument also achieved high levels of sensitivity.

1. Chapter One.

Introduction.

1.1 Evolution of mass spectrometry and its applications

In recent years, mass spectrometry has experienced rapid development, with new instrumental techniques introduced and, more importantly, novel applications being proposed. Those fresh uses expand the applicability of mass spectrometry from the traditional areas of inorganic and organic chemical analysis to the exciting areas of biological, medical and polymer research. Mass spectrometry is proving to be an extremely powerful analytical tool, exhibiting high sensitivity (down to the attomole level), high accuracy in the determination of molecular mass, and molecular structure information through the use of tandem instruments.

1.1.1 The dawn of mass spectrometry.

The evolution of mass spectrometry started just over one hundred years ago. Erich Goldstein [1] observed for the first time in 1876 the "Kathode Strahlen" (cathode rays), a luminous blue beam radiating directly from the cathode plate towards the anode of an evacuated discharge tube.* Experimenting with higher vacua in the discharge tube, Goldstein found in 1886 that luminous "rays" emanate from a perforated cathode plate [2]. Those newly found rays, named

* J. J. Thomson established that these rays, which actually were beams of electron, possessed a constant mass-to-charge ratio. ("Conduction of Electricity through Gases", Sir J. J. Thomson and G. P. Thomson, CUP, Cambridge, (1933), Vol. I, p. 237, refers to Thomson J. J., Phil. Mag. , 44 (1897) 293).

"Kanal Strahlen", were found to be deflected by a magnetic field, but in the opposite direction to the cathode rays [3]. They exhibited various mass-to-charge ratios. They later proved to have been the first ion beams ever observed.

Thomson continued the study of this phenomenon, building a positive ray analyser [4]. A narrow pipe through the cathode allowed a portion of the rays in the gas discharge tube to pass through superimposed parallel electric and magnetic fields. The ion detection was simply performed by observing the glow on the walls of the glass tube. The combination of the fields utilised made the ions strike the glass walls creating parabolic shapes. The intersection point of the parabolas corresponded to the non-deflected beam position. Each of the parabolas corresponded to a specific mass-to-charge ratio, with the arc length dependent upon the spread of initial velocities. For the derivation of these results, Thomson utilised the same motion laws that were found for the electron [3,5,6]. Apart from the sign of the charge, the only difference found between the ion and electron beams was that the mass-to-charge ratios for ionic species are much higher than that of the electron. Thomson established that the positively charged particles were formed by the removal of electrons from the neutral gas molecules in the discharge tube [7]. Further experiments with the same apparatus revealed the presence of isotopes [8].

The road for mass spectrometry had been opened, as scientists started to investigate the newly discovered species. Effort started being invested in the development of improved instruments and the study of fundamental

limitations, as well as ways to overcome them. Mass spectrometry became a solution looking for problems. Some of those "problems" that boosted international research on mass spectrometry were ion separation in nuclear technology, chemical research and analysis and, currently, biochemical analysis and biotechnology research.

1.1.2 Mass analysers.

1.1.2.1 Sector mass analysers.

The most obvious way of analysing a beam with charged species of different masses is to try to deflect them in distinct directions according to their mass. This can readily be done with the use of a magnetic field. The simplest magnetic-sector mass spectrograph consists of an ion source, a homogenous magnetic field region and a detector (for example a photographic plate) at the exit of the magnetic field. The ions are created in the source and accelerated by an electric field with potential difference V_0 towards the mass analyser. On the exit of the ion source the ions have kinetic energy E_k given by the equation:

$$E_k = qeV_0 = \frac{m\nu^2}{2} \quad \text{Eq. 1-1}$$

where q is the number of charges, e the electronic charge and m the mass of the particle. The operating principle of a single magnetic field mass analyser is based on the fact that charged particles enter a homogeneous magnetic field B and experience a force perpendicular to both the ion velocity ν and the magnetic field B . The absolute value of the magnetic force remains the same throughout the region of the magnetic field, and the ion follows a circular path

with radius r . The centrifugal force must balance the force on the ion due to the magnetic field:

$$\frac{mv^2}{r} = Bqe v \quad \text{Eq. 1-2}$$

Combining Eqs. 1-1 and 1-2 gives:

$$\frac{m}{qe} = \frac{B^2 r^2}{2V_0} \quad \text{Eq. 1-3}$$

or

$$r = \frac{1}{B} \left(2V_0 \frac{m}{qe} \right)^{\frac{1}{2}} \quad \text{Eq. 1-4}$$

It can be readily seen that, with B , V_0 and q constant, the radius r is directly proportional to the square root of the mass m . Therefore the initial ion beam, which may consist of ionic species of different masses, will separate within the mass analyser into a number of different ion beams following different circular trajectories with well defined radii. The individual beams will each arrive at a characteristic point on the detector, and each can be directly assigned to a particular mass.

Nevertheless, in practical terms, the ion source that could accelerate all the ions exactly to energy qeV_0 does not exist! There will always be an energy spread to blur the perfect picture that would be obtained for the ideal situation. The mass resolving power of an instrument using only a magnetic sector field

is limited to about $V_0/\Delta V_0$ where V_0 is the mean energy of an ion and ΔV_0 is the energy spread.

In order to tackle the energy spread problem, instrumental designs appeared that used a combination of electric and magnetic field to minimise the aberrations that a single magnetic field could not correct. In 1919 Aston built an instrument in which the electrostatic and magnetic fields were separated, i.e. not superimposed [9]. Inside this mass spectrograph (figure 1) ions of the same mass but different velocities would be deflected in a different way by the electric field: higher velocity ions would undergo a smaller amount of deflection and pass through a smaller portion of the magnetic field. Therefore they suffered a smaller deflection than ions of lower energy. A photographic emulsion plate was placed along the line where the trajectories of higher and lower energy paths of the same mass ions crossed. In this way, ions of the same mass but different velocities created a linear image on the photographic plate. This type of focusing is called velocity focusing and helps to minimise the effect of the energy spread on the resolution of the device. The presence of an ionic species with a certain mass-to-charge ratio was detected as an electron current at the focal point. A spectrum was obtained by varying the acceleration potential V_0 while recording the detected current.

About the same time Dempster modified Classen's electron analyser [10] for separation of positive ions [11]. In this instrument, the direction focusing of a π radian magnetic sector was utilised to focus a monoenergetic beam of ions

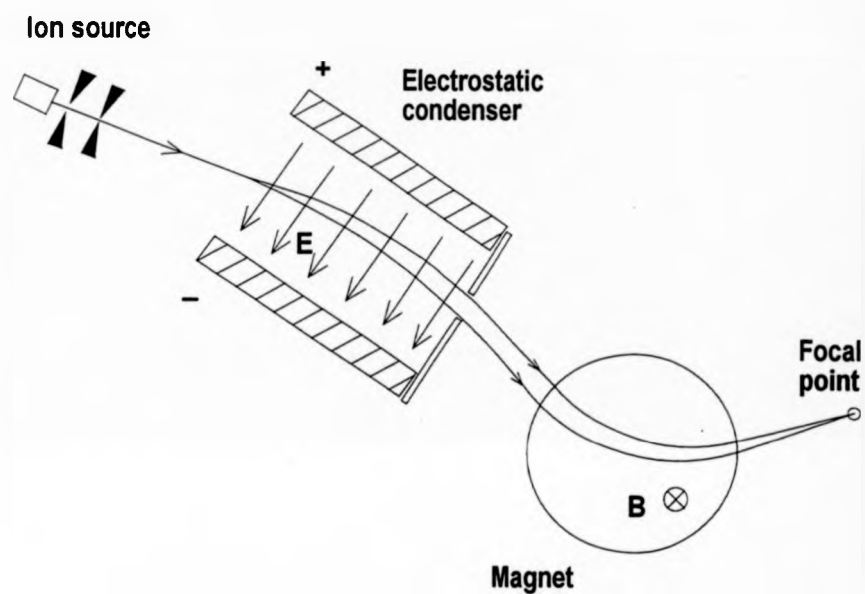


Figure 1. The diagram shows the operating principle of a "velocity focusing" mass spectrograph similar to the one designed by Aston (see text).

diverging from the entrance slit. High acceleration potential was used in order to lower the ratio of energy spread to mean kinetic energy for the ion beam. With the designs of Aston and Dempster, mass spectrometry became a tool of nuclear physics. Aston's velocity focusing instrument offered precision in mass measurements [12], and Dempster's direction focusing instrument measured relative isotopic abundance [13].

Herzog was the first to find a general solution for the paths of charged particles in magnetic and electric sectors [14]. Based on those calculations, Mattauch and Herzog matched complementary sectors in order to focus a diverging and non-monoenergetic ion beam [15]. Their design was eliminating first-order aberrations. It proved to be very popular, being used in the 100" Argonne isotope analyser built in the 1960's [16]. Johnson and Nier [17] improved on previous designs by discovering an arrangement that eliminated aberrations of the second order as well. A Nier-Johnson geometry instrument will be examined further in this work.

1.1.2.2 Time-of-flight mass spectrometry.

1.1.2.2.1 Linear time-of-flight mass spectrometers.

Time-of-flight mass spectrometers are based on one of the simplest mass separation principles imaginable: ionised species starting from the same place at the same time are accelerated by means of an constant homogeneous electrostatic field. Their velocities are unambiguously related to their mass-to-charge ratio and, for a given charge state, times of arrival on a detector directly indicate their masses.

The motion of an ionised particle with mass m and charge qe , inside a constant homogeneous electrostatic field $E_x=E$ can be described by the equation:

$$\ddot{x} = \frac{qeE}{m} \text{ and } \ddot{y} = \ddot{z} = 0 \quad \text{Eq. 1-5}$$

Assuming that the initial velocity has components in all x , y and z directions v_x, v_y, v_z and the initial position is $x_i=0, y_i$ and z_i , integration of the above equation gives (for $q=1$):

$$x = \frac{eEt^2}{2m} + v_x t \quad \text{Eq. 1-6}$$

$$\dot{x} = \frac{eEt}{m} + v_{x_i} \quad \text{Eq. 1-7}$$

$$y = y_i + v_{y_i} t \quad \text{Eq. 1-8}$$

$$z = z_i + v_{z_i} t \quad \text{Eq. 1-9}$$

If the length of the acceleration region is d , the "final" values (denoted by subscript "f") are obtained:

$$t_f = \frac{m}{eE} (v_{x_f} - v_{x_i}) \quad \text{Eq. 1-10}$$

$$v_{x_f} = \left(v_{x_i}^2 + \frac{2eEd}{m} \right)^{1/2} \quad \text{Eq. 1-11}$$

$$\begin{aligned} v_{y_f} &= v_{y_i} \\ v_{z_f} &= v_{z_i} \end{aligned} \quad \text{Eq. 1-12}$$

$$\begin{aligned} y_f &= y_i + v_{y_i} t_f \\ z_f &= z_i + v_{z_i} t_f \end{aligned} \quad \text{Eq. 1-13}$$

For high accelerating fields, it can be assumed in the first approximation that the initial velocities are negligible compared to the final velocity in the x direction. In this case, all the ions leaving the acceleration region, possess the same amount of energy due to the electric field which is equal to

$$E_k = eV_0 \quad \text{Eq. 1-14}$$

where $V_0 = Ed$ is the potential difference that ions experience during acceleration in the ion source. After ions of different masses have acquired different velocities according to Eq. 1-11, they are allowed to travel in a field-free region where they drift apart from each other according to their velocities. If a length L of field-free region is considered, the total time-of-flight of an ion is the sum of its times-of-flight through the acceleration and the field-free region:

$$t = \left(\frac{2md}{eE} \right)^{1/2} + L \left(\frac{m}{2eV_0} \right)^{1/2} \quad \text{Eq. 1-15}$$

Therefore time is directly proportional to the square root of the mass of the ion. Using a detector at the end of the field-free region the arrival times of the ionised species created in the ion source can be recorded. The arrival times of the ions can be readily translated into a mass spectrum.

1.1.2.2.2 Historical overview.

The principle of time-of-flight mass spectrometry described above was demonstrated for the first time by Stephens [18] in 1946. The time-of-flight (TOF) instrument offers a number of extraordinary advantages over most other

analysers. The theoretical mass range of a TOF instrument is unlimited, although in practice it is not so straightforward to ionise or detect very heavy molecules without inducing fragmentation. Time-of-flight instruments have the advantage of detecting all the ions of different masses without the need to scan the ion beam, offering an immediate advantage over sector instruments and quadrupoles in terms of sensitivity. This characteristic is described as the "Fellgett" advantage [19]. They also are very simple instruments, relatively easy to build and operate.

The first commercial TOF mass spectrometer that was produced in the 1950's, the Bendix instrument, fascinated the scientific community with the very high recording speed (10,000 mass spectra per second). For this very reason, time-of-flight mass spectrometry was for a long time used for the study of fast reactions, such as explosions. The ionisation method of TOF instruments of that time was electron impact. The resulting ion pack with this kind of source had a relatively high initial energy and spatial spread, which degraded mass resolution. Mass resolution for a peak pair can be defined as the ratio of the mean mass to the mass difference of the two peaks when separated by a valley of a specified depth. It can also be defined for a single peak as the ratio of the mass to the width of the mass peak measured at a given level. The basic formula for mass resolution of a single peak in time-of-flight mass spectrometry is very simple:

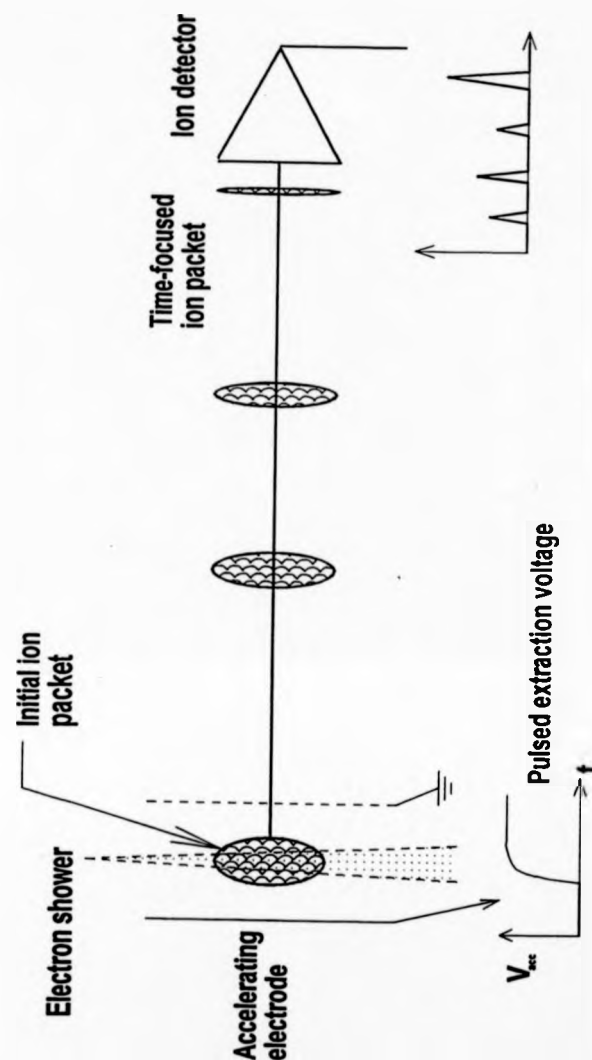


Figure 2. Schematic of the Wiley-MacLaren time-of-flight mass spectrometer.

$$\frac{m}{\Delta m} = \frac{1}{2} \frac{t}{\Delta t} \quad \text{Eq. 1-16}$$

where t is the time-of-flight corresponding to the middle of the peak and Δt the time-length of the peak at a specified height. The duration of the ion packet at the detector results from its initial position spread, and the initial velocity, energy and spatial spread. It is obvious that the longer the total time-of-flight and the shorter the time-length of the packet at the detector, the better is the resolution.

A method was devised by Wiley and MacLaren [20] to improve the resolutions of early TOF mass spectrometers to an acceptable level of a few hundreds. This involved applying suitable pulses to the ion source so as to compensate partially for the initial spreads of the ion packet. A typical ion source of the Wiley-MacLaren instrument (see figure 2) consists of two parts. The ions are created in the extraction region by a timed electron beam, and are allowed to drift apart from each other according to their random initial velocities. The pulsed electron beam has a typical time width of 1 μ s. At a certain time delay (about 1-1.5 μ s), a pusher pulse is applied to one of the sides of the extraction region. The ions start drifting towards the exit of the extraction region and ions in the rear of the packet will eventually acquire more energy than those in the front, therefore they will catch up with them further down the ion path.

After the extraction region the ions enter the acceleration region where they acquire more energy. An ion detector at the end of the field-free region is

utilised to record the arrival times of the ions. The Wiley-MacLaren focusing was a method to compress a "random" ion packet. This effectively means that the initial positions of the ions are in no way related to their initial energies prior to the extraction pulse. Therefore ions at the front of the ion pack can have higher or lower energies than those at the rear. For this reason Wiley-MacLaren ion focusing cannot achieve resolutions better than a few hundreds.

The first time-of-flight instruments were only able to analyse low-mass ions, due to the limitations imposed by the electron impact ionisation. The first attempt to use TOF for the analysis of high-mass ions was made by Dole et al in the late 60's [21,22]. The ionisation method used was electrospray and the sample was polystyrene.

The next step in time-of-flight mass spectrometry came when Macfarlane showed that high-mass molecules could be ionised efficiently by the fission fragments from radioactive ^{252}Cf [23,24]. A schematic of the plasma desorption mass spectrometer is shown in figure 3. The extraordinary characteristic of the plasma desorption instrument is the short time-length of the ionisation process (<1ns). This time is much shorter than the production times caused by any other ionisation method. Additionally, every cycle of the instrument is triggered by detecting fragments of the same fission event that created the analyte ions, therefore timing circuit jitter can be minimised. Resolution in plasma desorption linear time-of-flight instruments can be in excess of 1000–2000, limited by energy spread of the resulting ion beam.

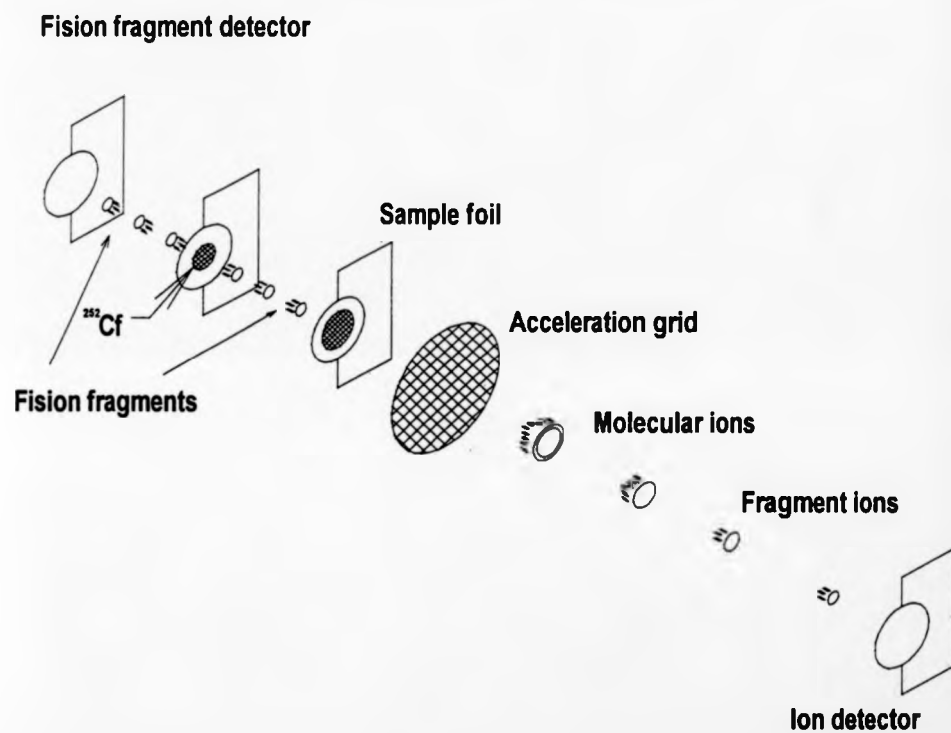


Figure 3. Schematic of a plasma desorption mass spectrometer.

1.1.2.3 Ion reflectron in time-of-flight mass spectrometry

In 1966 Mamyrin et al [25] proposed a way to correct the time spread which is due to the initial velocity spread of the ions, with the use of a decelerating and reflecting field. The idea was that for ions of the same m/q ratio (where q is the number of electron charges of the ion) entering such a field, those with higher energies will penetrate deeper into the field than those with lower energies. Therefore the former will spend more time into the reflecting field and they will "catch up" with the lower energy ions further down the flight path.

In the ideal case above, the time-width of the peaks of the mass spectrum will only depend on the time-width of ion formation. In practical cases, there are a number of time-widening parameters, including the spread in positions of ion formation, initial velocity spread, ion optical aberrations, metastable formation as well as technical/technological problems (electronic stability, time resolution of detection system). All of these degrade resolution to a certain extent.

1.1.2.3.1.1 Single stage reflectrons.

Single-stage reflectrons are the simplest form of ion reflectrons. The reflecting electrostatic field simulated by a single-stage ion mirror is a simple homogeneous field created by two flat grids. The first grid is at the entrance of the mirror and the second at its end. The latter can be replaced with a solid electrode, although usually a grid is used to allow ions to reach a detector behind the mirror for linear time-of-flight experiments when the ion reflector is grounded. In order to improve the homogeneity of the field, a number of

equally-spaced ring electrodes are placed between the two end-electrodes, connected with a chain of equal-value resistors.

A representation of a single-stage ion mirror, as well as a schematic diagram demonstrating the ion paths in such an instrument is shown in figure 4. The constant electric field \bar{E} within the mirror is parallel to the main axis of the instrument, defined as the x axis. It is assumed that \bar{E} follows a step function where $E_x=E$ for $x<0$ and $E_x=0$ for $x>0$. The ion velocity components perpendicular to the axis remain constant and do not affect the flight time. The velocity component considered in the following calculations is $v_x=v_0+\delta$, where v_0 is the axial velocity component after acceleration for an ion ejected from the target with zero velocity and δ specifies the velocity spread.

The incident angle of the ion beam to the field region being θ , the following relationship is obtained:

$$mv_0^2/2 = qeV_0 \cos^2 \theta = E_k$$

The flight time of an ion with zero initial velocity is calculated first. It is convenient to define a reference plane perpendicular to the x axis just out of the acceleration region, as shown on figure 4, and to calculate the time-of-flight from this plane to the detector. For the sake of simplicity, corrections due to the finite distance between the target and this plane will not be considered here. The distance between the reference plane and the boundary of the ion mirror is L_1 and that between the boundary of the mirror and the

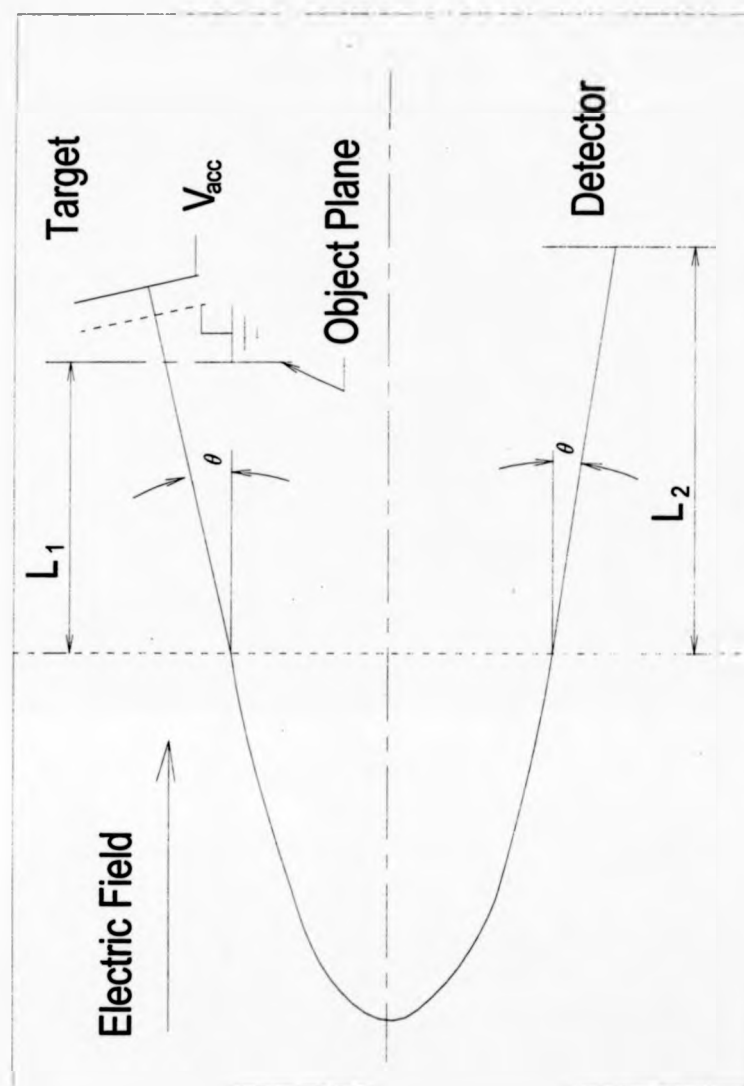


Figure 4. Schematic diagram showing the flight path of an ion in a single-stage reflectron time-of-flight analyser.

detector is L_2 . Since the axial velocity component is simply reversed by reflection, its magnitude is the same in both L_1 and L_2 , therefore the time spent in field-free flight is $t_f = L/v_0$ where $L = L_1 + L_2$. The time spent in the mirror is $t_M = 2v_0/\alpha$, where the acceleration $\alpha = qeE/m$ where qe is the charge and m is the mass. The total time of flight is:

$$t = t_M + t_f = \frac{2m}{qeE} v_0 + \frac{L}{v_0} \quad \text{Eq. 1-17}$$

When a deviation δ in the velocity is considered, the above equation becomes

$$t = \frac{2m}{qeE} (v_0 + \delta) + \frac{L}{v_0 + \delta} \quad \text{Eq. 1-18}$$

Expanding the second term as a function of δ gives

$$t = \frac{2m}{qeE} (v_0 + \delta) + \frac{L}{v_0} - \delta \frac{L}{v_0^2} + \delta^2 \frac{L}{v_0^3} - \delta^3 \frac{L}{v_0^4} + \dots \Rightarrow \quad \text{Eq. 1-19}$$

$$t = \left[\frac{2mv_0}{qeE} + \frac{L}{v_0} \right] + \frac{\delta}{v_0} \left[\frac{2mv_0}{qeE} - \frac{L}{v_0} \right] + \left(\frac{\delta}{v_0} \right)^2 \frac{L}{v_0} - \left(\frac{\delta}{v_0} \right)^3 \frac{L}{v_0} + \dots$$

The linear term in this expression is equal to zero when

$$\frac{2mv_0}{qeE} = \frac{L}{v_0}$$

or

$$E = \frac{2mv_0^2}{qeL} = \frac{4T_0}{qeL} \quad \text{Eq. 1-20}$$

T_0 is the kinetic energy of the ions. For this value of E , $t_M = t_R = L/v_0$, i.e. the ion spends the same amount of time in the mirror and in the field-free region. The flight time is:

$$t = \frac{L}{v_0} \left[2 + \left(\frac{\delta}{v_0} \right)^2 - \left(\frac{\delta}{v_0} \right)^3 + \dots \right] \quad \text{Eq. 1-21}$$

It is therefore independent of axial velocity to the first order for ions of every mass. To the first approximation the time of flight is:

$$t = \frac{2L}{v_0} = \left[\frac{2L}{\sqrt{2V_0}} \right] \sqrt{\frac{m}{qe}} \cdot \frac{1}{\cos\theta} \quad \text{Eq. 1-22}$$

The flight time is proportional to $\sqrt{m/qe}$, as in a linear time-of-flight instrument. The stopping distance can be calculated by the expression $T_0 = lqeE = l4T_0/L$, so $l = L/4$. As the average axial velocity inside the ion mirror is $v_0/2$, the effective length is twice $2 \times L/4 = L$.

1.1.2.3.1.2 Double stage reflectrons.

From the preceding section it is obvious that using a single stage ion reflectron as part of a time-of-flight instrument results in velocity spread correction to the first approximation. As Mamyrin has shown [25,26,27], it is possible to make the second order term vanish as well by introducing another free parameter in the equations of motion. This is achieved by using a double stage mirror. There is a second grid within the ion reflectron, in order to define two homogeneous field regions with different electrostatic field values. In figure 5 the schematic of a double stage reflectron is shown. Mamyrin introduced a

way to represent the energy spread of the ions: the ion energy after the ion source is $U=KU_0$, where U_0 corresponds to the mean energy of the ions ($=qeU_0$). For low relative energy spreads, K is close to unity and can be represented as $K=1+\varepsilon$ where $\varepsilon \ll 1$.

The total time of flight in this instrument from the exit of the ion source to the ion detector is $t = t_L + t_B + t_R$ where t_L is the total time of flight in the field free region, t_B and t_R are the flight times in the retarding and reflecting regions respectively. The following relationship applies:

$$t = \frac{L}{\left(2qe\frac{U_0}{m}\right)^{1/2}} K^{-1/2} + \frac{4d_B}{\left(2qe\frac{U_0}{m}\right)^{1/2}} \frac{U_0}{U_B} \times \left[K^{1/2} - \left(K - \frac{U_B}{U_0}\right)^{1/2} \right] + \frac{4d_R}{\left(2qe\frac{U_0}{m}\right)^{1/2}} \frac{U_0}{U_R} \left(K \frac{U_B}{U_0}\right)^{1/2} \quad \text{Eq. 1-23}$$

where d_B , U_B , d_R and U_R are parameters of the ion mirror regions (length and potential, Figure 5). The above equation can be reduced to

$$t = \frac{L}{\left(2qeU_0\right)^{1/2}} \left\{ K^{-1/2} + A_B \left[K^{1/2} - (K - P)^{1/2} \right] + A_R (K - P)^{1/2} \right\} \Rightarrow$$

$$t = \frac{L}{\left(2qeU_0\right)^{1/2}} F_1 \quad \text{Eq. 1-24}$$

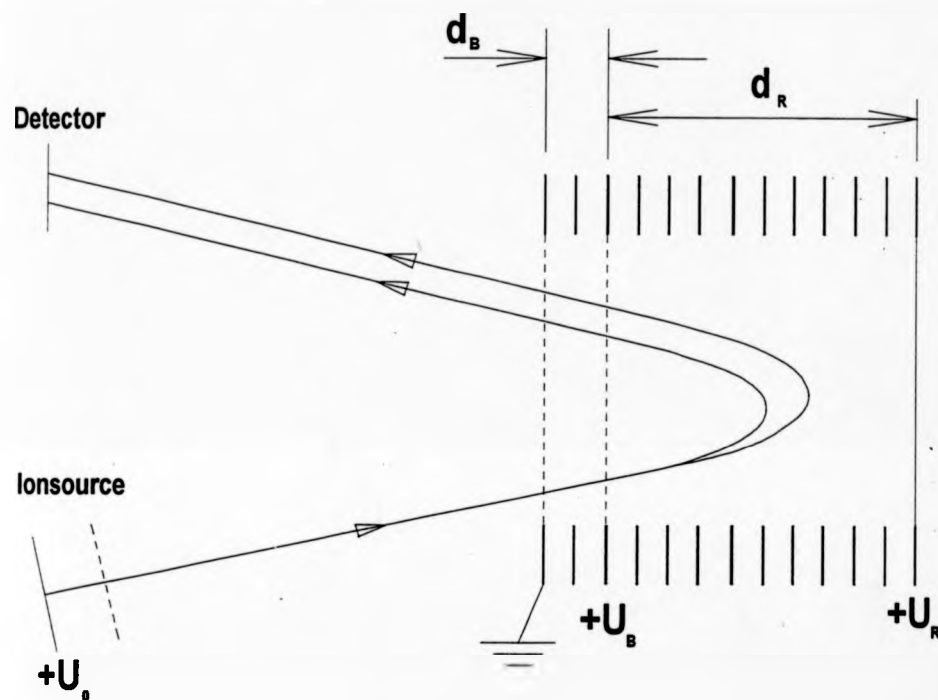


Figure 5. Schematic of a time-of-flight mass spectrometer with a double stage ion reflectron.

where F_1 is a function representing the dependence of t on $K=U/U_0$ with parameters

$$A_B = \frac{4d_B U_0}{L U_B}, \quad A_R = \frac{4d_R U_0}{L U_R}, \quad P = \frac{U_B}{U_0}$$

It can be seen from Eq. 1-23 that the flight time t is a function of 4 parameters

$$t = t \left[\frac{d_B}{L}, \frac{d_R}{L}, \frac{U_R}{U_0}, \frac{U_B}{U_0} \right]$$

and K , which is a representation of the range of the permitted ion energies U_{\max}/U_{\min} . In figure 6 a multiple graph is shown representing the above function for different values of the free parameters. Case (α) represents the optimum situation, where times-of-flight are equal at points 1 and 2 as well as 3 and 4 and $dt/dU=0$ at points 2 and 3. Hence there are four coupled equations (one for each of the four points) whose solution for the given value U_{\max}/U_{\min} enables the whole set of parameters to be determined. The resolution for the optimum case is

$$R_u = \frac{U}{\Delta U} = \frac{i_0}{2(t_{\max} - t_{\min})}$$

Schmikk and Dubenskij [28] first published such considerations. A more recent paper with a similar approach [29] reported that for $U_{\max}/U_{\min} = 1.05, 1.1$ and 1.2 the ultimate resolution becomes 370×10^3 , 50×10^3 and 7×10^3 respectively (ignoring other resolution-reducing parameters).

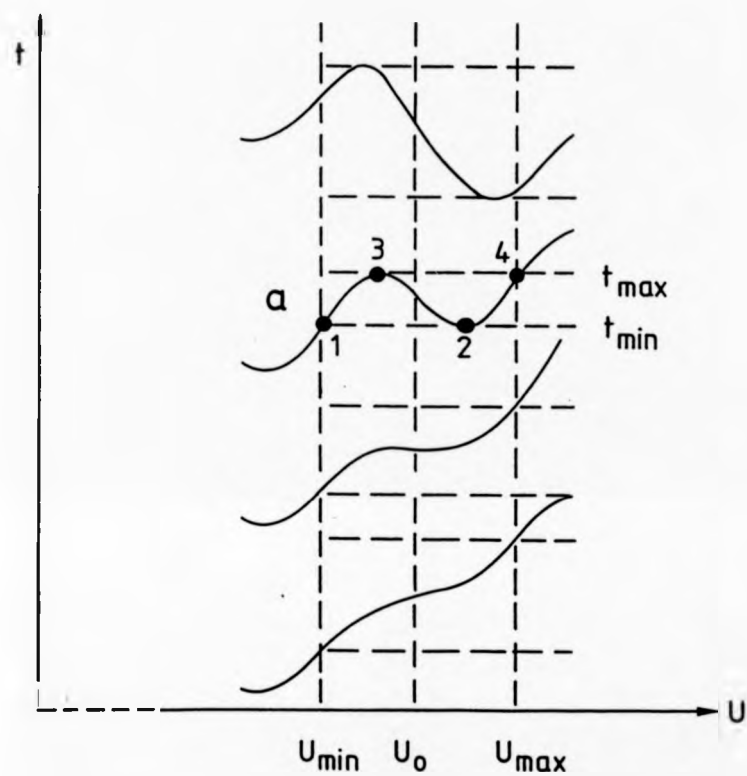


Figure 6. Ion flight times as a function of energy in a time-of-flight mass analyser with a double-stage reflectron [30].

1.1.2.3.1.3 Quadratic field reflectrons.

The addition of a second finite region of different potential gradient can make the second-order time aberration term vanish, resulting in large resolution enhancement for ion beams with higher energy spreads. Extending this reasoning further, if a field with an infinite number of appropriate changes of potential gradient was introduced, all orders of time aberrations could be made to vanish. Such a case would mean that the flight time in the ion reflectron would be completely independent of the initial velocity of the ions and would only depend on the mass over charge ratio. The physical analogue of a mirror with this characteristic is a pendulum, where the frequency of a body is only dependent on its mass and the length of the pendulum. The potential distribution equation that describes such an electrostatic field has the general form (figure 7):

$$U(x) = \frac{k}{2} \cdot (x - a)^2 + C \quad \text{Eq. 1-25}$$

k , a and C are constants. a is the coordinate of the point of potential minimum.

The equation of motion along x is:

$$\ddot{x} = -\frac{qe}{m} k \cdot (x - a) \quad \text{Eq. 1-26}$$

q is the number of charges of an ion. Adopting $qe/m > 0$ and $k > 0$, solution of the above equation is readily obtained:

$$x(t) = a + (x_0 - a) \cdot \cos \omega t + \left(2 \frac{V_0}{k}\right)^{\frac{1}{2}} \cdot \sin \omega t \quad \text{Eq. 1-27}$$

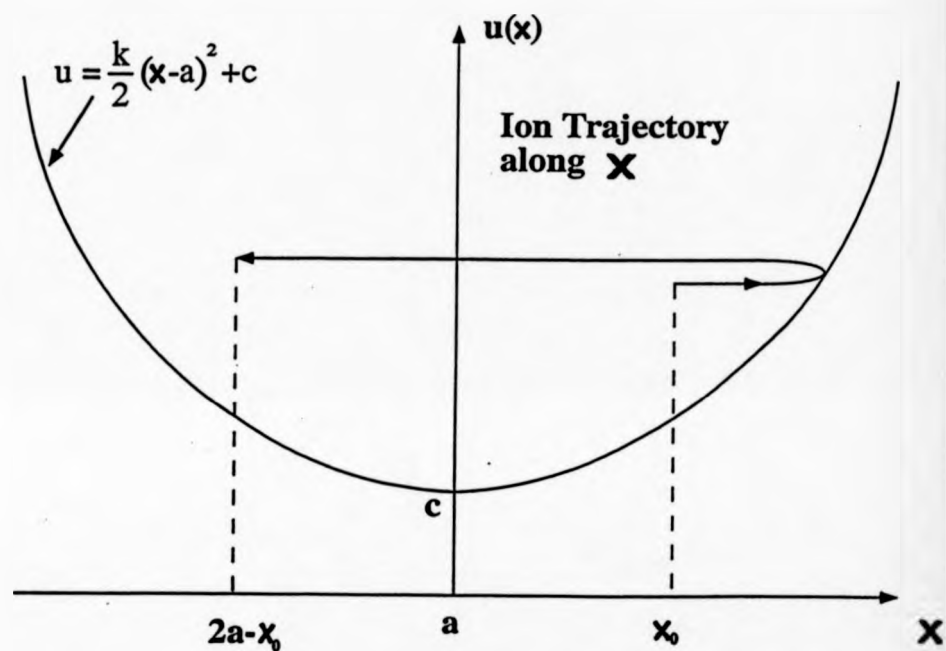


Figure 7. Potential distribution in quadratic fields along the ion optical axis x is the initial coordinate (starting point) of an ion. $2a-x_0$ is the coordinate of ideal time focusing.

The frequency of oscillations ω is given by:

$$\omega = \left(\frac{qe}{m} k \right)^{\frac{1}{2}} \quad \text{Eq. 1-28}$$

x_0 is the initial coordinate of an ion and V_0 is the accelerating potential experienced by the ion.

From Eq 1-27 it is obvious that after integer numbers of half-periods:

$$T_n = \left(\frac{\pi}{\omega} \right) \cdot n \quad n=1, 2, 3... \quad \text{Eq. 1-29}$$

That is to say that, after each reflection in the field coordinate x becomes:

$$x(T_n) = a + (x_0 - a) \cdot (-1)^n \quad \text{Eq. 1-30}$$

Thus reflection is completely independent of the initial energy qeV_0 .

The Laplace equation must be satisfied for any electrostatic field. As shown in [31], Eq. 1-25 becomes on applying this condition:

$$U(x, y, z) = \frac{k}{2} \cdot (x - a)^2 + W(y, z) \quad \text{Eq. 1-31}$$

where

$$\frac{\partial^2 W}{\partial y^2} + \frac{\partial^2 W}{\partial z^2} = -k \quad \text{Eq. 1-32}$$

Considering an ion beam with initial parameters ion energy spread $q\epsilon$, coordinate spread Δ and angular spread in all directions α reflected in a three-dimensional field as described above, flight time T_n remains independent of all initial parameters and depends only on specific charge qe/m [31]

$$TOF\left(q\varepsilon, \Delta, \alpha, \dots, \frac{qe}{m}\right) = T\left(\frac{qe}{m}\right) \quad \text{Eq. 1-33}$$

The above equation is equivalent to TOF focusing up to infinite order (including first-order, second-order, third-order etc.) for any set of the initial parameters, therefore the term "ideal time-focusing" seems to be the most appropriate.

As shown in [32], the variety of fields with ideal time-focusing is much wider than those described by Eq. 1-31, 1-32 above and includes a number of static electromagnetic fields. When demands of high transmission and especially simplicity of construction are taken into account, however, it appears that only a few fields can be practically useful, all of them being electrostatic. These are:

1) axially-symmetrical hyperbolic potential:

$$U(r, z) = \frac{k}{2} \cdot (z - a)^2 - \frac{k}{4} \cdot r^2 + C \quad \text{Eq. 1-34}$$

r, z are cylindrical coordinates. k, a and C are constants.

2) planar hyperbolic potential [33, 34]:

$$U(x, y, z) = \frac{k}{2} \cdot (x - a)^2 - \frac{k}{2} \cdot (y - b)^2 + d \cdot z + C \quad \text{Eq. 1-35}$$

a, b and d are constants (usually $b=d=0$).

3) axially-symmetrical hyper-logarithmic potential:

$$U(r, z) = \frac{k}{2} \cdot (z - a)^2 - \frac{k}{4} \cdot r^2 + b \cdot \ln\left(\frac{r}{d}\right) + C \quad \text{Eq. 1-36}$$

$d>0$ and $b>0$ are constants [35].

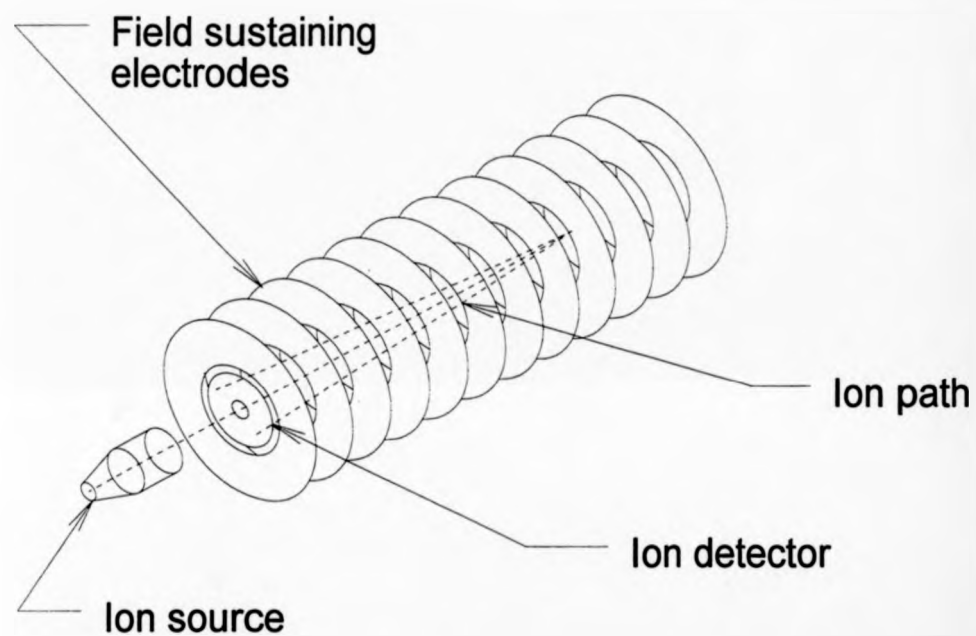


Figure 8. Schematic of the quadratic ion mirror time-of-flight instrument introduced by Yoshida [37].

The main drawback of fields described above is their high divergence in the r - or y -direction. For example, the equation of motion along y in the field described by Eq. 1-35 for $b=0$ is:

$$\frac{d^2 y}{dt^2} = \frac{qe}{m} \cdot k \cdot y \quad \text{Eq. 1-37}$$

or

$$y(t) = y_0 \cosh(\omega t) + \left(\frac{2V_0}{k} \right)^{\frac{1}{2}} \cdot \tan \alpha \cdot \sinh(\omega t) \quad \text{Eq. 1-38}$$

where y_0 is the initial y -coordinate and $\tan \alpha$ is the tangent of the initial angle to the y -axis. The hyperbolic functions in Eq. 1-38 means that the motion along y is unstable and a detector of large size is necessary. For ions starting from a narrow slit (i.e. when y_0 may be neglected) and reflected once in the quadratic field, it may be shown that the detector dimension in the y -direction should be $\sinh(\pi)/\pi \approx 3.676$ times larger than that in z -direction.

An account of theoretical considerations on quadratic fields was presented by Rockwood and [36] Yoshida [37] demonstrated the construction of a time-of-flight instrument featuring an ion mirror with a rotationally symmetric quadratic electrostatic field (figure 8). The field was sustained by a number of ring electrodes connected with a resistor chain. The resistors were appropriately chosen so that each electrode has the correct potential to approximate the chosen field function in the centre axis of the mirror.

A way of creating a rotationally symmetric quadratic field, without utilising flat finite electrodes, is to use a pair of cylindrical symmetry appropriately

shaped electrodes: one conical and one hyperbolic electrode arranged as shown in figure 9. A time-of-flight instrument with a pair of pure mathematical geometry large-scale electrodes is under construction in the department of Chemistry, University of Warwick. A laser ion source situated near the apex of the cone creates an ion packet that time-focuses at the theoretically optimum position for the mirror geometry.

Cotter and coworkers have described a reflectron time-of-flight mass spectrometer, where the potential distribution in the ion mirror empirically approximates that of a rotationally symmetric ideal ion reflectron [38]. The main difference between this instrument and that of Yoshida is the longer field-free region in the former.

Hamilton and coworkers have [39] described a pure-geometry prototype instrument featuring the planar symmetry quadratic field described by Eq. 1-35. It comprised a 90° vee electrode kept at ground potential and a hyperbolic surface at a high positive potential V_H (see figure 10). If the trajectory of an ion remains on the bisector of the vee, the ions time of flight from $x=0$ back to $x=0$ is given by

$$TOF = \left(\frac{\pi}{\sqrt{2}} \right) \left(\frac{x_0}{\sqrt{V_H}} \right) \sqrt{\frac{m}{q}} \quad \text{Eq. 1-39}$$

x_0 is the distance of the hyperbola from the vee along the x -axis, V_H is the potential of the hyperbola, and m is the mass of the ion and q is its charge. From the above equation it can be seen that the flight time is proportional to

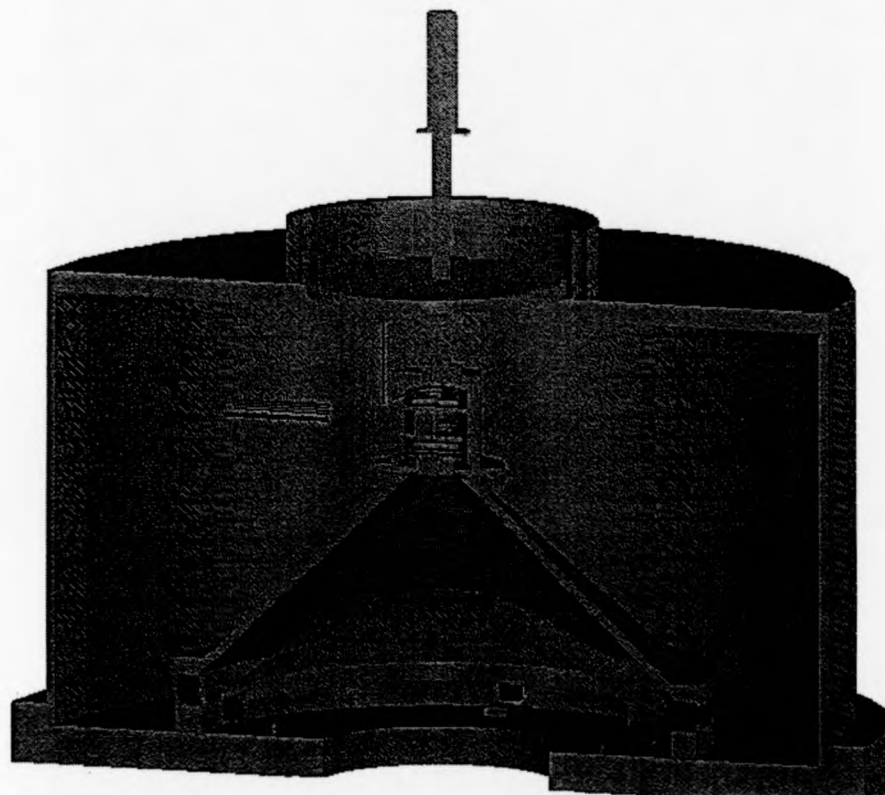


Figure 9. Assembly drawing of a time-of-flight instrument incorporating a quadratic ion mirror. The quadratic potential distribution is created by pure geometry field-sustaining electrodes.

the square root of the ion's mass to charge ratio and is independent from its energy.

This instrument was designed for in-space elemental analysis of ions in the solar wind. It was therefore compact in dimensions featuring very short flight times (up to 392 ns for Fe^+), making the achievement of high resolution problematic. Nevertheless, its ideal focusing characteristics allowed resolution in excess of 100 for high energy-spread beams.

1.1.3 Ionisation techniques.

1.1.3.1 Historical overview

Evolution of mass spectrometry has been as dependent on discovery of new ionisation techniques, which opened new horizons in new compounds to be studied and methods to be standardized, as on development of novel analysers. Discharge ionisation may have been what sparked the interest in the unexpected parabolic shapes in Thomson's first mass spectrometer, but broad acceptance of the technique came when electron beam ionisation (EI) was proven to ionise consistently gaseous atoms and small molecules. The next important step was field ionisation [40,41], chemical ionisation [42,43], and especially with the discovery of lasers, photo-ionisation [44,45].

The main limitation of all the above techniques was that they could only ionise volatile, and therefore relatively small compounds that could be readily transferred to the gas phase; no existing method could work with non-volatile liquids or solids. Probably the most important boost to the evolution of mass

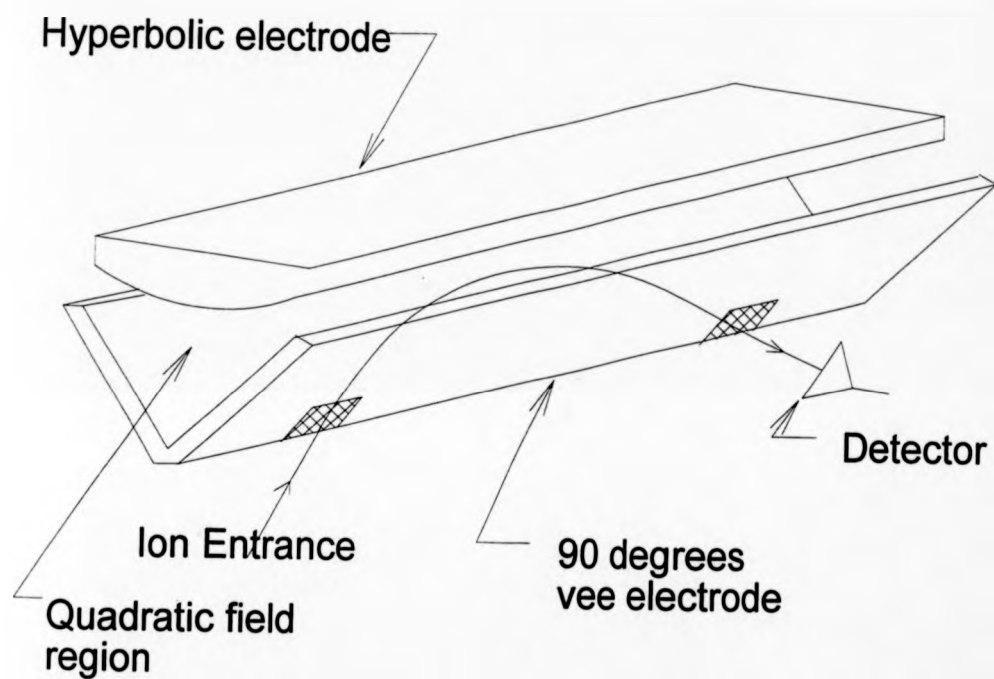


Figure 10. Schematic of the VMASS time-of-flight mass spectrometer

spectrometry after the discovery of EI was the introduction of various desorption/ionisation techniques that allowed large, non-volatile molecules to be brought to the gas phase, ionised and analysed in a mass spectrometer. The most important of these techniques are field desorption (FD) [46,47], thermospray ionisation (TI) [48], secondary ion mass spectrometry (SIMS) [49,50], fast atom bombardment (FAB) [51,52,53,54], plasma desorption (PD) [55,56], electrospray ionisation (ESI) [57,58], and laser desorption (LD) [59,60], of which matrix-assisted laser desorption/ionisation (MALDI) [61] is the most important branch. The most important desorption/ionisation methods are reviewed here.

1.1.3.2 Liquid - secondary ions mass spectrometry (L-SIMS).

Although initially SIMS was performed using dry samples, it was discovered that the use of a liquid matrix greatly enhanced stability, sensitivity and reproducibility of the technique. Hence fast atom bombardment (FAB) as well as liquid-SIMS (L-SIMS), techniques that evolved from SIMS, utilised liquid matrices. Most L-SIMS ion sources use Cs^+ as bombarding ions. The Cs^+ are typically accelerated to potentials in the order of 10 keV or higher (figure 11) and focused on the sample-droplet. The sample is a mixture of the analyte with a liquid matrix, such as glycerol. L-SIMS is routinely used for high-mass biological macro-molecules, up to approximately 10 000 Da in molecular mass [62]. It is a "soft" ionisation technique, inducing little fragmentation of the fragile biomolecules. It is an essentially continuous ionisation method, ideally

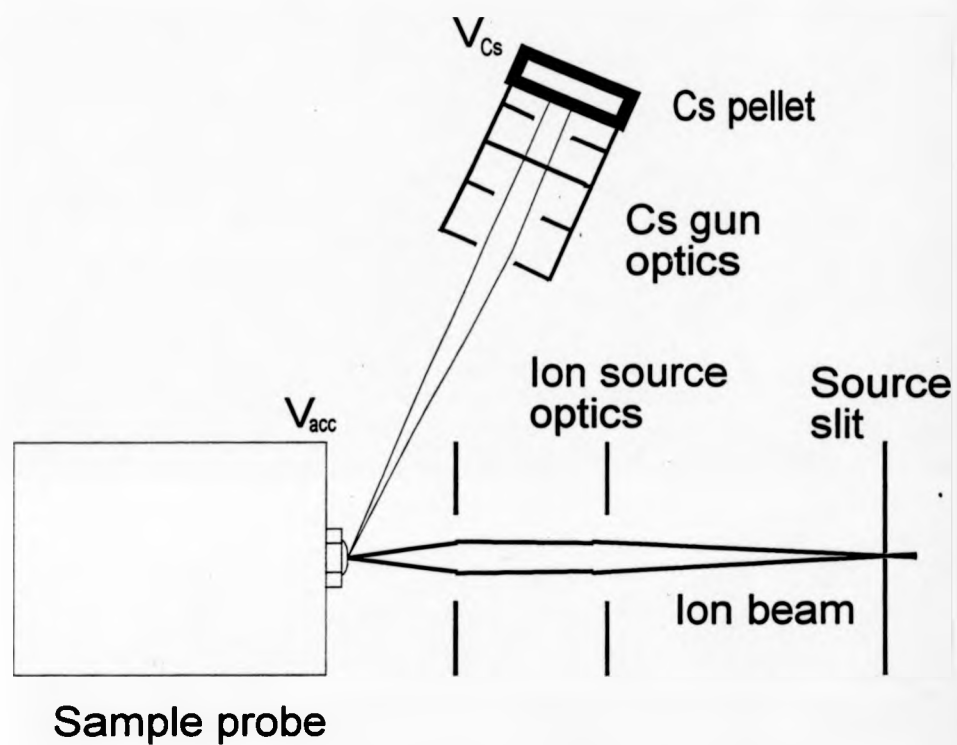


Figure 11. Schematic diagram of an L-SIMS ion source.

coupled with sector instruments and quadrupoles, although it could be pulsed if the Cs^+ beam were mechanically or electrostatically gated.

1.1.3.3 Laser desorption.

The first laser ion sources were introduced during the late 1960's-early 1970's. Inorganic and small organic ions were created from molecules in the gas phase, and analysed mainly by time-of-flight mass spectrometry [63,64]. A great variety of pulsed laser beams have been used for laser ionisation, with a wide variety of wavelengths from far-ultraviolet (UV) to infrared (IR) and various pulse time-lengths. The energy of a single photon from an ultraviolet laser is at the area of electronic excitation of most atoms and molecules, while infrared photons have enough energy to excite a molecule vibrationally and rotationally. By choosing the correct energy of photons, resonant multiphoton ionisation of a molecule or atom can be achieved, yielding very high sensitivity as well as selectivity. This task becomes especially feasible with the use of tunable wavelength lasers, like excimer-pumped dye lasers. In non-resonant multiphoton ionisation experiments, higher photon density is required, which may induce intense fragmentation of large organic molecules.

It has been possible to avoid thermal decomposition of thermally labile molecules, by carefully controlling the power density of the laser beam in the ionisation region. The monochromatic laser beam can be focused very tightly (into a very small spot), depending on the wavelength and on the power of the lens used. This feature, combined with the very short duration of a laser pulse, has made lasers particularly suitable for use with time-of-flight analysers.

1.1.3.4 Matrix assisted laser desorption and ionisation (MALDI).

The experiments described above involve direct laser desorption, where the laser strikes the pure solid or liquid sample deposited on a sample stage. It has been found that the upper mass of biopolymers which can be transferred into the gas phase intact using this method is about 1000 Da, while for synthetic polymers it can be a few thousands. Higher mass ions would require higher laser fluences and would therefore be destroyed by the laser light. In the 1980's Tanaka and coworkers [65] introduced the idea of using a matrix together with the biopolymer-analyte, in order to facilitate its desorption/ionisation without inducing fragmentation. This breakthrough came from the novel sample preparation method: the analyte was dissolved in glycerol and the glycerol solution was mixed with a fine metal powder. A droplet of this solution was irradiated with a focused nitrogen laser (337 nm) and the ions were analysed in a reflectron time-of-flight mass spectrometer. The glycerol is virtually transparent to 337 nm, but the light would have been absorbed by the metal powder with high efficiency. The metal particles used had dimensions smaller than the wavelength of the irradiating laser, therefore currents are created by the rapidly varying and spatially coherent electromagnetic field of the laser light. Consequently the metal particles heated up severely and, because of their low heat capacity, heat was transferred to the surrounding matrix. Although not totally understood, energy was consequently transferred to the analyte molecules, desorbing them into the

gas phase where they were detected as ions. Experiments performed with lysozyme yielded singly- and doubly-charged cluster ions.

In 1985, Hillenkamp et al [66,67] began promoting the hypothesis that large molecules could be ionised if an analyte was mixed with an organic matrix material, chosen to absorb strongly at the wavelength of the laser in use. The matrix would absorb sufficient light given a high enough fluence to result in its ablation. It was anticipated that ablated matrix would somehow carry into the gas phase the much larger analyte molecules. In the dense cloud just above the sample surface, chemical reactions occur giving a charge to enough of the analyte molecules to produce a mass spectrum by analysis in a time-of-flight mass spectrometer.

The above process describes what is believed to happen during the matrix-assisted laser desorption (MALDI) process. The first experimental demonstration was provided when nicotinic acid was used as the matrix with large polypeptide analytes [61]. Nicotinic acid is solid at room temperature with a low vapour pressure. Aqueous solution of the analyte biomolecule were mixed with nicotinic acid and dried. The crystals of the matrix molecules formed included molecules of the analyte at ratios of around 1000:1. Nicotinic acid absorbs light strongly around 266 nm, so the quadrupled Nd:YAG (base wavelength 1064 nm) was used to irradiate the crystallised mixture in the ion source of a reflectron time-of-flight mass spectrometer. Correct adjustment of the laser power and the matrix to analyte ratio resulted in very high signal-to-noise ratio mass spectra of the biological macromolecules studied.

The remarkable advantage of the method of sample preparation introduced by Hillenkamp over the one introduced by Tanaka lies in sensitivity: the former yields high quality results using picomoles or even femtomoles of the analyte [68] while the latter requires nanomoles. Sensitivity which is always a concern for all analytical methods, is especially important for precious biological samples. Apart from high sensitivity, MALDI also demonstrated extraordinary efficiency for the desorption and ionisation of very large molecules. Intact DNA molecules with mass of millions Da have been reported to be analysed successfully [69].

A lot of research has been devoted to studying and improving various aspects of MALDI. The analyte concentration is typically 10^{-5} or 10^{-4} M while that of the matrix solution is usually 10^{-1} M. Systematic study of various matrix-to-analyte ratios has shown that these can be varied from a few hundreds to a few hundred thousands [70]. It has been found that contaminants like salts, detergents or buffers do not significantly reduce the quality of the spectra, even at high concentrations [71,72].

One of the most important parameters for the MALDI process is the laser power. Low laser power does not yield any ions at first. As the power is increased, matrix and analyte ions start being recorded. This point is defined to be the threshold of the laser fluence for the specific matrix and analyte combination (see figure 12). The laser light fluence can be optimised for maximum signal-to-noise, which is usually found to be very near the threshold fluence. Higher laser power results in lower resolution and higher

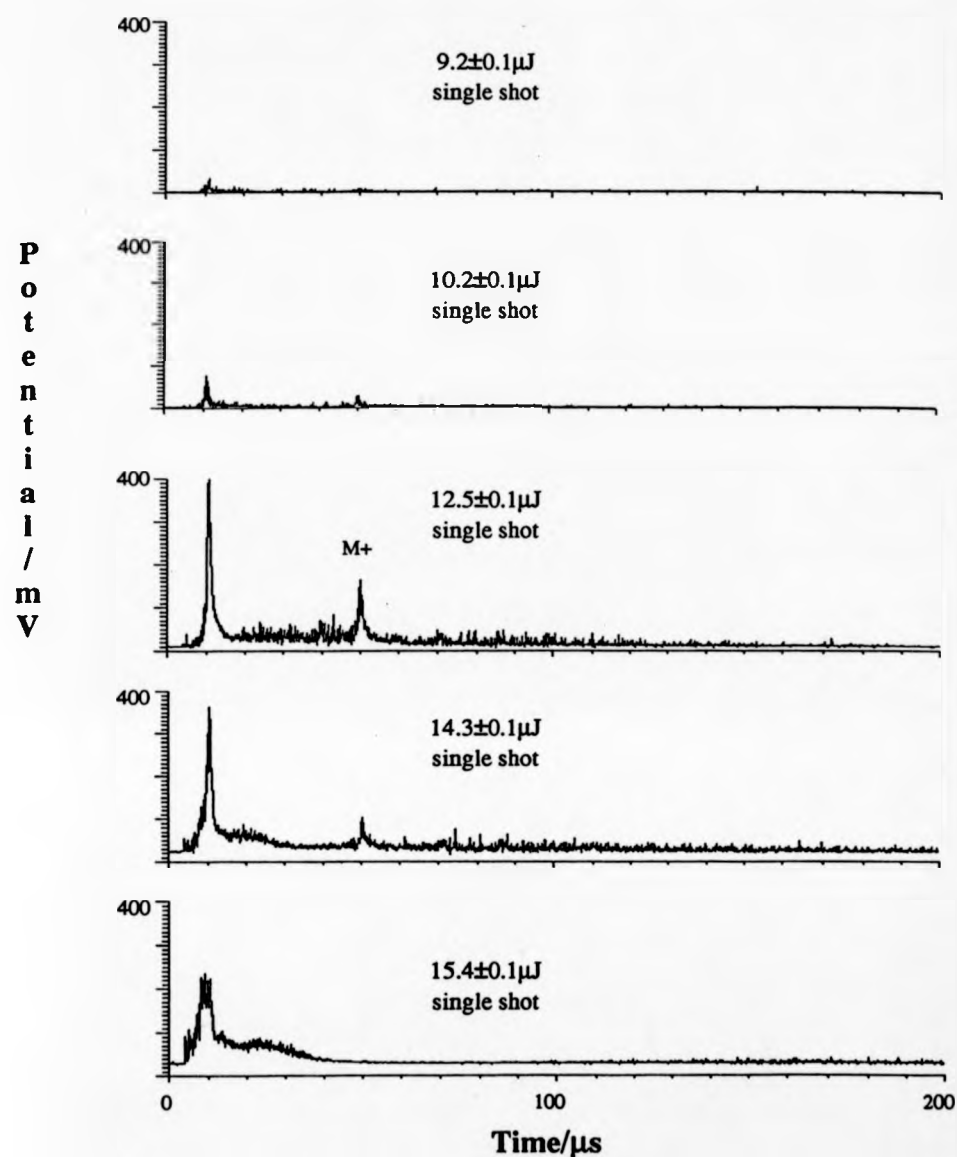


Figure 12. Positive ions MALDI spectra at 266 nm of bovine insulin with sinapinic acid as matrix at various laser fluences. The energy of the laser pulses is measured using a calibrated photodiode system [73].

noise, and eventually completely suppresses the analyte peak.

Under certain circumstances cluster ions (dimers, trimers, etc.) can be observed, especially when the analyte ratio is high. Sometimes doubly charged analyte ions are found. Careful choice of matrix and laser fluence can result in MALDI spectra where the analyte peak is the dominant and there are no matrix ions [74,75,76].

Often analyte molecules are ionised by proton attachment ($M+H^+$) but other adduct species have been observed [76]. Adduct peaks are caused by salts, and by fragments or intact matrix molecules. Chemical adduction has been found to increase with the mass of the analyte ion.

1.1.3.4.1 Matrices in MALDI

Firstly, in order for a compound to be suitable for use as a matrix it has to be readily introduced into solution together with the analyte biomolecule. Peptides and proteins are mainly dissolved in acidified water, water-acetonitrile mixtures or water-alcohol mixtures.

The second characteristic of a potential MALDI matrix is its absorption coefficient at the chosen laser wavelength. This may not be as straightforward as it sounds at first. It is easy to determine the coefficient for a solution of the compound, but it is a lot more difficult to do so for its solid crystals. The absorption curves of most compounds are red-shifted in the solid phase compared to their solution values, but the extent of this shift can vary from one compound to another. Although other wavelengths have been tested, it has

been found that UV light is more suitable for MALDI, probably because of the non-thermal manner in which it reacts with matter. Therefore the most successful matrices should absorb strongly at the near-UV wavelengths. Based on the solution absorption curves, the choice of matrices have been limited to aromatic compounds with electron-withdrawing groups on the ring.

The next requirement of the matrix molecule is to be chemically inert in terms of reactivity with biomolecules. Matrices that covalently modify proteins cannot be used. Oxidising agents should also be avoided in the case of proteins because of the lability of disulphide bonds and the tendency of cysteine and methionine groups to oxidise [77]. The N-terminal amino group of a protein and ϵ -amino groups of lysine are very susceptible to modifications such as Schiff base or amide formation. Aldehydes cannot be used for this reason.

Another necessary characteristic of a matrix is low sublimation rates. The sample must be introduced into vacuum for mass spectrometric analysis. High vapour pressure would disturb the vacuum and would result in significant changes during a single experiment due to the change of matrix-to-analyte ratio and the short life time of the sample.

Even when all the above criteria are met, most potential matrix compounds do not yield ions when tested experimentally. Apart from nicotinic acid mentioned earlier, a number of new matrices were introduced by Beavis and Chait [72] mainly aromatic carboxylic acids. These include 2-pyrazinecarboxylic acid and 4-hydroxy-3-methoxybenzoic acid (vanillic acid). The same researchers later introduced several derivatives of cinnamic

acid, such as 3,4-dihydroxycinnamic acid (cafeic acid), 3-methoxy-4-hydroxycinnamic acid (ferulic acid) and 3,5-dimethoxy-4-hydroxy cinnamic acid (sinapic acid)[78] (see figure 13). These matrices improved sensitivity and were found to yield $(M+H)^+$ ions while reducing adduct formation.

The cinnamic acid matrices family works equally well at the third or the fourth harmonic of the Nd:YAG laser (355 or 266 nm). Nitrogen lasers emit light of 337 nm of very low angular divergence and high enough power for MALDI. Nitrogen lasers are compact, very economical and require little maintenance, and are therefore ideal for use with MALDI instruments. The success of the nitrogen laser has been one of the important factors in the widespread use of MALDI.

A very favourable matrix molecule introduced by Karas et al [76] is 2,5-dihydroxybenzoic acid (DHB). It produces peptide and small protein ions at high sensitivity. It can be used with nitrogen lasers. Good results have also been observed for glycolipids [79], carbohydrates [80] and for profiling enzymatic digests [81]. Other matrices currently in wide use with proteins are gentisic acid [82] and α -cyano-4-hydroxycinnamic acid [83] (figure 13).

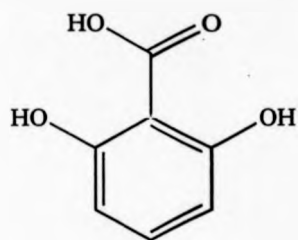
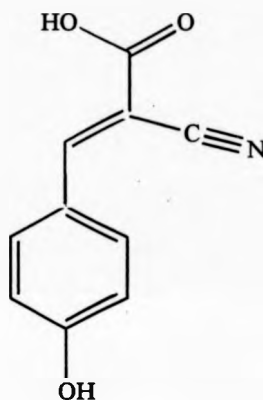
1.1.3.4.2 MALDI and time-of-flight mass spectrometry

MALDI being an essentially pulsed ionisation technique is naturally coupled with time-of-flight mass spectrometry. The great majority of the work reviewed above involves linear or various types of reflectron TOF instruments. Only recently have there been attempts to couple MALDI with other mass

analysers such as sector instruments or Fourier–transform ion cyclotron resonance (FT–ICR) mass spectrometers.

The only drawback of MALDI as far as time–of–flight is concerned is the high energy spread of the analyte beam. This energy spread is mainly due to the spread of initial velocities of the analyte ions [84]. The accepted remedy for minimising the effect of high energy spread on resolution in time–of–flight mass spectrometry had been to increase the accelerating potential. With MALDI there is one more valid reason to do so: unusually large ions have to be accelerated to high energies in order to be detectable. With matrix–assisted laser desorption and ionisation, however, problems crop up when there is a high potential gradient just above the sample surface. In fact, these problems lead to further increases in the energy spread. As molecules are ablated from the sample surface, they create a dense plume of mainly neutrals leaving the surface with velocities of the order of 500 to 1000 m/s [85]. As soon as analyte ions become ionised, they “feel” the high accelerating potential and they acquire extra velocity. Being in a dense plume, they randomly collide with neutral molecules, being severely deflected or even virtually stopped. They subsequently reaccelerate and perhaps collide again, until they escape from the dense plume region into the high vacuum region of the mass spectrometer. This process, apart from creating some unwanted fragmentation, causes two main effects: firstly, an energy deficit from the expected laboratory frame energy is observed (taking into account the initial velocities) because of the stopping

2,5-dihydroxybenzoic acid (DHB)

 α -cyano-4-hydroxy-cinnamic acid (α -CHC)

3,5-dimethoxy-4-hydroxy-cinnamic acid (sinapinic acid)

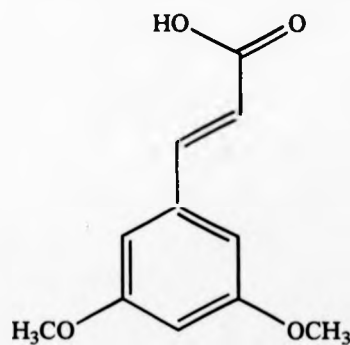


Figure 13. Chemical compositions of some of the most widely used matrices in MALDI mass spectrometry.

and re-accelerating of the ions. Secondly, because of the random nature of the process, energy spread is most likely to increase [85].

In response to the above, a "novel" solution has been recently proposed (reflecting all the way back to the Wiley-Maclaren instrument): delayed extraction. The principle is simply to allow ions to drift away from the sample surface field-free for a while after the laser pulse and then apply a step-function pulse to the extraction region. The key to this technique (and the reason why it works so much better than in the Wiley-Maclaren case) is that as ions drift field-free with their initial velocities, those with higher energy cover more space than the rest. At the end of their field-free expansion, they find themselves in a position directly related to their initial velocity. When the extraction pulse is switched on, ions at the front end of the extraction region (i.e. those that had higher initial energy) acquire less energy than those in the rear end. Correct choice of the delay and value of the extraction pulse can result in near-complete elimination of the energy spread effect on resolution, even for a linear mass spectrometer. An added bonus is that during the field-free expansion the plume has become less dense, therefore no further energy spread or unwanted fragmentation is induced because of collisions with neutrals.

Delayed extraction time-of-flight (DE-TOF) mass spectrometers have been reported to demonstrate mass resolution up to 10,000 [86]. The routine high mass resolution allowed further questions to be brought forward, such as mass accuracy of MALDI TOF mass spectrometry. It has been found that fine

adjustment of the shape of the extraction pulse, and/or taking into account initial velocities of various analytes in relation to their masses and the utilised matrices, can consistently afford mass accuracy better than 5 ppm [87].

1.1.3.5 Electrospray ionisation

Electrospray ionisation has recently enjoyed greatly increased interest from the mass spectrometry community. The initial idea was put forward almost 30 years ago in the 1960's by Dole et al [88]. The idea was taken up again in the 1980's by Fenn and coworkers. Much of the work that established electrospray has been carried out in the group of Richard Smith of Pacific Northwest Laboratories [89] and in Henion's group at Northwest University [90].

One of the advantages of electrospray ionisation is the non-elaborate sample preparation. Biological molecules are introduced in solution into a syringe and directly ejected through a liquid chromatography type capillary into a small diameter tip held at high potential (a few kV) at atmospheric pressure. A fine spray is produced with most of the droplets possessing high charge. To establish a stable spray, it is important to control the composition of the solution, the conductivity of the capillary and the needle-tip, the surface tension of the liquid and the flow rate of the liquid. In some electrospray source designs a part of the capillary is heated to assist in the fine spray formation by evaporation of the solvent. The spray is passed through one or two usually conical skimmers into increasingly higher vacuum regions. During this process evaporation of the solvent from the droplet leads to the desorption of the analyte molecule, which is commonly found at a high-charge state.

Various models have been proposed for the mechanism of ion creation. Dole and al proposed that ions originate from small droplets containing one molecule of the analyte. Thomson and Iribarne suggested field-induced evaporation from charged droplets [91]. As the droplet shrinks due to solvent evaporation, it is proposed that when it reaches a certain radius it becomes disrupted due to Rayleigh instability [92]. Another model suggests that the droplet electrohydrodynamically disintegrates by removal of an ion with part of its solvation sphere [93]. A definite model cannot be determined because many elements of the process remain unknown. For example, the final evaporation of the droplets may proceed through Coulombic explosions [94] for which the mechanism is not clearly understood.

A correctly tuned electrospray source results in a strong continuous ion current of analyte ions in a variety of high-charge states. A general rule is that larger analyte ions possess more charges than smaller ones. Because of that the mass-to-charge ratio remains fairly low even for large analyte molecules, allowing mass spectrometric analysis to be carried out with instruments with low mass-to-charge capabilities. Most commonly electrospray sources have been coupled with quadrupole mass spectrometers, although electrospray is recently extended to sector instruments, FT-ICR and ion trap mass spectrometers. The most recent development has been the coupling of electrospray with time-of-flight mass analysers, using ion extraction perpendicular to their original direction (orthogonal extraction TOF) [95].

Electrospray ionisation mass spectra often present difficulties in their interpretation due to the variety of charge states that a molecule may occur in. If the mass resolution is high enough for isotope separation, it becomes easy to identify the number of charges for every species by observing the mass difference between neighbouring isotopes, making the exact mass determination straightforward. If isotope separation is not possible, it may be a lot more difficult process, especially if a mixture of unknowns is analysed. In many cases, computer software may help to separate the mass from the charge distributions, while sometimes other mass spectrometric methods (like MALDI) have to be utilised.

1.1.4 Ion detectors.

The vast majority of time-of-flight instruments utilise one of two types of ion detectors: specially designed TOF electron multipliers or multi-channel plate (MCP) detectors. Electron multipliers feature a conversion dynode where the arriving ions collide and release electrons (figure 14). The electrons are accelerated towards the second dynode which results in the ejection of more electrons. They in turn are accelerated towards the next dynode and will create the next generation of electrons. After a certain amount of stages the amplified current is collected on an anode and measured with the help of a preamplifier. Typical electron multipliers demonstrate 10^6 amplification and a rise-time of a few ns. Electron multipliers designed specifically for use in TOF mass spectrometers feature a first dynode perpendicular to the ion path in order to

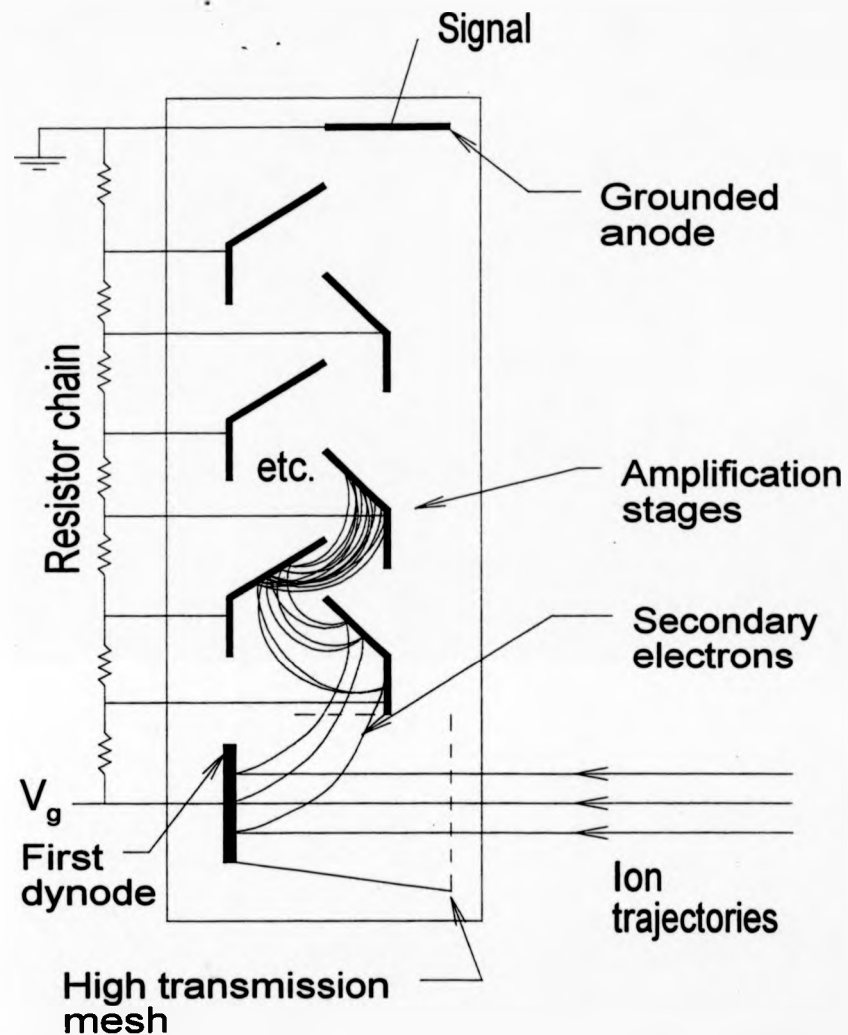


Figure 14. An electron multiplier optimised for time-of-flight use. The first dynode is perpendicular to the ion path to eliminate time-spread.

minimise time-of-flight aberrations. The flight time of the electrons from various parts of the first to the second dynode is minimised.

A multi-channel plate is a predominately glass plate which has a large number of small holes regularly arranged throughout its "active" surface. After special processing, the inside surface of the holes becomes enriched with a layer of a high-resistivity material. A potential difference is applied between the two faces of the plate, therefore a potential gradient is formed inside the holes. When an atom collides near the entrance of a hole, an ejected electron is accelerated towards the depth of the channel. An avalanche effect creates a large number of electrons coming out from the rear end of the plate. Signal is recorded by collecting the electrons on an anode. A matched pair of plates (both with the same resistivity and similar gain) is usually used to create a chevron assembly with gain of 10^6 – 10^7 depending on the potential across the plates.

Multi-channel plates are constructed by heating a large number of glass tubes until they fuse, then extruded to achieve the required channel diameter. The plates are sliced at appropriate angles and thickness and tested for dead channels. The flatness of the surface is critical when MCPs are to be used in time-of-flight mass spectrometers. The great advantage of multi-channel plates is that they can be very large in active dimensions, although a capacitively matched anode assembly may be required to quench signal reflections. They also are relatively compact as their thickness is around 1 mm per plate.

An important issue with ion detectors is their response linearity throughout a wide mass range (or its absence). Ion detectors are suspected to demonstrate mass discrimination effects, which is especially important for samples with a wide variety of different mass species. [96,97].

Both types of detectors described above have to destroy the ion in order to detect it. Induction detectors may detect ions that pass through their vicinity but are not appropriate for time-of-flight mass spectrometry due to their low efficiency and long rise time. In FT-ICR mass spectrometry, ions are inductively detected and they can be recollected for re-measurement.

1.2 Tandem mass spectrometry.

A tandem mass spectrometer is essentially a combination of two mass spectrometers in series with each other. The first mass spectrometer selects one of the ionic species present in the original sample, which is activated in the intermediate region and products are measured using the second mass analyser. This definition does not hold when ion trap-type mass analysers are involved. In this case the same analyser can be used to manipulate the ions, select the chosen species, activate it and measure its fragments.

The origin of tandem mass spectrometry has been the discovery of collision-induced dissociation (CID) [98]. When a molecular ion collides with a precursor gas atom, the collision energy absorbed by the ion will induce fragmentation characteristic of that ion.

CID is the most widely used activation method. Ideally a differentially pumped collision cell is installed in the intermediate region between the two mass analysers. The flow of the collision gas is controlled with a precision leak valve. Most commonly used collision gases are noble gases like He, Ar or Xe, although other gases can be used for specific purposes. Other activation methods include surface induced dissociation (SID), where parent ions fragment bouncing on a surface at shallow angles [99].

Initially tandem mass spectrometry was used for analysis of complex mixtures. Indeed, chemical purification of a mixture in order to extract a single substance is very laborious, time-consuming and often inaccurate. Tandem mass spectrometry is also capable of easily separating isomers present in the same sample by their distinctive fragmentation pattern [100]. Another application of complex mixture analysis using tandem mass spectrometry is described as selected parent-ion MS/MS. The first spectrometer is scanned while the second mass spectrometer is set to the mass of a specific fragment ion [101]. This technique can provide a measure of concentration of members of a class of closely related compounds in the mixture.

Apart from qualitative and quantitative determination of the components of complex natural and artificial materials, applications for tandem mass spectrometry include research on drug metabolites, characterisation of insect pheromones, trace contaminants in water, air or earth, polymer sequencing and petrochemicals. The list is becoming longer as more scientists and engineers

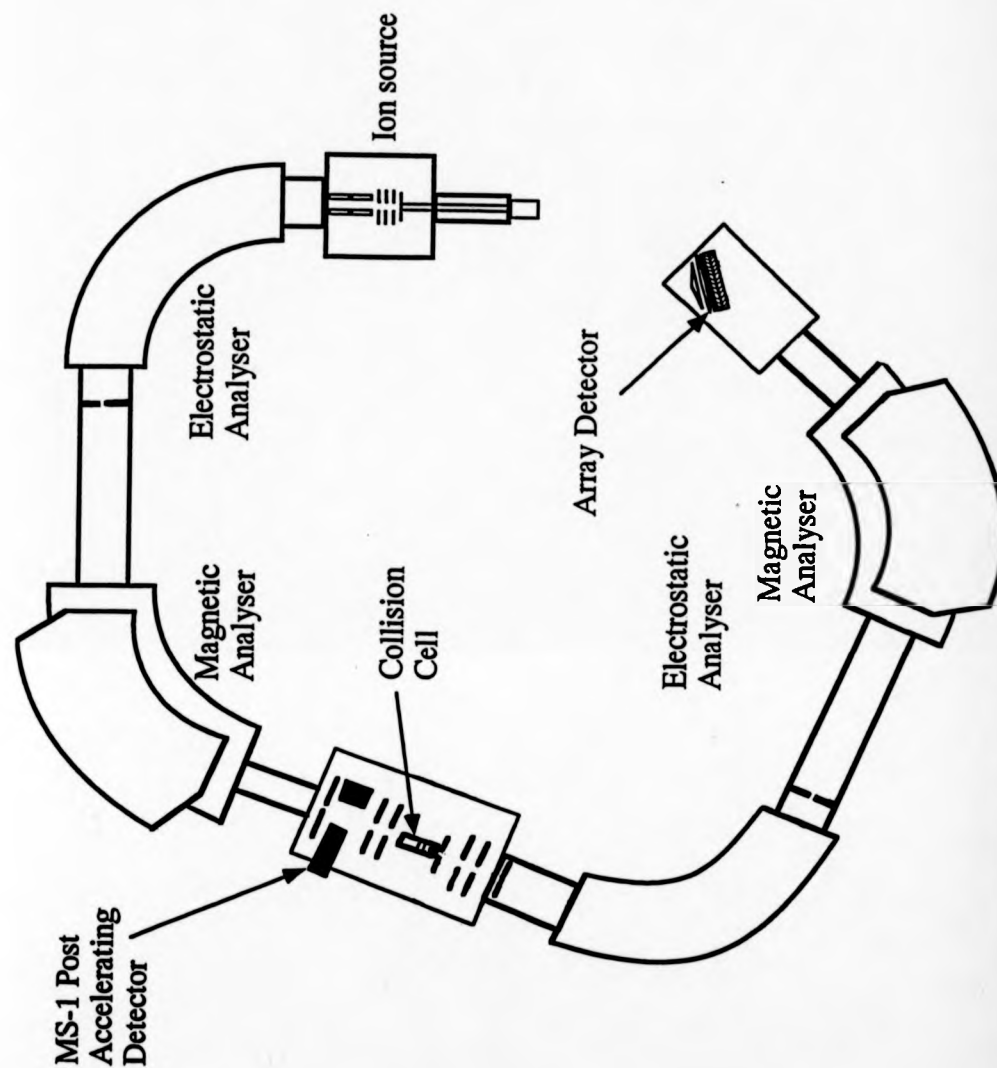


Figure 15. Schematic of the KRATOS 4-sector tandem mass spectrometer.

discover tandem mass spectrometry as the solution to more problems, and instruments become more affordable.

1.2.1 Instrumentation in tandem mass spectrometry.

The mass analysers most commonly used in tandem mass spectrometry are quadrupoles (Q), electric sectors (E) and magnetic sectors (B) in various combinations.

EBEB type instruments (four sector tandem mass spectrometers) comprise two double-focusing mass spectrometers (DFMS), most commonly utilising a CID cell in the intermediate region (figure 15). For steering the ions through the collision cell (CC), a series of electrostatic lenses and deflectors are installed throughout the intermediate region. The collision cell can be floated at different potentials for selection of collision conditions. In order to improve sensitivity, the second mass analyser is often equipped with an array detector. This is better than a point detector because more ions are transmitted and detected at every single moment throughout a tandem mass spectrometry experiment. Four-sector tandem mass spectrometers are highly sophisticated instruments, very effective but also complicated and expensive.

The most widespread type of tandem mass spectrometer is the QqQ combination (the lower case q reflecting the non-scanning nature of the middle quadrupole) (figure 16). A "soft" ionisation method is used like chemical ionisation or electrospray, which is becoming increasingly popular with this

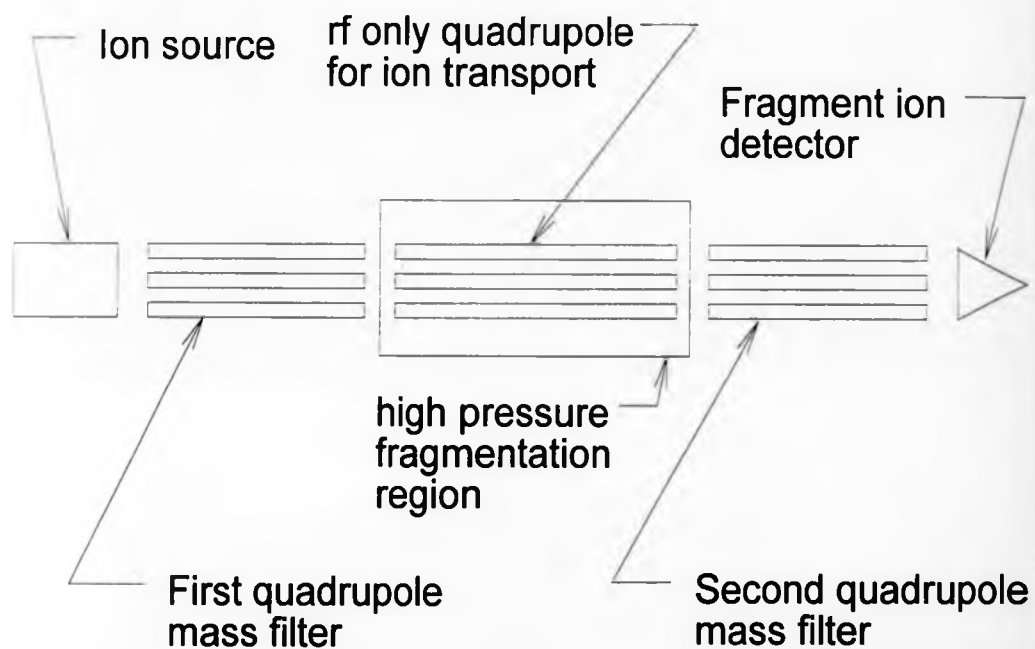


Figure 16. Schematic of a triple-quadrupole tandem mass spectrometer.

type of instruments. The ions are accelerated into the first quadrupole mass analyser where parent ion selection takes place. The ions enter the second quadrupole which is flooded with the collision gas at 10^{-3} to 10^{-4} torr. It is set to operate in the radio-frequency-only mode, thus no dc potential is applied on its rods. The result is that no mass separation takes place, but the quadrupole becomes a very efficient focusing device for scattered parent and fragment ions. Daughter ion spectra are measured using the third quadrupole.

Other hybrid combinations can be found such as EBqQ. Combinations of two time-of-flight analysis stages with a CID region between them have also been reported [102]. Other recent developments include an instrument similar to a triple quadrupole with the third quadrupole being replaced by an orthogonal extraction time-of-flight analyser (Qq-oaTOF) [103]. The advantage of the latter over the conventional QqQ instrument is higher sensitivity: TOF collects all ions after every orthogonal acceleration pulse.

Radio-frequency ion traps [104] and magnetic Fourier transform-ion cyclotron resonance (FT-ICR) [105] mass spectrometers are types of instruments ideal for tandem mass spectrometry. In these mass analysers rf-electric or high homogeneous magnetic fields are used respectively in order to trap the ions into known orbits near the centre of the trap cell. Ions can be selectively excited into higher orbits with a combination of appropriate electric fields, where they also acquire higher velocities. When a complex mixture has to be purified, all the unwanted ionic species can be excited until they collide with the walls of the trapping cell. The resolution of selective excitation is so

high in FT-ICR that isotopes of the same molecule can be totally quenched without the chosen mass being severely disturbed. If the pressure in the cell is increased by the introduction of a collision gas, excited parent ions undergo collision induced dissociation and fragment. Fragment ions can be collected back in the middle of the cell and detected with the standard methods used. In radio-frequency ion traps ions are highly excited during a mass scan and ejected out of the trap for measurement. In a magnetic Fourier transform – ion cyclotron resonance instrument, a broad band excitation bring all the ions in the trap near the walls of the trapping cell where they induce a current on the detector plates. The induced current is an actual representation of the frequency of ions as they orbit around the magnetic field. The frequency is directly connected to their mass according to the equation

$$m/z = B / 2\omega_c$$

B is the magnetic field and ω_c the cyclotron frequency of the ion. The Fourier transformation of the measured signal can be directly assigned to a mass spectrum with very high mass. Because fragment ions can be selected and re-fragmented in the same way as the parents, ion trap type instruments feature the capability of MS^n where for example a mixture can be purified as a first step, next one of its components sequenced, one of the fragments re-fragmented for exact identification and so on.

1.2.2 Collision-induced dissociation.

Even though the instrumentation and application of tandem mass spectrometry are so varied, most of the widely used instruments share a single common characteristic: collision-induced dissociation (CID), also referred to as collisionally activated decomposition (CAD). The dissociation of ions under poor vacuum conditions has been considered to be an unwanted drawback since the first steps of mass spectrometry [98]. Vacuum technology improvement eradicated the "problem" until it was put to work with linked scans at constant B/E in double-focusing analysers or in the activation region of tandem mass spectrometers. Until the 1970's a few works have been published examining the metastable decay of ions after collisional activation [106, 107, 108, 109]. McLafferty and coworkers recognised collisional activation as a tool in organic mass spectrometry [110, 111]. Two distinct types of collisional activation decomposition can be classified, according to the laboratory frame translational energy of the parent ions: low energy collisions, where the energy of the parent ions is below 100 eV, mainly appropriate for low energy instrumentation like quadrupole analysers [112] and high energy where the energy of the parent ions is a few keV, utilised in sector tandem mass spectrometers and time-of-flight analysers [113].

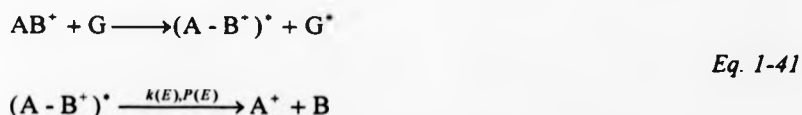
Collision-induced dissociation demonstrates a number of positive features. The cross section for collision-induced dissociation is generally between 10 to 200 Å², depending on mass. The cross section indicates the probabilities of the reactions, which are several orders of magnitude larger than those found with

photodissociation. The main aspect that controls the efficiency of the process is the local pressure of the collision gas in the activation region. This can be easily controlled over a wide range with the use of a differentially pumped collision cell, maintaining high vacuum conditions in the rest of the instrument. A type of Beer's law relationship applies to a typical tandem mass spectrometry experiment

$$I = I_0 e^{-n\sigma l} \quad \text{Eq. 1-40}$$

I_0 is the parent ion current without collision gas, I is the attenuated parent beam current, n is the target gas number density, l is the length of the collision cell and σ is the cross section of all the processes that contribute to parent ions' loss. These include fragmentation as well as charge exchange with the collision gas and severe scattering of the ions, making them undetectable. The competing loss processes can be controlled to a certain extent with the correct choice of collision gas and pressure in the collision cell.

The process of CID is believed to involve two steps [114,115]. The first step is collisional activation of the AB^+ ion with the neutral gas G and the second step is unimolecular dissociation.



where the rate of the second process depends on the unimolecular rate constant $k(E)$ and the internal energy distribution $P(E)$.

In 1970 Durup [116] created a classification of four processes for such a collisional energy transfer:

1. electronic excitation, which is predominant at higher energies
2. elastic scattering of one single atom of the ion
3. internal energy transfer in a long-lived ion-molecule complex, probable only at low energies and
4. perturbation to a highly excited species which leads to a transition to a repulsive electronic surface and subsequent dissociation.

Electronic excitation is believed to be the dominant pathway for collisions between atoms and small molecules. For larger projectile ions (i.e. 1000 Da) and translational energy of 8 keV the interaction times become of the order of the molecular vibrations (10^{-14} s). It is therefore possible that another pathway becomes possible. It has been found experimentally that the translational energy loss by the projectile ions decreases with increasing size of the noble gases used as target (He to Kr) [117]. In the same work by Bricker and Russell, this effect was correlated with the ionisation energy (IE) of the target gas. This hypothesis was disputed by Sheil and Derrick on the basis of experimental results [118] using He (IE 22.5) and D₂ (IE 15.5) when both appeared to be more efficient than Ar (IE 15.8). The impulsive collision transfer theory (ICT) proposed by Uggerud and Derrick [119] recognised the dependence on target gas mass as the primarily important factor and correlated

the process with the size of the part of the macromolecules that actually takes part in the collision.

The key assumption of ICT is that energy and momentum transfer takes place in a collision between the gas atom and one only atom of the ion (case 2 of the preceding list). Both atoms are considered to be hard spheres. The centre-of-mass collision energy E_{CM} of the system is

$$E_{CM} = \frac{m_g}{m_{ion} + m_g} E_k \quad \text{Eq. 1-42}$$

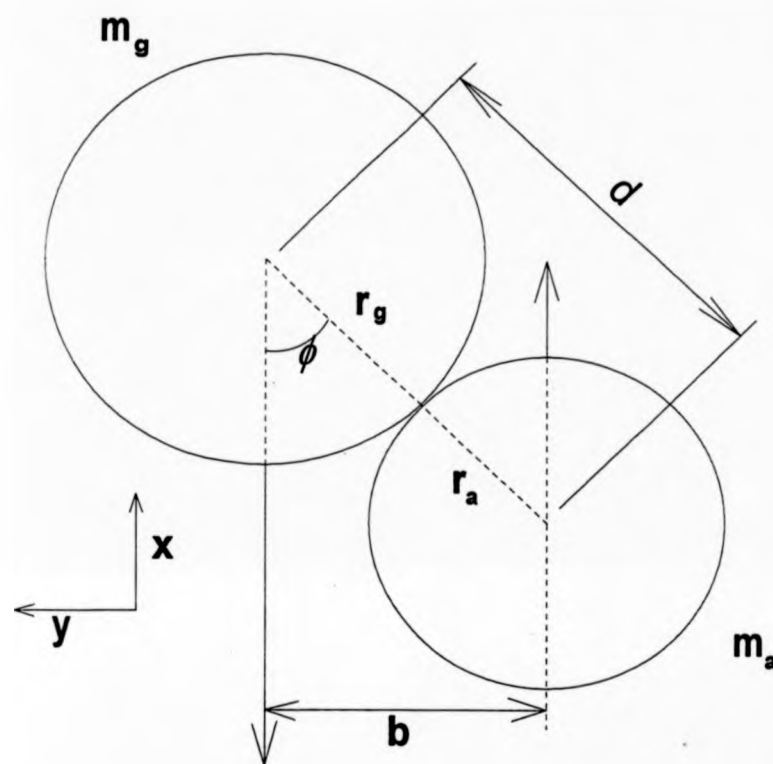
E_k is the laboratory frame kinetic energy of the projectile ion of mass m_{ion} and m_g is the mass of the collision gas. The theory derives expressions for the scattering angles of the parent ions, θ , as a function of the collision angle φ (figure 17) and the masses m_{ion} , m_g , and the mass of the particular atom of the large molecule that takes part in the collision m_a :

$$\tan \theta = \frac{2m_a m_g \cos \varphi \sin \varphi}{2m_a m_g \cos^2 \varphi - m_{ion} (m_a + m_g)} \quad \text{Eq. 1-43}$$

The internal energy taken up by the ion Q is given by the expression

$$Q = 4 \frac{m_a m_g}{(m_g + m_a)^2} \frac{m_g}{m_{ion}} \frac{m_{ion} - m_a}{m_{ion}} E_k \cos^2 \varphi \quad \text{Eq. 1-44}$$

When $m_a \ll m_{ion}$ and $m_g \ll m_{ion}$ which is the case for high mass projectiles, Q can be expressed as a function of E_{CM} :



$$\sin \phi = \frac{b}{r_g + r_a} = \frac{b}{d}$$

Figure 17. Definition of the impact angle, ϕ .

$$\langle Q \rangle \approx 2 \frac{m_a m_g}{(m_g + m_a)^2} E_{CM} \quad \text{Eq. 1-45}$$

The above equation predicts that when the centre-of-mass collision energy is increased the energy uptake also increases proportionally. The degree of scattering also depends on the mass of the atoms taking part in the collision. Heavier collision gases induce more scattering to the projectile molecules. Another conclusion of the model is that energy uptake correlates with average energy loss of the molecule. The model enjoys good agreement with many, but not all, experimental results involving valinomycin as well as CsI clusters [120].

The energy deposited into the projectile ion during the collision is transferred to the electronic, vibrational and/or rotational degrees of freedom of the parent ion. In the purely electronic excitation model, an electronic transition occurs vertically according to the Franck-Condon principle. According to this picture momentum transfer is not substantial in the collision, therefore the scattering of the parent ion remains low.

Two models were proposed for vibrational and rotational excitation. According to the first, collision takes place as described in the ICT theory. Elastic transfer of the translational energy to the atom that collides with the target gas results in vibrational and rotational excitation of the projectile. The second model introduced by Russek [121], proposes that for low-keV translational energy the electrons are able to adjust considerably during the collision. In a modified Born approximation developed by Russek the

adiabatic behaviour of electrons is taken into account. The parent ion induces a dipole in the target atom, which in turn interacts with the permanent or induced dipole moment of the parent molecule resulting in vibrational/rotational excitation. This mechanism would become important for ions with large polarizabilities, although for such ions that also possess high mass the momentum transfer model is also important.

The dissociation of collisionally activated ions has been successfully described with the quasi-equilibrium theory (QET) which is equivalent to microcanonical Rice-Ramsperger-Kassel-Marcus (RRKM) theory for unimolecular reactions [122,123,124]. According to this model the molecule is assumed to be a system of loosely coupled oscillators, therefore energy can flow among the normal modes. RRKM is a statistical model that considers explicitly individual vibrational frequencies and activated complexes of the molecule. As energy flows throughout the molecule there is a possibility that enough energy may be concentrated around one single bond for its cleavage to occur. The more internal energy in the system the greater the possibility becomes. A theoretical study of intramolecular energy redistribution by Oxtoby and Rice [125] showed that energy flow will take place when resonances overlap, i.e. when their effective coupling is strong. Because of small anharmonicities of a typical molecular potential, resonances may not overlap for low levels of excitation per oscillator [126].

1.2.3 Post-source decay.

Although not strictly a tandem mass spectrometric method, time-of-flight/post-source decay mass spectrometers have recently become direct competitors of CID type tandem instruments, at least for specific applications like peptide and protein sequencing. In very much the same way as with collisional activation, the phenomenon that is the key to post-source decay was initially regarded as a nuisance. Heavy proteins were reported to undergo metastable decay in the field-free regions of MALDI time-of-flight analysers. The metastable decay resulted in kinetic energy release which degraded resolution to no more than 50 for ions above the range of 100 000 Da.

Metastable decay following MALDI is increased by setting the power density of the laser higher than the threshold value that would normally be used for optimum resolution. It is believed to arise because of excess internal energy deposited in the ions during desorption and ion-neutral collisions in the dense plume over the sample surface. Spengler and coworkers studied the metastable decay of laser-desorbed proteins and peptides [127, 128]. The energy release during metastable decay, although high enough to compromise resolution, is too low to allow fragment ion separation in a linear time-of-flight mass spectrometer, therefore the use of an ion reflectron is required. Metastable fragments have about the same velocity as their parent ions but widely different kinetic energies depending on their masses, thus they will penetrate the ion reflectron to different lengths and be separated in time. Metastable

fragmentation inside the mirror results in scattered-noise peaks on the baseline of the spectrum, while fragmentation after the reflectron degrades resolution.

Single- [129, 130] as well as double-stage reflectrons have been used for metastable ion separation. Alternatively a deceleration region can be used [128], where the ions separate according to their kinetic energy. The disadvantage of the latter is that it discriminates against low-mass fragment ions. The disadvantage of the uniform reflectrons is that they cannot successfully time-focus all the ions of the beam, due to the high energy range. Therefore stepping of the mirror voltage is required to achieve acceptable resolution throughout the mass spectrum. This could in principle be solved if an ideal focusing quadratic (curved) mirror were used, as discussed in this thesis.

Post-source decay has been recently coupled with pulsed-extraction to offer higher resolution. Depositing higher laser power resulted in fast metastable decay, before the extraction pulse was applied. Thus, the fragment ions were time-focused in the same way as the parents, and high resolution could be achieved even for linear mass spectra [131].

Commercial instruments featuring post-source decay are offered by most time-of-flight instruments manufacturers. The major application is peptide and protein sequencing [132]. The great advantage of post-source decay is sensitivity: complete sequence of a protein can be obtained using as little sample as 10 femtomoles [133]. Also, it has been reported that fragmentation efficiency increases for masses up to 12360 (cytochrome *c*) [128]. Comparison

of low-energy CID, high-energy CID and PSD spectra for des-Arg¹ bradykinin, des-Arg⁹ bradykinin and Angiotensin I [134] suggests that the internal energy deposited in the ions follows the following pattern: MALDI \approx low energy CID < High energy CID. The inherent time for [M+H]⁺ decomposition in MALDI-PSD-TOF is 4 and 45 times longer than that for low- and high-energy CID respectively. MALDI-PSD spectra show more similarities with low-energy CID spectra than with high energy CID. This may reflect the fact that PSD ions are primarily products of low-energy collisions of the parent ions with the neutral matrix molecules in the region above the sample surface.

1.3 Mass spectrometry in biological analysis.

1.3.1 Biological macromolecules.

The observation of very small depressions of freezing points and small osmotic pressures for some colloidal solutions intrigued chemists at the beginning of this century. These results were attributed to formation of aggregates or the supposition that the law of Raoult and Van Hoff did not apply to colloidal solutions. In the 1920's it was finally recognised that this behaviour was due to the existence of giant molecules. Proof came with the crystallisation of urease and pepsin by Summer [135] and Northrop [136] respectively. They discovered that the unit cell weight of a protein crystal was always a multiple of the molecular weight determined in solution and not some small fraction.

Amino acid	Three (one) letter code	Elemental composition	Average residue* mass	Immonium ion	Side chain mass
Glycine	Gly (G)	C ₂ H ₃ NO	57.05	30	1
Alanine	Ala (A)	C ₃ H ₅ NO	71.08	44	14
Serine	Ser (S)	C ₃ H ₅ NO ₂	87.08	60	31
Proline	Pro (P)	C ₅ H ₇ NO	97.12	70	42 ^b
Valine	Val (V)	C ₅ H ₉ NO	99.13	72	43
Threonine	Thr (T)	C ₄ H ₇ NO ₂	101.11	74	45
Cysteine	Cys (C)	C ₃ H ₅ NOS	103.15	76	47
Isoleucine	Ile (I)	C ₆ H ₁₁ NO	113.16	86	57
Leucine	Leu (L)	C ₆ H ₁₁ NO	113.16	86	57
Asparagine	Asn (N)	C ₄ H ₆ N ₂ O ₂	114.10	87	58
Aspartic acid	Asp (D)	C ₄ H ₅ NO ₃	115.09	88	59
Lysine	Lys (K)	C ₆ H ₁₂ N ₂ O	128.17	101	72
Glutamine	Gln (Q)	C ₅ H ₉ N ₂ O ₂	128.13	101	72
Glutamic acid	Glu (E)	C ₅ H ₇ NO ₃	129.12	102	73
Methionine	Met (M)	C ₅ H ₉ NOS	131.20	104	75
Histidine	His (H)	C ₆ H ₇ N ₃ O	137.14	110	81
Phenylalanine	Phe (F)	C ₉ H ₉ NO	147.18	120	91
Arginine	Arg (R)	C ₆ H ₁₂ N ₄ O	156.19	129	100
Tyrosine	Tyr (Y)	C ₉ H ₉ NO ₂	163.18	136	107
Tryptophan	Trp (W)	C ₁₁ H ₁₀ N ₂ O	186.21	159	130

* An aminoacid residue -NH-CHR-CO- (R is the amino acid side chain) is defined as a neutral amino acid molecule minus the element of water

^b Pro has a cyclic side chain

Table 1. Name, code, elemental composition and residue mass of the naturally occurring amino acids [137].

Proteins are today recognised to be among the most important components of a living system. Although proteins can be extremely large and complex molecules, they are all built with a combinations of about 20 building blocks, the aminoacids. The structure of all aminoacids is $(H_2N-CH(R)-COOH)$, where side chain R differs from one natural occurring aminoacid to the other (see Table 1). Aminoacids are linked together by peptide bonds $(-CO-NH-)$ in chains that extend to as many as 1000 units. When proteins are digested with the use of different enzymes, cleavage of the bonds between aminoacids occurs, resulting in a large number of different peptides.

Peptides are created in living organisms by DNA molecules. A certain sequence of nucleotide bases, a gene, can be responsible for reproducing three possible types of aminoacid sequence (the so-called reading frames). The codon for each aminoacid corresponds to three bases in the DNA chain. Peptides are responsible for most of the vital processes taking place in a living cell.

1.3.2 Peptides and proteins sequencing.

1.3.2.1 Standard techniques.

The determination of the aminoacid sequence of peptides has always been one of the fundamental problems of biochemistry and biology. During the 1960's and 1970's mass spectrometry was already being used for sequencing small peptides [138]. The process was possible only after extensive chemical conversions of the peptides to derivatives that were sufficiently volatile to be introduced into a mass spectrometer through a gas chromatograph (GC/MS).

The standard technique used by biochemists for peptide sequencing is the manual or automated Edman degradation [139], a chemical method that removes and identifies one amino acid after the other in a stepwise fashion, using phenylisothiocyanate (PITC) as the reagent. The Edman degradation has its limitations and has often been complemented by the GC/MS technique.

Around the 1980's chemical methods of protein sequencing yielded the structure of proteins that consisted of more than 1000 amino acids [140]. At the same time, a method was introduced for the simple, fast and reliable determination of the base sequence of the gene coding for a certain peptide [141]. Consequently, the known DNA sequence can be translated to the amino acid sequence of the peptide. Recombinant DNA techniques made the process of DNA sequencing and gene mapping even easier. Sometimes, though, the work of finding and identifying the gene responsible for a protein is not an easy task. Nevertheless, mass spectrometric techniques are still required to complement the DNA mapping method, to overcome ambiguities as to which of the three possible strings of the amino acid sequence belong to the studied peptide.

1.3.2.2 Pure mass spectrometric techniques.

The door of biological analysis with purely mass spectrometric methods was opened by the introduction of the aforementioned "soft" desorption/ionisation techniques that can ionise intact peptides and proteins and lately oligonucleotides and DNA molecules. The first step was molecular mass determination, which was often used to verify sequencing information derived

with the DNA sequencing technique [142]. Otherwise, sequential enzymatic or chemical cleavage was combined with FAB mass spectrometry of the truncated peptides for sequence identification.

Dissociation techniques, like collision-induced dissociation, were quickly employed to allow structural information to be obtained directly from tandem mass spectrometry of a peptide. Large proteins have to be digested into smaller peptides before they can be sequenced by this method. When a peptide collides with a target gas the internal energy deposited will most likely induce cleavage of an amide bond of the peptides backbone. A generally accepted nomenclature for peptide fragments labelling has been proposed [143,144] (figure 18). N-terminal fragment ions are labelled with the first letters of the alphabet (a, b, c), while the last letters are used for C-terminal ions (x, y, z). If transfer of hydrogens has occurred during fragmentation they are explicitly noted (i.e. a_n+1). Numerical subscripts are used to identify the position of bond cleavage. Counting of the amino acids for the determination of the appropriate subscript starts from the N-terminus for N-terminal fragments and from the C-terminus for C-terminal ions. When part of the side chain of an amino acid is lost (usually in high energy CID) the letters d and w are used for N-terminal and C-terminal ions, respectively. Sometimes for C-terminal fragments loss of the entire side chain of an amino acid is observed, and labelled with the letter v. Such losses are not observed for N-terminal fragments. Sometimes both the N- and C-terminus of a peptide are cleaved from the backbone, creating internal fragments. They are labelled as a

combination of the two losses, i.e. $y_n b_m$. Especially in high energy CID spectra, immonium ions ($\text{HN}=\text{CH}-\text{R}$) are observed at low masses, giving useful information about the presence or absence of a particular amino acid. They are labelled with the single letter code of the particular amino acid. Finally, sometimes intact precursor ions are observed with loss of a side chain of one amino acid. Those ions are designated as $-X$ or $-R_X$, where X is the one letter code of the amino acid. They are not very useful for the interpretation of a spectrum, because they appear in an area of the spectrum where a multitude of other ions are observed.

It is relatively easy, using an accurately calibrated tandem mass spectrometer to obtain a fragmentation spectrum of a medium-size peptide. Care must be taken to isolate the ^{12}C , ^{16}O isotope of the peptide, especially at heavier masses where it may not be the most abundant isotope of the envelope. Otherwise mass determination of the fragments provides an indication of the present amino acids and their sequence, although sometimes interpretation of tandem mass spectra is far from trivial. However from the large number of peptides and proteins that have been sequenced with CID, empirical rules have been devised and even computer software has been written to assist interpretation. Nevertheless, although the technique is mainly used to sequence

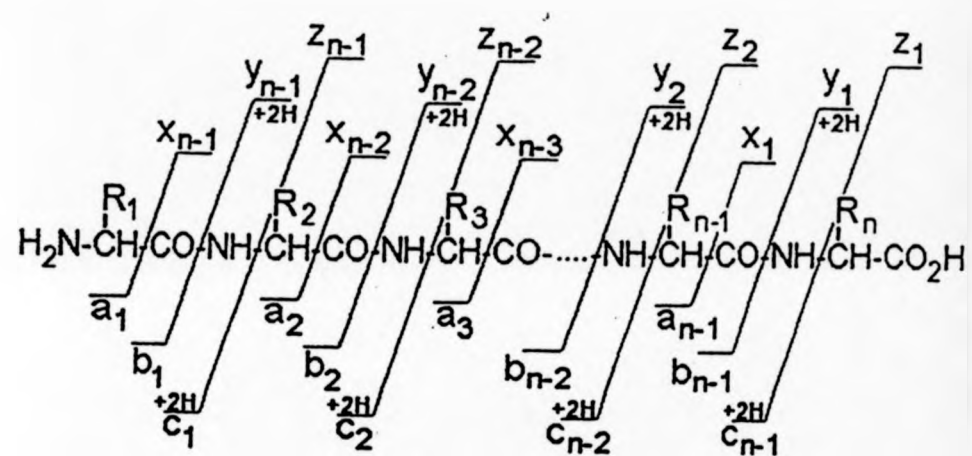


Figure 18. Nomenclature scheme for the labeling of peptide fragments.

peptides up to 3000 to 5000 Da, the complete primary structure of chromatium vinosum has been determined, solely with mass spectrometry from a 100 nmol sample [145].

2. Chapter Two.

Large-scale time-of-flight mass spectrometer.

2.1 Introduction.

The objective of the first part of this work is to evaluate the feasibility and performance of MALDI ion source designs. For this purpose, a large-scale time-of-flight mass spectrometer was designed and fabricated. The instrument was designed to offer flexibility and easy adaptation to various experiments to investigate the matrix-assisted laser desorption/ionisation process, as well as other instrumentation ideas.

A flight path of approximately 2 meters was chosen to ensure long flight-times and consequently improved resolution. The laser system used was a tunable dye laser, optically pumped by an excimer laser. This would allow the use of a wide variety of matrices that absorb at different wavelengths. To ensure the detectability of high-mass species, the ion source was designed to sustain high accelerating potentials (30 kV). The ion detector was designed and fabricated so that it could be floated at high potential, allowing additional post-acceleration for efficient detection of heavier ions.

2.2 Instrumentation.

2.2.1 The vacuum chamber.

Although in the initial stage of development the instrument was planned to be a simple linear TOF, it was decided that the vacuum chamber should allow easy accessibility for other instrumental developments. Therefore, the chamber

had a square section with internal dimensions 300×300 mm. The internal length of the chamber was 2000 mm. The top of the chamber was made up of three separate lids, vacuum-sealing with the aid of a specially made VITON seal. The lids could be completely removed for easy access to the interior of the chamber. One large flange (type ISO 200) was placed at each end of the chamber, and three similar flanges were placed on each side wall. Two smaller flange attachments (ISO 160) were made on the floor of the chamber for the vacuum pumps (figure 19).

The large scale of the chamber in combination with its square section raised some engineering problems which needed to be investigated. It was necessary to ensure that the chamber walls would not sag extensively or even collapse under atmospheric pressure, while the chamber was evacuated. Firstly, a pair of cross-bracings was introduced in the chamber to lower the distance between restraints for the side walls. The cross-bracings were 50 mm thick, had a large hole in the middle (diameter 220 mm) and their top corners were deep-welded with the side walls so that they could house the o-ring grooves for the seals of the three lids. The second measure taken was to introduce a lip in the design of the lids in order to offer a restraint throughout the top edge of the walls.

Another concern for the chamber design was that the total weight should be kept down to a manageable level. A lightweight material was required, which would be strong enough not to collapse under pressure. The material also had to be a non-porous, vacuum suitable material, that could be successfully

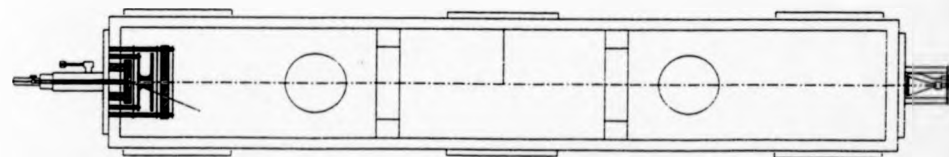


Figure 19. Photograph and schematic diagram of the large scale time-of-flight mass spectrometer.

vacuum-welded. Stainless steel and high strength aluminium-alloys were the most promising candidates. Stainless steel would have been stronger, therefore thinner walls would have been adequate, but aluminium-alloys would have been three times lighter than stainless steel. Although vacuum-welding of stainless steel was known to be a well proven standard technique, novel welding techniques for aluminium alloys supported its feasibility for vacuum use. Finally, the oxide layer formed on aluminium surfaces made its degassing vapor-pressure comparable to that of stainless steel.

Different combinations of material and thickness were considered. The maximum deflection and strain of the side walls under these design characteristics were calculated using theoretical engineering formulae as well as finite element analysis software. It was concluded that the use of aluminium-alloy plate with 25 mm thickness should withstand the atmospheric pressure, while the total weight of the chamber remained under 250 kg.

The chamber was manufactured by Kratos Analytical (Manchester, UK). A supporting frame for the vacuum chamber was designed and manufactured in house. Provision had been taken for the housing of the vacuum system within the supporting frame. Two 700 l/s Edwards Diffstak diffusion vacuum pumps were used. They featured a liquid nitrogen trap each, in order to increase the pumping speed and maintain an oil-free vacuum. Two butterfly valves were used between the liquid nitrogen traps and the vacuum chamber. The diffusion pumps were backed by one Edwards 11 l/s rotary pump. The diffusion pumps

could be bypassed for initial "roughing" of the chamber. A leak valve was also installed to facilitate breaking of the vacuum.

A thermocouple gauge was used to monitor the roughing pressure of the chamber, as well as the backing pressure under high vacuum. An Edwards ion gauge was used to measure high vacuum. A residual gas analyser (RGA) unit was initially used to locate possible vacuum leaks. All the welds of the chamber proved to be vacuum-tight and only the VITON seals had to be improved. In order to achieve high vacuum the chamber had to be baked at temperatures around 100° C for 3 days, using heating tapes and insulation. The best vacuum achieved with the help of the nitrogen traps was 4×10^{-7} mbar.

2.2.2 The ion source.

The design of an ion source for any time-of-flight mass spectrometer imposes a number of considerations. The main purpose is to achieve the highest possible sensitivity without compromising resolution. Therefore, the ions created in the ion source should be collimated towards the detector with minimum loss, while the time aberrations imposed in the source region should be kept low. When MALDI is used with a solid sample, another important requirement is the ability to raster the sample stage under the focused laser beam.

While sensitivity may be compromised by highly diverging ion beams and scattering on ion optical components, resolution is affected by three main factors:

- a) the finite time of ion formation
- b) the finite volume of ion formation and
- c) the initial velocity of the ions

For MALDI ion beams, the first parameter is caused by the duration of the laser pulse that can vary from a few picoseconds to a few nanoseconds. Additionally, ions can be created in the gas phase above the sample surface even after the laser is switched off. This gives rise to both temporal and spatial distributions. Finally it is known that MALDI ions possess mean velocity of about 500–1000 m/s with a considerable velocity distribution [146]. The flight-time broadening due to the initial velocity distribution can be separated into a pseudo temporal and a pseudo spatial effect [147]. Although spatial effects can be corrected for by means of energy compensation (spatial focusing, reflectron), temporal focusing need other means of correction such as time-lag focusing, post-source pulse focusing, shorter laser pulses and high extraction fields.

Another approach to studying the effect of initial energy spread is to consider two ions with mass m and charge e formed in the same position $x=0$ at the same time, but with different initial energies zero and ε respectively. The difference in time-of-flight for the two ions in the extraction region is

$$\Delta t = T_1 - T_2 = \frac{d}{\frac{1}{2} \cdot \left(\sqrt{\frac{2e}{m} V_0} \right)} - \frac{d}{\frac{1}{2} \left[\sqrt{\frac{2e}{m} \varepsilon} + \sqrt{\frac{2e}{m} (V_0 + \varepsilon)} \right]} \quad \text{Eq. 2-1}$$

d is the length and V_0 the potential across the acceleration region. Equation 2-1 can be rearranged to:

$$\Delta t = \frac{2d}{\sqrt{\frac{2e}{m}V_0}} \cdot \sqrt{\frac{\varepsilon}{V_0}} + \frac{2d}{\sqrt{\frac{2e}{m}V_0}} \left(1 - \sqrt{1 + \frac{\varepsilon}{V_0}} \right) \quad \text{Eq. 2-2}$$

Expansion gives:

$$\Delta t = \frac{2d}{\sqrt{\frac{2e}{m}V_0}} \cdot \sqrt{\frac{\varepsilon}{V_0}} + \frac{2d}{\sqrt{\frac{2e}{m}V_0}} \cdot \left[-\frac{\varepsilon}{V_0} + \frac{1}{2} \left(\frac{\varepsilon}{V_0} \right)^2 - \dots \right] \quad \text{Eq. 2-3}$$

The second term of the above expression, being a series of integral powers of the term ε/V_0 , can be compensated with a device such as an ion mirror. This is because time-of-flight in the ion mirror can be expanded into similar series. The resulting coefficients in the case of a double stage mirror, for instance, can be chosen to correct the first and second order of the above aberration (see Eq. 1-21). The first term, sometimes described as the Zavoiskii-Fanchenko effect [148], has the term ε/V_0 in a non-integral power and therefore cannot be corrected by any type of ion mirror. This aberration can be corrected by time-lag focusing applied in the source region or further down the flight tube.

A typical dye laser pulse length of 20 ns would limit mass resolution for a linear TOF with 2 m flight path and 20 kV accelerating potential to about 250 for mass 100 Da and 2500 for mass 10000 Da (ignoring all other parameters that may cause energy spread). By adjusting the laser power near the threshold of ion production, the ion emission area and the ion velocity spread can be optimised. Also, the use of a high extraction field (i.e. higher values of V_0 or

lower values for d in Eq.2-3) can lower the Zavoiskii–Fanchenko aberration. In the particular case of MALDI, higher extraction fields will result to higher energy spread due to the finite volume of ion formation, therefore the strength of the extraction field employed should be a tradeoff between the two above aberrations.

2.2.2.1 The wobble probe.

The surface of a sample prepared for MALDI consists of solid crystals of the matrix material incorporating the analyte molecules. Different parts of the surface of the same sample may yield very different results in terms of ionisation efficiency, optimum laser power and so on. It has also been reported that the irradiation of a single spot typically gives ions for no more than about 100 laser shots [149], depending on the laser power. Thus one of the practical problems with MALDI of solid samples is the need for sample manipulation during the acquisition of a mass spectrum.

For our installation, given that the pressure would probably not be less than 10^{-7} mbar, a simple approach was adopted to solve this problem. The wobble probe (see figure 20) was based on the following principle: a metal shaft was housed within a highly polished hollow tube, with outer diameter to match that of a standard Kratos Analytical (Manchester, UK) sample insertion probe. A pivot point was created by two VITON o-rings, slightly compressed between the shaft and the inner surface of the tube. The shaft could be wobbled around the pivot point, which also served as the vacuum seal.

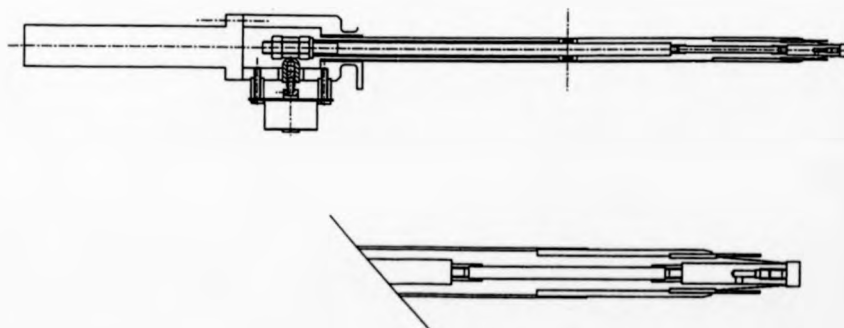
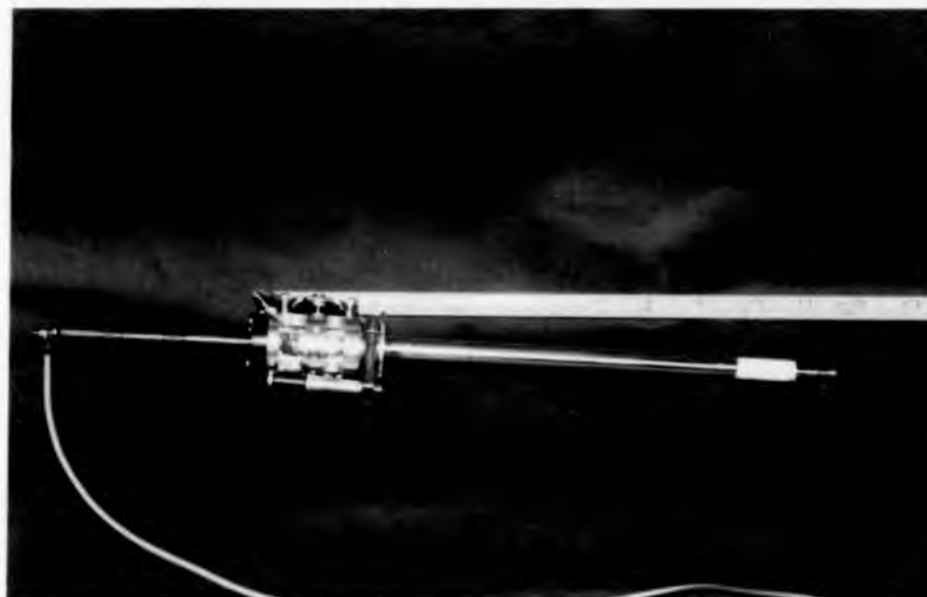


Figure 20. Mechanical drawing and photograph of the wobble probe.

The vacuum-end of the probe was designed to float at the high accelerating potential of the ion source. Both, the ends of the shaft and the tube were electrically insulated from the rest of the probe with machinable ceramic parts long enough to withstand 25–30 kV potential difference. The stainless steel end-part of the tube makes electrical contact with the first electrode of the ion source by means of a brass spring, and was electrically connected with the end of the shaft by means of a piece of flexible thin tungsten wire. The stainless steel sample tip could be screwed on to the end of the shaft, and could be easily replaced when contaminated. Its surface has a radius equal to its distance from the pivot point, so that the angle of the sample surface with respect to the ion optical axis did not change, when the angle of the shaft was altered.

The manipulation of the shaft was performed by moving the end near the handle of the probe (figure 20). The rotational motion of two thumb-wheels (one for each independent axis of manipulation) was translated to linear motion of two actuators that controlled the position of the rear end of the shaft with the help of a spring. The aspect ratio of the two parts of the shaft on either side of the pivot point was 1:1 (atmospheric and vacuum part respectively). As the amplitude of manipulation on the atmospheric side had a diameter of 2 mm, the actual amplitude of the manipulation of the sample tip was approximately 2 mm.

A lock provided by Kratos Analytical (Manchester, UK) was used to insert the probe into the vacuum. It featured a ball valve and a differentially pumped region (when the probe was inserted) created by means of two spring loaded

PTFE seals, with the necessary inlet vacuum provided by a separate Edwards 11 l/s rotary pump. The insertion lock was positioned in the middle of the ISO 200 stainless steel flange at the source end of the vacuum chamber.

2.2.2.2 Acceleration and ion collimation region.

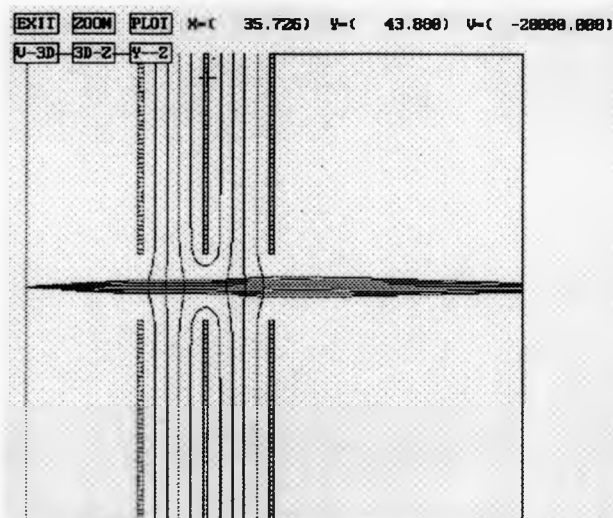
Homogeneous acceleration field ion sources are very well understood and in principle create a relatively well collimated ion beam with little time aberration. Their main drawback is that they require the use of wire meshes. A fairly high density mesh is required to ensure low field penetration, but the transmission should be as high as possible, typically 90%. This means that a 10% compromise in sensitivity is made for every mesh used. Even if it is assumed that meshes are tensioned well and parallel (which is technically challenging in its own right, [150]), small field irregularities around the mesh wires result in high deflection of ions that do not pass through the middle of the mesh [151]. Such deflection results in lower sensitivity as well as lower resolution, because of the different paths taken by the ions. Nevertheless there are detailed theoretical analysis of the mesh-created deflections [152], and their effect upon resolution can be minimised by optimising experimental parameters.

The alternative to meshes is the grid-less ion source. The extraction and/or acceleration fields in a grid-less ion source are created with the help of flat electrodes with usually circular or rectangular holes/slits. The fields in the vicinity of such electrodes cannot be readily described analytically, therefore numerical methods are employed with computer software to define ion

trajectories as well as their times-of-flight. In general, smaller diameter holes decrease field penetration creating more homogeneous fields, but more ions are likely to be lost by collisions on the electrode surfaces or from extreme deflection near the edges of the hole. Mesh-free ion sources are also extremely sensitive to the alignment of their components. If the ion production position or the electrodes with each other are not all centred on the same axis (within about 10–50 μm for a typically sized assembly with 5–10 mm between electrodes), strong deflection of the ion beam may well occur.

Ionic species in the ion source possess initial velocities which can be analysed into components in the axial and perpendicular directions with respect to the ion optical axis. The perpendicular component may be amplified by space charge effects from the dense ion cloud near the ion formation point, causing the ion trajectories to diverge from each other. Various methods have been used to collimate or focus diverging ion beams, most of which have relied on using electrostatic fields. One of the most common type is the “Einzel” lens, which is usually created by a combination of three rotationally or planar symmetric metallic electrodes with appropriate voltages applied to them (figure 21). The curved electrostatic field created in the region between the electrodes can be made to focus electrons or ions. Einzel lenses can be created by tube- or thin aperture- electrodes. They can be of two types: accelerating, where for positive ions the middle electrode has a more negative potential than the two end-electrodes or decelerating lens where for positive ions the middle electrode is more positive than the two end-electrodes. In the decelerating lens

a)



b)

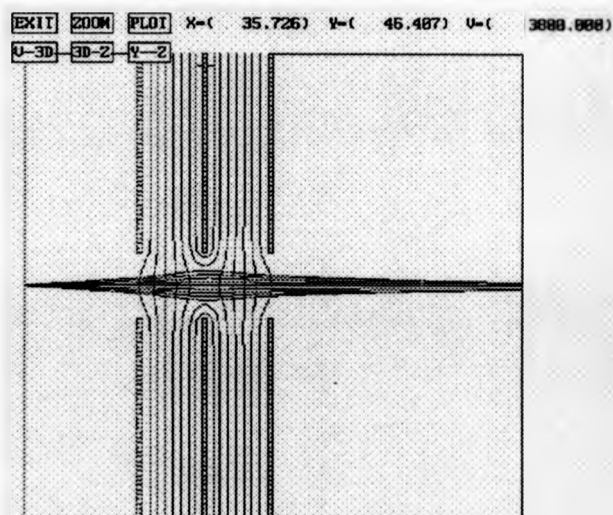


Figure 21. SIMION ion trajectory simulations illustrating the effect of an accelerating and a decelerating "Einzel" lens on the same diverging ion beam. The two lenses have identical geometry. The decelerating lens can achieve the same focusing conditions as the accelerating, for lower values of potential.

ions are focused strongly, while in the accelerating type they are focused weakly. The advantage of accelerating lenses with time-of-flight mass spectrometry is the lower time-aberrations they introduce, while their disadvantage is that higher voltages are required to achieve the same focusing effect as a similar geometry decelerating lens. Other advantages of both types of "Einzel" lenses are simple construction, good image quality, high flexibility and stability and simple power supply requirements (usually only one is necessary as the end-electrodes are kept to ground). Electrostatic lenses have been extensively studied [153], mainly because of their use in electron microscopy. Numerical methods and computer software are employed for their evaluation especially in time-of-flight mass spectrometry.

2.2.2.3 Ion trajectory simulations.

Computer simulations of ion trajectories were performed as part of this study in order to optimise the design of the ion source for the large scale TOF mass spectrometer. The SIMION software (Idaho National Engineering Laboratory, Idaho Falls, USA) was used to calculate the potential distribution created by the combinations of different electrode geometries at different potentials. Typical initial conditions were defined for MALDI ions in order to calculate ion trajectories and flight times in the source region. The SIMION software has an intuitive user interface which allows the graphical design of the electrode geometry, command-line control of most important parameters and graphical output of the ion trajectories, while information about total times-of-flight and final trajectory angles are recorded.

EXIT ZOOM PLOT X=(70.649) Y=(39.877) U=(OUTSIDE GRID)

U-3D 3D-Z Y-Z

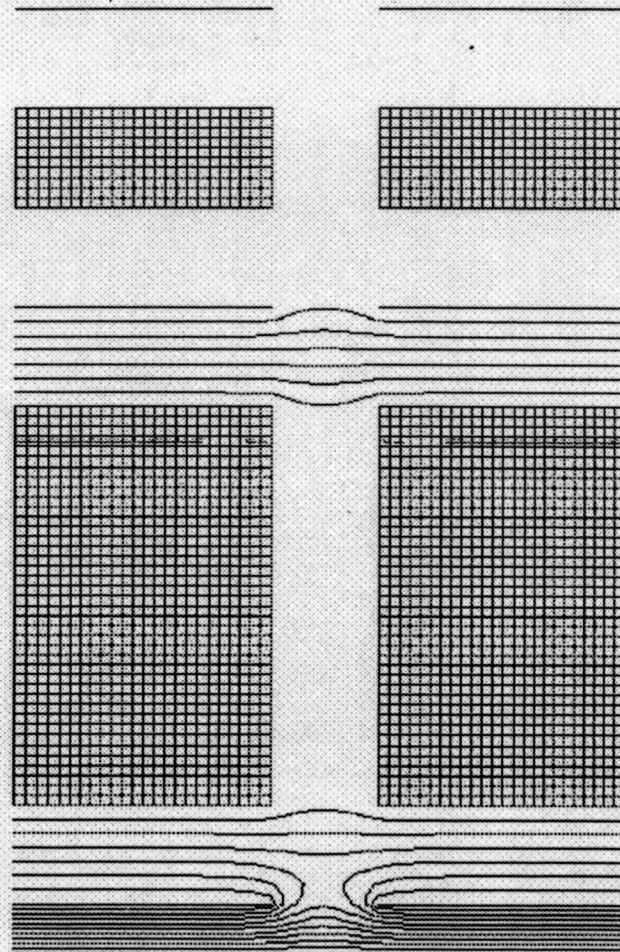


Figure 22. The ion source model as implemented in the SIMION software.

It was decided to implement a grid-free ion source design. The electrodes were rotationally symmetric with circular holes of 10 mm diameter. The tip of the sample probe was "hidden" behind a hole in the accelerating electrode so that manipulation of the probe did not affect the field in the extraction/acceleration region. The probe tip and the accelerating electrode were at the same high potential U_{acc} , while a grounded electrode with a 10 mm hole was situated at distance d_{acc} . An Einzel lens was included in the model: a tube electrode of length d_{Ein} was placed at a distance d_{l1} from the first ground electrode. The potential of the lens-electrode was U_{lens} . A second ground electrode was introduced at distance $d_{l2} = d_{l1}$ after the tube electrode. The model of the ion source was introduced in the SIMION software and ion trajectory simulations were performed to evaluate the performance of the design (figure 22).

Ion beams with various initial conditions were studied to evaluate different aspects of the design. A typical MALDI ion beam was considered with ion mass 1000 Da, initial energy 5 eV, energy spread 20 eV, angular spread 10 degrees and initial coordinate spread 200 μm . The exact position of the probe in respect to the accelerating electrode was investigated. It was found that a micro-lens created in the vicinity of a small diameter hole for some probe positions, could over-focus ions, resulting in a highly divergent beam (figure 23). This effect was eliminated for larger diameter holes and when the probe tip was as close to the inside of the hole as possible. Also the thickness of the electrode around the hole had to be minimal. As the position of the probe tip

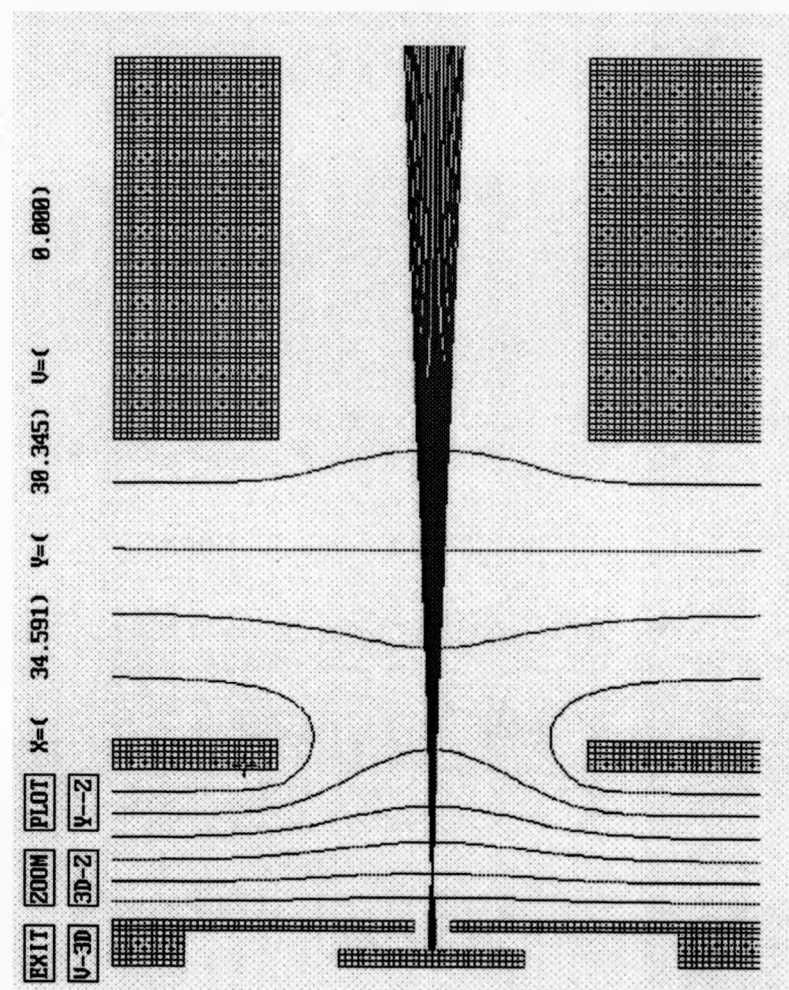


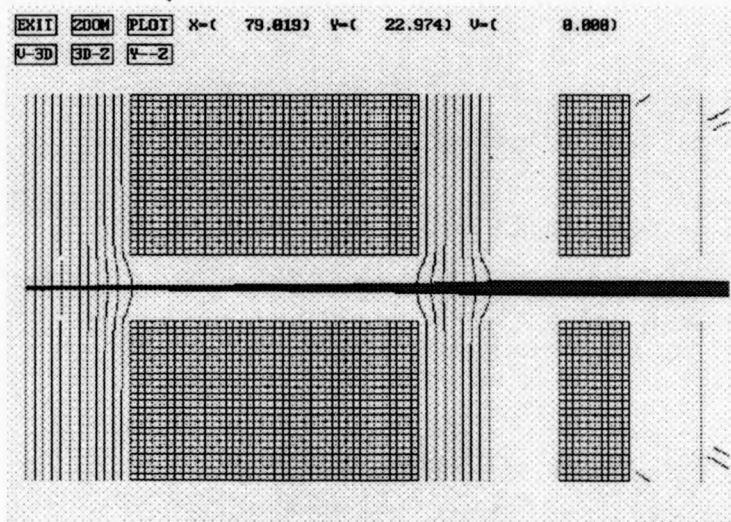
Figure 23. A micro-lens created in the vicinity of the hole on the accelerating electrode, may over-focus ions coming out of the sample surface for certain electrode geometries and positions of the sample probe.

proved to be a critical parameter, a micrometer actuator was added to the wobble probe assembly to control precisely and reproducibly the intrusion of the probe.

A number of Einzel lens designs were investigated to evaluate the ability of the lens to collimate or focus the beam towards the detector, and more importantly to estimate the time aberrations imposed on the ion beam in the source region. For a specific geometry and accelerating potential $U_{acc}=20$ kV, the lens potential U_{lens} was changed until the ion trajectories of initially diverging ions were collimated. Then, the arrival times of the ions to the end of the simulated region were recorded and the maximum time spreads identified. This time spread is due to different ion paths in the source, as well as the Zavoiskii–Fanchenko effect. Accelerating lenses gave less aberrations but required higher voltages (figure 24). The chosen geometry offered high sensitivity (collection of most diverging ions) with aberrations less than 2 ns for 20 kV accelerating potential.

Another factor which was examined was the effect of imperfections of the laser spot alignment. It was found that small misalignments (50–100 μm) could be tolerated, if a pair of electrostatic deflectors was introduced after the collimating region. For a differential voltage amplitude of ± 150 V applied to the electrodes of the deflectors, it was found that a length of 20 mm was adequate for steering the ion beam towards the deflector. Higher misalignments of the laser beam (i.e. >100 μm) would have severely deflected the ion beam and made it undetectable.

a)



b)

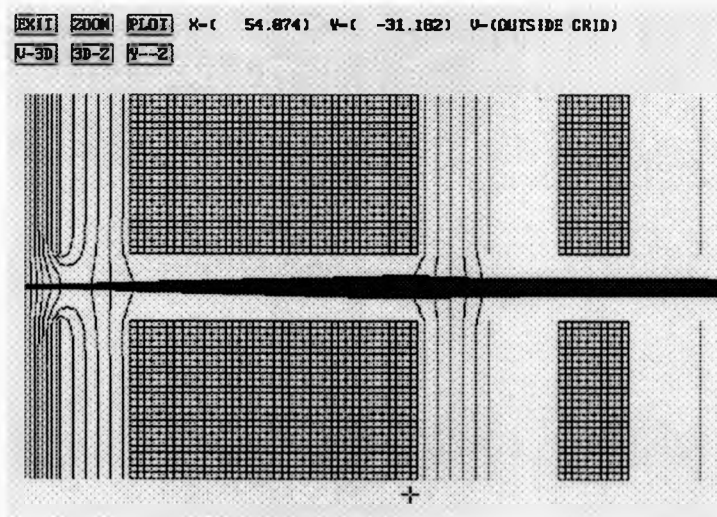


Figure 24. SIMION simulations of ion trajectories in the chosen geometry for the ion source of the large-scale time-of-flight mass spectrometer. (a) accelerating lens, (b) decelerating lens.

2.2.2.4 Design and construction.

The ion source should be able to sustain very high accelerating potentials. If an accelerating lens were to be used, the potential difference between the accelerating and the lens electrodes could be more than 50 kV. It was decided that three independent sets of insulating posts were needed: one for the accelerating electrode assembly, one for the lens electrode and one for the ground electrodes and deflector assembly. The insulating posts were made of PEEK (polyetheretherketone). Grooves were machined along the insulating posts for the accelerating and lens electrodes to increase the tracking distances.

The accelerating electrode was made of two parts. The first part was bolted on the four insulating posts and houses the electrical contact spring for the sample probe. The second part was separated by the first part of the accelerating electrode by means of four PEEK spacers and could be screwed on it with the help of metal or insulating screws. This design allowed the two parts of the electrode to be kept at slightly different potentials, controlling the field strength near the tip of the sample probe. The second part of the accelerating electrode had a hole with 4 mm diameter in its centre (figure 25). The hole diameter was such that when the probe moved behind the hole (the tip diameter was 6 mm and the amplitude of manipulation was 2 mm), the shape of the active ion optical elements did not change. As dictated by the ion trajectory simulations, the thickness of the electrode near the hole had to be minimal, thus the centre of the electrode was machined to a thickness of 100 μm .

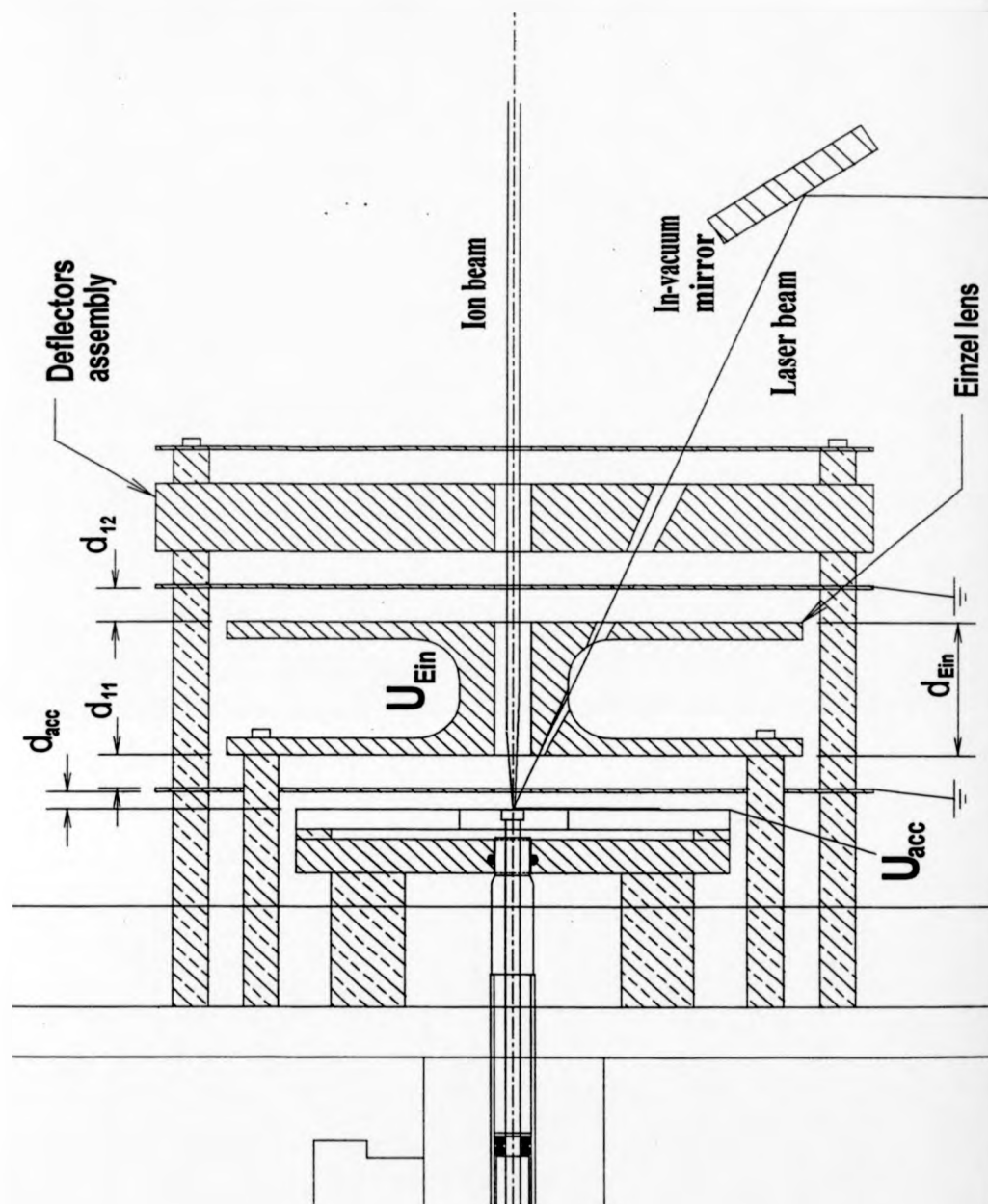


Figure 25. Assembly drawing of the ion source of the large-scale time-of-flight mass spectrometer.

As the lens electrode was 40 mm long with a 10 mm aperture, the weight had to be minimised to ensure that the four PEEK insulating posts did not sag. The chosen material was aluminium. The electrode was machined to a reel-like shape to lower the weight further. An appropriate hole/slit was made on the electrode for the laser beam.

The ground electrodes assembly was mounted on four identical sets of insulating posts that could screw into each other. The ground electrodes assembly could be aligned with the accelerating and lens electrode using a special tool. For the deflectors, an aluminium disk with thickness 20 mm was slit in four quarters. The central edge of each quarter was machined flat so that when the disk was assembled together, the distance between flat surfaces was 10 mm (figure 25). Holes for the laser beam were drilled where necessary. All the electrodes were highly polished to optimise the field shapes.

A 30 kV (for acceleration) and a 50 kV (for focusing) Spellman (Pulborough, UK) high voltage power supply were used to apply the potentials to the source electrodes through a home-made high-voltage feedthrough. A special power supply was designed and built to provide the differential voltages for the deflectors. One knob per deflecting direction (y, z) differentially adjusted the voltage on the deflectors from -150 V to +150. It was theoretically predicted and experimentally proved that this deflection voltage could deflect a well collimated, 20 keV ion beam beyond both ends of the detector. The setting of the deflector served as a good measure of the accuracy of the laser beam alignment.

2.2.3 The laser system and beam delivery optics.

An excimer-pumped dye laser was used to produce the laser beam for the MALDI ion source. A optical system was used to steer and focus the ion beam to the centre of the sample tip, while the laser power could be controlled by means of a variable attenuator.

2.2.3.1 The excimer and dye lasers.

A Lambda Physik (Gottingen, Germany) type LPX100 excimer laser was used to optically pump a Lambda Physik dye laser type FL3002. Excimer is a word produced by the combination of the words "excited" and "dimer", which hints at the way the laser radiation is produced in this kind of laser. An appropriate blend of a rare (Ar, Kr, or Xe) with a halogen gas (Cl or F) is mixed with an excess of a buffer gas, usually helium. This mixture is circulated around the optical cavity of the laser, created by a set of two mirrors. The back mirror of the cavity is made by a UV-grade fused silica substrate with a dielectric coating deposited on its rear side, with respect to the optical cavity. The thickness of the coating is chosen to be proportional to one quarter of the laser light wavelength, to provide 100% reflection of the optical beam. The front mirror is a UV-grade fused silica window, providing 1-2% reflectivity. Fast-rising high-voltage pulses applied on electrodes throughout the cavity create discharges in the high pressure gas mixture. The discharge excites electronically the rare gas molecules which reacts with the halogen to create excited dimer ions. These species quench into an excited metastable state with long lifetime (upper laser state), therefore a population inversion is created. Some of the excited dimer ions will spontaneously quench to the

lower laser state. A number of the emitted photons will be reflected by the optical cavity mirrors and subsequently cause stimulated emission creating new identical photon generations, thus laser radiation. The lower metastable laser level is depleted as a result of collisions with the buffer gas. Excimer lasers emit ultraviolet (UV) laser radiation. The exact wavelength depends only on the gases in the mixture (ArF \rightarrow 193 nm, KrF \rightarrow 248 nm, XeCl \rightarrow 308 nm XeF \rightarrow 351 nm) [154].

A dye laser uses the light of an excimer laser to excite a solution of an organic dye, flowing through quartz cuvettes with the help of a high-flow circulator. Dye lasers are continuously tunable, therefore laser light of all wavelengths, from near-ultraviolet to near-infrared can be produced with the same apparatus, by using different dye solutions and perhaps different pumping laser wavelengths. Dyes are organic compounds that fluoresce in the near-ultraviolet, visible or near-infrared wavelengths. The electronic transitions that emit the laser photons are not to a single state, but to a band of densely spaced states arising from the superposition of vibrational and rotational energy states upon the base electronic energy state. The tunability of a dye laser stems from this fact.

There are a number of steps to creating laser radiation in a dye laser [155]. During the initial step a small percentage of the excimer light is used to excite dye molecules situated within an optical cavity created by a mirror and an optical grating. This optical cavity has the characteristic of trapping only photons with wavelengths within a short bandwidth. Those photons will cause stimulated emission, hence amplification of radiation of this particular

wavelength. Change of the angle of the grating results in change of the output wavelength. The laser photons pass through two amplification stages and exit the laser through an iris. If shorter wavelength UV laser light is required, a non-linear doubling crystal (for example BBO) can be used.

2.2.3.2 The optical components.

Four UV-grade aluminium mirrors (Comar, UK) were used to steer the laser beam to the middle of the sample spot. The last mirror was inside the vacuum chamber. All the mirrors were cemented onto adjustable mirror stages (Newport, UK). The laser beam entered the vacuum chamber through a quartz window installed in one of the side flanges. A quartz lens with 500 mm focal length was placed at the appropriate position to focus the laser beam onto the sample surface. The minimum diameter of the beam at its focal point was 100 μm . The lens was placed in a Newport translation stage mount, so that the position of the lens could be adjusted transversely across the laser beam.

A variable attenuator (Newport, UK) was placed in the path of the laser beam to allow adjustment of the laser fluence on the sample. The attenuator consisted of two wedged quartz windows placed on two rotational stages next to each other. At minimum attenuation, the windows were parallel. With the help of a linear actuator an accurate mechanism rotated the two tables at the same angle, one of them clockwise and the other anti-clockwise. The increase of the incident angle of the light on the windows increased the amount of light reflected from the windows, which in turn increased the attenuation of the system. The displacement of the beam due to refraction on the first window

was cancelled by an equal and opposite displacement on the second window, therefore the position of the final beam remained exactly the same.

The alignment of the system was carried out using thermal paper on the sample stage. A circle was marked on the paper by friction against the 4 mm circle of the accelerating electrode. The lens and mirror mounts were adjusted until the laser-mark burned on the thermal paper was found to be exactly in the centre of the circle. The position of the burn-mark was measured precisely with the aid of an optical microscope.

2.2.4 The ion detector.

The floatable detector assembly was built around a Galileo (Sturbridge, MA, USA) chevron multi channel plate assembly with 30 mm active area diameter and anode with conical capacitive coupling to a 50 ohm rf connector. The maximum gain of the unit was 5×10^6 at 2000 V potential across the plates. The Galileo assembly was contained inside a cylindrical box, including a high transmission grid to shield the field-free region from the potential of the front surface of the MCP. It was mounted on a metal flange, which was isolated from the main vacuum chamber with a 150 mm long PEEK cylinder. The metal flange and the detector could have been floated at high potentials with minor modifications and additions to the existing design. This might have been essential, if very heavy ions were to be detected.

2.3 Experimental.

The excimer laser was set to emit radiation at 308 nm, using a mixture of Xe and Cl as the active gases. The power achieved was 150 mJ per pulse. For the

initial experiments it was decided to tune the dye laser to emit light of 337 nm, the same wavelength as the nitrogen laser which was the most widely used wavelength for MALDI. The dye solution utilised was p-Terphenyl dissolved in dioxan. The output power of the dye laser was 4 mJ.

Caesium iodide (CsI) was used for the first testing and tuning experiments with the time-of-flight mass spectrometer. CsI is a standard compound used to tune or calibrate mass spectrometers for desorption/ionisation techniques. It typically provides a series of different mass clusters, from mass 133 Da (Cs^+) up to very large cluster ions with masses of tens of thousands Da. One droplet of a saturated solution of the compound in water was deposited on the sample probe and dried, forming a thin film of white colour crystals. The sample was introduced into the vacuum and placed in the optimum position as determined during the alignment of the optical system. Various acceleration potentials were used from 5 to 20 kV. The Einzel lens was used in decelerating mode. Careful adjustment of the lens and the deflectors yielded the first time-of-flight spectra of CsI cluster ions (figure 26). Alignment of the optical system was fine-tuned by adjusting the laser beam optics, so that lower voltages on the deflectors were necessary.

The detector signal was inverted and amplified directly with a home-made preamplifier. Spectra were recorded with a LeCroy 9400A 175 MHz digital oscilloscope which could be triggered from a photodiode or from the trigger-out pulse of the excimer laser. Recorded spectra could be transferred to a Sun Microsystems (San Francisco, USA) computer and displayed, mass calibrated

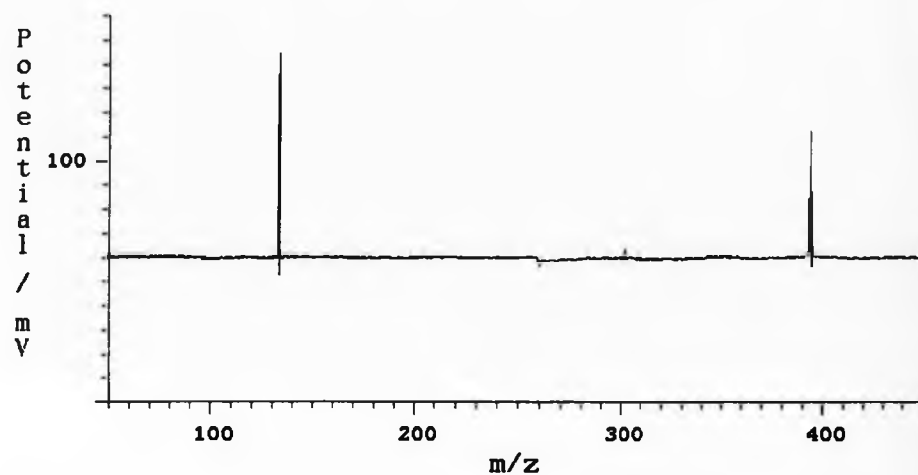


Figure 26. Time-of-flight mass spectrum of CsI clusters received in the large scale TOF mass spectrometer. The resolution of this spectrum is 400 FWHM, although resolution of 700 has been observed for single shot experiments.

and printed using specially written software [149].

Protein and peptide time-of-flight mass spectra were obtained using the matrix-assisted laser desorption/ionisation technique. The matrices utilised were sinapinic acid and 4-hydroxy α -cyanocynamic acid. The matrices were dissolved to give a 0.1 M solution in a 1:1 mixture of acetonitrile and water with the addition of 0.1% fluoroacetic acid (CF_3COOH). One or two drops of the matrix solution (1 μl) were deposited to form a concentrated spot in the centre of the probe, and dried in the vacuum of the insertion lock or under a flow of dry air [156]. Half a μl of 10^{-4} molar concentration of the analyte solution in water was deposited on the dried matrix. The mixture was dried and inserted in the source for measurement.

The matrix used for the analysis of polymers was 2,5-dihydroxybenzoic acid (DHB). 0.1 M matrix solution was prepared in the same way as described above. Polymer samples were dissolved in acetone or tetrahydrofuran with 10% water. The concentration of the polymer solution, although impossible to define accurately due to the mass polydispersity of the sample, was approximately 10^{-3} M. A thin layer of salt (NaCl , KCl , CsCl , LiCl , AgCl) was deposited on the sample stage before the matrix droplet, to enhance the ionisation efficiency. For polymer analysis, the wavelength of the dye laser was shifted to 360 nm to correspond with the maximum of the absorption curve of DHB.

2.4 Results and discussion.

As mentioned above, the first experiments were performed using CsI (figure 26). The signal-to-noise ratio was generally very good (better than 100), although better for high accelerating potentials. The best resolution observed for a single-shot spectrum was $m/\Delta m=870$ for m/q 653 Da. (27850 ns flight time and 16 ns full width at half maximum) and $m/\Delta m=780$ for m/q 393 Da (21880 ns flight time and 14 ns full width at half maximum) with 20 kV acceleration, 14 kV on the lens and no deflection. When an acquisition of 100 shots was recorded, peak-width broadening was observed and the resolution degraded to around 150–200. This is partially attributed to time jitter of the electronic components, i.e. trigger line, oscilloscope and preamplifier. The most important contribution, however, was the fluctuation of the laser power and the inhomogeneous nature of the crystals of the sample. The combination of these two factors may have caused some of the 100 acquisition shots to be well above the laser fluence threshold and these shots may have yielded an exceptionally large amount of ions with very wide energy spread. Resolution would have been degraded as a result. Accordingly, improving the laser power stability did allow for consistent resolution of around $m/\Delta m=350$ –400.

Experiments were performed with peptides including bombesin and melittin, as well as small proteins in particular bovine insulin and mixtures of the above (figure 27). The mass resolution achieved with these samples was dependent on the matrix used and varied from shot-to-shot. When sinapinic acid was

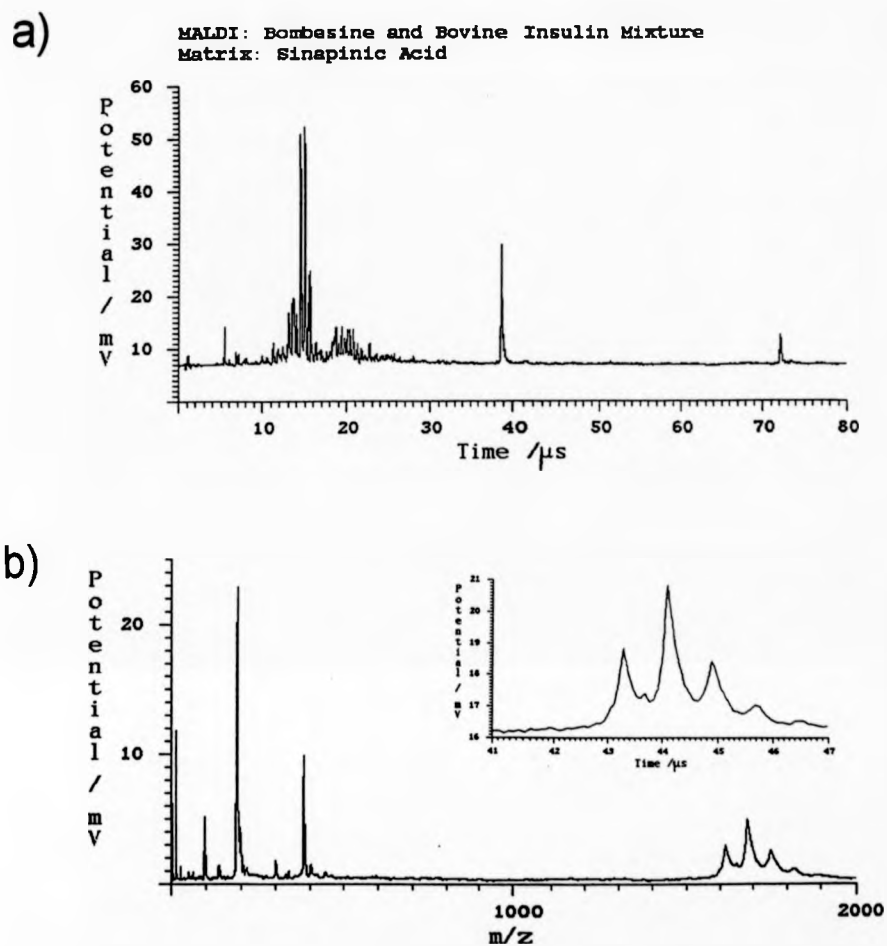


Figure 27. a) MALDI mass spectrum of mixture of bombesin and bovine insulin with sinapinic acid matrix, received in the large scale time-of-flight mass spectrometer. b) MALDI mass spectrum of bombesin with 4-hydroxy α -cyanocynamic acid matrix, demonstrating matrix-adduct peaks.

used resolution was about 100–150, while 4-hydroxy α -cyanocynamic acid gave spectra of bombesin demonstrating resolution of $m/\Delta m=400$.

Various polymer samples were analysed, including polymethylmethacrylate (PMMA), polystyrene and polyethylene glycol (PEG) with masses ranging from 200 to 7000 (Figure 28 a, b and c). The expected shapes of the polydispersity envelopes were observed. The resolution was in the region of 150, allowing the separation of peaks with different adducts.

Ignoring the effect of the lens on flight time and time aberrations in the source, the flight of the ions could be considered to be through a field-free region with effective length $L_{\text{eff}}=L+2d$, where L was the length of the actual field-free region and d the length of the acceleration region. Time broadening in a linear TOF due to energy spread can be calculated using the formula

$$\Delta t = L_{\text{eff}} \sqrt{\frac{m}{2}} \left(\frac{1}{\sqrt{E_{\text{min}}}} - \frac{1}{\sqrt{E_{\text{max}}}} \right)$$

E_{max} and E_{min} are the maximum and minimum kinetic energies of the ion packet respectively. The energy spread is $\Delta E=E_{\text{max}}-E_{\text{min}}$. Assuming that time spread in the experiments was primarily caused by energy spread, an experimental value could be derived for the energy spread. For bombesin, the minimum time spread observed was 50 ns for 20 kV acceleration, corresponding to 50 eV energy spread. This energy spread is due to two main factors: On one hand, ions are formed in the gas phase, within the extraction region above the sample surface. Ions formed at different positions will experience different initial accelerations and acquire different final energies. On the other hand, after their

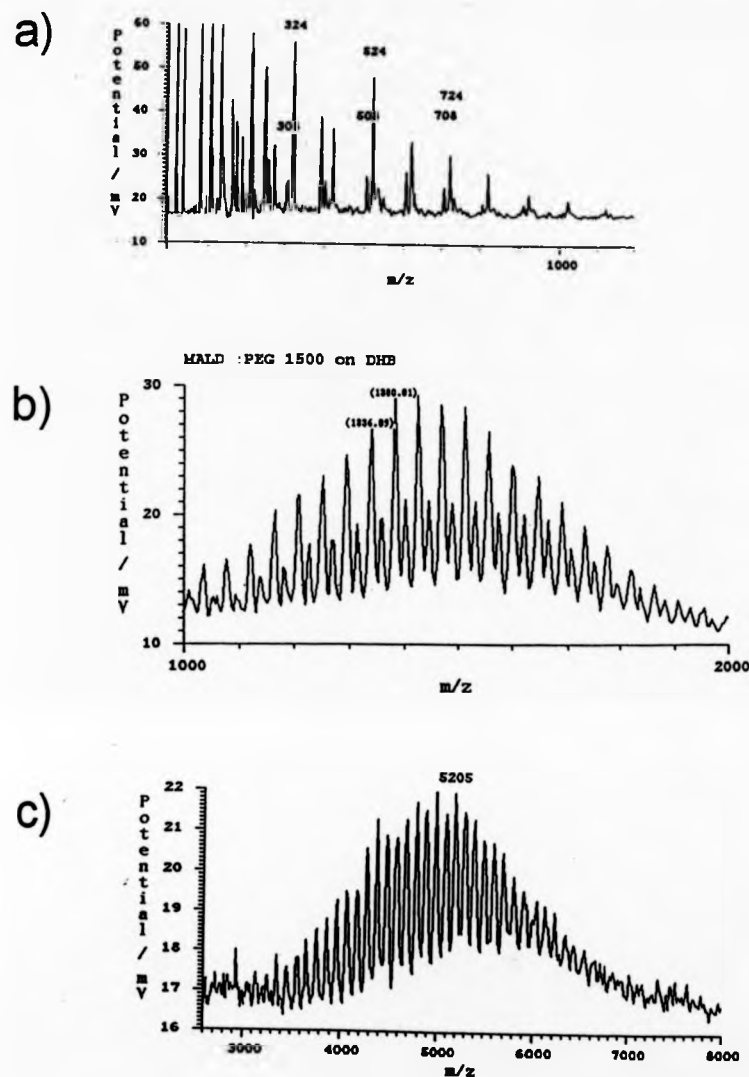


Figure 28. Polymer samples analysed using the large scale time-of-flight mass spectrometer, with DHB matrix . a) PMMA 583 average mass with Li and Cs adducts, b) PEG 1500 average mass with Na⁺ and K⁺ adducts and c) polystyrene 5000 average weight with Ag⁺ adducts.

formation, ions acquire higher velocities due to the extraction field and may collide with slower neutral molecules in the dense plum above the sample surface. This results to random kinetic energy loss, adding to the energy spread.

It has been mentioned that the main cause of resolution degradation in the acquisition of mass spectra was the fluctuation of the laser power, in combination with the different behaviour of different parts of the sample. One of the most promising methods to solve this problem is on-line "screening" of each spectrum before its addition to the acquisition. If the resolution were not within acceptable limits, the spectrum would be discarded. More advanced techniques use the peak height and resolution values as feedback to optimise laser attenuation, using complex software algorithms for decision taking.

3. Chapter Three.

Matrix-assisted laser desorption/ionisation (MALDI) in a double-focusing mass spectrometer with an array detector.

3.1 Introduction.

In the second part of this work, a matrix-assisted laser desorption/ionisation (MALDI) ion source was introduced into the intermediate region of a four-sector tandem mass spectrometer equipped with an array detector [157]. The purpose was to assess the ability of a double-focusing mass spectrometer to compensate for the energy and angular spreads of ion beams.

It has been mentioned in the previous chapter that MALDI ion beams suffer from relatively high energy and angular spread. The resolution achieved in a linear time-of-flight mass spectrometer may be further degraded because of the existence of ions with masses near to that of the analyte (ions with adducts of cations (Na^+ , K^+) or with parts of the matrix molecule), and which consequently contribute to the analyte peak. The ion optics of a double-focusing mass spectrometer should eliminate the factors that contribute to peak broadening of a MALDI ion packet, offering high resolution enough to resolve not only the protonated analyte peak from the adduct peaks but also their isotopic distributions. However, scanning double-focusing mass spectrometers are not directly compatible with pulsed ion sources. This difficulty can be overcome through the use of an array detector which can simultaneously detect a whole range of neighbouring mass species [158].

3.2 The CONCEPT 4-sector double focusing tandem mass spectrometer.

The instrument used for this part of the work was a Kratos IIHH tandem mass spectrometer [159]. Under normal operation, the first double-focusing mass spectrometer is used for production and isolation of a single-mass ion species which is focused into the collision cell region to undergo collision-induced dissociation. The fragment ions are ejected into the second mass analyser, which also is a double focusing mass spectrometer with identical characteristics to the first.

The geometry of the Concept double-focusing mass spectrometers follows the Nier-Johnson scheme, where the ion beam is spatially-focused between the two sectors (figure 29). The combination of the electric with the magnetic sector brings ions with the same mass but different initial parameters to be both energy- and space-focused at a single point, where angular and energy aberrations up to second order are eliminated [17]. This is the point where the exit slit of a double-focusing mass spectrometer would typically be positioned. In practice, initial energy and angular spreads should be within the acceptance limits set by the actual dimensions and design of the specific instrument. When an array detector is used, the ions are focused on an image plane [160] with a small compromise in resolution but large gain in sensitivity.

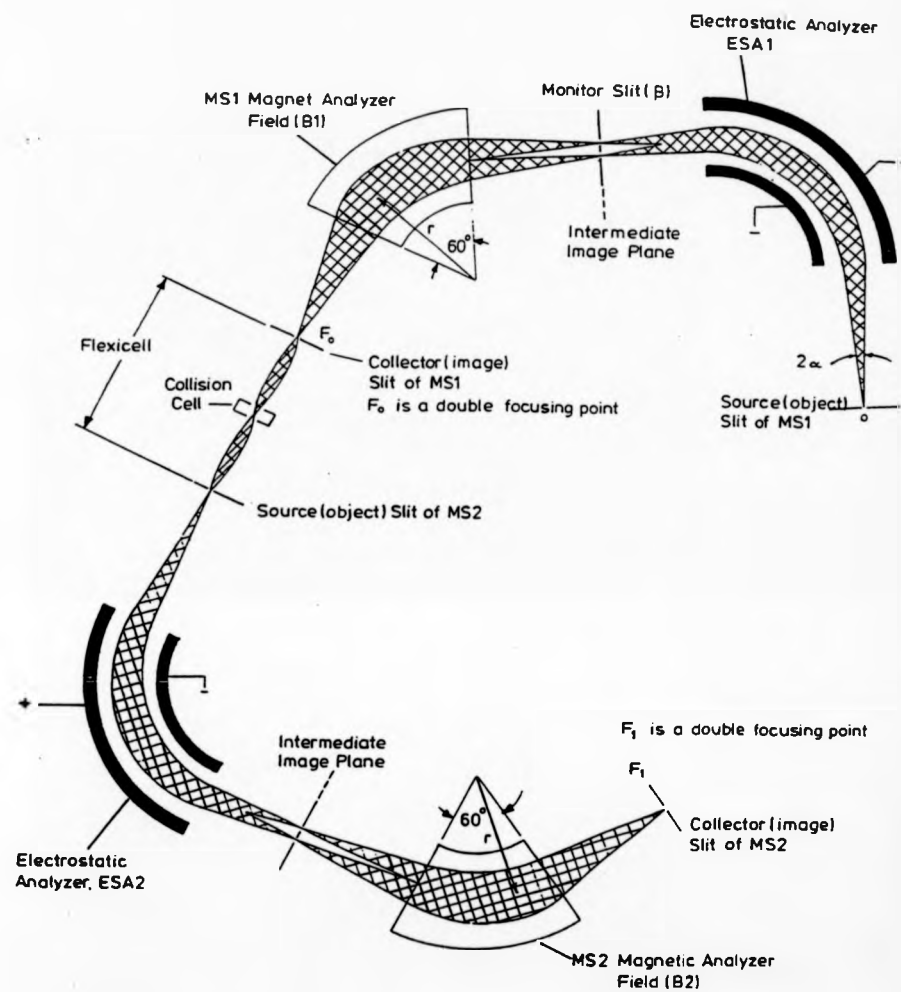


Figure 29 Schematic diagram of the ion optical configuration of the Kratos Concept IIHH four-sector tandem mass spectrometer.

3.3 The MALDI source.

The collision cell was situated in a vacuum chamber, in the region between the two parts of the Concept 4-sector instrument, called the flexicell. A number of ion optical elements existed before and after the collision cell region, which served to steer and focus the precursor ion beam in the middle of the cell and to optimise the fragment ion beam for ejection into the second mass-analyser. It had been decided that the modifications undertaken in order to incorporate the MALDI ion source should not interfere with the normal operation of the instrument as a tandem mass spectrometer, i.e. no significant change to the ion optics was to be imposed.

Under normal operation of the instrument, external calibration experiments could be performed in the second mass analyser using $(\text{CsI})_n\text{Cs}^+$ clusters. These ions were created on the tip of a specially designed probe incorporating a FAB gun. The probe was inserted exactly through an insertion lock into the collision cell. This same insertion lock was exploited for the introduction of the MALDI sample to the required position inside the collision cell. A special probe was designed and manufactured, having a flat surface for sample deposition. The probe was rotated so that the sample surface was perpendicular to the path of the ions towards the entrance slit of the second double-focusing mass spectrometer.

3.3.1 The nitrogen laser.

For MALDI ion production the sample surface was irradiated by a focused UV laser beam. An optical bench was designed and secured against the frame of

the mass spectrometer to support the laser and other components of the optical path (figure 30). The laser utilised was a Laser Science Inc. (Newton, MA) model VSL-337ND pulsed nitrogen laser. The average energy per pulse was 250 μ J and could not be adjusted from the laser controls. The time-length of the pulse was approximately 3 ns and the wavelength of the laser radiation was 337 nm.

The optical resonator of the nitrogen laser was created between two mirrors on either side of a tube containing nitrogen gas. The nitrogen gas molecules were electronically excited with a high voltage discharge, which created population inversion. Both mirrors were 100% reflective. The rear mirror was concave; the exit mirror was convex and had the shape of one-quarter of a circle. The resonator created between the two mirrors was unstable, which meant that photons were reflected only a small number of times (2-4). The main characteristic of unstable resonators is that the laser beam produced usually has a divergence less than 1 mrad.

3.3.2 The optical components.

The power density of the laser beam used in MALDI should normally be near the ion production threshold, in order to optimise the ion throughput and minimise the energy spread. Because the nitrogen laser does not offer any control of the laser pulse power, it was essential to include a beam attenuator in the laser path. A Newport (Fountain Valley, CA, USA) attenuator identical to the one used in the apparatus described in the previous chapter was employed.

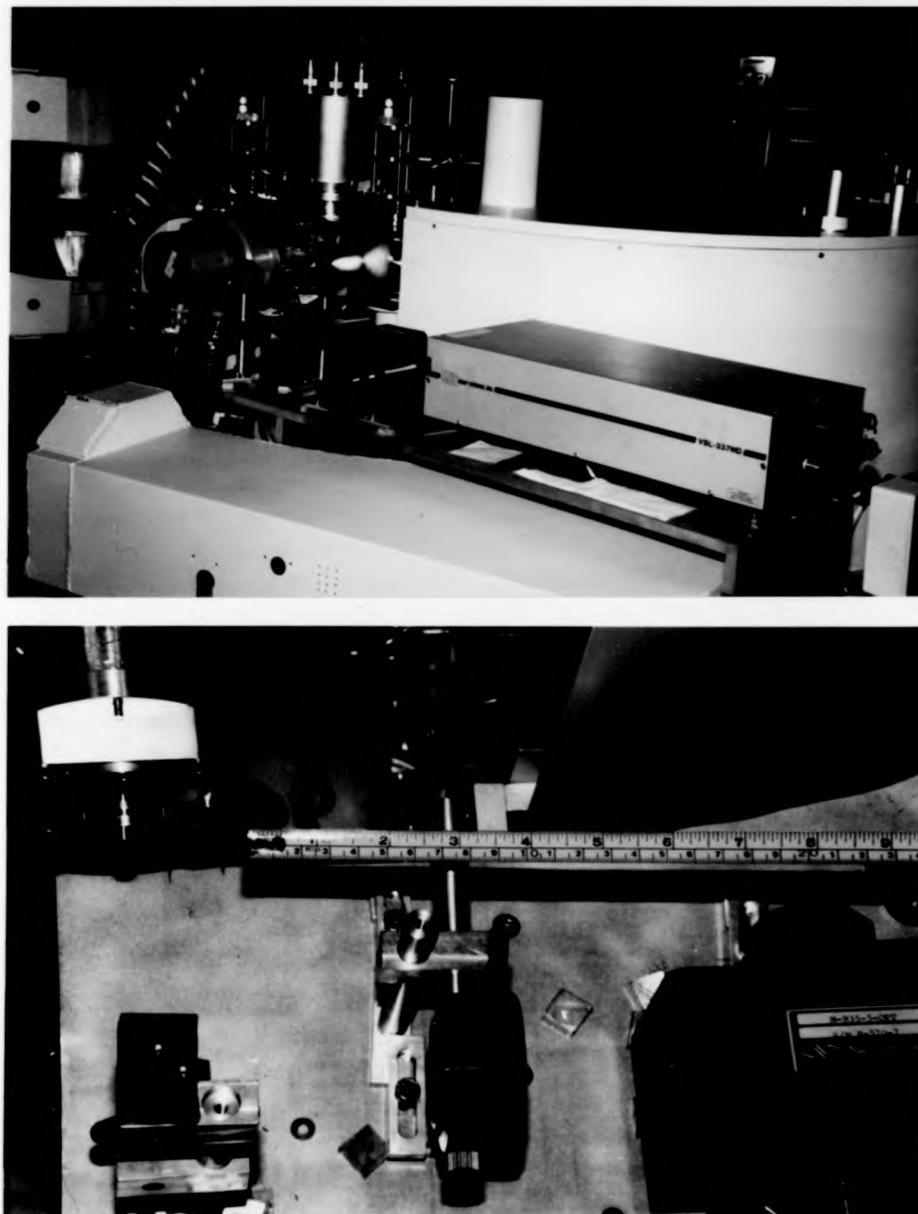


Figure 30. Photograph of the optical bench for the nitrogen laser and close-up photograph of optical components of the MALDI source of the second double-focusing mass analyser of the four-sector mass spectrometer. A metal-sheet cover was made to enclose stray laser radiation.

The laser beam was focused with a Comar (Cambridge, UK) Spectrosil-B 500 mm lens mounted on a Newport lens mount, which allowed manipulation of the lens position with respect to the final target. A set of two aluminium-coated mirrors mounted on Newport mini-mirror mounts constituted a beam steering device. Manipulation of the first or the second mirror could adjust the starting point or the direction of the final optical axis respectively.

The laser beam entered the vacuum chamber through a quartz window positioned on a specially made flange. The flange was mounted on the flexicell, in the place where the electron multiplier of a disused post-accelerating detector used to be situated. This detector had been used during initial development experiments of the instrument to optimise the transmission through the collision cell. It was situated after the extraction region of the collision cell. A specially designed tube was welded to the flange that housed the UV window (figure 31). The tube was long enough to protrude further than the ion optical path and its end was cut in a vertical plane at an angle of 45 degrees to the ion path. A large diameter hole was drilled through the part of the cylinder that coincided with the ion optical path. Two appropriately shaped (part of a half ellipse) stainless steel parts were screwed on the 45 degree-cut face of the tube leaving a 10 mm gap between them for ion beam transmission. An aluminium coated flat mirror was mounted on the lower of the semi-elliptical parts to reflect the laser beam towards the target surface. The plane of the lens was tilted 7 degrees upwards for this purpose. A convex mirror was mounted on the upper semi-elliptical part to allow observation of the target surface and the surrounding area. The insulating surfaces of the mirrors that

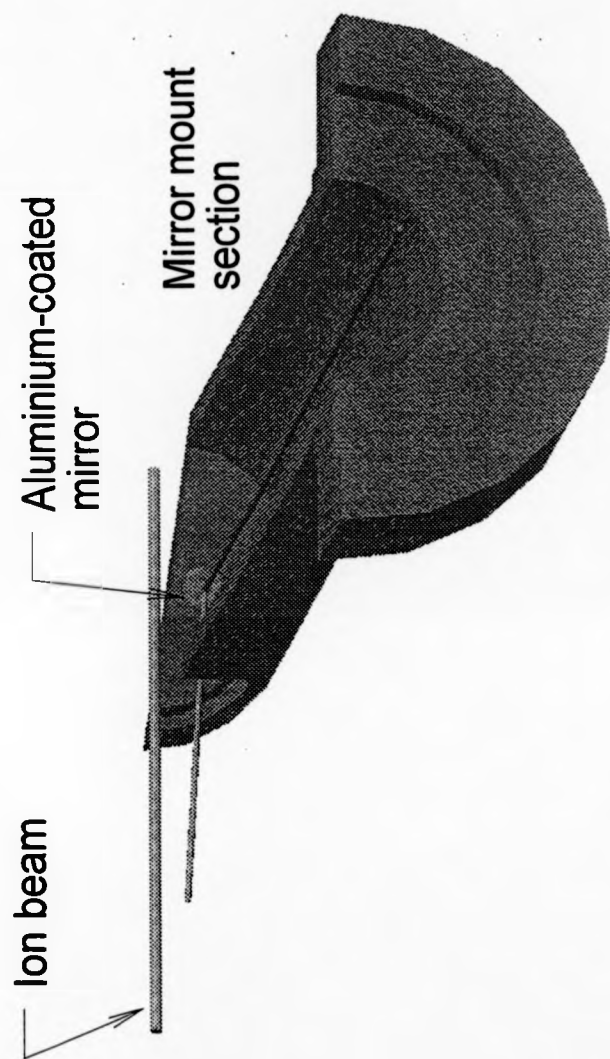


Figure 31. Three-dimensional schematic drawing of the in-vacuum mirror mount/tube.

might have been exposed to the ion current were covered with metal foil to avoid charging effects.

3.3.3 Ion optics.

Although the ion optics of the exit of the collision cell were not designed for MALDI ion beams, they did have the ability to prepare the diverging fragment ion beam for ejection into the double-focusing analyser. A schematic of the ion optical system can be found in figure 32. The collision cell, the collision cell guard electrode and the sample probe were all floated to 8 kV accelerating potential. The ions were initially accelerated in the region between the sample probe and the first y -focus and deflection electrode. The focusing potential of this electrode could be adjusted over the range between 4 and 8 kV, while the differential deflection voltage was ± 50 V [161]. Further down the ion path there was a second y -focus electrode that can be adjusted over the range between 4 and 6.5 kV. It was followed by a split electrode used for y -deflection, with maximum differential voltage ± 100 V. The above electrodes were used to focus the ion beam into the entrance slit of the double-focusing mass spectrometer. After the mirror mount assembly, there was one z -slit which was kept at fixed potential 1000 V. Another y - and z -slit assembly was situated after the entrance slit, to optimise the image of the ion beam and maximise transmission through the sectors.

SIMION ion trajectory simulations were performed to evaluate the performance of the ion optical system with MALDI ion beams and find the optimum potentials for the lenses. Experimentally, the ion optical elements

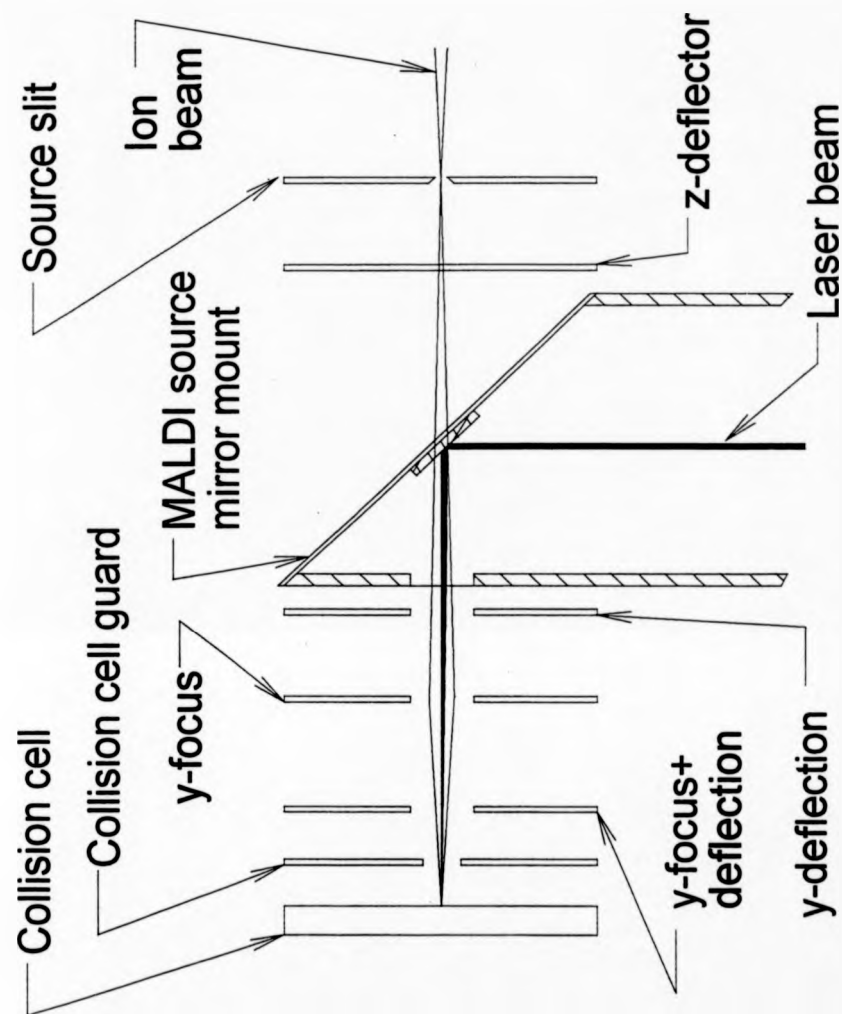


Figure 32. Schematic of the ion optics of the collision cell exit of the KRATOS Concept IIHH four-sector tandem mass spectrometer.

were tuned, using the current of the CsI clusters from the special FAB source—probe described earlier.

3.3.4 The electrostatic analyser.

After the ion beam diverged from the source slit with average kinetic energy qeV_0 electron volts, it entered the electrostatic field between the two cylindrical geometry plates of the electrostatic analyser (ESA). The sector had an angle 90 degrees and mean radius 381mm. The radial field of the ESA made the ions converge into focal points on an image plane after the sector, according to their energies. Small variations in the energies of the ions caused ion-velocity dispersion across an image plane. The potential difference between the two plates of the electrostatic sector was given by the expression:

$$V_{el} = k_{el} \cdot V_0 \quad \text{Eq. 3-1}$$

The constant k_{el} is equal to $2\ln(R_2/R_1)$, where R_2 and R_1 are the outer and inner radii of the ESA plates.

After the electric sector of the second mass analyser of the 4-sector tandem mass spectrometer an adjustable β -slit was situated, which could be used to limit energy spread or to perform energy-resolved experiments. This slit was kept at maximum width for the MALDI experiments.

3.3.5 The magnetic analyser.

The magnetic field was generated between the poles of an electromagnet, the strength of which was controlled by direct current measurement or by feedback measurement provided by a Hall probe. It has been shown in Eq. 1-3

that for a specific set of magnet parameters the mass dependence on radius r is given by the expression:

$$\frac{m}{qe} = \frac{B^2 r^2}{2V_0} \quad \text{Eq. 3-2}$$

For a single-charge ion, this expression can be converted by expressing mass M in atomic mass units (Da) to

$$M = 4.83 \times 10^3 \frac{B^2 r^2}{V_0} \quad \text{Eq. 3-3}$$

B is in Tesla, r in cm and V_0 in volts. The angle of the magnetic sector was 60 degrees and the central radius was 686 mm. The maximum magnetic field strength created by the electromagnet was approximately 1.87 Tesla, therefore the upper mass limit was in the area of 10000 Da.

The gap between the magnet poles was wedge-shaped. The resulting inhomogeneous magnetic field allowed the magnet to be closer to the intermediate image plane than a homogeneous magnet would have been. It also brought the focal point of the magnet closer to its exit. The benefit of using an inhomogeneous magnetic field was that the overall dimensions of the instrument were kept smaller and the ion path length was minimised, while the double-focusing property remained the same [162].

As the ions were focused in the y -direction in the magnetic sector, they were experiencing a defocusing action in the z -direction. In order to compensate for this an Einzel z -lens and deflector had been introduced before the magnetic sector. A set of current shims was used to fine-tune the shape of the magnetic

field in order to optimise resolution and peak shape. Finally, in order to correct beam distortions and rotation that occurred in the fringing field in the entrance and exit boundaries of the magnetic field, two hexapole lenses were employed, the first in the region between the two sectors and the second after the magnet.

3.3.6 The array detector.

The passage of the ions through the magnetic sector created an equal and opposite velocity dispersion to that created by the ESA. This made the ions focus at different positions in an image plane, according to their mass. An array detector [163] was positioned to coincide with the optimum image plane (figure 33). This arrangement did not include a collector slit. Thus a range of different mass ions were allowed to reach the surface of the position-sensitive detector.

The detector assembly consisted of a pair of matched multi-channel plates, a phosphorous screen, an optical fiber coupling and a photodiode array (CCD). When an ion struck one of the channels of the first multi-channel plate an electron shower exited the end of the second plate in the corresponding position. When the electrons reached the phosphor screen, it was illuminated and light travelled through the optical fiber coupling to a certain position on the photodiode array. The complete image of different light intensity values from the photodiode array was transformed into a spectrum that could be assigned to masses for any given value of the magnetic field. In practice as the magnet was monotonically scanned during an acquisition, the image from the array detector was continuously accumulated and the signal

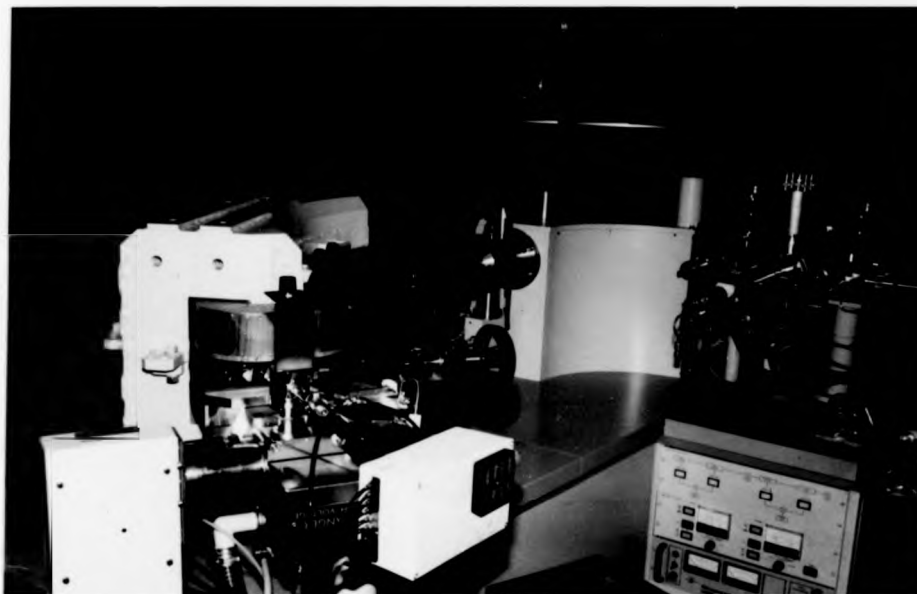


Figure 33. Photograph of the second mass analyser of the KRATOS Concept IIHH four-sector tandem mass spectrometer. The detector assembly of the instrument is designed to allow quick substitution of the point detector with an array detector, allowing simultaneous detection of ions with masses within approximately 4% of the mass range.

corresponding to each individual mass was integrated by the acquisition software of the mass spectrometer.

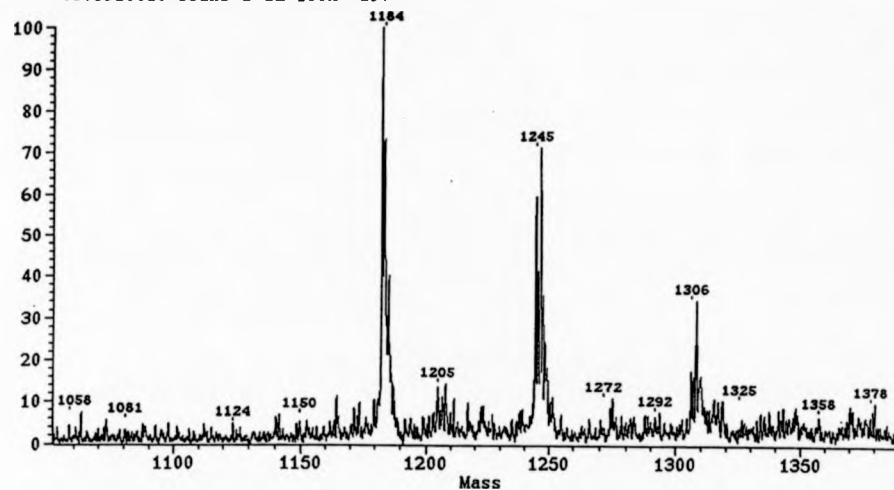
At any given moment of the acquisition, a range of masses approximately $\pm 2\%$ around the middle mass was being detected. As a result there was a significant sensitivity gain compared to the case of a point detector. In the particular case of the pulsed ion source, the array detector allowed simultaneous acquisition of all the ions of the isotopic distribution of a peptide without the need to scan the magnet (*vide infra*).

3.4 Experimental results and discussion.

The laser spot was aligned to the centre of the sample probe with the help of the beam steering device. Thermal paper was attached to the surface of the sample and the probe was introduced to the desired position. The laser beam was irradiated at full power on the thermal paper surface and the position of the burn-mark was optimised. External calibration of the double-focusing mass spectrometer had been performed with CsI cluster ions, as mentioned.

A number of experiments were performed with small peptides as well as polymers. The matrices utilised in the experiments were sinapinic acid, 4-hydroxy α -cyanocynamic acid, 2,5-dihydroxybenzoic acid (DHB) and nitroanthracene. They were dissolved in a 1:1 mixture of acetonitrile and water with the addition of 0.1% fluoroacetic acid (CF_3COOH) to give a 10^{-1} M solution. One 1 μl droplet of the matrix solution was deposited at the centre of the flat probe surface probe, and dried in the vacuum of the insertion lock or

a)

MALDI EB LHRH 6 Mar 95 1:11 pm LRP +LSIMS
0603950010 scans 1-12 100%= 19V

b)

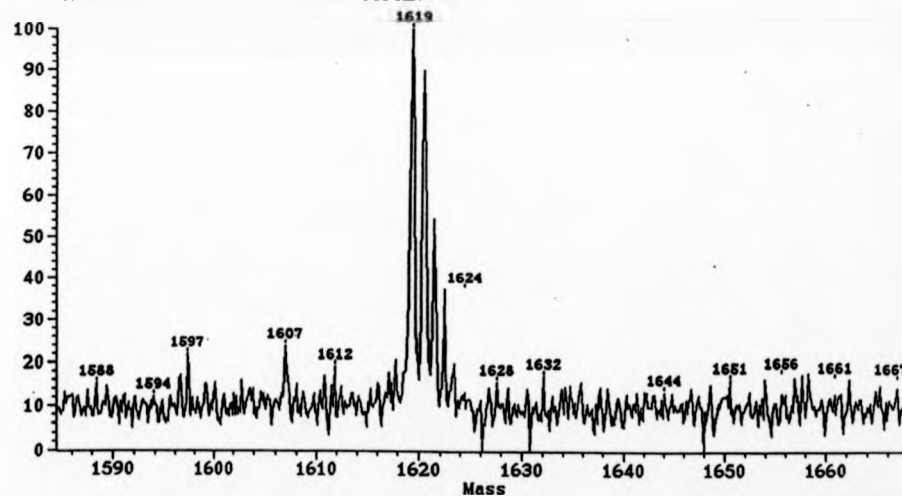
Bombesin MALDI-Concept 29 Mar 94 1:57 pm LRP +LSIMS
Maldi0034 scans 24-24 100%= 3698mV

Figure 34. Mass spectra received with the MALDI ion source in the collision cell area of the KRATOS Concept IHH tandem mass spectrometer. a) LHRH with resolution 1000 (FWHM); b) bombesin with resolution 3500 (FWHM).

under flow of dry air. Half μl of 10^{-4} to 10^{-5} molar concentration of the analyte solution was deposited on the dried matrix. The mixture was dried and inserted in the source for measurement.

The sample probe was manually manipulated during an acquisition in order to expose fresh sample area to the $100\ \mu\text{m}$ laser spot. The laser was operated at high repetition rate (10–20 Hz), and the laser beam fluence was adjusted by means of the attenuator while the main mass peak height was monitored by acquiring snapshots of the mass spectrum with 1 s integration time. After tuning of the ion optics the ion source yielded a number of high quality results demonstrating the good resolution and sensitivity of the apparatus. The MALDI mass spectrum of LHRH was measured with resolution higher than 1000 (FWHM) (figure 34a). The double-focusing instrument could easily resolve the mass peaks with water or matrix adducts. In figure 34b a MALDI mass spectrum of bombesin is shown with resolution 3500 (FWHM). The isotopic pattern of the bombesin molecule is clearly resolved. This level of resolution for MALDI ions is out of the reach of most electrostatic time-of-flight mass spectrometers, while it has been achieved with a similar apparatus by Biemann and coworkers [164] and more recently with FT-ICR instruments and time-lag focusing (delayed extraction) time-of-flight mass spectrometers.

In figure 35 a medium resolution mass spectrum of part the polydispersity envelope of the polymer polystyrene in nitroanthracene is shown. This polymer is non polar and Ag salt was added on the sample stage to enable the polymer molecules to become ionised. The detected ion peaks

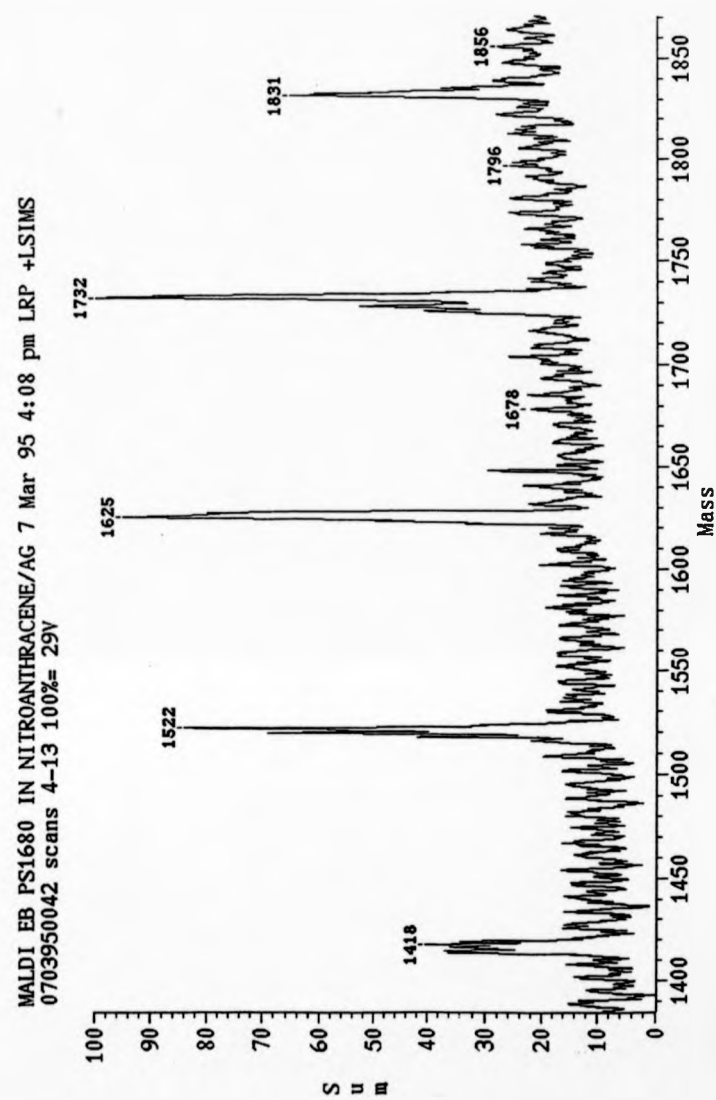
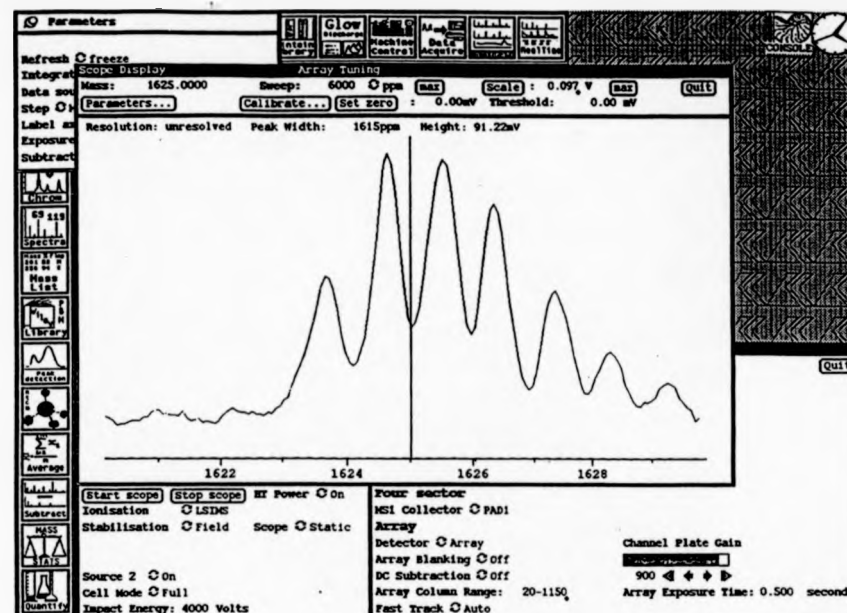


Figure 35. Medium resolution mass spectrum of polystyrene (PS1680) with Ag^+ adduct.

a)



b)

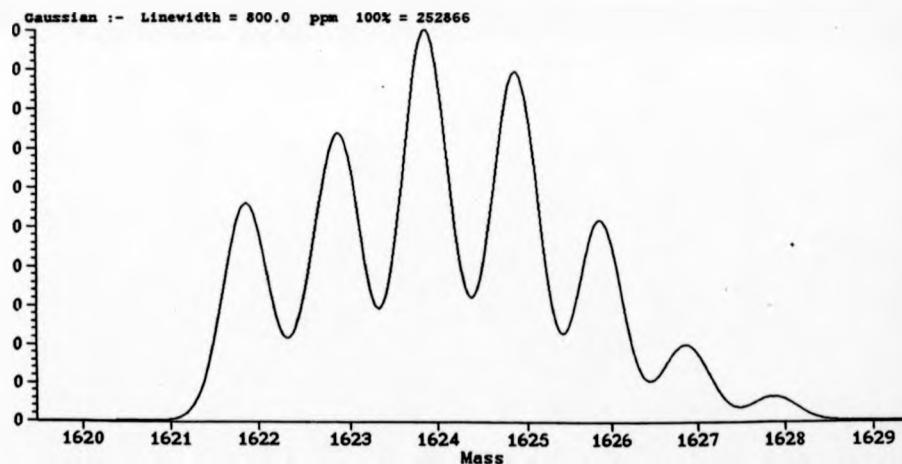


Figure 36. a) A "snapshot" of the 1625 Da mass ion peak of polystyrene with Ag^+ adduct is shown. The magnet is kept static and signal of ions of the chosen mass range is integrated with the array detector. b) theoretical isotopic distribution of the 1625 Da mass ion peak of polystyrene with Ag^+ adduct.

corresponded to the polymer molecules with Ag^+ adducted. On figure 36 a snapshot of the 1625 Da mass ion peak of the above polymer displaying single mass resolution is compared to the theoretical isotopic distribution of the polymer ion with adducted Ag^+ .

It has been shown that a MALDI ion beam has been successfully transmitted through a double-focusing mass spectrometer. Although the ion optics of the collision cell were not designed for use with a MALDI ion beam, the sensitivity of the device under good experimental conditions was excellent, as demonstrated by the single scan spectrum of bombesin shown above (approximately 1 s acquisition at 10 Hz repetition rate). Nevertheless, improvements in the sample manipulation would enhance the usability of the device further. The ion transmission and the efficiency of sample usage might also be increased, if the laser beam were focused to a line 100 μm wide and 5 mm tall, resembling the precursor ion beam shape when it passed through the collision cell. This could be achieved with the appropriate use of a cylindrical lens in the laser beam path.

4. Chapter Four.

The magnetic sector time-of-flight tandem mass spectrometer (Mag-TOF).

4.1 Introduction .

As the application of mass spectrometry in general and tandem mass spectrometry in particular extends into biochemical and biomedical research, sensitivity becomes an overriding concern. Even though mass spectrometry is often clearly superior to most other rival techniques in terms of sensitivity, some biological samples can be extremely scarce and valuable and often much information has to be drawn from the minute amounts available. In this context, scanning mass spectrometers have an inherent disadvantage. Mass spectra are acquired by intentionally filtering a continuous ion beam, literally throwing away all but one single mass ionic species during any given moment of the acquisition cycle. In a scanning double-focusing mass spectrometer, for instance, if a 10 s acquisition cycle is assumed for a mass range of 1000 Da with approximately one-mass resolving power, each different mass species is being detected for an average of 10 ms only, and therefore 99.9% of the ions produced are not measured. This situation becomes worse when wider mass ranges or higher resolutions are necessary.

In the case of tandem mass spectrometry utilising activation methods like CID, the situation is particularly demanding given the relatively low efficiency of the activation methods. A definite improvement on the picture described above was achieved with the introduction of scanning array detectors in the second

mass analyser of four-sector type instruments, as described in the previous chapter of this work. Different size scanning array detectors have been introduced in commercial instruments, allowing detection of 10–20% of the total mass range [165]. Nevertheless, array detection is still far from ideal, as the construction of a 100% scanning array detector would impose practical and technological challenges difficult to overcome.

Another practical concern arises with the use of continuous ion sources like L-SIMS. Such ion sources produce approximately the same throughput of ions during “warm-up”, tuning, acquisition and breaks between acquisitions. Tandem mass spectrometry experiments in particular require a high variety of parameters to be tuned, increasing sample waste. It can be estimated that actual data acquisition time may not be much more than 10% of the total running time of a tandem mass spectrometer employing a continuous ion source.

It has been recognised that, if a time-of-flight mass analyser was used instead of a scanning analyser as the second part of a tandem instrument, there would be an immediate gain in sensitivity. As TOF possess Fellgett's advantage, it would act as a scanning analyser with a 100% array detector. A time-of-flight analyser would couple naturally to a pulsed ion source, improving sample usage conditions. A number of attempts have been made to employ a TOF analyser as the MS2 of a tandem mass spectrometer, utilising a double-focusing analyser [166, 167] or another TOF [168, 169, 170, 171] for parent ion selection. Russell and coworkers [167] demonstrated an instrument consisting of a double-focusing mass analyser coupled with a linear TOF for

separation of CID fragment ions. This instrument produced poor results, demonstrating the basic difficulties of coupling those two different types of mass analysers.

The first issue to be tackled is the design of a pulsed ion source, e.g. a MALDI ion source, to produce an ion beam optimised for transmission through the electric and magnetic sector. The second problem comes from the fact that time-of-flight mass analysers require the ion beam to start from a minimum length point-source. Apart from the potentially substantial time aberrations imposed by the sectors, the energy spread of a MALDI ion beam is enough to create a far from ideal parent ion packet in the virtual source of the TOF analyser. This time-spread would have the same effect as a very long time-duration ionisation technique, severely degrading resolution.

There are two main strategies which could be adopted to tackle the latter, both involving high-voltage pulses. The first strategy, which will be called the orthogonal scheme, involves a push-out pulse that accelerates the ion packet orthogonally to its original direction. In this case, the resolution of the device will depend on the width of the initial ion beam, which can be minimised using a lens system. The second strategy, namely the longitudinal scheme, involves time-compression of the initial ion packet by means of a high-voltage pulse. When the time-spread ion packet lies between two initially grounded electrodes, a high-voltage pulse is applied on the rear electrode. As the ions accelerate towards the exit of the region, those in the rear end of the packet will acquire more energy than those in the front, therefore they will catch up further down the ion path. This device is called an ion buncher. The

focal point of the device can be adjusted by selecting the amplitude of the high-voltage pulse. Using an ion buncher, a short-time-length virtual ion source can be created for time-of-flight analysis in the original direction of the ion beam.

Both schemes have advantages and disadvantages. In the orthogonal scheme, the kinetic energy of the primary beam cannot be very high due to practical requirements for the size of the detector. Therefore, the parent ion beam has to pass through a deceleration stage prior to fragmentation. This creates two problems: firstly it is widely known that the use of decelerating lens imposes practical difficulties that may compromise sensitivity and secondly, low laboratory frame energies of the precursor ion beam limit experimental parameter choice. Heavy collision gases like xenon are required which may impose a high degree of scattering on the fragment ion beam, which may in turn have a detrimental effect on sensitivity and resolution. The most important advantage of this scheme is its simplicity, as a simple linear time-of-flight analyser with a large ion detector is adequate.

The ion buncher employed for a longitudinal scheme device, on the other hand imposes a significant energy spread on the parent ion beam, which may be as high as 20-30% of the kinetic energy of the ions. Therefore it is essential that the time-of-flight part of the instrument includes an energy spread correction device, namely an ion mirror. After the precursor ions fragment in the collision cell, fragment ions maintain approximately the same velocity as their parents. Hence, as the ion beam exits the collision cell region, the different mass fragments have a wide range of kinetic energies, ranging from the parent ion

kinetic energy to that of the smallest fragments. If a conventional ion mirror were to be used, it would have to be scanned to achieve acceptable resolution for ions of all masses. Such an approach would defeat the purpose of having a 100% mass analyser in the first place. The solution is to use a quadratic ion mirror, where the flight times of the ions are independent of their kinetic energy and only dependent on the mass-to-charge ratio. Such a device would offer good resolution by correcting the energy spread of every fragment ion in the spectrum in exactly the same way, without the need to scan. An instrument incorporating a quadratic ion mirror would be suitable for CID at high laboratory-frame collision energies of the precursor ions, which have been found to offer more efficient fragmentation [172,173]. This scheme would also offer a wider choice of collision gases and other experimental conditions. However, the task of achieving the optimum acceptance parameters for a quadratic mirror is not trivial, mainly due to the defocusing of the ions in the transverse direction [37]. Also, such a device would be much more complex than that of the orthogonal scheme, although still a lot simpler than a second double-focusing mass analyser with a scanning-array detector.

Prototype instruments for both schemes above have been constructed. Bateman and coworkers [174] installed a decelerating lens, a collision cell and an orthogonal acceleration time-of-flight mass analyser in the end of a EBE geometry Autospec (Fisons Instruments, Manchester, UK) mass spectrometer, equipped with a MALDI ion source. At the same time, the prototype instrument described in this work was created (magnetic sector/time-of-flight tandem mass spectrometer, Mag-TOF), based on the longitudinal scheme

geometry. The first mass analyser is a KRATOS Analytical Concept IIH double-focusing mass spectrometer. The second mass analyser is a quadratic ion mirror which is preceded by a beam interfacing region including delivery ion optics and an ion buncher. Fragmentation of the parent ions is performed in a grounded, differentially pumped collision cell. In the remaining part of this chapter, a number of theoretical considerations for the design of the Mag-TOF prototype instrument will be presented. Chapter Five will be devoted to the description of the construction of the instrument and the presentation of some experimental results.

4.2 The double-focusing mass spectrometer as the first stage of a tandem mass spectrometer.

4.2.1 Time and spatial aberrations in the two sectors.

The first mass analyser of the magnetic sector/time-of-flight (Mag-TOF) tandem mass spectrometer is a Nier-Johnson type double-focusing instrument [17]. In general terms, the passage of ions through the electric and magnetic sectors results in spatial and time aberrations. The Nier-Johnson combination of sectors can eliminate spatial aberrations up to the second order –which is the reason for the high resolution this type of instruments can afford. Unfortunately the same does not hold for time aberrations, and ions with the same mass but different initial conditions may have different flight times through the sectors. The initial conditions, of a parent ion with mass m leaving the source slit of the double focusing mass spectrometer, that contribute to time aberrations are the angle α of the ion velocity from the perpendicular

direction, the distance y of the ion from the central axis of the source slit, the relative energy spread ε and the absolute time that the ion passes through the slit compared to the average time for ions of the packet (figure 37). In the case of a MALDI ion source, the initial time deviation t_i arises directly from the time-length of the laser pulse and the time aberrations due to ion source components (i.e. accelerating electrodes, grids, lenses and deflectors).

Consider a parent ion with mass-to-charge ratio m_p/q that passes through the source slit at time $t=T_{ss}$ with mean energy qV_0 and initial conditions as described above. After flight through the sectors, the ion reaches at time T_d position $x(T_d)$ within the ion buncher region. The velocity and position coordinate of the ion are given by the expressions

$$\dot{x}(T_d) = \sqrt{\frac{2q}{m_p} V_0 (1 + \varepsilon)} \quad \text{Eq. 4-1}$$

and

$$x(T_d) = x_0 - x_\varepsilon \varepsilon - \Delta x_{ab} \quad \text{Eq. 4-2}$$

x_0 is the coordinate of the mean ion of the packet at the moment $t=T_d$, x_ε is coefficient of chromatic aberration, Δx_{ab} is overall displacement of the ion relative to the mean ion due to aberrations from all other initial parameters. In the first-order approximation, the spread Δx_{ab} depends on the initial angular spread α , the half-size of the source slit y and the initial time deviation t_i (see figure 37) according to the equation:

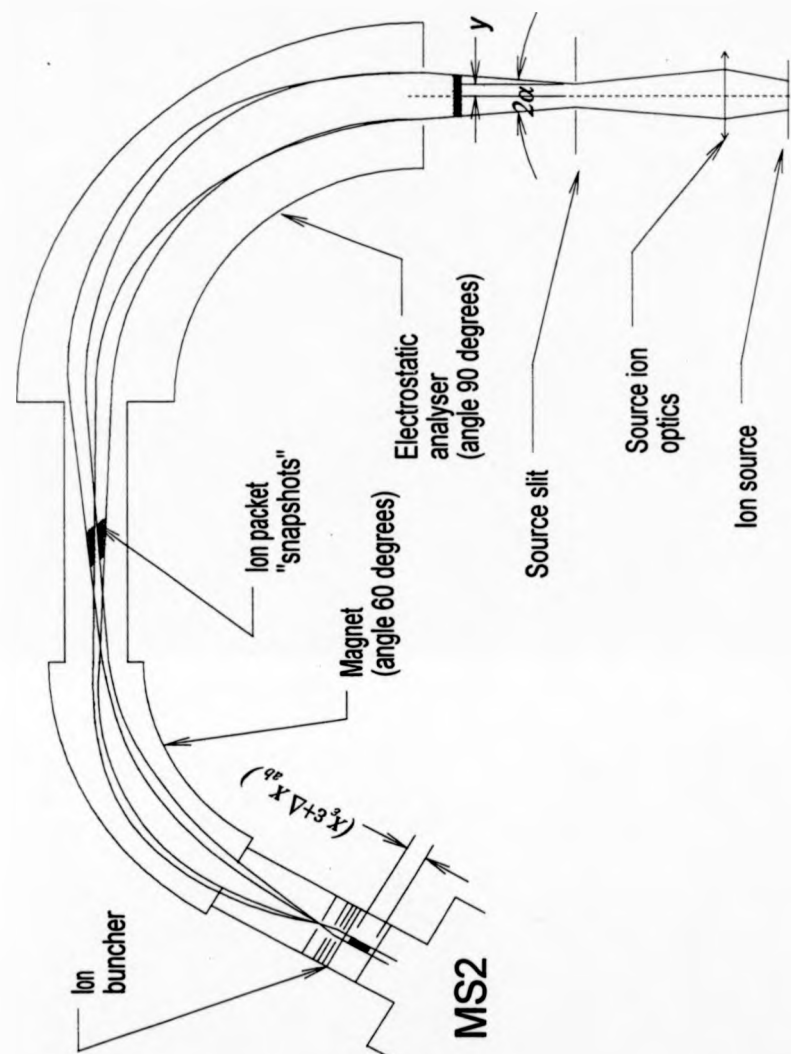


Figure 37 Schematic of a Nier-Johnson double-focusing mass spectrometer, demonstrating the geometric parameters of the sectors and the initial parameters of the beam, as well as the parameters describing the final ion packet.

$$\Delta x_{ab} = x_a \alpha + x_y y + \sqrt{\frac{2q}{m_p}} V_0 \cdot t_i \quad \text{Eq. 4-3}$$

Following Poschenrieder [175, 176] the aberration coefficients x_a , x_y , x_e can be acquired as

$$\begin{aligned} x_a &= r_e T_a^e + r_m T_a^m \frac{1}{M} \\ x_y &= r_e T_y^e + r_m T_y^m M \\ x_e &= r_e T_e^e + r_m T_e^m \end{aligned} \quad \text{Eq. 4-4}$$

expressed in terms of the radii r_e , r_m of the electric and magnetic sectors respectively, the magnification of the electric sector M and the terms

$$\begin{aligned} T_a^* &= \frac{1-k_*}{\omega_*^2} (1 - \cos \omega_* \psi_*) + \frac{L_{1*}}{r_*} \frac{1-k_*}{\omega_*} \sin \omega_* \psi_* \\ T_y^* &= \frac{1-k_*}{\omega_*} \sin \omega_* \psi_* \\ T_e^* &= \left(\frac{1-k_*}{2\omega_*^2} - \frac{1}{2} \right) \psi_* - \frac{(1-k_*)^2}{2\omega_*^3} \sin \omega_* \psi_* - \frac{L_{1*} + L_{2*}}{r_*} \end{aligned} \quad \text{Eq. 4-5}$$

where $*$ is used to symbolise both the electric sector and the magnet, i.e. instead of "e" or "m". Frequencies in the equations above are expressed as $\omega_e = (1+B_1)^{1/2}$ and $\omega_m = (1+A_1)^{1/2}$, where A_1 , B_1 are the first order coefficients of expansion of the corresponding inhomogeneous fields. The parameters $k_e = -1$ and $k_m = 0$ are used to generalise the form of the equations. Finally, L_{1e} , L_{2e} , L_{1m} and L_{2m} are the lengths of the first and second field-free regions for the electric and magnetic sectors, and ψ_e and ψ_m are the angles of the electric and magnetic sectors, respectively. The end-point of L_{2e} and the starting point of L_{1m} are both in the focal plane of the electric sector. The end-point of L_{2m} is located at co-ordinate $x(T_d)$.

The contribution of the time deviation t_i to the final spatial spread is quite low, because of the short time-length of the laser pulse (3 ns) and the low aberrations imposed by the ion source (<5 ns, vide infra). The values of the initial parameters α and y are limited by the acceptance characteristics of the double-focusing mass spectrometers, while energy spread is the most "volatile" contributor being affected by various parameters in the ionisation source. Calculations of the total time-of-flight throughout the Concept double-focusing instrument using the above expressions demonstrated that the effect of the angular deviation a for an ion packet with mass 1000 Da (singly charged), accelerated to 8 keV energy, maximum angular spread 0.7 degrees and typical slit width 200 μm gives rise to approximately 11.5 ns time spread at the exit slit. A similar amount of time spread can be induced by approximately 5 eV of energy spread, while 50 eV of energy spread would give rise to 150 ns spread. It is therefore obvious that the main contributor to the time spread (or otherwise mentioned longitudinal spatial spread) after the sectors is the initial energy spread produced in the ion source.

A conclusion that can be drawn from Eqs. 4-2 and 4.3 is that ions arriving at time T_d at a specific point x within the ion buncher region may have started from the source region with a different set of initial parameters. More specifically, spatial spread arising from small initial energy differences, may be exactly cancelled by a specific set of the other parameters, with the result that ions with slightly different initial energies arrive at the same point in the buncher at the same time.

4.2.2 The ion buncher.

It is obvious from the preceding discussion that the ion packet has to be time-compressed before injection into the time-of-flight analyser of the Mag-TOF prototype. This is achieved by means of an ion buncher. The ion buncher is effectively a pair of thin planar electrodes positioned at $x=0$ and $x=D$ (figure 38). When the ion packet lies within the two electrodes (at time T_d), a push-out high-voltage pulse with rise-time τ is applied to the rear electrode. Neglecting fringing fields, the equations of ion motion along x are

$$\left. \begin{aligned} \ddot{x} &= \frac{q}{m_p} E \\ x(T_d) &= x_0 - x_\varepsilon \varepsilon - \Delta x_{ab} \\ \dot{x}(T_d) &= -\sqrt{\frac{2q}{m_p} V_0 (1 + \varepsilon)} \end{aligned} \right\} \quad \text{Eq. 4-6}$$

wherein

$$\left. \begin{aligned} E &= -E_0 (1 - e^{-(t-T_d)/\tau}) & T_d \leq t \leq t_0 + T_d \\ E &= 0 & t < T_d, t > t_0 + T_d \end{aligned} \right\} \quad \text{Eq. 4-7}$$

A dot over x indicates differentiation with respect to time, t_0 is the flight time from $x(T_d)$ to $x=0$. E_0 is the asymptotic value of the field in the ion buncher. Negative signs of initial velocity and field indicate that they are directed towards lower x values. Direct integration of Eqs. 4-6 and 4-7 gives:

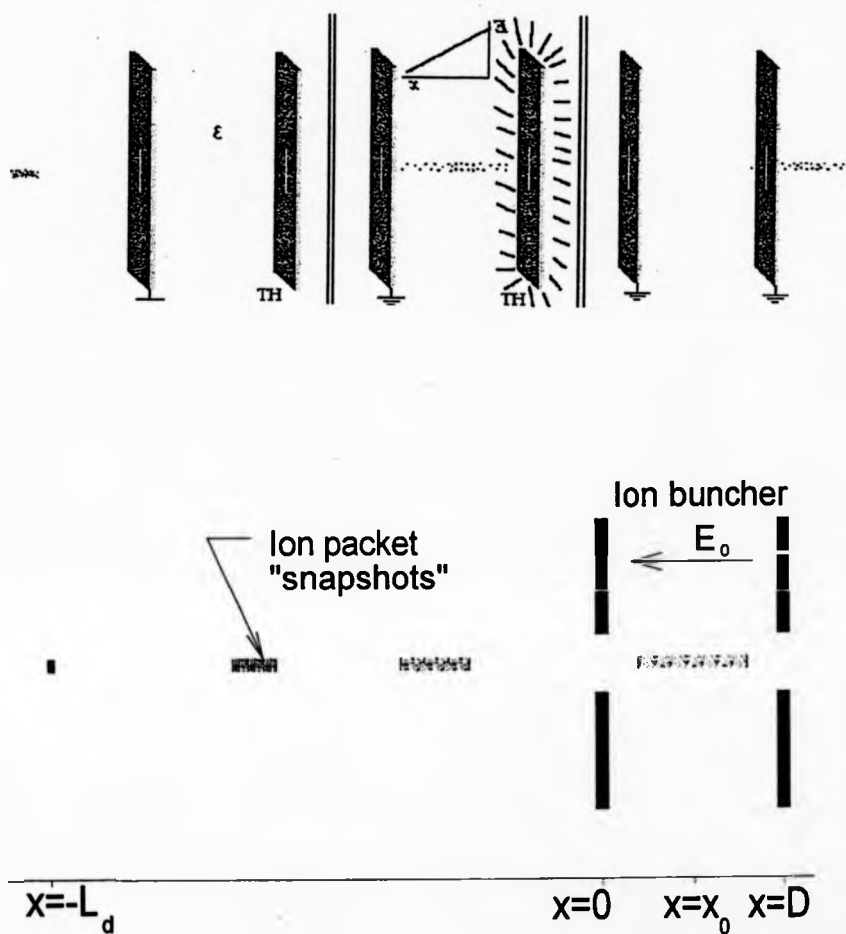


Figure 38. a) Illustration of the time-focusing action of the ion buncher.
b) Schematic of the ion buncher.

$$\dot{x}(t) = - \left[\dot{x}(T_d) + \frac{q}{m_p} E_0 t + \frac{q}{m_p} E_0 \tau (e^{-t/\tau} - 1) \right], T_d < t \leq t_0$$

$$\dot{x}(t) = \dot{x}(t_0 + T_d) = - \left[\sqrt{\frac{2q}{m_p} V_0 (1 + \varepsilon)} + \frac{q}{m_p} E_0 t_0 + \frac{q}{m_p} E_0 \tau (e^{-t_0/\tau} - 1) \right], t > t_0$$

Eq. 4-8

and

$$x(t) = x(T_d) - t \sqrt{\frac{2q}{m_p} V_0 (1 + \varepsilon)} - \frac{q}{m_p} \frac{E_0}{2} t^2 + \frac{q}{m_p} E_0 \tau \left[t + \tau (e^{-t/\tau} - 1) \right], T_d < t \leq t_0$$

$$x(t) = \dot{x}(t) \Big|_{t=t_0+T_d} \cdot (t - t_0), t > t_0$$

Eq. 4-9

For time $t=t_0$ the position of an ion is by definition $x(t_0)=0$, and the value of t_0 can be determined by the equation 4-9 for

$$x_0 - x_s \varepsilon - \Delta x_{ab} - t_0 \sqrt{\frac{2q}{m_p} V_0 (1 + \varepsilon)} - \frac{q}{m_p} \frac{E_0}{2} t_0^2 + \frac{q}{m_p} E_0 \tau \left[t_0 + \tau (e^{-t_0/\tau} - 1) \right] = 0$$

Eq. 4-10

Due to the fact that $\tau \ll t_0$, terms proportional to τ^2 in the above equation can be neglected. Hence the appropriate root of this second-order equation in t_0 is

$$t_0 = \tau + \frac{\sqrt{\frac{2q}{m_p} V_0 (1 + \varepsilon)} + \frac{2q}{m_p} E_0 (x_0 - x_s \varepsilon - \Delta x_{ab} - \xi) - \sqrt{\frac{2q}{m_p} V_0 (1 + \varepsilon)}}{\frac{q}{m} E_0}$$

Eq. 4-11

where

$$\xi = \tau \sqrt{\frac{2q}{m_p} V_0 (1 + \varepsilon)} \quad \text{Eq. 4-12}$$

The time-focus of the ion buncher lies at the position $x=-L$, which corresponds to the object plane of the ion mirror. The total TOF T for a parent ion (ignoring the flight time up to the source slit) is obtained from Eq. 4-9 for $x(T)=-L$.

$$T = T_d + t_0 + \frac{L}{\sqrt{\frac{2q}{m_p} V_0 (1 + \varepsilon) + \frac{q}{m_p} E_0 t_0 + \frac{q}{m_p} E_0 \tau (e^{-t_0/\tau} - 1)}} \quad \text{Eq. 4-13}$$

Replacing the value for t_0 found above Eq. 4-13 leads to:

$$T = T_d + \tau + \frac{L}{\sqrt{\frac{2q}{m_p} V_0 (1 + \varepsilon) + \frac{2q}{m_p} E_0 (x_0 - x_\varepsilon \varepsilon - \Delta x_{ab} - \xi) + \frac{q}{m_p} E_0 \tau e^{-t_0/\tau}}} \quad \text{Eq. 4-14}$$

This expression for T may be expanded into a series involving energy spread ε , rise-time τ and other aberrations:

$$T = T_0 + T_\varepsilon \varepsilon + T_{ab} \Delta x_{ab} + T_\tau \tau + \mathcal{G}(\varepsilon^2, \Delta x_{ab}^2, \tau^2) \quad \text{Eq. 4-15}$$

Function \mathcal{G} represents all second-order terms. Mean time T_0 and first order time-aberration coefficients are:

$$T_0 = T_d + \frac{L}{\sqrt{\frac{2q}{m_p} V_p}} \left[1 + \frac{2D}{L} \frac{v(v-1)}{w} \right] \quad \text{Eq. 4-16}$$

$$T_{\epsilon} = \frac{D}{\sqrt{\frac{2q}{m_p} V_0}} \left\{ \left(\frac{1}{w} - \frac{x_{\epsilon}}{D} \right) \left(1 - \frac{L}{2D} \frac{w}{v^2} \right) - \frac{v}{w} \right\} \quad \text{Eq. 4-17}$$

$$T_{ab} = \frac{1}{\sqrt{\frac{2q}{m_p} V_0}} \left(1 - \frac{L}{2D} \frac{w}{v^2} \right) \quad \text{Eq. 4-18}$$

$$T_{\tau} = \frac{L}{2D} \frac{w}{v^2} \left[\frac{1}{v} - e^{-t_0/\tau} \right] + 1 - \frac{1}{v} \quad \text{Eq. 4-19}$$

The notation V_p represents the final ion energy after acceleration from the ion buncher: $qV_p \equiv q(V_0 + E_0 x_0)$. v and w are dimensionless parameters of acceleration:

$$v \equiv \sqrt{\frac{V_p}{V_0}} = \sqrt{1 + \frac{x_0}{D} w} \quad \text{Eq. 4-20}$$

and

$$w \equiv \frac{E_0 D}{V_0} = \frac{V_k}{V_0} \quad \text{Eq. 4-21}$$

V_k is the maximum value of the push-out voltage. The expansion described in Eq. 4-15 can be used to evaluate the temporal width of the ion packet at the virtual ion source of the quadratic mirror. Consideration of the equations 4-15 to 4-19 shows that the chromatic aberration cannot be completely eliminated at the same time as the aberrations from the other initial parameters. It is readily shown that the initial parameters *other than the energy spread* will not influence the total TOF T (i.e. they will be corrected by the ion buncher to the first order) if

$$\frac{L}{2D} \frac{w}{v^2} = 1 \quad \text{Eq. 4-22}$$

or

$$V_k = \frac{D}{\frac{L}{2} - x_0} V_0 \quad \text{Eq. 4-23}$$

On the other hand in order to obtain time-focusing conditions for the spatial spread induced by the energy spread ε , Eq. 4-17 should be solved for $T_\varepsilon=0$.

The following expression is obtained

$$\frac{L}{2D} \frac{w}{v^2} = 1 - \frac{\frac{v}{w}}{\frac{1}{w} - \frac{x_\varepsilon}{D}} \quad \text{Eq. 4-24}$$

Because in practice the main contributor to the total spatial spread of the ion pack in the buncher is the initial energy spread ε , the length of the buncher D is chosen to be equal to or slightly larger than the spatial spread $x_\varepsilon \varepsilon$ imposed by the energy spread ε . Thus, it can be seen that $x_\varepsilon/D \approx 1/\varepsilon$ and hence $x_\varepsilon/D \gg 1$. As a result, the right hand side of Eq.4-24 is approximately equal to 1, since the value of $1/w$ is small (i.e. $V_0=2-3V_k$). Thus the root of the equation 4-17 for T_ε has been made very similar to that of Eq. 4-18 for T_{ab} i.e. focusing for both aberrations will occur for similar values of V_k . Nevertheless, the voltage for optimum time-focusing of a MALDI ion packet at the object plane of the quadratic field can be precisely determined experimentally, as described in the following chapter.

Finally, it should be noted that the term T_r from the rise-time cannot be regarded as a classical aberration, because it can not be expanded as powers of a small parameter in the same way as for the other aberration coefficients. Therefore a pragmatic approach is adopted to minimise this aberration. Electronics that typically provide rise-times τ of 10-100 ns should be utilised, which ensures that $t_0 \geq (3-4)\tau$ for all ions of interest. Jitter in rise-time τ from the electronics directly affects the TOF, and in order to keep this factor from compromising reproducibility low jitter-values, typically less than 1 or 2 ns, should be achieved. Shot-to-shot irreproducibility in the shape of the transient curve could be modelled by using variable τ in the appropriate formulae. In Eq. 4-7 which describes the time-dependent electric field, overshoot and ringing of the buncher pulse are neglected. The real-world transition could be modelled by adjusting τ in such a way that the integral of Eq. 4-7 over time is equal to the integral of the actual transition curve.

4.2.3 Time-of-flight aberrations on electrostatic lenses.

Time-of-flight aberrations induced by focusing lenses or by the exit slit of the buncher constitute another potential source of temporal broadening. In the case of electrostatic potentials, total ion energy (i.e. the sum of kinetic energy and the electrostatic field potential energy) does not change along the entire ion trajectory. However, focusing (or de-focusing/scattering) of the ions is performed by transferring kinetic energy from one direction of motion to another. In the case of an ion passing through a two-dimensional planar electrostatic field, conservation of energy results in the following:

$$\frac{m}{2}(v_x^2 + v_y^2) = \frac{m}{2}((v_x + \Delta v_x)^2 + (v_y + \Delta v_y)^2) + qe\Delta U \quad \text{Eq. 4-25}$$

The x -direction corresponds to the main ion beam motion direction while v_y is the orthogonal component of the initial velocity. Δv_x and Δv_y are changes in the corresponding components, ΔU is the change of potential energy between the initial and the final states. For the case of a typical lens system, both regions before and after the lens are field-free and therefore $\Delta U=0$.

The longitudinal direction x is the direction of TOF dispersion, thus the resulting change in TOF is proportional to the change of velocity in the same direction. It can be shown [177] that the resulting time aberration Δt is proportional to the distance L_{\min} between the focusing element and the nearest plane of TOF focusing with respect to energy spread (for example the image or object plane of an ion mirror)[†]. The relationship is

$$\frac{\Delta t}{T} = -\frac{L_{\min}}{L_x} \cdot \frac{\Delta v_x}{v_x} \quad \text{Eq. 4-26}$$

where L_x is the total effective path length and T is the total flight time. For $\Delta v_x \ll v_x$, this expression could be rewritten using Eq.4-25 as

$$\frac{\Delta t}{T} = \left(y'_0 + \frac{\Delta y'_0}{2}\right) \cdot \Delta y'_0 \cdot \frac{L_{\min}}{L_x} \quad \text{Eq. 4-27}$$

[†] For an electrostatic linear TOF, where no time-of-flight focusing on energy spread occurs, length L_{\min} is considered to be the distance from the ion optical element to the ion detector.

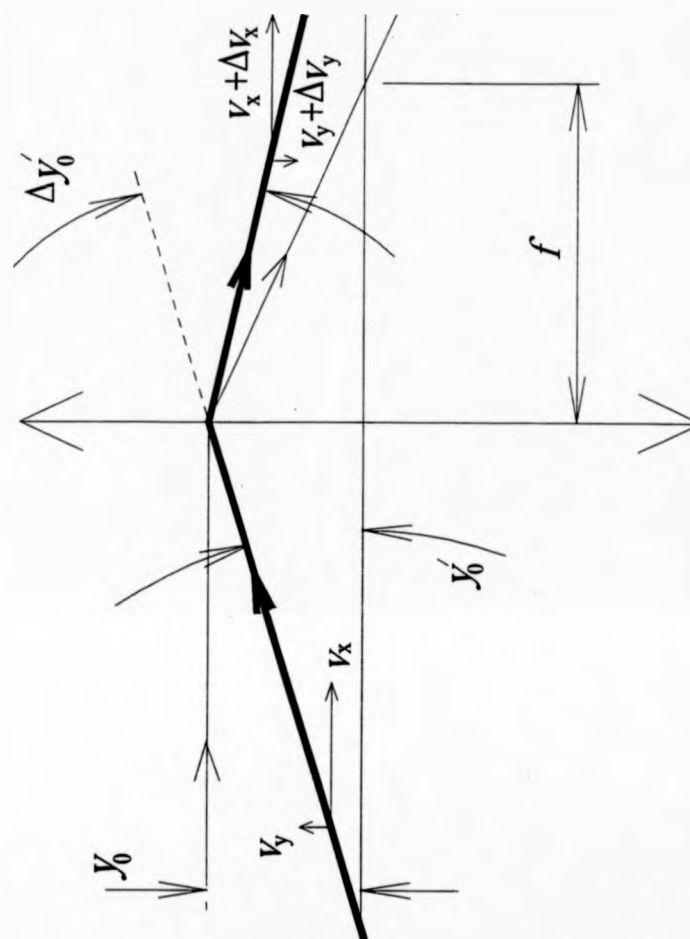


Figure 39. Schematic of an electrostatic lens.

y_0' is the initial inclination of the trajectory to the direction x ($dy/dx|_{x=0}$) and $\Delta y_0'$ is the change of inclination due to focusing (figure 39). According to the definition of focal length f [178],

$$\Delta y_0' = -\frac{y_0}{f} \quad \text{Eq. 4-28}$$

where y_0 is the y -coordinate at the point of entrance into the field. Substituting for $\Delta y_0'$ in Eq. 4-27 gives:

$$\frac{\Delta t}{T} = \left(-y_0' + \frac{y_0}{2f} \right) \cdot \frac{y_0}{f} \cdot \frac{L_{\min}}{L_z} \quad \text{Eq. 4-29}$$

In the case where a collimated ion beam enters the field parallel to the plane (or axis, for cylindrically symmetrical systems) of symmetry, i.e. when $y_0' = 0$, it is obvious from Eq. 4-29 that ions flying closer to this plane always have shorter flight times than peripheral ions. This conclusion holds for any type of electrostatic lens: decelerating or accelerating, converging or diverging. Another conclusion drawn from the above equation is that more powerful lenses produce higher time-aberrations, as time-spread Δt increases with the inverse square of the focal length f .

This formula (Eq. 4-29) could be used for estimating the temporal peak broadening for a specific ion packet by averaging over its angular and spatial distributions. It is assumed that the distributions in y_0 and y_0' are uniform and independent with minimum and maximum values y_m and $\pm(y_a' - \Delta y_0')$ respectively, i.e. $-y_m \leq y_0 \leq y_m$, $y_a' - \Delta y_0' \leq y_0' \leq y_a' + \Delta y_0'$ (where $\Delta y_0' \ll y_a'$ for the vast majority of practical cases). Time-broadening of an ion peak passing through a planar symmetry lens (full-width at half-maximum, FWHM) is

$$\left(\frac{\Delta t}{T}\right)_{50\%} = 2 \cdot rms\left(\frac{\Delta t}{T}\right) \approx \frac{2}{\sqrt{3}} \cdot \frac{y_m}{f} \cdot \frac{L_{\min}}{L_{\Sigma}} \sqrt{\left(y_a'\right)^2 + \frac{4}{15} \left(\frac{y_m}{f}\right)^2} \quad \text{Eq. 4-30}$$

omitting all higher-order terms of angular spreads. This formula can be used for evaluation of a wide variety of practical designs.

For the case of time aberrations imposed by the electric field created by the electrodes of an ion buncher, the focal length of the exit slit is expressed as [179]:

$$f_b = \frac{2V_k}{E_0} = L \quad \text{Eq. 4-31}$$

Taking into account that $L_{\min}=L$, Eq. 4-30 becomes:

$$\left(\frac{\Delta t}{T}\right)_{50\%} \approx \frac{4}{3\sqrt{5}} \cdot \frac{y_m^2}{L \cdot L_{\Sigma}} \quad \text{Eq. 4-32}$$

In order to estimate the full effect of this time aberration on the ion beam, L_{Σ} must include the effective path length of the ion beam in the mirror and T must be the total flight time.

4.3 The quadratic-field mirror as the second stage of a tandem mass spectrometer.

4.3.1 Theoretical considerations on resolution in an ideal-focusing mirror.

It has been mentioned above that an ideal-focusing ion mirror can in principle afford high resolution throughout the fragment mass spectrum for ion beams with large energy spreads, if combined with an ion buncher. There are however, a number of processes and technical challenges that may

compromise resolution in a realistic situation. In particular, resolution may be compromised due to what amounts to substitution of the low-field region of the ideal potential distribution with a field-free region between the collision cell and the physical assembly of the ion mirror. This is essential for practical reasons in order to separate spatially ion optical elements of the construction. Another potential cause of resolution degradation is energy release during collisions, as well as metastable decay in the mirror region.

4.3.1.1 Fundamental limitations on mass resolution.

4.3.1.1.1 Length of field-free region

For the purposes of this part the one dimensional parabolic equation is considered, as discussed in the introductory chapter:

$$U(x) = \frac{k}{2} \cdot (x - a)^2 + C \quad \text{Eq. 4-33}$$

If constant C in the equation above is chosen in such a way that $U(0)=0$, then with $x \geq 0$

$$U(x) = \frac{k}{2} \cdot (x - a)^2 - \frac{k}{2} \cdot a^2 = \frac{k}{2} \cdot x^2 - k \cdot x \cdot a \quad \text{Eq. 4-34}$$

A field-free region of length L_d is considered extending from the time-focus of the ion buncher to the entrance to the actual quadratic field.

Yoshida has shown [37] that for any length L_d of field-free region greater than zero, the field loses its unique property of ideal time-focusing but still provides first-order time-focusing when an appropriate value of a is chosen. To achieve

this first-order time-focusing for a fragment ion with mass m_f and energy qV_f on entering the field ($V_f = V_p m_f / m_p$), the value of a is given by the condition:

$$-k \cdot a = 2 \frac{V_f}{L_d} \cdot \left\{ 1 - \left[1 - \left(\frac{L_d}{L_p} \right)^2 \right]^{1/2} \right\} \quad \text{Eq. 4-35}$$

The notation $L_p = [2(V_f / k)]^{1/2}$ is introduced, where L_p is approximately equal to the depth of penetration of ions with energy qV_f into the field. For a small field-free region length L_d ($L_d / L_p \ll 1$) the above equation gives:

$$a \approx -\frac{L_d}{2} - \frac{L_d}{8} \left(\frac{L_d}{L_p} \right)^2 + \dots \quad \text{Eq. 4-36}$$

Although the TOF aberration coefficients of the second and higher orders are not zero, their values are small, being of the order of magnitude of $L_d / (\pi L_p)$. To take into account the energy spread of the ions, the energy of a fragment ion is represented as $q\epsilon_f$, while the ideal energy of the same ion is qV_p . The dependence of the TOF on ion energy $q\epsilon_f$ for an ion of a given mass is shown in figure 40, and demonstrates very good time-focusing for ions with energies $q\epsilon_f > 0.4qV_p$. The case shown is for $V_f = 0.7V_p$, i.e. the fragment ion mass is 0.7 that of the parent ion. It can be concluded that mass resolution is limited by the presence of a field-free region only for lower energy ions ($q\epsilon_f < 0.1-0.3qV_p$) or long field-free regions L_d ($L_d > 0.1-0.2L_p$).

In order to improve resolution, especially for lower masses, the time-focus of the buncher can be shifted a little beyond the exit slit of the collision cell (CC)

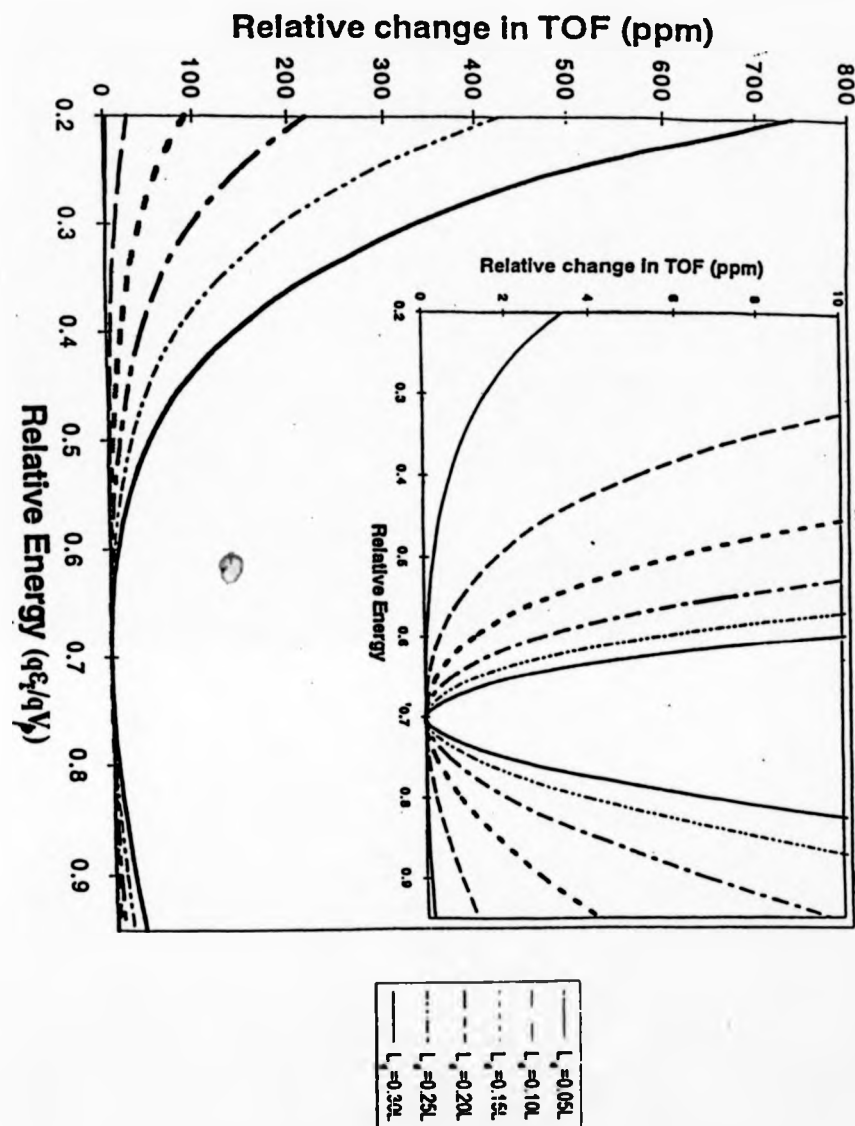


Figure 40. Deviation of TOF (relative to TOF of ions with energy qV_f) as a function of the ratio of energy $q\epsilon_i$ to maximum ion energy qV_p , for different L_d/L_p values and $V_f = 0.7 V_p$.

(vide infra) instead of its entrance slit. Additionally, "shifting" the fragment ion energies to higher values by introducing a slight acceleration, will also reduce the influence of L_d to total TOF. It can be concluded from figure 40 that a post-accelerating potential V_a of value $V_a = (0.2-0.3)V_p$ would be sufficient. It is actually mandatory to introduce post-acceleration after fragmentation for practical reasons, particularly the need for adequate detection efficiency at low fragment mass[‡].

Post-acceleration is performed in an acceleration region of length L_a situated after the collision cell. In practice the time-focus of the buncher lies in this region, rather than the exit slit of the collision cell. The accelerating region L_a is separate from and precedes the field-free region L_d . For $L_a > 0$, a is given by the expression

$$-k \cdot a = \frac{2}{c} \cdot \frac{V_f}{L_d} \cdot \left\{ 1 - \left[1 - \left(\frac{L_d}{L_p} \right)^2 \cdot c^2 \right]^{1/2} \right\} \quad \text{Eq. 4-37}$$

where

$$c = 1 + \frac{L_a}{L_p} \cdot \frac{V_f}{V_a} \cdot \left[\frac{1}{\left(1 - \frac{V_a}{V_f} \right)^{1/2}} - 1 \right] \quad \text{Eq. 4-38}$$

[‡] Energies of smallest fragment ions should exceed 0.5-1 keV in order to register on the micro-channel-plates.

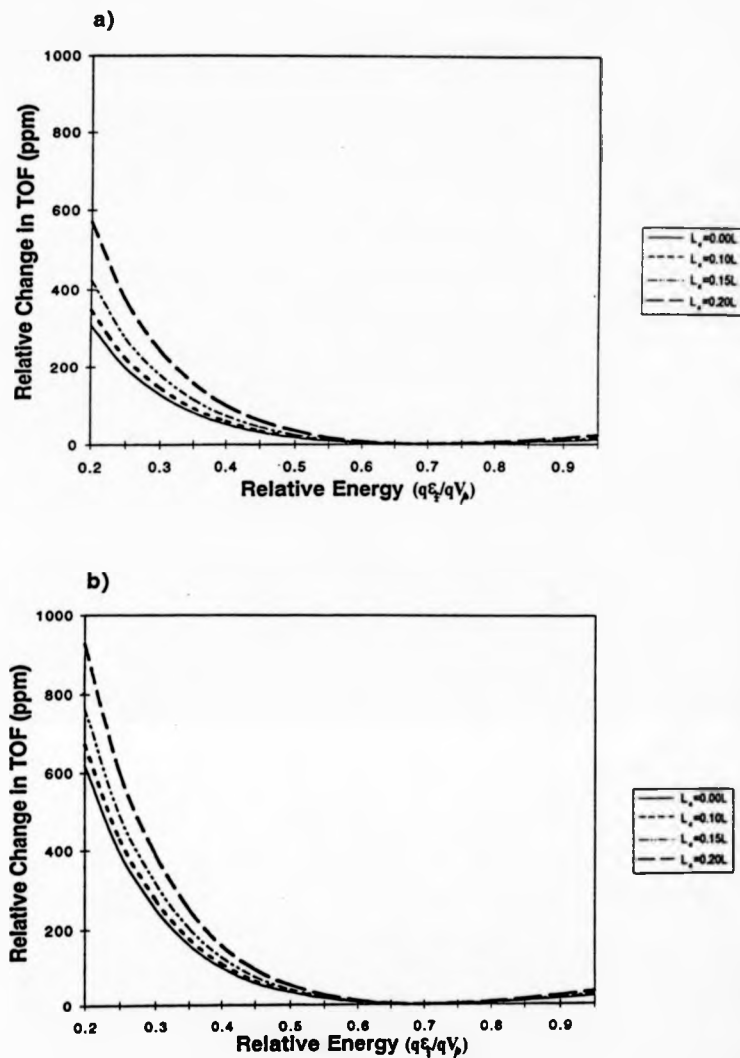


Figure 41. Deviation of TOF (relative to TOF of ions with energy qV_f as a function of the ratio of energy $q\xi$ to maximum ion energy qV_p for different L_a/L_p values and $V_f = 0.7 V_p$ at acceleration gaps L_a/L_p : (a) $L_a/L_p = 0.01$; (b) $L_a/L_p = 0.02$.

As before, L_p is the depth of penetration into the field of the mirror. For $L_a < L_p$, $L_d < L_p$, Eq. 4-37 can be expanded to:

$$a \approx -c \cdot \frac{L_d}{2} - c^3 \cdot \frac{L_d}{8} \cdot \left(\frac{L_d}{L_p} \right)^2 + \dots \quad \text{Eq. 4-39}$$

The introduction of L_a results in additional aberrations which may be more serious than those caused by L_d . Nevertheless, for a short acceleration region L_a the overall aberrations still remain acceptably small, as shown in figure.41 a) and b) for two different values of L_a and various L_d .

4.3.1.1.2 Limitations inherent to the fragmentation process

4.3.1.1.2.1 Velocity spread caused by collision-induced dissociation

Collision-induced dissociation may be considered as a two-step process (though the time-lag between them may be quite small). The first step is the impact of the precursor ion with a collision gas molecule. According to the impulsive collision transfer theory [180], the change of ion velocity after the collision is approximately given by the following formulae:

- Along the collision direction (x-direction of ion optical axis of the mirror):

$$\Delta v_x = -2 \cdot \frac{m}{m_p} \cdot \frac{m_a}{(m_a + m)} \cdot v \cdot \cos^2 \varphi \quad \text{Eq. 4-40}$$

- Orthogonally to the collision direction:

$$\Delta v_y = 2 \cdot \frac{m}{m_p} \cdot \frac{m_a}{(m_a + m)} \cdot v \cdot \cos \varphi \cdot \sin \varphi \quad \text{Eq. 4-41}$$

$v = \left(\frac{2 \cdot q \cdot V_p}{m_p} \right)^{\frac{1}{2}}$ is the precursor ion velocity, qV_p is the mean energy of precursor ions, m is the mass of a collision gas molecule, m_a is the mass of the particular atom (or group of atoms) of the parent ion interacting with the collision gas and φ is the angle of impact [180] ($-\pi \leq \varphi \leq \pi$). If m is increased, m_a also increases [180] reflecting the increased "area of contact" between the larger collision gas molecule and the precursor ion (e.g., $m_a \approx 7$ Da for helium ($m = 4$ Da), $m_a \approx 32$ Da for argon ($m = 40$ Da), $m_a \approx 49$ Da for xenon ($m = 131$ Da) [180]).

Assuming that the average number of collisions in the CC is 1, the maximum spreads Δ_x and Δ_y of velocities within the precursor ion beam following collision are:

$$\Delta_x = 2 \cdot \frac{m}{m_p} \cdot \frac{m_a}{m_a + m} \cdot v \quad \text{Eq. 4-42}$$

and

$$\Delta_y = \pm \frac{m}{m_p} \cdot \frac{m_a}{m_a + m} \cdot v \quad \text{Eq. 4-43}$$

A similar velocity spread (to that described in Eq. 4-43) will also occur in the other transverse direction, z .

The second step of the collision process is the decay of the collisionally-activated precursor ion into two fragments of masses m_f and $m_p - m_f$, accompanied by kinetic energy release qw in the centre-of-mass coordinate

system. Using the laws of energy and momentum conservation, the velocity of the charged fragment m_f in the centre-of-mass coordinate system is:

$$v_f = \left[2 \cdot \frac{q \cdot w}{m_p} \cdot \left(\frac{m_p}{m_f} - 1 \right) \right]^{\frac{1}{2}} = v \cdot \left[\frac{w}{V_p} \cdot \left(\frac{m_p}{m_f} - 1 \right) \right]^{\frac{1}{2}} \quad \text{Eq. 4-44}$$

In the centre-of-mass coordinate system this velocity may be considered as distributed isotropically, so that the corresponding velocity spreads are:

$$\Delta_{x_f} = v_f \text{ and } \Delta_{y_f} = \pm v_f$$

Thus both stages of CID result in small changes in fragment ion velocities. Comparing the spreads of fragment ion velocities for realistic values where $qw = 0.1$ eV, $qV_p = 10000$ eV and $m_p = 2000$ Da, the first factor gives $\Delta_x = 2.55 \times 10^{-3} \cdot v$ for helium ($m = 4$ Da, $m_a \approx 7$ Da) and more substantial $\Delta_x = 35.7 \times 10^{-3} \cdot v$ for xenon ($m = 131$ Da, $m_a \approx 49$ Da). The second factor results in $\Delta_{y_f} = \pm 1.05 \times 10^{-3} \cdot v$ for $m_f = 0.9m_p$, $\Delta_{y_f} = \pm 3.16 \times 10^{-3} \cdot v$ for $m_f = 0.5m_p$, and $\Delta_{y_f} = \pm 9.5 \times 10^{-3} \cdot v$ for $m_f = 0.1m_p$.

4.3.1.1.2.2 Limits to mass resolution due to the length of the collision cell.

The velocity spread caused by CID results in beam broadening, because the positions of collision and fragmentation are randomly distributed along the length of the CC. It can be considered [181] that the parent ion collides and fragments at coordinate x (for the purposes of this section $x=0$ corresponds to the entrance slit of CC, $x=h$ is the exit slit) and then its velocity changes from v to $(v \pm \delta v)$, so that the TOF in the CC is

$$T_c = \frac{x}{v} + \frac{(h-x)}{(v+\delta v)} \approx \frac{h}{v} - \frac{(h-x)}{v} \cdot \frac{\delta v}{v} \quad \text{Eq. 4-45}$$

The uncertainty in the fragmentation coordinate x results in beam broadening which cannot be compensated by ideal time-focusing. There is no way for the mirror to "distinguish" ions formed at different x coordinates, as they may have similar masses and velocities. The ratio of the maximum spread Δt of time-of-flight arising in the collision cell due to this factor to the time-of-flight T_f in the quadratic field is:

$$\frac{\Delta t}{T_f} \approx \frac{1}{\pi} \frac{h}{\left(\frac{2 \cdot V_p}{k}\right)^{\frac{1}{2}}} \cdot \frac{\Delta_x + \Delta_{xf}}{v} \cdot \left(\frac{m_p}{m_f}\right)^{\frac{1}{2}} \quad \text{Eq. 4-46}$$

The relationship $\delta v = \Delta_x + \Delta_{xf}$ has been taken into account. Mass resolution considering the base of a peak may be defined using the formula:

$$R_{0\%} = \frac{1}{\frac{2 \cdot \Delta t}{T_f}} \quad \text{Eq. 4-47}$$

Therefore, mass resolution of the longitudinal scheme can be estimated using the equations 4-42, 4-43, 4-44, 4-46 and 4-47 as:

$$R_{0\%}^{long} = \frac{\pi}{4} \cdot \frac{L_p}{h} \cdot \frac{\left(\frac{m_f}{m_p}\right)^{\frac{1}{2}}}{\left\{ \frac{m}{m_p} \cdot \frac{m_a}{(m_a + m)} + \left[\frac{w}{V_p} \cdot \left(\frac{m_p}{m_f} - 1\right) \right]^{\frac{1}{2}} \right\}} \quad \text{Eq. 4-48}$$

The notation

$$L_p \approx \left(2 \frac{V_p}{k} \right)^{\frac{1}{2}} \quad \text{Eq. 4-49}$$

is introduced, representing the penetration length of the precursor ions in the mirror.

At very low fragment-ion masses ($m_f \ll m_p$), scattering due to collisions may be neglected and expression 4-48 simplifies to:

$$R_{0\%}^{long} \approx \frac{\pi}{4} \cdot \frac{L_p}{h} \cdot \frac{m_f}{m_p} \cdot \left(\frac{V_p}{w} \right)^{\frac{1}{2}} \quad \text{Eq. 4-50}$$

Thus for low-mass fragments resolution is proportional to mass. In order to guarantee unit mass resolution at low masses, the CC length should be:

$$h < \frac{\pi}{4} \cdot \frac{L_p}{m_p} \cdot \left(\frac{V_p}{w} \right)^{\frac{1}{2}} \quad \text{Eq. 4-51}$$

The precursor ions penetrate almost to the back-end of the ion mirror, thus $L_m \approx L_p$. For an ion mirror of length $L_m = 0.6$ m, $L_d \ll L_m$ and with w and V_p as above, the formula Eq. 4-51 for the maximum length of the collision cell gives $h < 0.3$ m.

At higher masses as $m_f \rightarrow m_p$, the kinetic energy release may be neglected and Eq. 4-48 simplifies to:

$$R_{0\%}^{long} \approx \frac{\pi}{4} \cdot \frac{L_p}{h} \cdot \frac{(m_a + m)}{m_a} \cdot \frac{m_p}{m} \quad \text{Eq. 4-52}$$

To guarantee unit mass resolution at high masses, the CC length should be:

$$h < \frac{\pi}{4} \cdot L_p \cdot \frac{(m_a + m)}{m_a} \cdot \frac{1}{m} \quad \text{Eq. 4-53}$$

For the same parameters as above, Eq. 4-53 gives: $h < 0.19$ m for helium as the collision gas and $h < 0.013$ m for xenon. These values would be lower if the assumption of a single collision in the CC were not valid. If the average number of collisions were n , the values of h would be diminished about n times.

It should be noted that statistical modelling of the peak shape (as done in [181]) would give more accurate evaluation of beam broadening. However, it would require thorough treatments of the statistical distributions of all the random variables in the formulae above, which would be hindered by the lack of experimental data especially for high-mass molecules [180].

4.3.1.1.3 Metastable decay

In matrix-assisted laser desorption/ionisation experiments, metastable decay is expected to take place due both to excess energy deposited in the precursor ion during MALDI (see introductory chapter) and to energy deposited by collisions in the collision cell. Metastable fragmentation in the electric and magnetic sector region will not affect resolution, as the metastable ions will not be transmitted through the exit slit of the double-focusing mass spectrometer. Mass resolution may be affected by the ions that fragment in the region between the exit slit of MS-1 and the CC. The mass resolution is limited only by the kinetic energy release and may be calculated using Eq. 4-48 (where $m=0$, as there is no collision gas). In this situation, h represents the length of the region between the exit slit of MS-1 and the collision cell. For

realistic parameters, these fragment ions will not compromise resolution in the quadratic ion mirror when the collision cell is grounded and $h < 0.1$ m. If, however, $h = 0.2$ m for example, metastable decay could result in poorly resolved fragment ions at $m_f < 0.85m_p$, while at $h = 0.3$ m the limit is raised to $m_f < 0.94m_p$, i.e. resolution degrades quite fast as the length of field-free region is increased.

If metastable decay occurs after the collision cell, the picture becomes more complex because fragment ions can be formed at different potentials inside the mirror and mass peaks can be considerably broadened even for $w=0$ (i.e. without bunching). This problem is inherent to TOF mirrors and ideal time-focusing can not help here at all. The only advantage offered by ideal mirrors in this case is a broader dispersion of metastable mass peaks, as a consequence of the monotonously changing field. Therefore these peaks should be easily distinguishable from the sharp peaks due to fragment ions formed in the collision cell.

The detrimental influence of metastable decay on mass resolution is illustrated in figure 42, where TOF dependence on decay time is given for different fragment ions and $L_a = L_d = 0$. The bend of the graph in the middle (i.e. around the turning point) reflects the fact that ions travel with lower velocities and spend more time in this region. It is expected that smooth "ghost" peaks may appear in the region of the mass spectra between the parent and fragment mass peaks, if the metastable decay-time is comparable with the parent ion TOF. It should be emphasised again that analogous "ghost" peaks must be expected in

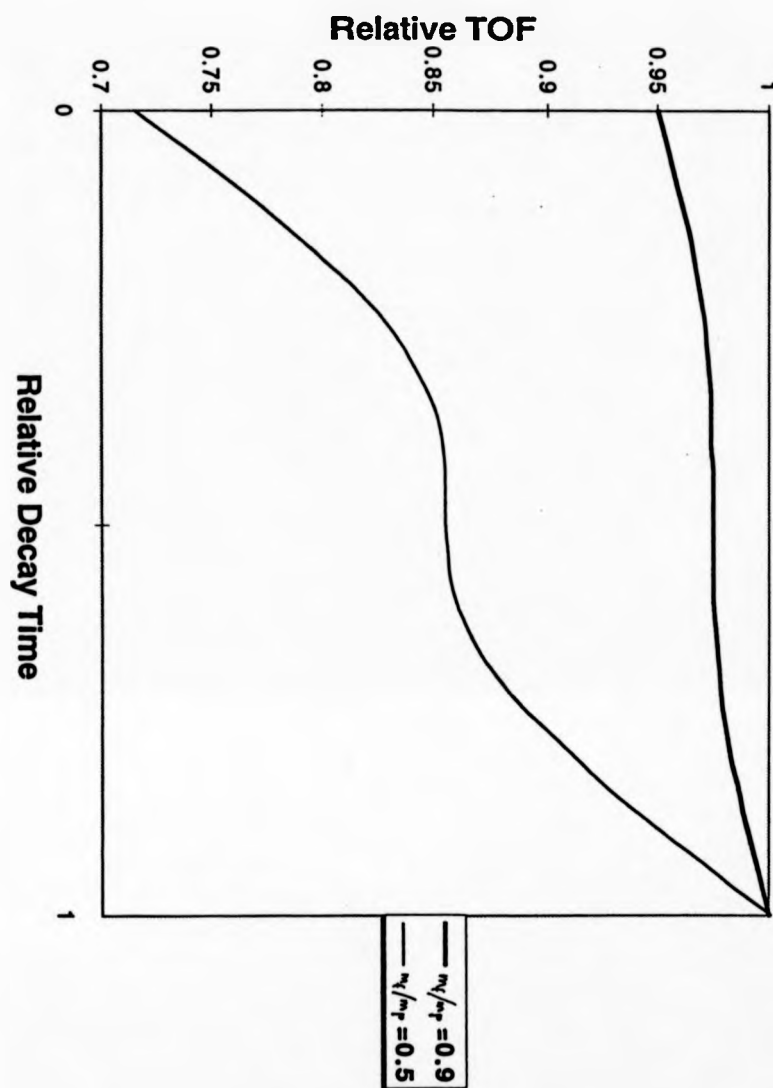


Figure 42. TOF for different fragment ions as a function of decay time inside the quadratic field, in units of precursor ion TOF. $L_d = L_a = 0$. The decay time is given relative to the flight time of the precursor ion through the mirror.

any other type of ion mirror (and they will be even more complex in double-grid reflectrons).

4.3.1.2 Comparison with the orthogonal scheme.

When all the above factors are listed, a false impression might be created that the longitudinal geometry of MS-2 in a tandem mass spectrometer inherently provides worse mass resolution than the orthogonal scheme. In the orthogonal arrangement, an interrelation between mass resolution and the length h of the collision cell arises from scattering of ions after collision and energy release during fragmentation. The beam widening resulting from the angular spread should be kept to an acceptable level by introducing small values for the collision cell length h .

Formulae 4-42, 4-43 and 4-44 show that collisions introduce small velocity spreads in the direction orthogonal to the collision, i.e. along the direction of TOF. In the orthogonal scheme, the very large range of fragment ion energies prohibit the use of any focusing optics before the push-out region, thus any velocity spread remains unchanged until the moment that the push-out pulse is applied.

A TOF spread arises from the "turn-around time" in the push-out field [20] as well as from the Zavoiskii-Fanchenko effect ("start-up" aberration, [182]) and is given by the simple formula

$$\alpha = \pm \frac{\delta v}{\frac{q}{m_f} \cdot E_{on}} \quad \text{Eq. 4-54}$$

$E_{\text{ori}} = U_{\text{ori}}/d$ is the strength of the push-out field, U_{ori} is the push-out potential, d is the gap over which it is applied and δv is the velocity spread in the direction orthogonal to that of the collision. The minus sign corresponds to acceleration of those ions which have a turning point, and the plus to those which are directly accelerated (without a turning point). Assuming that all other parts of the analyser do not introduce any TOF aberrations, the collision-limited mass resolution of the orthogonal scheme is given by the formula:

$$R_{0\%}^{\text{ori}} = \frac{1}{8} \cdot \frac{L_e}{d} \cdot \frac{\left(\frac{U_{\text{ori}}}{V_p} \cdot \frac{U_{\text{ori}}}{U_i} \cdot \frac{m_p}{m_f} \right)^{\frac{1}{2}}}{\frac{m}{m_p} \cdot \frac{m_a}{(m_a + m)} + \left[\frac{w}{V_p} \cdot \left(\frac{m_p}{m_f} - 1 \right) \right]^{\frac{1}{2}}} \quad \text{Eq. 4-55}$$

L_e is the effective path length in the orthogonal scheme time-of-flight analyser (i.e. the length of field-free region with the same time-dispersion) and U_i is the overall acceleration potential in the orthogonal scheme. The last formula may be expressed with the help of Eq. 4-48 in terms of the mass resolution of the longitudinal scheme for the same initial energy of precursor ions

$$R_{0\%}^{\text{ori}} = R_{0\%}^{\text{long}} \cdot \eta \cdot \frac{h}{2d} \cdot \frac{m_p}{m_f} \cdot \left(\frac{U_{\text{ori}}}{V_p} \cdot \frac{U_{\text{ori}}}{U_i} \right)^{\frac{1}{2}} \quad \text{Eq. 4-56}$$

$\eta = \frac{L_e}{\pi \cdot L_p}$ approximately equals the ratio of effective path lengths in the

orthogonal and the quadratic field schemes respectively. It has been mentioned above that the maximum initial energy of the precursor ions in the orthogonal scheme is limited mainly by considerations of the size of the detector.

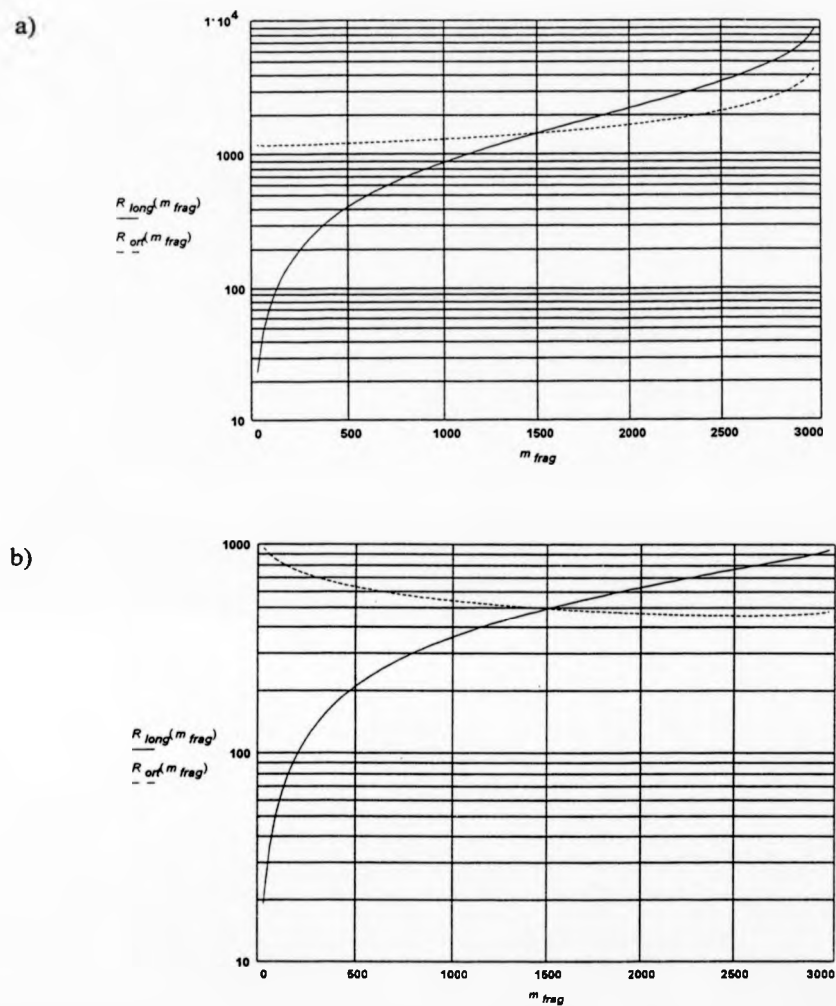


Figure 43. Comparison of resolution for the longitudinal and the orthogonal scheme for ideal TOF analysers and 20 mm collision cell length: a) collision gas He, b) collision gas Xe.

Practically the maximum value of V_p is about $V_p = 1000$ V. Considering typical values for experimental parameters such as $h = 0.01$ m, $U_i = 4$ kV, $U_{\text{ort}} = 1$ kV over $d = 0.01$ m, and equal effective lengths ($\eta=1$), Eq. 4-56 gives:

$$R_{0\%}^{\text{ort}} \approx \frac{m_p}{m_f} \cdot 0.25 \cdot R_{0\%}^{\text{long}} \quad \text{Eq. 4-57}$$

According to the equation above the orthogonal scheme offers better resolution than the longitudinal only for low-mass fragments $m/m_p < 0.25$, where high resolution is of little practical value. For higher masses the orthogonal scheme is up to 4-8 times worse (and may be insufficient for unit-mass resolution). Even in the extreme case of metastable decay (i.e. $m = 0$) and with $h = 0.03$ m, the orthogonal scheme is not able to compete in the higher mass-range, but still offers better resolution for lower masses. Only for $h > 0.1$ - 0.2 m does the orthogonal scheme become better than the longitudinal, although in this situation the gap d must be increased to cope with the larger width of the fragment ion beam. It may therefore be concluded overall that correct choice of collision cell parameters can easily give the longitudinal scheme the edge in terms of resolution, in comparison to the orthogonal scheme.

4.3.2 Theoretical considerations on ion transmission.

4.3.2.1 Ion transmission in the quadratic field

Apart from limitations because of imperfections of the delivery ion optics, there are other factors that potentially may compromise sensitivity. These include the inherent defocusing of ions in the transverse direction in a

quadratic mirror, practical aspects of the ion mirror design and scattering due to collisions. In order to study the transmission of ions through the ion mirror, it is necessary to consider the 3-dimensional shape of the actual field in the ion mirror of the Mag-TOF prototype instrument. The potential distribution of the chosen quadratic field follows the planar-symmetric equation (figure 44):

$$U(x, y, z) = \frac{k}{2} \cdot (x - a)^2 - \frac{k}{2} \cdot y^2 + C \quad \text{Eq. 4-58}$$

The apex of the field, i.e. the point where $x=y=z=0$, corresponds to the centre of the exit slit of the CC, (a and C are constants). The constant k is a coefficient reflecting the field strength, corresponding to the spring constant in a mechanical analogue. The solution of Newton's equations for a fragment of mass-to-charge ratio m_f/q and energy V_f is:

$$x(t) = -a + a \cdot \cos \omega t + \left(\frac{2V_f}{k} \right)^{\frac{1}{2}} \cdot \sin \omega t$$

$$y(t) = y_0 \cosh(\omega t) + \left(\frac{2V_f}{k} \right)^{\frac{1}{2}} \cdot y'_0 \cdot \sinh(\omega t) \quad \text{Eq. 4-59}$$

$$z(t) = z_0 + \left(\frac{2qV_f}{m_f} \right)^{\frac{1}{2}} \cdot z'_0 \cdot t$$

where $\omega = \left(\frac{q}{m_f} k \right)^{\frac{1}{2}}$, y'_0 and z'_0 are inclinations of trajectories to axis x , and

$x_0=0$, y_0 and z_0 are coordinates at time $t=0$. The point $x_0=0$ may be considered to be the object of TOF focusing of the ion mirror. When ions are reflected

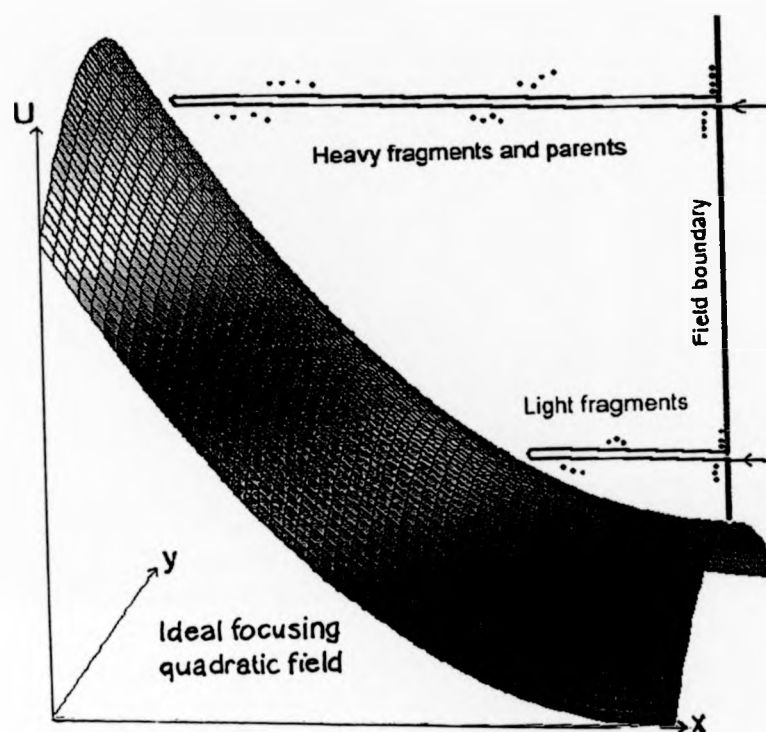


Figure 44. A two-dimensional representation of the parabolic potential of Eq. 4-58. The third dimension (z) is field-free.

along the x -direction and the TOF reaches the value

$$T_0 = \frac{\pi}{\omega} = \frac{\pi}{\sqrt{\frac{qk}{m_f}}} \quad \text{Eq. 4-60}$$

all ions are time-focused into the detector of the ion mirror, which lies at the image plane $x=2a$.

It has been discussed above that practical considerations require substitution of part of the low potential region of the field by a field-free region (the region between $x_0=0$ and $x=2a$). Thus the entrance of the field is also located at $x=2a$. This can be realised without significant deterioration of mass resolution, provided that the depth of penetration of the ions in the actual field is much greater than a . In order to fulfil this requirement for the lightest fragments, their depth of penetration should be increased, as discussed earlier, by means of a post-accelerating region installed after the collision cell. After the post-accelerating region, energy V_f of fragment ions includes a proportion of the precursor ion energy V_p prior to CID and energy acquired by post-acceleration by voltage V_a

$$\frac{m_f \dot{x}^2}{2} = qV_f \equiv q \left(\frac{m_f}{m_p} V_p + V_a \right) \quad \text{Eq. 4-61}$$

m_p is the mass of the parent ion and m_f the mass of the collision-induced fragment ion. The implications of the field-free region and the post-accelerating voltage V_a in mass resolution are examined in more detail later in this chapter.

Provided that the parameters of the ion mirror are appropriately chosen, the equation for the TOF remains the same with k being given by the expression

$$k = \frac{2U_m}{L_m^2 \left(1 + \frac{2a}{L_m}\right)} \quad \text{Eq. 4-62}$$

U_m is the maximum voltage applied to the end of the mirror and L_m is the ion-mirror length. The coordinates of arrival of ions at the detector can be expressed in terms of initial positions and inclinations on the y and z axis:

$$y_k = y_0 \cosh(\pi) + L_m \sqrt{1 + \frac{2a}{L_m}} \cdot \left(\frac{V_f}{U_m}\right)^{\frac{1}{2}} \cdot y'_0 \cdot \sinh(\pi) \quad \text{Eq. 4-63}$$

$$z_k = z_0 + \pi L_m \sqrt{1 + \frac{2a}{L_m}} \cdot \left(\frac{V_f}{U_m}\right)^{\frac{1}{2}} \cdot z'_0 \quad \text{Eq. 4-64}$$

The above formulae show clearly that, if the mirror length L_m is increased arrival coordinates y_k and z_k increase. Therefore, resolution improvement by increasing TOF dispersion would result in lower transmission, given fixed detector dimensions and angular divergence y'_0 and z'_0 .

For uniform and independent distributions of initial parameters ($-y_m \leq y \leq y_m$, $-z_m \leq z \leq z_m$, $-\alpha \leq y'_0 \leq \alpha$ and $-\beta \leq z'_0 \leq \beta$), the root mean square values of the arrival coordinates of the ion beam in the y and z directions are:

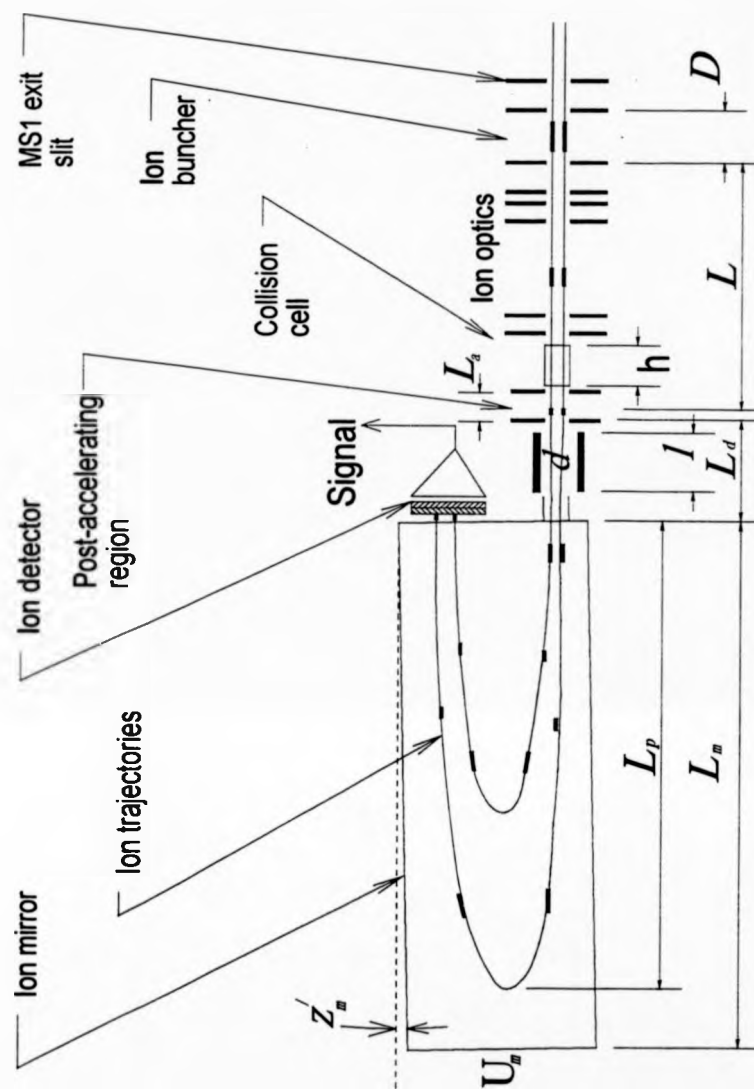


Figure 45. Schematic of the MS2 region of the Mag-TOF tandem mass spectrometer prototype.

$$\begin{aligned}
 Y &= 2 \cdot r.m.s.(y_k) \approx \frac{2}{\sqrt{3}} \cdot \sinh(\pi) \sqrt{y_m^2 + L_m^2 \left(1 + \frac{2a}{L_m}\right) \frac{V_f}{U_m} \alpha^2} \\
 Z &= 2 \cdot r.m.s.(z_k) \approx \frac{2}{\sqrt{3}} \cdot \sqrt{z_m^2 + \pi^2 L_m^2 \left(1 + \frac{2a}{L_m}\right) \frac{V_f}{U_m} \beta^2}
 \end{aligned}
 \tag{Eq. 4-65}$$

where $\tanh(\pi) \approx 1$ has been assumed. The above expressions offer a means of estimating the acceptable detector size given the initial parameters of the ion beam. Although lighter fragments have lower energies than heavy ones, they are not expected to demonstrate lower values of Y or Z , because of their higher angular divergences α and β stemming from the fragmentation processes.

4.3.2.2 Limits to transmission due to angular scattering

Angular scattering of the fragment ions stemming from collision and more directly from energy release is a problem associated with high-energy collision-activated decomposition. Indeed, the change of ion velocity ($\Delta_y + \Delta_{yf}$) in the orthogonal y -direction (which is the defocusing direction of the ion mirror) means that the ion beam receives an additional angular spread $\tan \zeta = (\Delta_y + \Delta_{yf}) / v$. On transforming Eq. 4-59 for y -motion using expressions 4-43 for Δ_y and 4-44 for Δ_{yf} , the additional broadening in the y -direction is obtained as:

$$D_y \approx \pm \left[2 \cdot \frac{m}{m_p} \cdot \frac{m_a}{(m_a + m)} + \left[\frac{w}{V_f} \cdot \left(\frac{m_p}{m_f} - 1 \right) \right]^{\frac{1}{2}} \right] \cdot L_p \cdot \sqrt{\frac{m_f}{m_p}} \cdot \sinh(\pi) \tag{Eq. 4-66}$$

Notation L_p is given by Eq. 4-49. In the field-free z -direction, the additional broadening D_z is given by $D_z = \pi / \sinh(\pi) D_y \approx 0.272 D_y$. Typical parameters of

the ion beam and the mirror as described above lead to values of $D_y \approx \pm 17$ mm and $D_z \approx \pm 5$ mm for $m_f = 0.9m_p$ and helium as the collision gas.

For heavier collision gases, however, the situation drastically changes. With xenon, which is the heaviest of the commonly used collision gases, the beam broadening reaches values of $D_y \approx \pm 125$ mm and $D_z \approx \pm 34$ mm. Fortunately, all of these estimations represent "worst-cases". In reality, the size of the core of the beam remains lower than the above values and can be accepted by a reasonable-size detector.

4.3.3 Beam deflector design.

As the entrance of the field and the detector of the quadratic ion mirror of the Mag-TOF prototype instrument both lie at the position $x=2a$, they are separated in space by placing the detector above the entrance slit (figure 45). Therefore ions must be deflected upwards before injection into the ion mirror. The task of manipulating the ion beam with an electrostatic deflector becomes non-trivial because of the large range of energies of fragments of different masses. For a parallel-plate deflector of length l and voltage U_d across a gap d , the angle of deflection is mass-dependent following the expression

$$\Delta z' = \frac{U_d}{2 \left(\frac{m_f}{m_p} V_p + V_a \right)} \cdot \frac{l}{d} \quad \text{Eq. 4-67}$$

This mass-dependence would result in severe mass discrimination unless its effect was counterbalanced. The most effective way of compensating for this mass-dependence is to introduce some additional angular deflection which

results to an opposite trend with mass. The simplest solution is to tilt the mirror by a small angle z_m' away from the direction of the deflection) so that an additional mass-independent angle of trajectory inclination z_m' is introduced. Then the vertical displacement z_k becomes

$$z_k(m_f) = z_0 + \pi L_m \sqrt{1 + \frac{2a}{L_m}} \cdot \left(\frac{\frac{m_f}{m_p} V_p + V_a}{U_m} \right)^{\frac{1}{2}} \cdot \left(z_m' + \frac{U_d}{2 \left(\frac{m_f}{m_p} V_p + V_a \right)} \cdot \frac{l}{d} \right) \quad \text{Eq. 4-68}$$

and has a minimum at a fragment mass \bar{m}_f given by

$$\frac{\bar{m}_f}{m_p} = \frac{1}{V_p + V_a} \left(\frac{U_d}{2z_m'} \cdot \frac{l}{d} - V_a \right) \quad \text{Eq. 4-69}$$

In order to determine a "best" value for the tilt z_m' the condition $z_k(m_f = 0) = z_k(m_f = m_p)$ can be imposed upon the above equation:

$$z_m' = \frac{U_d}{2} \cdot \frac{l}{d} \cdot \frac{1}{\sqrt{V_a(V_a + V_p)}} \quad \text{Eq. 4-70}$$

Substituting Eq. 4-69 and Eq. 4-70 into Eq. 4-68, all the parameters of the deflector can be derived:

$$\left. \begin{aligned} z'_m &= \frac{Z_{\max}}{\pi L_m} \cdot \sqrt{\frac{U_m}{V_a}} \cdot \frac{1}{g+1} \\ \frac{\bar{m}_f}{m_p} &= \frac{V_a}{V_p} \cdot (g-1) \\ U_d &= \frac{2Z_{\max}}{\pi L_m} \cdot \frac{d}{l} \cdot \sqrt{V_a U_m} \cdot \frac{g}{g+1} \\ \Delta H &= Z_{\max} \frac{(\sqrt{g}-1)^2}{g+1} \end{aligned} \right\} \quad \text{Eq. 4-71}$$

Notation $g = (1 + V_p/V_a)^{1/2}$ is introduced. Z_{\max} is the coordinate at the detector of the maximum deflection of the parent ion, ΔH is the total dispersion at the detector in the z -direction of the beam for ion masses from 0 to m_p . Due to the tilt of the mirror by an angle z'_m , additional TOF aberrations could arise [181]. Fortunately, given the relatively small size of the ion beam at the entrance of the mirror, the values of these aberrations lie in the region of a few parts-per-million relatively to the total TOF and can therefore be neglected.

5. Chapter Five.

Construction and performance of the magnetic sector/time-of-flight (Mag-TOF) instrument.

5.1 Overview.

The theoretical considerations discussed in the previous chapter demonstrated the feasibility of the longitudinal scheme magnetic sector/time-of-flight combination. The remaining part of this thesis will describe the development and performance of the Mag-TOF prototype instrument (figure 46), based on the longitudinal geometry. Critical dimensions and other instrumental parameters were fixed on the basis of the preceding theoretical analysis and ion trajectory simulations. The precise aim of the project has been to allow near-100% transmission for fragment ions produced by collision-induced dissociation of MALDI-produced peptide or small protein ions, with unit-mass resolution for ions up to approximately 3000–5000 Da mass.

Parent-ion selection was performed in a Kratos Concept H double-focusing mass analyser of the Nier-Johnson type geometry. Two different types of MALDI ion source designs were developed to be coupled with the standard Concept ion source chamber. The electric sector electrodes and housing were modified to incorporate a linear time-of-flight analyser for sample evaluation and initial source tuning. The main mode of operation allowed transmission



Figure 46. Photograph of the Mag-TOF prototype tandem mass spectrometer.

of the MALDI ion beam through the whole of the double-focusing instrument.

A separate vacuum chamber was built to house the interfacing ion optics, including an ion buncher. The collision cell was housed in a differentially pumped chamber to ensure optimum vacuum conditions in the remainder of the second mass analyser. A multi-electrode system was constructed to sustain the quadratic potential for ion reflection. Control and acquisition hardware and software was developed, integrating to some extent the two mass analysers and allowing selection of the operation mode, timing control of the experiment as well as computerized data acquisition and management.

5.2 Ion production and transmission in the double-focusing analyser.

5.2.1 Design and construction of a MALDI ion source for the Concept double-focusing mass spectrometer.

The magnetic sector / time-of-flight tandem mass spectrometer could in principle utilise any type of pulsed ion source. The main practical requirement would be that the ion beam produced could be time-focused by the ion buncher. Potential ion source candidates also include continuous ion sources like electrospray or L-SIMS, where the parent ion beam would be gated by means of pulsed electromagnetic deflectors into packs suitable for the specific design of ion buncher. However, the ideal candidate for the Mag-TOF prototype instrument was matrix-assisted laser desorption / ionisation (MALDI) source. Although the ion beam produced by a MALDI ion source

might have relatively high energy and angular spreads, it could be made to match the acceptance parameters of the double-focusing mass analyser with a suitable ion optical design. A MALDI ion source was seen to be particularly suitable for efficient ionisation of peptides in the required mass range, and it was relatively straightforward to implement with the aid of a nitrogen laser.

The source housing of the Concept mass spectrometer was designed to house a number of interchangeable ion sources. It was decided that the design of the MALDI ion source should be fitted around the existing source housing design with little interference to parts utilised by other ion source types. The source assembly would be mounted on a stainless steel cradle designed in accordance with the existing source housing specifications. The cradle was secured on the source housing by means of two stainless steel screws and aligned with the aid of two permanent dowels. All the remaining components of the source would be mounted on the source cradle, therefore its exact shape defined the ion optical axis. The source cradle was kept at ground potential and acted as the physical barrier between the extraction/collimation region and the ion optics that prepare the ion beam for ejection into the double focusing analyser.

The accelerating electrode was directly mounted on the ion source cradle by means of three PEEK mounting posts. It was aligned using a specially designed aluminium tool. The electrodes of the acceleration / collimation region were all mounted from the accelerating electrode in both source designs described further in this chapter. The standard electrical feedthrough that carried the high voltage accelerating potential from the control console of the

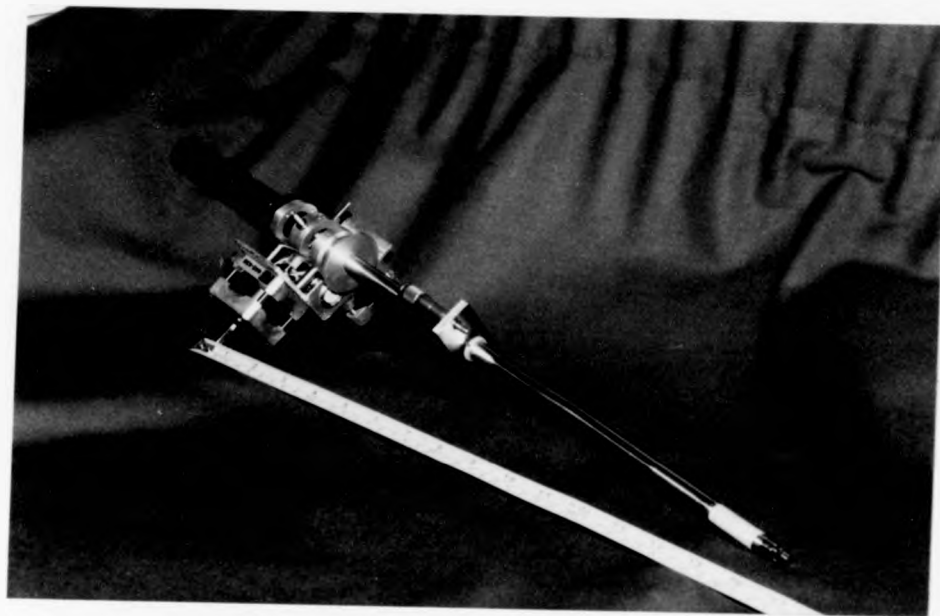


Figure 47. Photograph of the wobble-probe of the MALDI source of the Mag-TOF prototype tandem mass spectrometer.

Concept mass spectrometer was utilised for the MALDI sources. The high voltage was connected to the sample probe by means of a contact spring made of brass wire, housed in a special slot in the accelerating electrode.

The utilisation of solid matrices in MALDI made the use of sample rastering imperative. A wobble probe similar to the one described in Chapter 2 was employed. The main differences with this wobble probe were its greater overall length and the different aspect ratio of the two parts of the inner shaft: the atmospheric pressure part (before the sealing / pivot-point) was twice as long as the in-vacuum part. The design of the push-activators in the manipulation region was identical, allowing travel of the atmospheric end of the shaft of approximately 2 mm. Due to the 2:1 aspect ratio, the travel of the stainless steel sample stage was 1 mm. Another difference was that the Mag-TOF probe was required to operate to voltages up to 8 kV, therefore the insulating parts of the probe were shorter. Finally, a pair of stepper motors have been installed in order to allow computer manipulation of the sample surface (figure 47).

A nitrogen laser identical to the one described in Chapter 3 (Laser Science Inc., Newton USA model VSL337ND) was installed on an appropriately designed platform attached onto the main supporting frame of the Concept mass spectrometer. The laser produced light of 337nm wavelength, with maximum energy-per-pulse 250 μ J. The time-length of the light pulse was 3 ns. A variable density wheel attenuator (Ealing Scientific) was installed in the path of the laser beam to allow control of the laser power reaching the

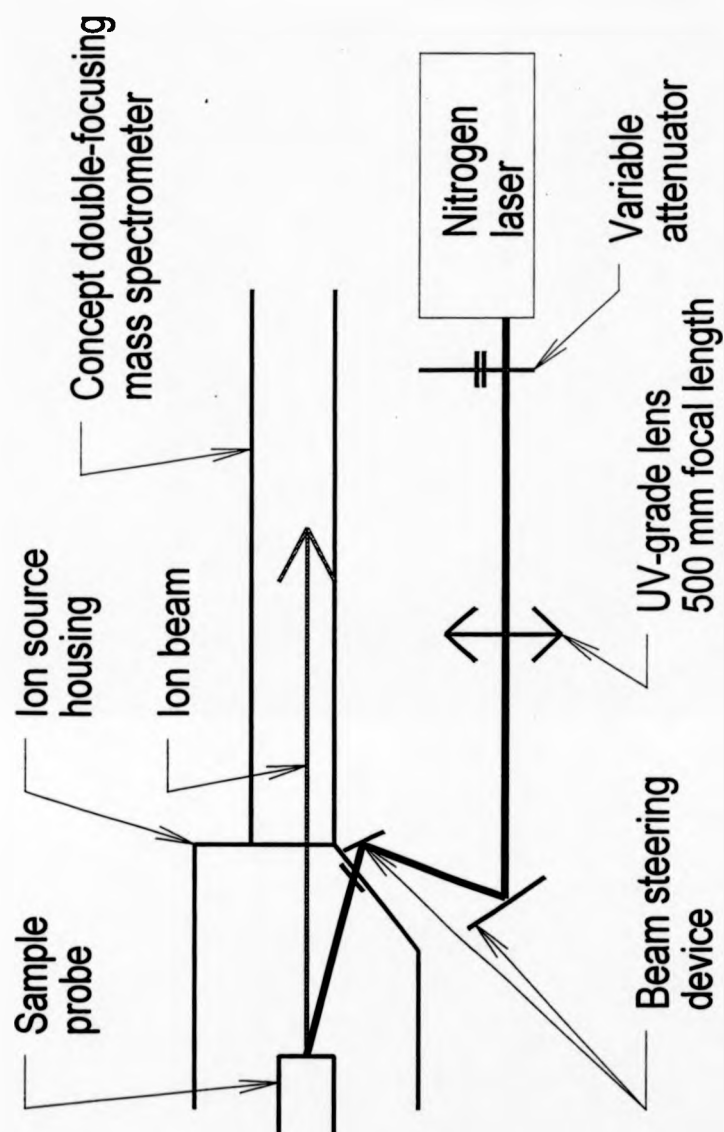


Figure 48. Schematic of the optical path of the laser beam of the Mag-TOF prototype tandem mass spectrometer.

sample surface. This attenuator consisted of a UV transparent disk coated with a varying density material which increased its reflecting efficiency in such a way that the optical transmission changed monotonically with its angle of rotation. The attenuator disk was attached to a device specially designed to define the limits of rotation for consistent calibration. A stepper motor was also included to allow computer control of the laser power.

The laser beam was transmitted through a covered path in order to stop stray laser radiation. Optical components included a 500 mm focal length Spectrosil-B lens (Comar, Cambridge, UK), and two UV-grade mirrors. One of these mirrors was a dielectric and the other an aluminium-coated type. The lens was positioned on a mount supported with the aid of two pieces of stainless steel studding. The position of the lens relative to the sample surface could be adjusted by means of different length spacers placed around the studding. The two mirrors were mounted on appropriate adjustable mounts (Newport) and constituted a beam steering device utilised for laser beam alignment. The laser beam entered the source housing through a specially designed Spectrocil-B, UV-grade window installed on a flange in the bottom of the source housing.

Due to space limitations underneath the source housing chamber, a reversed approach was used for initial adjustment of the optical system. A continuous red colour diode laser was mounted in such a way that its light beam was made to pass through an iris placed on the approximate spot of optimum ion production, as well as through the middle of the window in the bottom of the source housing. The position of the aluminium mirror was adjusted in such a

way that the red light beam was reflected from its middle to the middle of the dielectric mirror mounted below. The angle of the dielectric mirror mount and the position of the laser platform were adjusted, so that the reflection from the first surface of the dielectric mirror struck the exit aperture of the laser. When the UV pulsed laser beam passed through the middle of the lens to the same spot on the dielectric mirror as the diode laser beam, it should have laid on the desired optical path. Fine alignment of the laser beam was performed with small adjustment of the dielectric mirror mount. A special insertion probe was placed on the theoretically optimum position with thermal printing paper attached to the sample tip. A laser spot was marked on the thermal paper and its position was measured with the aid of an optical microscope. The laser path was consequently adjusted and the procedure repeated until the laser spot was found to be in the theoretically optimum position. The laser spot position could be fine-adjusted experimentally by slightly withdrawing the probe tip. It had been recognised that the exact position of the laser spot could be critical and small adjustments of the ion beam direction might have to be performed by means of electrostatic deflection in the ion source region.

The ion source design has to fulfil two main requirements: firstly, time aberrations should be kept to a minimum and secondly the ion beam shape should be made to match the acceptance parameters of the double-focusing mass spectrometer. In view of the first requirement, start-up aberrations and the Zavoiskii-Fanchenko effect were minimised by employing a high

extraction potential[§]. For fulfilment of the second requirement, two entirely different sources were designed, manufactured and experimentally tested. The first approach uses a collimating region after the extraction electrode in combination with a quadrupole doublet for beam shape optimisation. The second design utilised planar geometry electrostatic lenses for ion transfer and beam shaping. In both schemes provisions were made for some ion beam steering, to account for possible small inaccuracies in the construction and assembly or a degree of misalignment of the laser beam.

5.2.1.1 Ion source employing quadrupole doublet.

A number of limitations on the ion source design were imposed by practical requirements like the actual size and design of the ion source housing chamber. For example, the maximum possible length of the ion source was determined by the maximum possible inclination of the laser beam path. From an ion optical point of view the main requirement for the ion source was to prepare the beam for maximum transmission through the electric and magnetic sectors. The acceptance angles of the Concept mass spectrometer for an ion beam passing through the source slit were ± 0.7 degrees in the horizontal plane (y -angular divergence) and ± 0.1 degrees on the vertical plane (z -angular divergence). The height of the source slit was 7 mm, while its width could be varied from 0 to approximately 250 μm with typical values being around 200 μm . It was obvious that a significant magnification of the source object could be tolerated in the vertical z -direction. On the other hand, the initially

[§] The strength of the extraction field, however, should be balanced with requirements imposed by the MALDI method (see Chapter 2).

diverging beam would have to be focused in the horizontal y -plane as it passed through the source slit.

The size and shape of the ion production area would be determined by the size and shape of the laser spot at the sample tip of the wobble probe. The profile of the nitrogen laser beam was resembled a square with one of its quarters missing. As the incident angle of the laser beam to the ion optical axis was quite steep (27 degrees), the shape of the focused laser spot was rectangular with the horizontal side only slightly smaller than the vertical. The theoretical minimum spot size expected from the given laser divergence and the focal length of the lens utilised was approximately 100–150 μm . The position of the lens was adjusted until a similar size spot was observed on the thermal paper.

It can be deduced from the above that the originally square ion beam had to be transformed into a thin-rectangular shape in the source slit. This focusing action was to be performed by means of a quadrupole doublet lens system. However, it has been mentioned earlier in this work that the MALDI ionisation technique produced ion beams with significant initial angular spread. In order to achieve acceptable input characteristics of the ion beam into the quadrupole doublet region, additional focusing had to be envisaged. The ion source design employed a high potential gradient extraction area (8 kV in 5 mm) appropriately shaped to offer some initial focusing action, and a cylindrical-symmetry electrostatic lens in order to collimate further the ion beam.

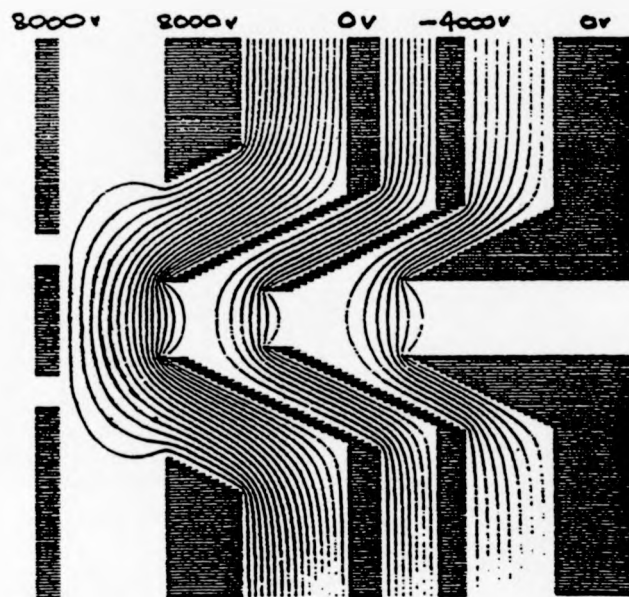


Figure 49. A SIMION model of the extraction and collimation region of the MALDI ion source incorporating a quadrupole doublet.

5.2.1.1.1 The extraction and collimation regions

The best position at which to effect focusing would be the extraction region itself. This was because the ions were moving at lower velocities and have more time to experience the forces. Focusing action in the extraction region could be performed by curving the field shape in the appropriate way. This was achieved by using conical electrodes in the extraction region, rather than planar ones (figure 49). The effect can be accentuated further by means of a field-shaping electrode between the accelerating electrode and the extraction cone. The potential of the field-shaping electrode could be the same as that of the accelerating electrode.

Additional focusing action was introduced with a cylindrical symmetry electrostatic lens after the extraction region. Two more nested conical electrodes were combined with the extraction cone to form an Einzel lens for additional ion collimation prior to ejection into the quadrupole doublet. Extensive ion trajectory simulations were performed using the SIMION software in order to optimise various parameters of the design, including cone angles, spacing between the electrodes, electrode aperture size as well as optimum electrode potentials. The software allowed the study of the effects of various initial beam parameters on ion trajectories as well as on total time aberrations in the source region.

The complete ion optical design of the extraction / collimation region can be found in figure 49. Ion trajectory plots (figure 50) demonstrated that adequate beam collimating action could be achieved with minimum time

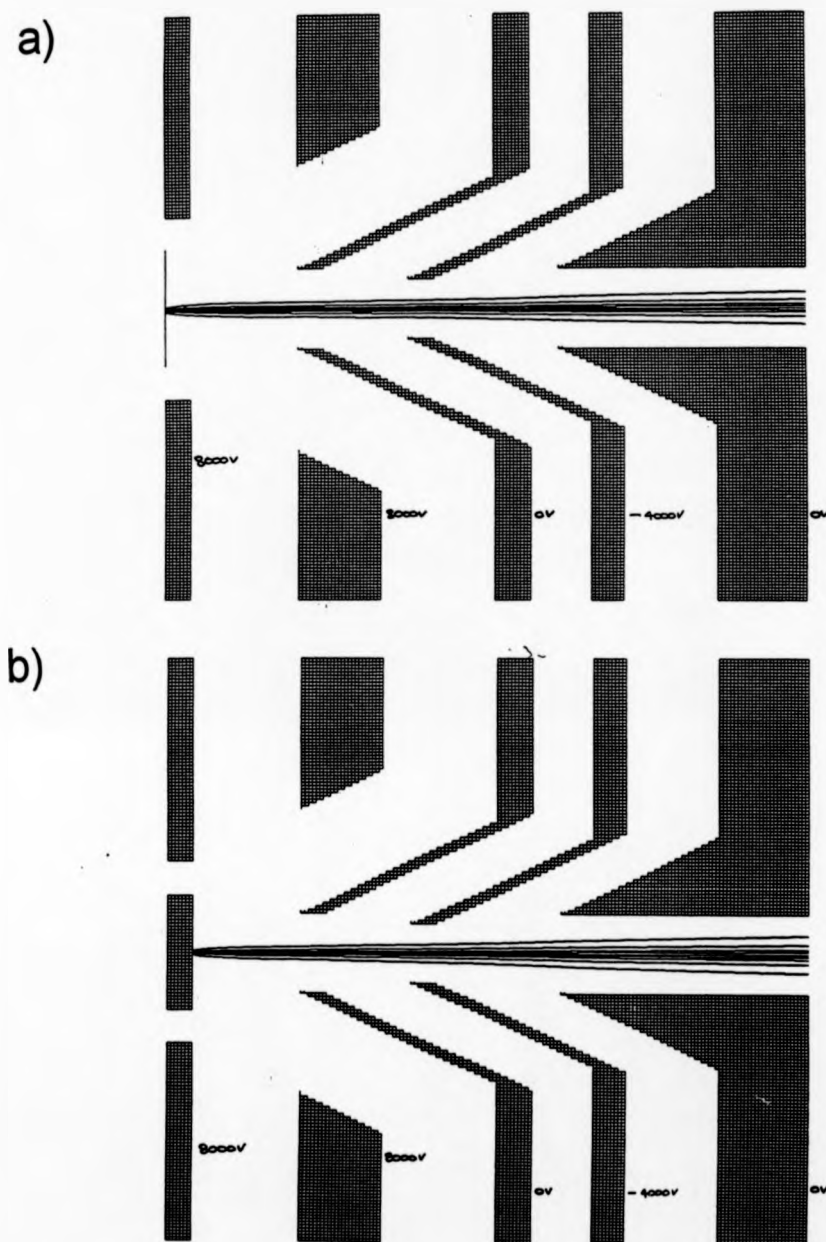


Figure 50. Ion trajectory simulations performed with the SIMION software for two different ion energies: a) initial energy 10 eV; b) initial energy 20 eV.

aberrations by floating the lens electrode at approximately -4 kV. The maximum time aberrations with a beam with 10 eV energy spread, 200 μm initial coordinate spread and 40 degrees maximum angular spread was as low as 4 ns (see table II).

Initial angle Degrees	Initial distance off axis, mm	Exit angle degrees	Exit distance off axis, mm	Total flight time ns
0	0	0	0	890.5
5	0.01	0.19	0.127	890.5
10	0.021	0.379	0.254	890.7
20	0.043	0.744	0.502	891.4
40	0.1	1.382	0.955	894.2

Table II. Flight-times of ions with various initial conditions through the extraction and collimation region

The mechanical design of the extraction and collimation region was based on these calculations. The final grounded electrode was designed as a conical attachment on the actual ion source cradle. The field shaping electrode, at the same potential as the accelerating electrode, was mounted from the accelerating electrode using three metal spacers. The two remaining electrodes were appropriately shaped to avoid contact with each other and were also mounted by means of PEEK insulating spacers from the accelerating electrode. Provision had been taken for electrical contacts, and holes were

drilled where necessary for the transmission of the laser beam. All the electrodes were aligned with each other and with the source cradle using a specially designed tool.

5.2.1.1.2 The quadrupole doublet

The main distinguishing characteristic of the first ion source design was the quadrupole doublet. Theoretical analysis [183] of a quadrupole doublet suggested that it was able to transform effectively a divergent beam of circular symmetry into a pseudo-rectangular cross-section matching the input criteria of the double-focusing mass spectrometer. Circular quadrupole rods were utilised to approximate the true hyperbolic shape electrodes. The total length of the quadrupole doublet was 90 mm, determined by the available space between the ion source cradle and the source slit assembly. Thus, accounting for ground electrodes in the assembly, the length available for each quadrupole lens was 40 mm. In order to minimise the effect of fringing field the length of the quadrupole should have been at least 10 times the radius r_0 of the region between the quadrupole rods, i.e. the distance between the poles of the electrodes was chosen to be 8 mm ($r_0=4$ mm). The radius of the cylindrical rods was chosen to be 1.1468 times the radius r_0 [184], i.e. 9.2 mm.

The schematic of the quadrupole doublet was shown in figure 51. The up and down rods of the first quadrupole carried the negative voltage $-V_1$, while the polarities of the second quadrupole were opposite (rotated 90 degrees). The first quadrupole performed a focusing action in the y -plane and a defocusing action on the z -plane. The second quadrupole was operated at a lower voltage

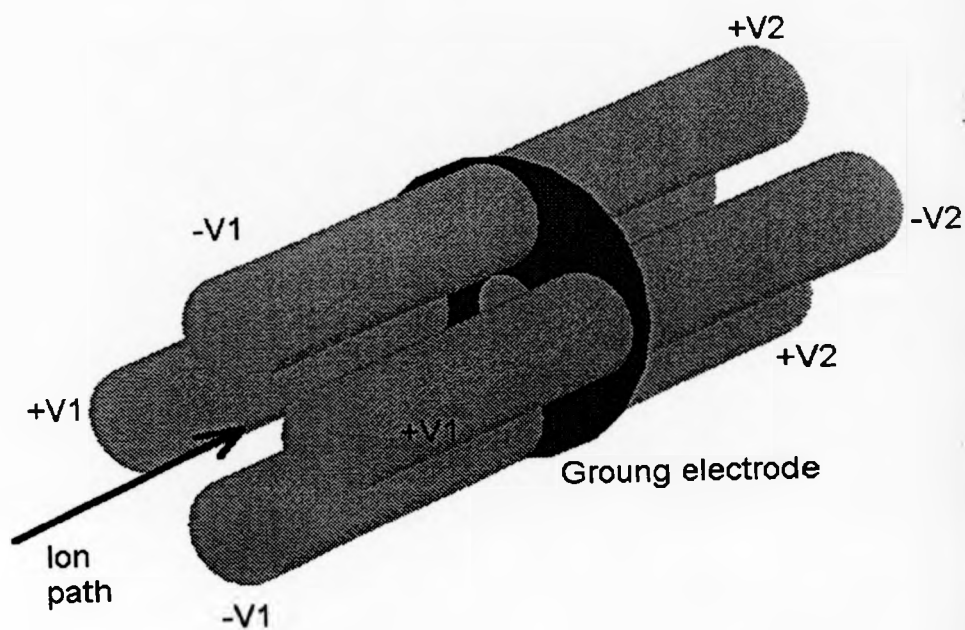


Figure 51. Schematic diagram of the quadrupole doublet.

than the first, so that its defocusing action in the y -plane was less than the focusing action of the first quadrupole. The defocusing action of the first quadrupole magnified the beam in the z -direction, which means that the ion entered the second quadrupole further from the ion optical axis, where the field strength was greater. The effect of the second quadrupole in the z -direction was to collimate the beam with its size being smaller than 7 mm, the source slit height.

Solution of the equations of motion for the ion beam through the quadrupole doublet (appendix I) demonstrated that for realistic input parameters, voltages of 94 V and 46 V for the first and second quadrupoles respectively should be adequate to prepare an 8 kV acceleration ion beam for ejection into the double-focusing mass spectrometer. However optimum voltages for the quadrupoles were very sensitive to the input parameters of the beam.

It had been decided to design and manufacture a power supply for the quadrupole doublet that offered the possibility for individual adjustment of each pair of quadrupole rods. The power supply of the quadrupole doublet offered the ability to bias differentially the voltage of each rod of a pair around its offset value, thereby introducing some electrostatic deflection on the ion beam and accounting for minor misalignments of the components of the ion source and/or the laser beam. However, the focusing and deflecting actions were completely independent. The maximum available values for each potential of the power supply were limited for reasons of design simplicity by the available electronic components to approximately 150 V, which should have been adequate according to calculations. Finally, the power supply

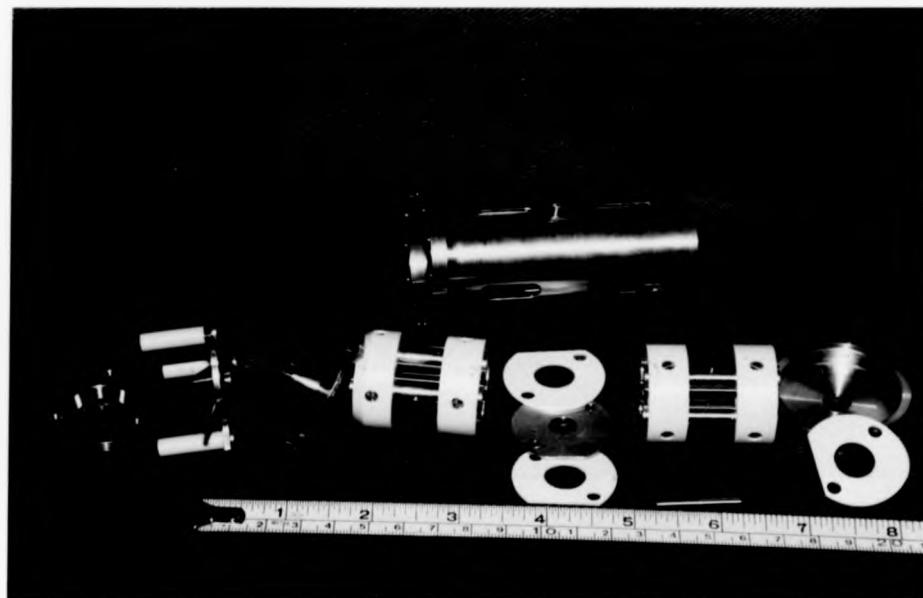


Figure 52. Photograph of the ion optical components of the MALDI source assembly, including the conical extraction electrodes and the quadrupole doublet. The ion source cradle is not shown.

featured a switch that could inverse all voltages, allowing for quick adjustment for negative ions.

The quadrupole doublet assembly was designed to be contained inside a appropriate size cylinder attached to the cradle of the ion source. The cylinder was made of stainless steel and carried eight 4 mm wide slots for efficient vacuum pumping as well as access to the quadrupole rods for electrical connections. The quadrupole rods were screwed on appropriately designed insulating mounts made of PEEK. A circular ground electrode was placed between the two quadrupoles, separated from them by means of two PEEK insulating disks. All the components of the assembly were aligned to each other and to the ion source cradle with the help of the PEEK mounts and a number of permanent dowels. Finally, the stainless steel cap of the cylinder, also acting as the last ground electrode, held the assembly together.

The design described above was manufactured (figure 52) and its performance evaluated in practice during the first stage of development of the magnetic sector / time-of-flight prototype tandem mass spectrometer. It was generally established that under near-ideal circumstances the theoretical considerations described above could successfully predict its performance. Nevertheless, there were some limitations that consistently compromised the operation of this ion source. Firstly, minute misalignments of the laser beam or irreproducibility of the position of the sample probe proved to be a problem, mainly due to severe scattering of the ion beam in the shaped extraction region. Therefore, a lot of time and sample was consumed adjusting the deflecting voltages of the quadrupole rods. On the other hand, optimisation of

the quadrupole doublet proved to be very sensitive, and often different sample or laser power conditions would require different offset voltage settings. It has been suggested that the addition of a third quadrupole lens would radically improve the practical situation, but limitations of space in the existing source housing chamber could make such a modification time-consuming.

5.2.1.2 Ion source employing electrostatic lenses.

In view of the impracticality of the ion source design described above, a new ion source design was required which would be less sensitive to minor misalignments and had ion optics with less sharp optima of focusing conditions. In order to meet the first requirement, a homogeneous extraction region would be employed. The second requirement would be fulfilled by a set of planar-symmetry electrostatic lenses. Simplicity of manufacturing and construction was pursued, in an effort to use some of the components manufactured for the first ion source.

The same ion source cradle was utilised with minor modifications for mounting and alignment of the lens system. The same accelerating electrode was also retained, with some adjustments to improve the homogeneity of the extraction field. Although the tip of the wobble probe and the accelerating electrode were both kept at the same potential, the field shape near the sample surface might have changed as the position of the probe tip changed. To eliminate this potential problem, a piece of tungsten foil with a 4 mm hole was attached on the high-field side of the accelerating electrode and aligned with a special tool. The thickness of the foil was just 0.1 mm, in order to avoid any

possible lens-effect that would compromise transmission. When the probe tip (diameter 6 mm and manipulation travel 1 mm) moved just behind the hole of the foil, no change in the field shape would be caused. This design feature also allowed another improvement. When thermal paper was placed on the tip of the sample probe for laser alignment, a 4 mm diameter circular mark could be made on the paper by friction to mark the exact position of the hole. This, apart from offering an unambiguous proof of the position of the probe tip, allowed exact measurement of the laser spot position with respect to the ion optical axis.

The extraction electrode (figure .54 a) was constructed from thin stainless steel plate (1 mm thickness) with a small size slit (2 by 1 mm). High-transmission grids were not used, in order to avoid the rise of scattering and associated time aberrations. The extraction electrode was grounded and mounted on the accelerating electrode by means of three purpose-made M1.6 PEEK screws and 6 mm long insulating spacers. Although this design of extraction region did not offer any additional collimation of the beam, the time aberrations imposed for an ion beam with typical initial parameters (sample spot size 100 μm , angular spread 10 degrees, energy spread 20 eV) were about 1 ns. The extraction electrode was followed by a short field-free region up to the ion source cradle.

The electrostatic focusing and deflecting system was mounted on the other side of the source cradle. It had been decided that two independent electrostatic lenses would be included, one for each of the z - and y -planes. The potential of the y -plane Einzel lens would be chosen to focus the ion

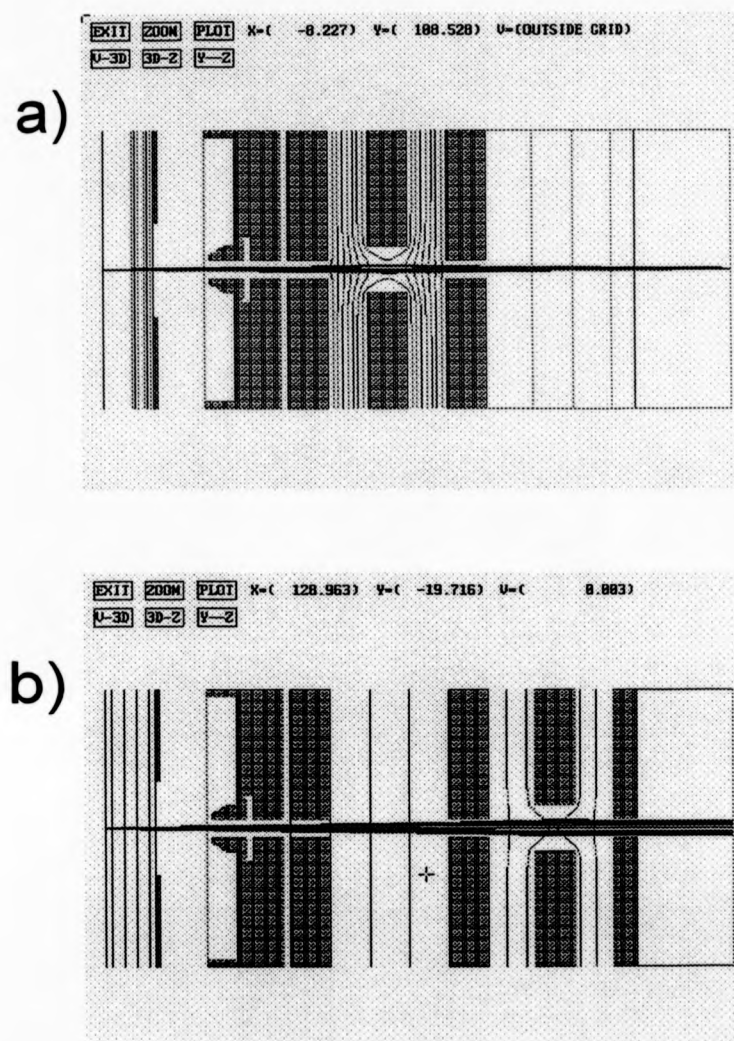


Figure 53. Ion trajectory simulations of the focusing and collimation characteristics of the MALDI ion source in two planes: a)y-plane, b)z-plane

beam into the source slit position, while the z -plane lens should collimate the ion beam maintaining its vertical height appropriate for transmission through the sectors. Although in principle focusing and deflection of the beam could be performed by the same ion optical elements (split lenses), for reasons of availability of appropriate power supplies, the electrostatic lenses had to be independent from the deflectors. Because of limited space, only one deflection stage could be envisaged, and it was decided that this would be in the y -plane due the stricter requirements for this direction. Deflection in the z -plane was not as critical and could still be performed by one of the permanent z -deflectors of the Concept mass spectrometers situated between the source slit and the entrance of the electrostatic sector. In order to keep the necessary deflecting voltages to low values, the split electrode of the y -deflector was the first ion optical component after the ion source cradle.

SIMION ion trajectory simulations separated for the two different y and z planes (figure 53) were performed to identify the optimum ion source. The final design would be capable of meeting the requirements imposed by the acceptance characteristics of the double-focusing mass spectrometer. A drawing of the electrostatic focusing and deflection region can be found in figure 53 b. The ion source electrodes were made of stainless steel and mounted one four pieces of stainless steel studding screwed on the cradle of the ion source (figure 54 a). Specially designed PEEK spacers allowed for electrical isolation of the active electrodes of the lenses and the deflector. The assembly was aligned by means of four long 3 mm diameter dowels. The

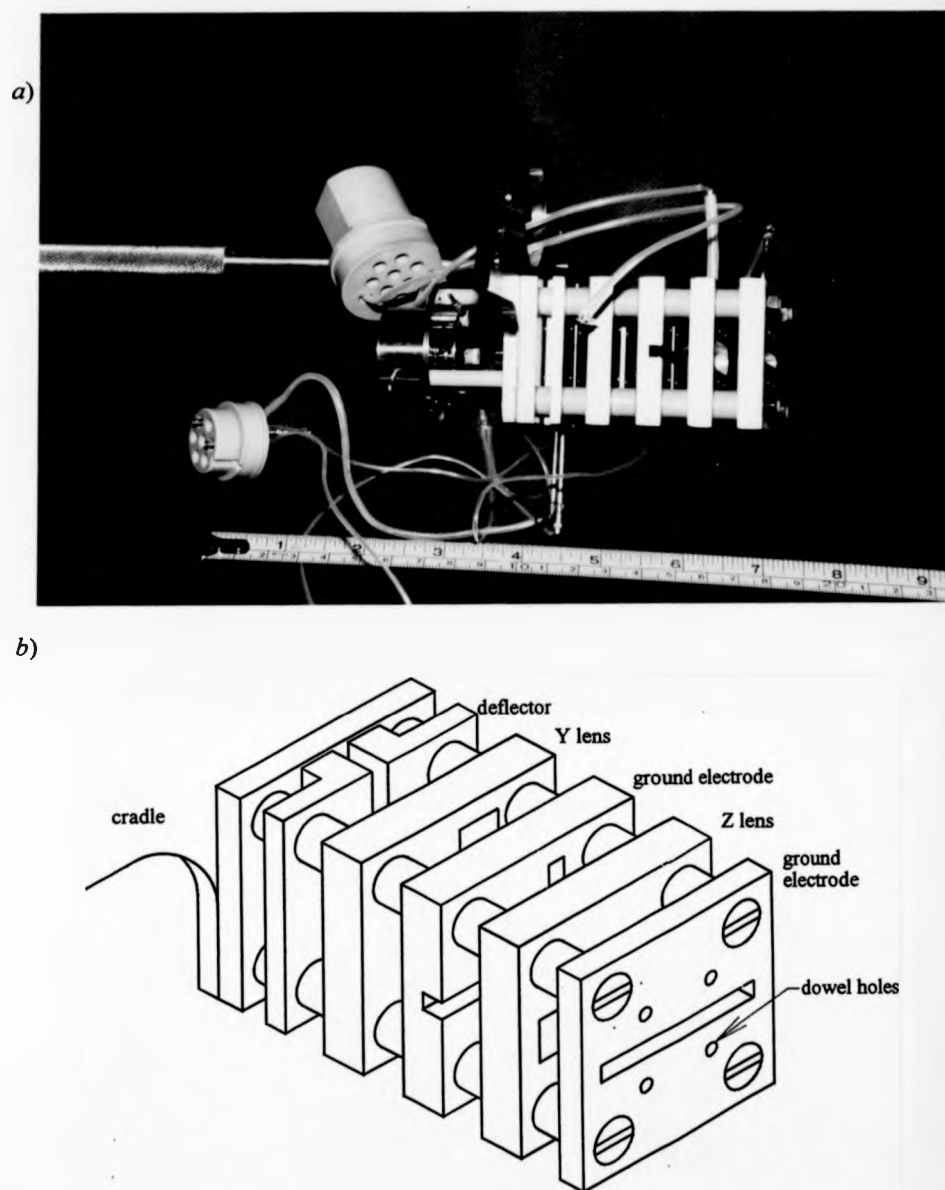


Figure 54. a) Photograph of the MALDI ion source assembly. b) Mechanical drawing of the planar-symmetry focusing and collimating ion optics.

experimental results presented in this work were obtained using this ion source design.

5.2.2 The parallel time-of-flight analyser and intermediate detection system.

For the purpose of optimising the transmission of the ion beam through the double-focusing mass analyser, two intermediate detection stages were introduced. The first of these comprised of a linear time-of-flight analyser used for sample quality evaluation and laser power adjustment, while the second was used for optimising the ion source parameters to match the acceptance parameters of the Concept.

The main modifications required in order to realise the linear time-of-flight mass analyser was a hole in the large-radius electrode of the electric sector, positioned at a point coaxial with the ion optical axis of the ion source. The size of the hole was small enough so that the electrostatic field created between the plates of the electric sector during normal operation was not disturbed significantly. The vacuum chamber of the electric sector was also drilled along the same axis and an appropriate stainless steel tube was welded on it, in order to increase the length of ion drift. At the end of this tube an ion detector was positioned. The detector utilised was an ETP electron multiplier capable of maximum amplification of approximately 10^6 . The high voltage for the electron multiplier was supplied by a custom-made high voltage power supply unit. The signal output of the detector was connected directly to the analogue-to-digital converter data acquisition board of the computer (*vide infra*). It was obvious that in this mode of operation (TOF 1-mode) the

electrostatic sector plates should be both grounded, in order for the ions to reach the linear time-of-flight detector. This was performed by a specially designed electronic circuit introduced in the power supply of the sector plates and controlled by the main computer of the instrument.

The second mode of operation of the Mag-TOF prototype instrument required that the electrostatic sector plates were switched back on. The ions were transmitted through the electric and magnetic sectors. The chosen parent ions were passed through the end-slit of the double-focusing mass spectrometer, and were detected by the post-accelerating detector. The signal out of the preamplifier of the post-accelerating detector was monitored by a LeCroy 7200A oscilloscope.

The ion sources conditions that gave optimum transmissions for each of the modes of operation were different. Nevertheless, the TOF 1 mode of operation was used for quality control of every individual sample, as well as for determination of the laser power threshold. The resolution achieved in the linear time-of-flight was directly related to the energy spread of the MALDI ion beam produced. By maximising the mass resolution of the linear time-of-flight spectra (typical value 200–400 measured at full-width at half-maximum, corresponding to 40–25 eV energy spread respectively at 8 kV acceleration), it was ensured that the size of the ion packet at the exit of the double-focusing mass spectrometer would be sufficiently small to be totally contained within the ion buncher electrodes. This was necessary in order to achieve high resolution through successful time-focusing of the beam.

During tuning of the precursor ion signal in the transmission-mode, the ion source parameters (i.e. y and z lens voltage, deflector voltage) were set to match precisely the optimum acceptance characteristics of the Concept. Various other tuning parameters of the Concept mass spectrometer were optimised at this stage (deflectors, hexapoles, magnet shims, width of the source and detector slits). In this mode of operation, the magnetic field was fine-tuned in order to select the most intense isotopic species of the precursor ion (that was the pure- ^{12}C isotope, as the heaviest mass ions analysed were below 3000 Da). This post-accelerating detector was not suitable for measurement of the time-length of the ion packet, due to the poor resolution achieved with the conversion dynode.

5.3 Construction of the time-of-flight mirror of the Mag-TOF tandem mass spectrometer.

5.3.1 Introduction and vacuum system

In the third mode of operation (TOF 2-mode) the conversion dynode and the electron multiplier of the post-accelerating detector were both grounded and the ions were transmitted through towards the second mass analyser. This action was also controlled by the main computer of the instrument by means of electronic components added in the power supply units of the post-accelerating detector. Beyond the post-accelerating detector region, the parent ions passed through the ion buncher electrodes, a number of electrostatic lenses, the collision cell region, the post accelerating region and the z -deflector before entering the quadratic-field ion mirror.

The ion buncher was housed in a small intermediate vacuum chamber used to connect the vacuum tube of the Concept mass spectrometer with the custom built vacuum chamber that housed the ion mirror. This custom-built stainless-steel vacuum chamber had a rectangular section and its top face was detachable for easy access to the interior space. A special groove around the top edge of the chamber walls housed a 5 mm diameter VITON o-ring for vacuum sealing. The lid of the chamber contained two stainless steel flanges, one of which was used for mounting the detector assembly. The bottom of the vacuum chamber was constructed to support a Balzers (Milton Keynes, UK) 330 l/s turbomolecular vacuum pump, as well as the differentially-pumped collision cell chamber. The latter was equipped with a Leybold (Koln, Germany) 50 l/s turbomolecular vacuum pump, which pumped away the collision gas in order to maintain low pressure in the main vacuum chamber.

Other flanges on the side walls of the vacuum chamber supported high-voltage electrical feedthroughs, an ionisation gauge, a linear actuator for movement of the whole mirror in the x -direction and a pair of specially designed flanges to allow some manipulation of the y -position of the ion mirror under high vacuum. The chamber was cleaned with various solvents and baked for a number of hours under vacuum to a temperature of approximately 100°C with the aid of heating tapes. Ultimate vacuum of approximately 5×10^{-7} mbar had been achieved and could be consistently attained.

5.3.2 The ion buncher and delivery ion optics.

The first active ion optical component that the ions entered after they passed through the final slit of the double-focusing mass spectrometer was the ion buncher (figure 55). The electrodes of the ion buncher were made of 1 mm thick stainless steel plate with rectangular slits. The first electrode of the buncher was mounted on the wall of the small interfacing vacuum chamber with the aid of 4 PEEK spacers. It was electrically connected with a high-voltage matched-capacity type feedthrough situated at a very small distance, in order to minimise reflections and electronic noise created by the fast-rising high voltage pulse. The second electrode was situated at a distance of 30 mm from the first, allowing complete containment of an ion beam with a 25 eV energy spread. The second electrode was always kept grounded and was mounted by means of four metal spacers.

The high voltage pulse was applied with a BEHLKE (Frankfurt, Germany) fast high voltage switch. A custom made high voltage power supply was used to bias the input of the switch at the high voltage required to time-focus the ion packet in the desired position. The output of the switch was brought at high potential while the trigger pulse provided by the timing board of the main computer of the instrument was switched on. The timing board of the computer receives a zero-time signal from a photodiode placed in the path of a small reflection of the laser beam. The delay of the trigger pulse was calculated by the control software given the mass of the parent ion and the effective path length of the first mass spectrometer.

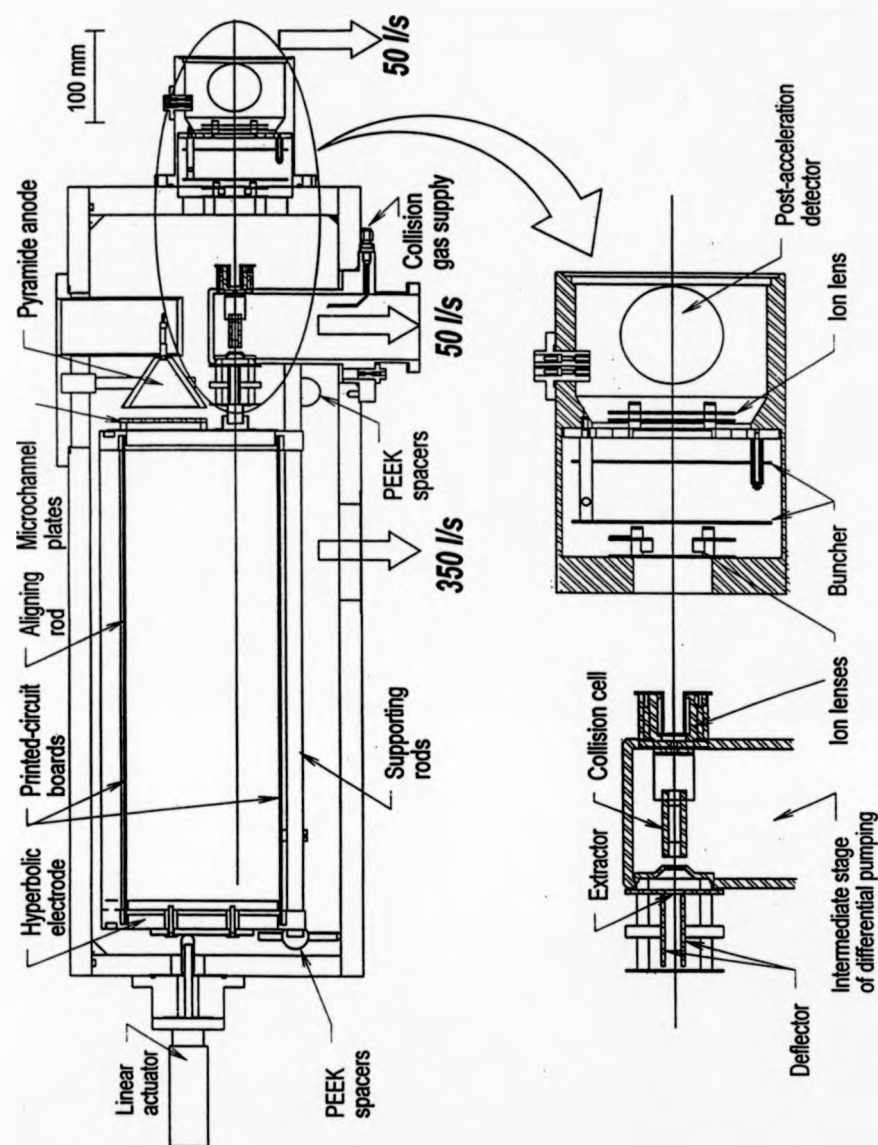


Figure 55. Schematic of the MS2 region of the Mag-TOF prototype tandem mass spectrometer.

Experiments have been performed to establish the reproducibility of the high-voltage pulse. The high-voltage switch was biased at 100 volts and the output signal was recorded with a LeCroy oscilloscope, through a 1:10 attenuation rf probe. The waveform was downloaded to the computer for further analysis. The jitter of the delay line was found to be less than 1 ns, and the general shape of the waveform was reproducible. However, some non-reproducible signal ripples could be observed that might have been detrimental to the operation of the ion buncher. It has been mentioned in the previous chapter that even when the exact shape of the push-out pulse was not perfectly reproduced, the ion buncher would have fulfilled its purpose if the integral of the voltage curve for the time that the ions spent inside the ion buncher remained within less than 1% of its mean value. This condition was found to be fulfilled, when the areas under 10 different waveforms were calculated and statistically treated.

A number of experiments were performed in order to evaluate the time-focusing function of the ion buncher. An ETP electron multiplier optimised for use with time-of-flight mass spectrometry was placed after the collision cell area in the path of the ions. CsI clusters as well as peptide ions were transmitted through the double-focusing mass spectrometer, and their arrivals on the electron multiplier were recorded using a LeCroy oscilloscope. The potential applied to the buncher plates was optimised in order to achieve minimum width of the precursor ion peak. The values of the optimum voltage were very close to that predicted by Eq. 4-23 in the previous chapter. During adjustment of the buncher voltage, it was evident that as the time-width of the

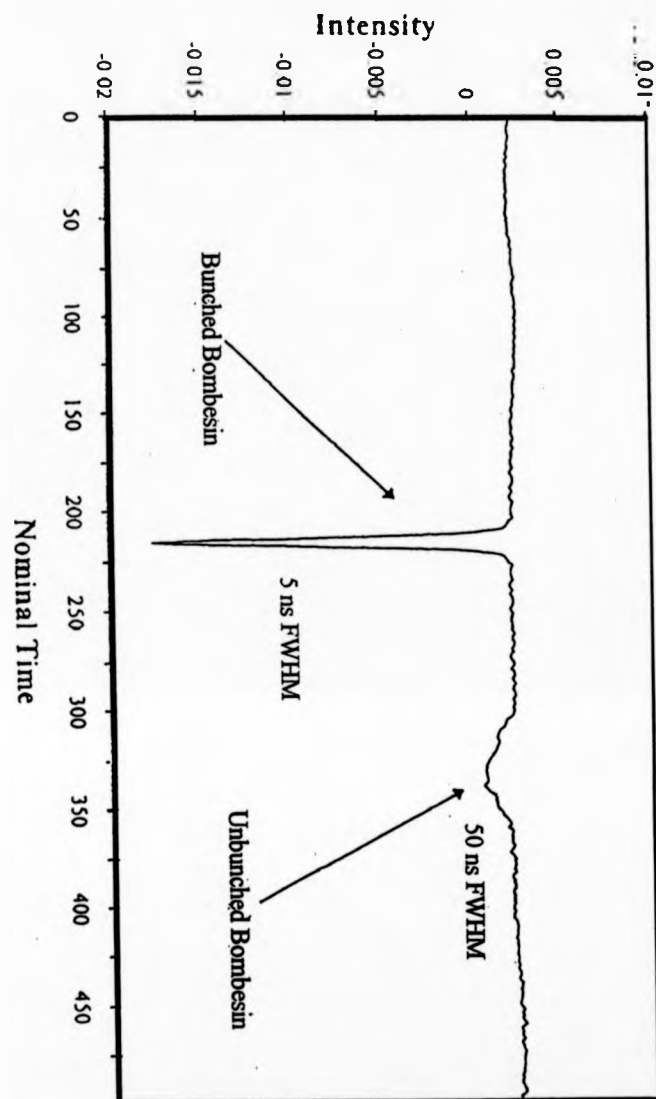


Figure 56. Experimental results illustrating the time-focusing action of the ion buncher. The FWHM of the unbunched and bunched peaks were 50 and 5 ns respectively.

peak became shorter its height became larger, with the area under the peak remaining the same. This proved that the ion packet was actually being compressed and that the scattering of the beam was minimal.

The minimum time-lengths achieved for CsI clusters and bombesin ions were approximately 5 ns and 6 ns respectively (full-width at half maximum). This corresponded to maximum resolution in the ion mirror of 4000. The experimental result shown in figure 56 was obtained after an acquisition of 100 shots. During the first 50 shots the ion buncher remained switched off, thus the unbunched ion peak was acquired, while in the last 50 shots of the acquisition the buncher was time-focusing the ion packet with the optimum voltage. The width of the unbunched peak was one order of magnitude larger than that of the bunched peak, while the total numbers of ions were about the same in both cases.

The ion beam should have passed through a number of small slits in its path (particularly the collision cell slits) and been ejected into the ion mirror with spatial and angular spread matching the acceptance parameters of the quadratic field. For this purpose, a number of beam collimation and steering elements were introduced in the ion path. The double-focusing mass spectrometer was effectively creating in its exit slit an identical image of the ion beam at the source slit. The precursor ion packet was slightly defocusing in the y -plane and nearly parallel in the z -plane, and therefore a number of ion optical elements were required to prepare the beam for transmission through the quadratic mirror. Because of the large energy spread introduced by the ion

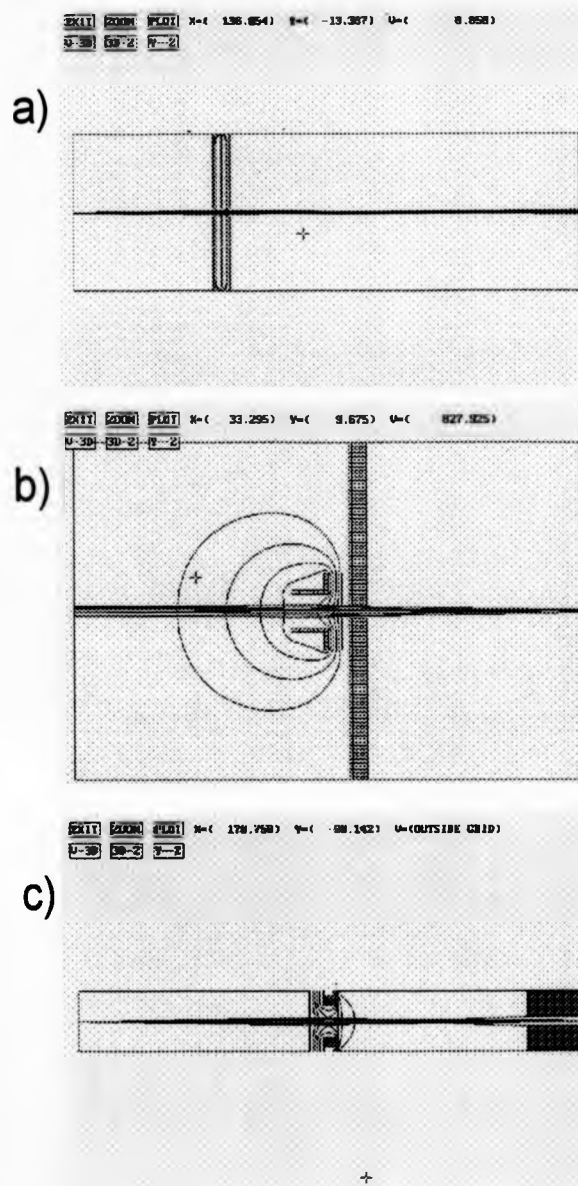


Figure 57. SIMION ion trajectory simulations of various components of the interfacing ion optics region of between the double focusing mass spectrometer and the quadratic ion mirror.

buncher, electrostatic lenses were weak and provided ion transport rather than sharp focusing. Three planar symmetry split-electrodes situated at different distances from the exit slit may be used for focusing and deflection of the ion beam in the y -plane. The availability of different lenses was essential because focusing in the y -direction with variable magnification was necessary in order to cope with different widths of the detector slit for different resolutions of the double-focusing mass spectrometer. Additionally, if the ion beam exited the slit of the Concept mass spectrometer at an angle to the axis of the quadratic mirror different than zero, a minimum of two y -deflectors were required to align the ion beam back on the ion optical axis.

A drawing demonstrating the positions of the lenses was shown in figure 55. The first of the y -lens/deflectors was situated 45 mm after the source slit, before the ion buncher entrance. The second y -lens/deflector was positioned after the ion buncher and mounted on the entrance aperture of the vacuum chamber. Its distance from the source slit was 200 mm. The third y -lens/deflector was mounted on the differentially-pumped chamber of the collision cell. The electrodes of this lens/deflector were 20 mm long. The optimum combination of voltage values for the above lenses were estimated using ion trajectory simulations with the SIMION software (figure 58), although the final values were established experimentally.

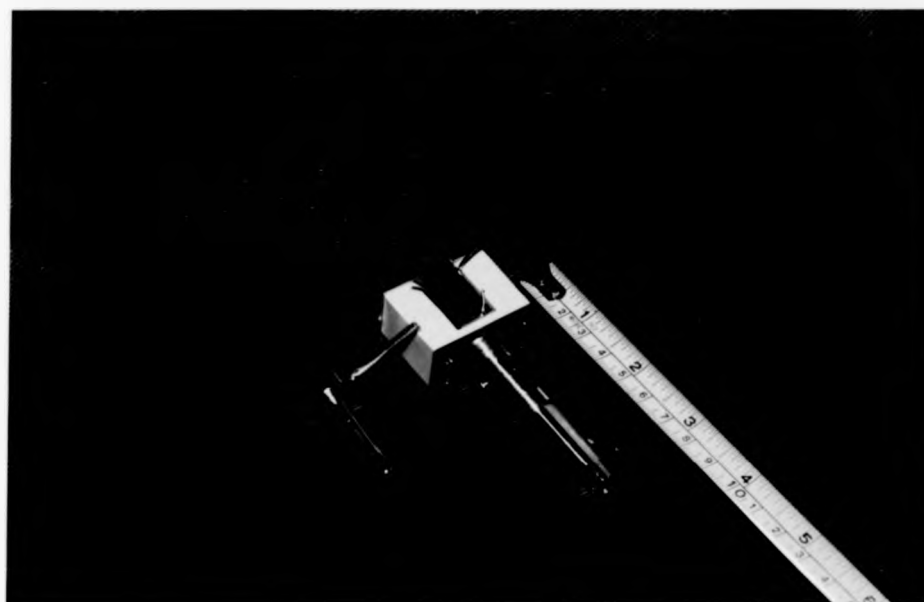


Figure 58. Photograph of the two different-design collision cells of the Mag-TOF prototype tandem mass spectrometer.

5.3.3 The collision cell, post-accelerating region and z-deflector.

The theoretical considerations connecting the length of the collision cell with the resolution of the quadratic ion mirror were presented in the previous chapter. Two different designs of collision cells were developed (figure 59), the main difference between them being their lengths and the sizes of their slits. Both collision cells were designed to sustain collision gas density at a level of 10^{16} molecules/m³. The pressure inside of the collision cell was of the order of magnitude of 10^{-4} , torr while the pressure of the differentially-pumped chamber (figure 55) was estimated to be in the region of 10^{-5} torr. Gas flow calculations were performed to establish the size and length of the slits between the differentially-pumped chamber and the high vacuum region required to maintain pressures lower than 5×10^{-7} torr within the latter.

The length of the first of the two collision cells was 10 mm. The slits of this collision cell were 1 mm wide and 7 mm high. According to Eq. 4-52, any collision gas including xenon could be used without compromising resolution in the quadratic ion mirror. The main limitation imposed by this collision cell was in terms of transmission because of the small size slits. This collision cell was mounted from the top of the differentially-pumped chamber. The flow of the collision gas was controlled by means of Negretti leak valve. The collision gas entered the vacuum chamber through a feedthrough at the bottom of the differentially-pumped chamber and was channelled towards the collision



Figure 59. Photograph of the region before the quadratic mirror, including the differentially-pumped chamber. A number of ion optical elements can be seen including one of the y -lenses and the z -deflector, as well as the ion detector.

cell through a PTFE tube with internal diameter of 2 mm.

The width of the slits of the second of the collision cells was 2 mm, and their height was 7 mm. The length of this collision cell was 30 mm, therefore this design would be unsuitable for heavier collision gases like xenon whereas lighter collision gases like helium or argon would not impose any limitation on mass resolution. This collision cell was made of two stainless steel halves, which were screwed against each other and mounted from the side wall of the differentially-pumped chamber with the aid of a slotted tubular-shaped part (figure 58).

During CID experiments, the collision gas flow was adjusted to provide approximately 50% attenuation of the parent ion beam. As the ions left the collision cell they entered the post-acceleration region. The extraction electrode was floated at -2.19 kV (approximately 0.2 of the average precursor ion energy) and was located 5 mm away from the exit slit of the differentially-pumped chamber. Both these electrodes of the gap were shaped on the basis of SIMION simulations to provide lower divergence for low-mass fragments ions (figure 60). All of the ion optical elements following the post-acceleration region including the front end of the ion mirror assembly, were floated at the same potential as the extraction electrode.

The z-deflector necessary to direct the ion beam towards the ion detector (as discussed in the previous chapter) was mounted, together with the extraction electrode of the post-accelerating region, from the side wall of the differentially-pumped chamber. The length of the deflector was 40 mm and

EXIT ZOOM PLOT X=(136.854) Y=(-13.387) U=(0.183)
U-3D 3D-2 Y-2

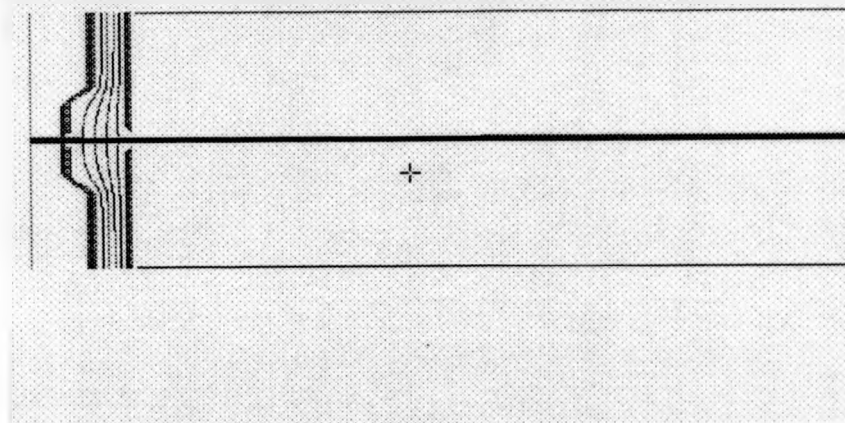


Figure 60. SIMION simulation of ion trajectories in the post-accelerating region.

the gap between the plates was 10 mm. Both plates of the detector were floated at 2 kV, while the bias between them was 90 V in order to deflect the ion beam upwards. The combination of this deflecting potential, as calculated by Eq. 4-70, with an optimum mirror tilt of approximately 1.2 degrees should have ensured maximum transmission of lighter as well as heavier mass fragment ions through the ion mirror.

5.3.4 Design and construction of the quadratic field mirror.

The practical design of the ion mirror had to fulfil a number of potentially conflicting requirements. Its specifications and dimensions had to be chosen so that high transmission and adequate resolution were ensured for the input parameters of the ion beam. However, steps had to be taken to achieve any permissible compromise in an effort to increase the simplicity of the construction. The electrostatic field of the ion mirror was approximated by a multi-electrode system, which might in itself produce perturbations that compromise a resolution. Additionally, the electrode representing the front boundary of the ion mirror that served as the ion detector mount needed to be flat, therefore the field shape near the entrance of the ion mirror was not defined ideally. The implications of such design considerations are discussed below in more detail.

5.3.4.1 Multi-electrode system for sustaining the quadratic field.

The 3-dimensional potential distribution describing the field of the quadratic mirror was given by the following equation:

$$U(x, y, z) = \frac{k}{2} \cdot (x-a)^2 - \frac{k}{2} \cdot y^2 \quad \text{Eq. 5-1}$$

For simplicity the arbitrary constant C of Eq. 4-57 has been omitted. A system of N electrodes was utilised to sustain the field shape.

Within this section, it is supposed that the field in the planes $x=0$ and $x=L_m$ was defined perfectly, so that the only source of field perturbations is the step-like approximation on the boundaries $y = \pm H$ (see figure 61).

If the individual electrodes have width $\Delta = L_m/N$, i.e. the gaps between them are negligible, the method of variables separation [185] gives the solution of the two-dimensional Laplace equation inside the mirror as:

$$\Phi(x, y) = \sum_{n=1}^{+\infty} A_n \cdot \sin\left(\frac{\pi n x}{L_m}\right) \cdot \frac{\cosh\left(\frac{\pi n y}{L_m}\right)}{\cosh\left(\frac{\pi n H}{L_m}\right)} + U(x, y) \quad \text{Eq. 5-2}$$

$U(x, y)$ is given by Eq. 5.1. The Fourier coefficients A_n are given by the expression:

$$A_n = \frac{2}{L_m} \cdot \sum_{m=0}^{N-1} \int_{m\Delta}^{(m+1)\Delta} \left[u_m - \frac{k}{2} \cdot (x-a)^2 \right] \cdot \sin\left(\frac{\pi n x}{L_m}\right) dx \quad \text{Eq. 5-3}$$

u_m is the potential on m^{th} electrode. It is obvious that the best approximation to the ideal field would have been obtained when all the Fourier coefficients were equal to 0. However, there were only N free parameters (i.e. the potentials on individual electrodes) so that only N number of harmonics A_n could have been made to equal zero.

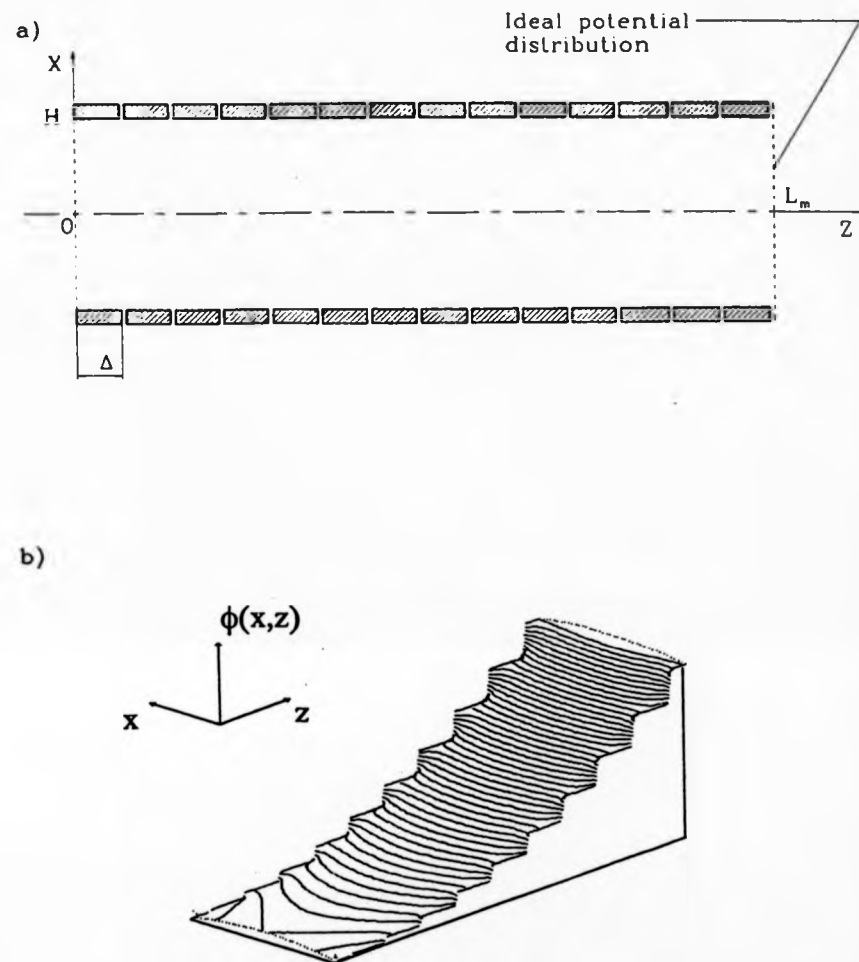


Figure 61. Simulation of field sustaining system on the side of a mirror with planar hyperbolic field (see text for notation): a) cross-section of the mirror; b) SIMION illustration of the potential distribution inside the mirror.

5.3.4.2 Long-range field sag and its correction.

In conventional reflectrons, the potentials u_m on the electrodes are chosen so as to be equal to the desired potentials in the central axis of the electrodes. However, this is justified only for the case of uniform fields. For any non-uniform field, this approach generally results in non-zero harmonics A_n beginning from $n=1$. For the case of quadratic field mirrors, all Fourier coefficients for even n are zero, while the odd harmonics $A_1, A_3, A_5 \dots$ become non-zero and can reach quite substantial values (see Table 2). Increase of the number of electrodes would reduce these harmonics almost proportionally, but construction complexity would also increase substantially. The presence of high-value lower harmonics is equivalent to large-scale field sag, which spans across the whole ion mirror and introduces significant TOF aberrations. Because of the low rate of decrease along the y -direction, this sag cannot be reduced efficiently merely by increasing the mirror width. It has been found [186] that for quadratic fields, harmonics for low values of n may be successfully reduced by simply shifting the whole potential distribution to lower potentials by amount equal to:

$$\delta V = \frac{\pi}{4} A_1 \quad \text{Eq. 5-4}$$

Solution of the Laplace equation for the corrected potential distribution gives Fourier coefficients where the first harmonic becomes $B_1=0$, while corrected higher harmonics $B_3, B_5 \dots$ differ from zero by very small amounts (see Table

	N=20		N=30		N=40		N=50		N=60	
n	A _n	B _n	A _n	B _n	A _n	B _n	A _n	B _n	A _n	B _n
1	132.3	0	58.9	0	33.1	0	21.2	0	14.7	0
3	43.2	-0.9	19.5	-0.2	11.0	-0.05	7.1	-0.02	4.	-0.01
5	24.8	-1.6	11.5	-0.3	6.5	-0.1	4.2	-0.04	2.	-0.02
7	16.5	-2.4	8.0	-0.45	4.6	-0.14	3.0	-0.06	2.1	-0.03
9	11.5	-3.2	6.0	-0.6	3.5	-0.2	2.3	-0.08	1.6	-0.04
11	8.0	-4.0	4.6	-0.7	2.8	-0.23	1.8	-0.09	1.3	-0.04
13	5.13	-5.1	3.6	-0.9	2.3	-0.28	1.5	-0.11	1.1	-0.05
15	2.6	-6.2	2.9	-1.1	1.	-0.32	1.3	-0.13	0.9	-0.06
17	.15	-7.6	2.2	-1.3	1.6	-0.37	1.1	-0.15	0.8	-0.07
19	-2.4	-9.4	1.7	-1.5	1.3	-0.42	1.0	-0.17	0.7	-0.08

Table III. Fourier coefficients of the perturbing field for multi-electrode systems with N electrodes: A_n without correction, B_n with correction (in units $10^{-6} \cdot k / 2 \cdot L_m^2$, coefficients with even n are zero).

2). In practice this approach is equivalent to shifting the potential distributions on the end planes instead of that on the multi-electrode system. For $N > 30$, this correction alone would be sufficient to solve the problem of long-range field sag, even if resolution in excess of 10000 were required.

5.3.4.3 Short-range perturbations

A side-effect of shifting the potential distributions would be to increase higher-order harmonics (for $n > N/2$, see Table 2). For this reason, it was necessary to estimate the influence of these higher-order harmonics more thoroughly. Figure 62 represents a typical amplitude distribution for higher-order harmonics as a function of n . It is clearly seen that maximum values are achieved around $n = 2N$ and their amplitude is given by the expression:

$$B_{2N} \approx \frac{1}{2\pi N} \cdot \frac{k}{2} \cdot L_m^2 \quad \text{Eq. 5-5}$$

These higher-order harmonics may give rise to significant TOF aberrations (especially near turning points in the field), but their influence may be successfully suppressed [186] by appropriate choice of the dimensions of the ion mirror so that

$$\frac{NH}{L_m} \geq 4 - 5 \quad \text{Eq. 5-6}$$

H is the width of the mirror. Then, according to Eq. 5-2, all harmonics with $n > N$ (or even $n > N/2$) would perturb potentials at a level less than 1 ppm, and flight times at a level much less than 10 ppm [186].

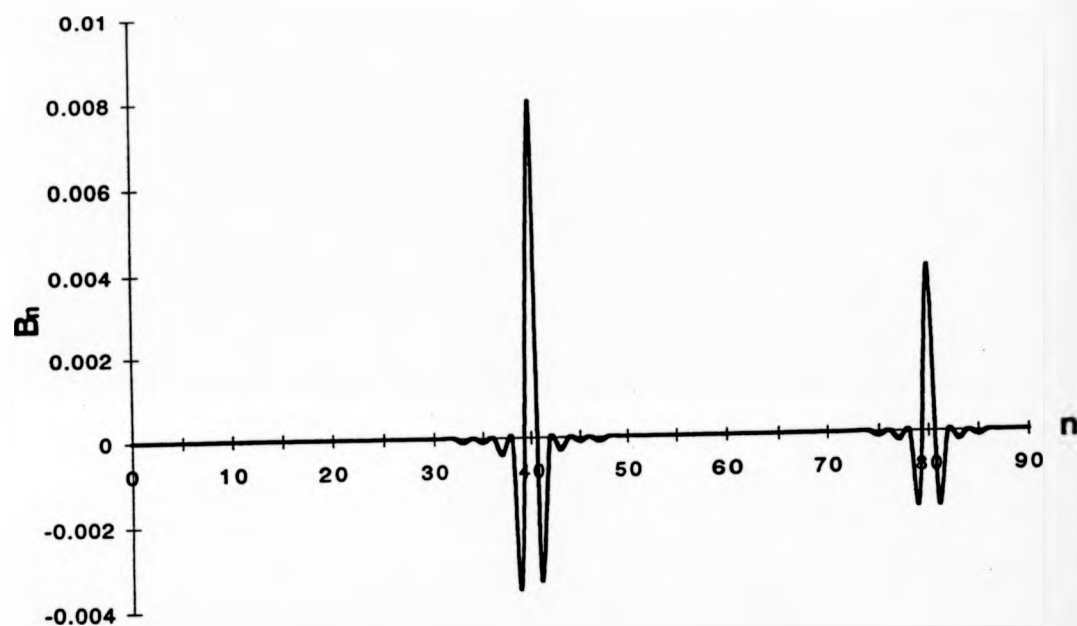


Figure 62. Dependence of Fourier coefficients B_n on the number of harmonics n , when the total number of electrodes, $N=20$.

5.3.4.4 Perturbations on the field boundaries

5.3.4.4.1 The front boundary of the ion mirror.

In the treatment above, the potential distribution was supposed to be ideal in the planes $x=0$ and $x=L_m$. The plane $x=0$ was intersected twice by the ions and also served as the base for the planar micro-channel plates detector. The simplest construction of this part of MS-2 was a single planar electrode, serving to support the detector in this same plane directly above the entrance aperture (figure 63). The Fourier expanded potential distribution produced by introducing such a planar electrode into a quadratic field, may be written as:

$$\Phi(x, y) = \sum_{n=1}^{+\infty} A_n \cdot \sin \left[\pi n \cdot \frac{(y+H)}{2H} \right] \cdot \frac{\sinh \left[\pi n \cdot \frac{(L_m - x)}{2H} \right]}{\sinh \left[\pi n \cdot \frac{L_m}{2H} \right]} + U(x, y) \quad \text{Eq. 5-7}$$

The Fourier coefficients A_n are given as:

$$A_n = \frac{1}{H} \int_{-H}^H \left(u_1 + \frac{k}{2} \cdot y^2 \right) \cdot \sin \left[\pi n \cdot \frac{(y+H)}{2H} \right] \cdot dy, \quad n = 1, 3, 5, \dots \quad \text{Eq. 5-8}$$

$$A_n = 0, \quad n = 2, 4, 6, \dots$$

The potential u_1 on the first electrode is the only free parameter. By adjusting u_1 the first harmonic A_1 could be made zero. This was achieved by choosing

$$u_1 = -k \cdot \frac{H^2}{2} \left(1 - \frac{8}{\pi^2} \right) \quad \text{Eq. 5-9}$$

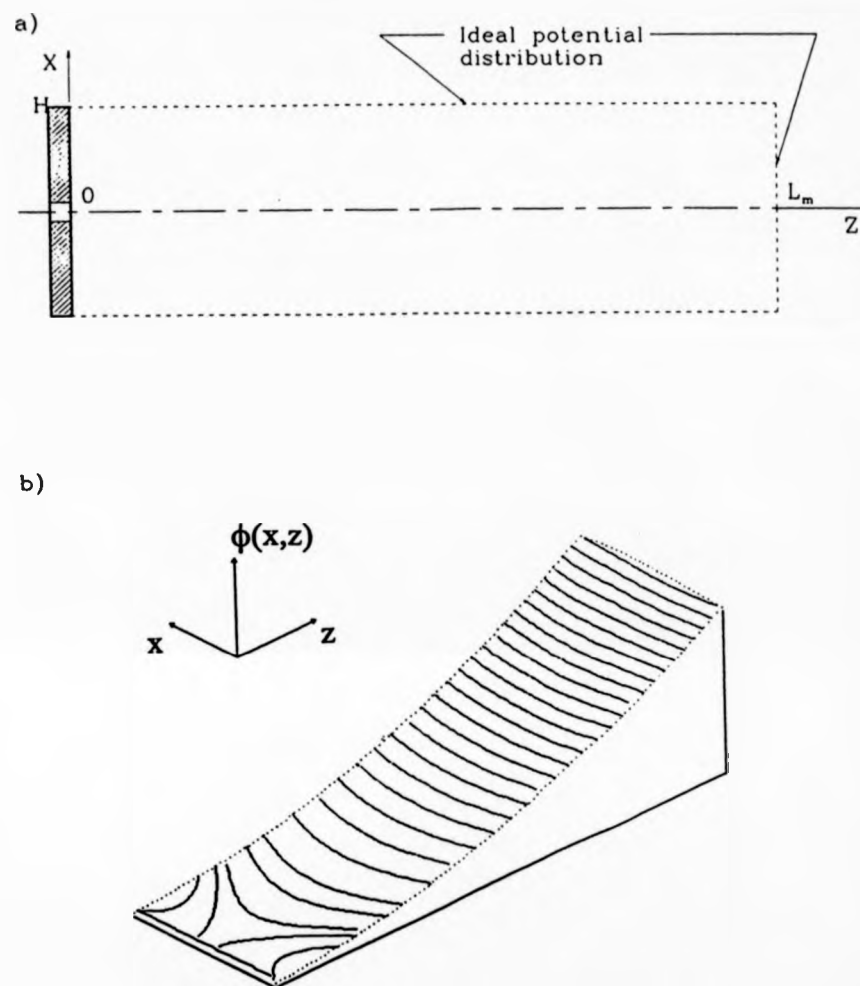


Figure 63. Simulation of field sustaining system on the flange of a mirror with planar hyperbolic field: a) cross section of the mirror; b) SIMION illustration of the potential distribution inside the mirror.

This adjustment also increased the rate at which field perturbation reduces with coordinate x . Additionally, all other Fourier harmonics were slightly reduced. The overall time-of-flight aberrations were significant only for very light fragment ions (mass smaller than 5% of the parent ion mass) [186]. Further, the use of post-acceleration as described above achieves unit mass-resolution for the whole of the required mass range.

5.3.4.4.2 The end-electrode of the ion mirror.

The high potential boundary of the ion mirror was defined by a stainless steel electrode. The shape of the electrode surface followed the theoretical shape of the equipotential lines of the quadratic field. For purposes of construction simplicity, the ideal hyperbolic shape was approximated by a number of steps. The exact dimensions of the steps were calculated using numerical methods in combination with the Bruns-Bertein method [187] correlating the geometry perturbations with potential perturbation. The final calculated shape did not introduce any practical limitations on mass resolution for ions with turning points further than 30–50 mm away from the electrode [188].

5.3.5 Practical design considerations.

The final design of the quadratic mirror was based on the theoretical considerations described in this work. In order to simplify the construction of the mirror, the potential distribution was created in the parallelepiped region contained between four 520×150 mm flat fiberglass epoxy plates internally coated with a copper layer (type of board typically used for printed circuit construction). The shapes of each of the 38 field sustaining electrodes was

calculated according to the chosen quadratic equation. Insulating 2 mm wide gaps separating the different potential regions were etched on the internal surface of the boards with 5 μm accuracy. The shapes of the electrodes at the top and bottom surface followed the quadratic equation ($U(x,y)$), while the electrodes in the side surfaces were parallel, corresponding to the field-free z -direction (see figure 64). The widths of the electrodes varied from 25 mm to 5 mm. This was done in order to reduce the variety of the resistors required for the resistor chain. The density of the electrodes was higher towards the back of the mirror, because this was the region to which higher-mass ions penetrated, therefore higher resolution was required. All four boards were clamped between two aluminium end-frames aligned and held together by three stainless steel rods. The boards were aligned with each other by means of eight 6 mm dowel holes. The end-frames were held at the same potential as the first electrode of the mirror (same as the post-accelerating potential). The mirror assembly was situated on two stainless steel rails, allowing manipulations of its position with respect to the collision cell by means of a linear actuator in the back-wall of the vacuum chamber. The rear end of the rail-assembly was supported against the bottom surface of the vacuum chamber by means of two long screws to allow adjustment of the tilt-angle of the mirror.

The high voltages for the front and the end of the mirror were supplied by a specially made power supply (HD Technologies, Manchester, UK). The calculated potentials were distributed to the different electrodes of the mirror using a resistor chain made of Welwyn (Bedlington, UK) metal film resistors



Figure 64. Photograph of the MS2 of the Mag-TOF prototype tandem mass spectrometer. The electrode boards seen on the top of the vacuum chamber were the exact negative image of the actual electrodes of the ion mirror.

(figure 65). The resolution for the quadratic field was estimated with ion trajectories simulation, using the SIMION software (table 3). Two external variable resistors were used to supply the two electrodes closest to the detector for optimisation of resolution. The nominal values of the resistors were between 0.5 and 1.5 M Ω . The effects of inaccuracy in the resistors has been simulated by SIMION in planar two-dimensional geometry. Modelling predicted that mass resolution would not decrease below 5000 for random variation of resistor values up to 0.5–1% and systematic shifts up to 0.05–0.5 %. The error in the individual resistor values utilised was measured to be less than 0.2%.

The end-flange of the mirror (see previous section) was mounted using four PEEK self-aligning mounting rods on a stainless steel plate. The latter was mounted on the rear aluminium end-frame using four screws and dowels for alignment. The front flange of the mirror was made from a 1 mm thick stainless steel plate directly mounted on the front-end aluminium frame and aligned with four dowels. This plate housed the entrance slit of the mirror and two 60 mm diameter holes covered with metal mesh. The purpose of the holes was to provide adequate pumping speed for the volume within the ion mirror boards. A large rectangular area of the front flange above the entrance slit was cut away to allow ions to exit the mirror and reach the detector. The hole was covered with Buckbee-Mears 70 high transmission mesh. The gap between the mesh and the front surface of the first multi-channel plate was biased with a low potential gradient (approximately 50 V) in order to prevent secondary electrodes being accelerated towards the back of the mirror.



Figure 65. Photograph of the MS2 region of the Mag-TOF prototype tandem mass spectrometer, illustrating ion optics, the collision-cell differentially-pumped chamber, the ion mirror and the resistor chain.

Initial angle (degrees)	Initial energy excess (%)	TOF for parent ion (mass m_p) (μ s)	TOF of 0.66 m_p fragment (μ s)	TOF of 0.50 m_p fragment (μ s)	TOF of 0.33 m_p fragment (μ s)
-0.20	0	17.51804	14.30456	12.38848	10.11347
-0.18	1	17.51774	14.30404	12.38796	10.11451
-0.16	2	17.51814	14.30330	12.38691	10.11409
-0.14	3	17.51796	14.30378	12.38693	10.11367
-0.12	4	17.51792	14.30404	12.38744	10.11472
-0.10	5	17.51854	14.30352	12.38718	10.11473
-0.08	6	17.51795	14.30404	12.38822	10.11409
-0.06	7	17.51793	14.30330	12.38744	10.11493
-0.04	8	17.51864	14.30404	12.38796	10.11471
-0.02	9	17.51824	14.30432	12.38692	10.11472
0	10	17.51874	14.30428	12.38718	10.11430
0.02	11	17.51845	14.30352	12.38692	10.11452
0.04	12	17.51843	14.30433	12.38877	10.11450
0.06	13	17.51864	14.30430	12.38744	10.11451
0.08	14	17.51854	14.30427	12.38877	10.11472
0.10	15	17.51886	14.30456	12.38796	10.11367
0.12	16	17.51882	14.30326	12.38692	10.11388
0.14	17	17.51914	14.30352	12.38770	10.11367
0.16	18	17.51944	14.30300	12.38795	10.11430
0.18	19	17.51974	14.30430	12.38797	10.11431
Average flight time		17.51851	14.30388	12.38754	10.11430
Time difference between minimum and maximum flight time (ns)		2.00	1.56	1.56	1.47
Mass resolution		4380	4585	3970	3440

Table IV. Flight times and corresponding mass resolutions for various fragment ions of different energies in the quadratic mirror, produced by SIMION simulations.

The multi-channel plate assembly of the ion detector was mounted on the front plate of the mirror by means of four 10 mm long insulating spacers. The assembly consisted of two 100×80 mm Galileo (Sturbridge, MA, USA) multi-channel plates clamped together between two rectangular stainless steel plates forming a frame. Typical potential difference across the multi-channel plates was around 2 kV. Electrons coming out from the rear surface of the multi-channel plate assembly were accelerated by 300 V in a 10-15 mm gap, towards the surface of the anode. The large surface anode was made in the shape of a pyramid (figure 66) in order to be capacitively coupled to a small diameter feedthrough that carried the signal out of the vacuum to a preamplifier/comparator.

5.4 Control and acquisition system.

A partially computer-automated control and acquisition system was developed to manage experimental mode, stepper motors, timing of the experiment, and other parameters (figure 67). Precursor ion choice was done independently, using the control and acquisition console of the Concept double-focusing mass spectrometer. The control and acquisition system of the time-of-flight part of the Mag-TOF prototype instrument was built around a 90 MHz Pentium® personal computer (Gateway 2000, Dublin, Ireland). Three ISA standard expansion cards were custom-designed and built by HD Technologies (Manchester, UK). These included one input/output (I/O) control and two data acquisition cards. The I/O control card was connected to a stepper-motor control unit used to drive the three stepper motors involved with the experimental process (two for manipulation of the wobble probe and



Figure 66. Photograph of the pyramid-shape capacity coupled detector anode of the Mag-TOF prototype tandem mass spectrometer.

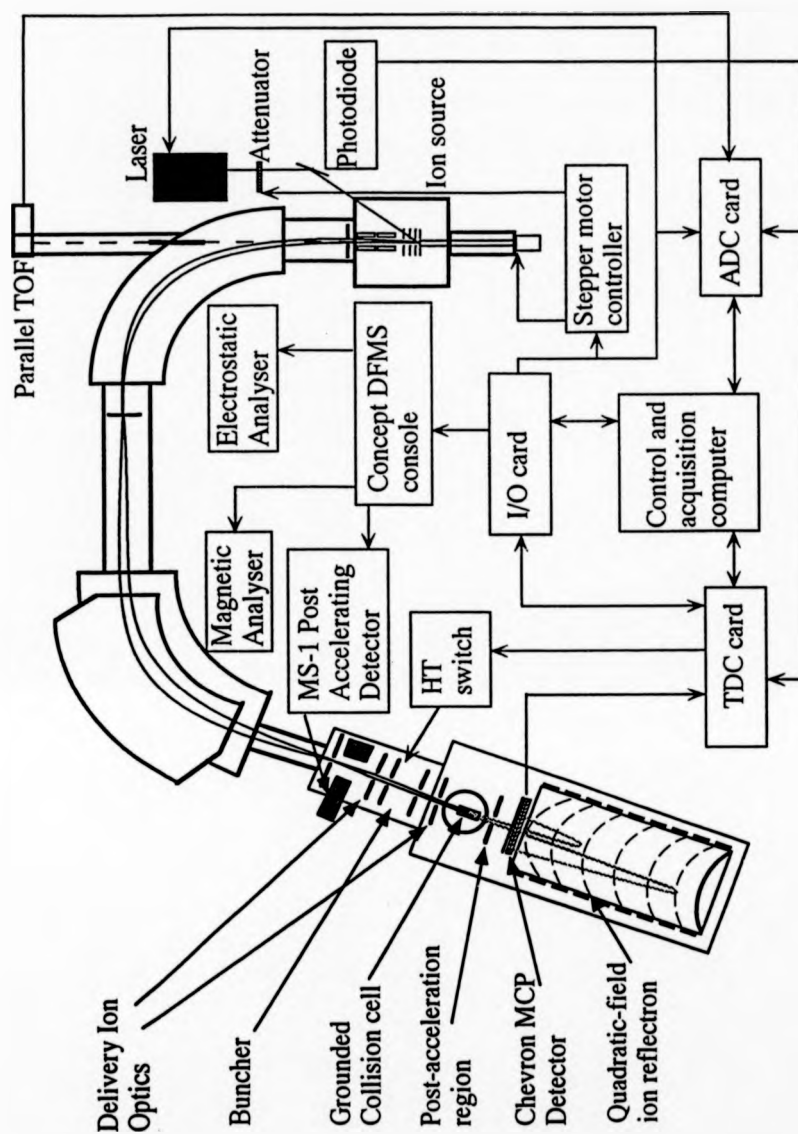


Figure 67. Schematic of the control and acquisition system of the Mag-TOF prototype tandem mass spectrometer.

one for the laser beam attenuator). The I/O control card was also used for switching between different modes of operation. It has been described earlier how the electrostatic sector plates and the post-accelerating detector of the Concept mass spectrometer were grounded using electronic circuits inserted in the appropriate power supplies in the control console. These electronic circuits were triggered by the control card by means of two board-mounted photodiode lasers and optical fibers. The I/O control card produced the trigger pulse for the nitrogen laser. However, in order to avoid the jitter of the internal laser circuits, the zero-time of the time-of-flight experiments was obtained with a fast UV-grade photodiode placed in the path of a small reflection of the laser beam.

The first acquisition card was an analogue-to-digital converter (ADC) with 400 MHz bandwidth, utilised for data acquisition from the linear TOF1 mass analyser. The second data acquisition card was a time-to-digital converter (TDC) used for ion counting at the quadratic ion mirror. The signal of a single ion from the detector of the quadratic mirror (amplitude 8 mV, width 5 ns) was transformed into a 5 V TTL pulse in a specially made preamplifier/comparator which was connected to the TDC card. The dead time of the preamplifier/comparator was 16 ns, while the time resolution of the TDC card was 1 ns. The jitter of the delay line of the TDC card was better than 1 ns. The TDC card was also used to produce the triggering pulse for the fast high-voltage switch of the ion buncher.

The control and acquisition system was managed using software specially written for the purpose. Instrumental parameters were introduced in the

software, including effective path length of various regions of the instrument and accelerating potentials of the ion source, buncher and ion mirror. The software was used for choice of operation mode, input of experimental parameters (i.e. laser repetition rate, laser power, sample rastering conditions) and display of the acquired spectra. It had spectrum-averaging capabilities as well as some spectrum-smoothing algorithms. It also allowed for mass calibration of the mass spectra, using calibration files and the given instrumental parameters.

5.5 Results and discussion.

5.5.1 Transmission optimization and alignment experiments.

In the initial stages of the experiments, much effort has been devoted to the physical alignment of the various parts of the instrument and the optimisation of the transmission of an ion beam throughout the ion path. A red-colour diode laser (Sumicem Opto-Electronics Ltd, Limerick, Ireland) was employed to aid in the alignment of the individual components of the ion optical interface region, the collision cell and the ion mirror, and in the alignment of all of them with the exit slit of the Concept. The vacuum chamber of the ion mirror was situated on a purpose-built support frame that allowed some adjustment of the angle of the whole chamber with respect to the double-focusing mass analyser.

The most important transmission optimisation experiments were performed with a stable continuous Cs⁺ ion beam produced by a standard Kratos Analytical (Manchester, UK) L-SIMS ion source. The ion current of the ion

beam was in turn measured onto various metal surfaces throughout the instrument. Some of these were permanent standard components of the instrument, including the longer radius electric sector plate, the conversion dynode of the post-accelerating detector, the parabolic end-electrode of the ion mirror and the coated surface of the first multi-channel plate. Others were built into the design especially for this purpose (plates near the ion path in the collision cell area) and others were attached on temporary jigs (for example replacing the linear time-of-flight detector with a collector plate). A Keithley electrometer was used for current measurement, with the electrometer and the collector being biased by 9 V to avoid escape of secondary electrons. After improvement of alignment and adjustment of all relevant instrumental parameters, 50% of the ions leaving the source slit were reaching the detector of the quadratic field mirror, when the source and exit slit of the Concept mass spectrometer were adjusted to give resolution 2500. For maximum slit width the transmission was approximately 30%, in terms of the proportion of ions passing through the source slit.

5.5.2 Experiments with the MALDI ion source

After a number of experiments to evaluate and improve the ion buncher operation (as described in a previous section), CsI clusters were used to optimise transmission through the instrument of a pulsed beam produced in the MALDI ion source. Similar transmission to that observed with the L-SIMS source was achieved. Additionally, it was proved that the ion mirror could time-focus the high energy-spread parent ion beam to a time-length

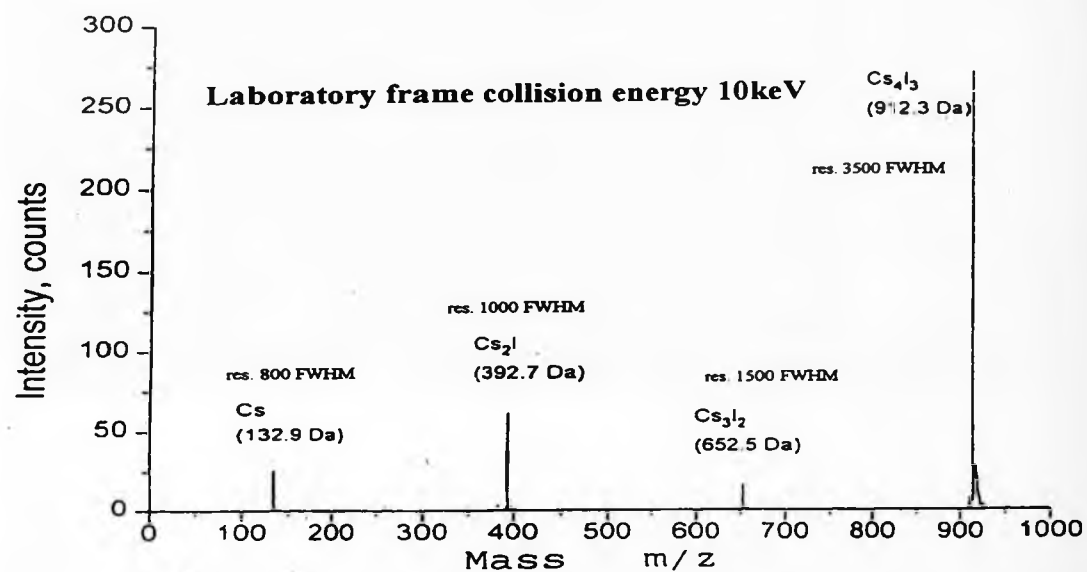


Figure 68. Tandem mass spectrum of Cs_4I_3 . The resolution achieved for the parent and fragment ions demonstrates the proof of the concept of the Mag-TOF prototype tandem mass spectrometer.

equal to that created by the buncher, i.e. output time equalled the input time-length.

The next step in the development process was to prove the operational concept of the ion mirror by performing CID experiments on a model molecule and monitor the mass resolution for various fragment ions. CsI clusters were used to study the effect of various parameters on mass resolution. Small variations around the optimum value of the time-delay of the ion buncher pulse (which would affect the exact position of the ion beam in the buncher when the high voltage pulse was switched on) did not seem to have any significant effect on mass resolution when the ion mirror was at the correct position in respect to the collision cell. This was expected because the focusing action of the buncher was expected to be the same regardless of the exact position of the ion beam. The only value that would have changed was the total average energy of the ion packet, which should have made no difference to the behaviour of the ion mirror. The amplitude of the high voltage pulse applied to the ion buncher was critical for the resolution achieved. As predicted theoretically, optimum resolution was achieved when the focal point of the ion buncher was near the exit of the collision cell.

Collisions appeared to cause only insignificant degradation of mass resolution. In fact for the collision gases helium and argon, the change from one collision cell design to the other did not affect resolution. However, the longer collision cell was preferred, because it offered better transmission due to its wider slits. The collision gas flow did not affect resolution but it was very important for optimising the efficiency of the collision-induced dissociation process.

Practically, it proved to be a difficult parameter to adjust. No direct measurement of the pressure in the collision cell or the differentially pumped chamber was possible. An indication of the collision gas flow could only be taken from the pressure measured with an ionisation gauge on the high-vacuum chamber. Due to the efficient design of the differentially-pumped chamber, relatively large changes in gas flow would have been hard to measure, thus extreme care was required when adjusting the leak valve.

The final adjustment of the potential of the mirror was settled on values near the theoretically predicted optimum values, which gave confidence in the accuracy of the calculations. The values of the first two variable resistors could affect resolution, especially for low-mass fragments. A CID tandem mass spectrum of Cs_4I_3 (mass 912 Da) was shown in figure 68. Mass resolution increased from 800 for m/q 133 Cs^+ to approximately 3500 for the m/q 912 precursor ion, which were values very close to those theoretically predicted.

5.5.3 Tandem mass spectrometry experiments with peptides.

The next step of the development of the instrument was the tandem mass spectrometry of small and medium size peptides using MALDI. Matrices used were 4-hydroxy- α -cyanocinnamic acid and 2,5 dihydroxybenzoic acid (DHB). They were diluted in 70:30 and 50:50 mixture of acetonitrile and water respectively, to approximately 0.1 M concentration. A small amount (0.1%) of trifluoroacetic acid was added to enhance the signal-to-noise ratio of the MALDI spectra. Approximately 1 μl of the matrix solution was

deposited in the middle of the tip of the wobble probe in two droplets of 0.5 μ l each, in order to keep the final size of the sample spot smaller than 1.5-2 mm in diameter. The matrix droplet was dried under air flow and one 0.5 μ l droplet of the peptide solution in water was deposited. The concentration of the peptide solution was between 10^{-4} and 10^{-6} M. The amount of analyte ions per sample loading was varied between 50 pmole and 500 fmole. Peptides measured included bombesin substance-P and renin substrate tetradecapeptide. All samples were supplied by Sigma (UK).

Some fresh adjustments were made for acquiring the first tandem mass spectra of peptides using MALDI. The accelerating potential of the ion source was slightly increased to compensate for the energy deficits associated with the MALDI process. The collision gas flow was adjusted on a trial-and-error basis to optimise the pattern of fragmentation. The optimum position of the leak valve was generally reproducible. The first peptide fragmentation mass spectra acquired (figure 69), clearly demonstrated the pattern expected on the basis of the literature but suffered from relatively high noise. The noise most likely stemmed either from metastable decay in the ion mirror or from fragmentation of ions in the tails of the precursor ion pack which were not properly bunched by the ion buncher.

Improvement of the initial energy spread conditions by careful adjustment of the laser power, combined with improvement of the resolution of the double-focusing mass spectrometer improved the signal-to-noise of the mass spectra obtained. Tandem mass spectra of bombesin, substance-P and renin substrate with Ar collision gas were presented in Figures 70, 71 and 72 demonstrating

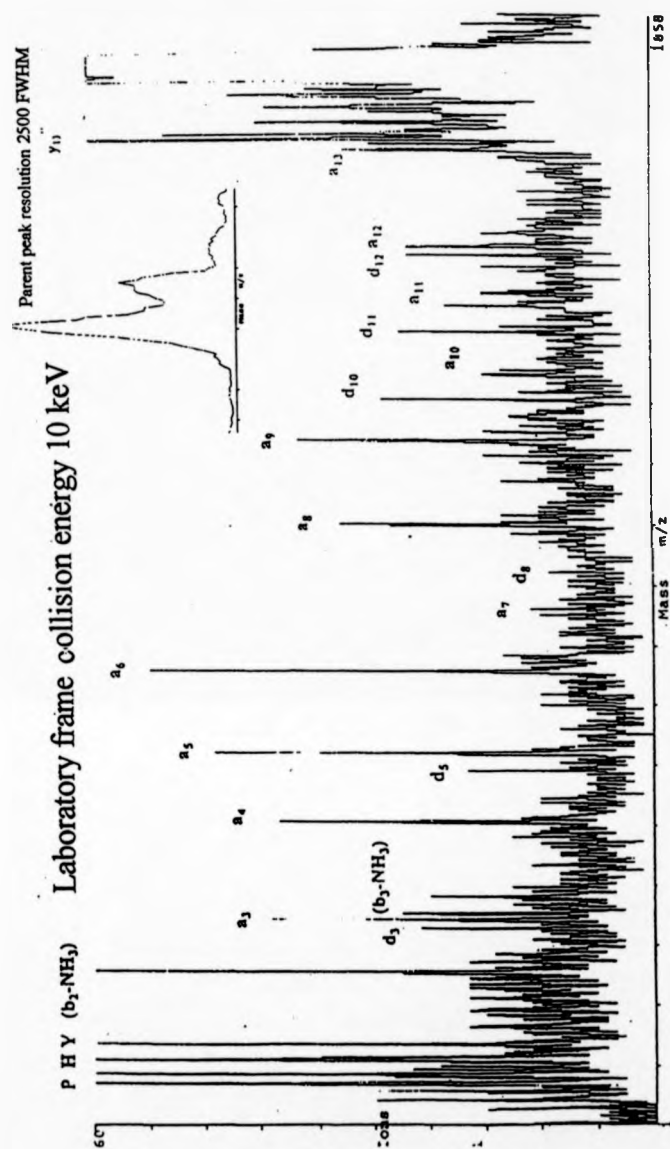


Figure 69. The first tandem mass spectrum of renin substrate tetradecapeptide received with the Mag-TOF prototype tandem mass spectrometer.

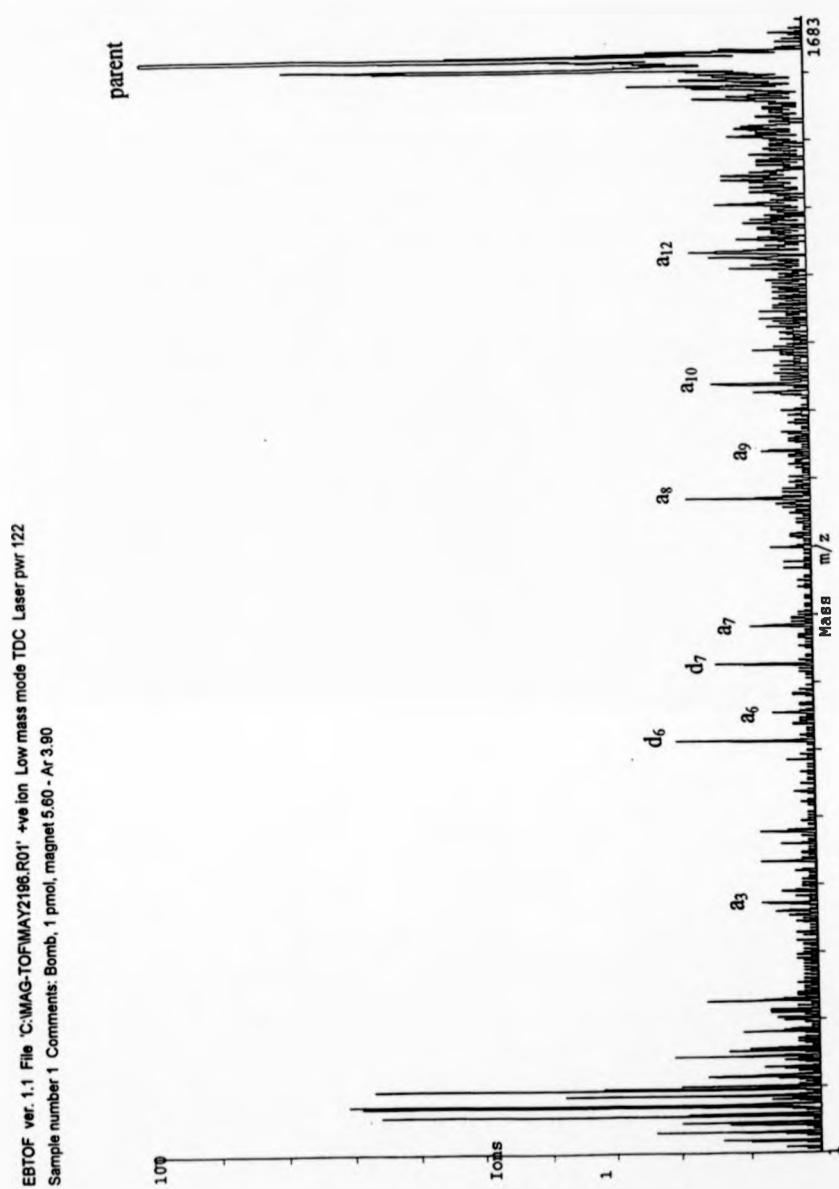


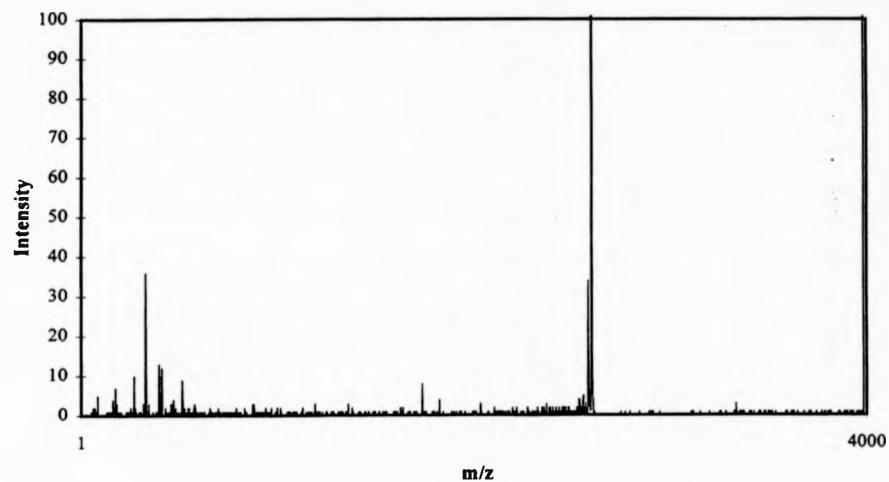
Figure 70. Tandem mass spectrum of bombesin achieved with the Mag-TOF prototype tandem mass spectrometer.

the complete sequencing information for the peptide. The average laboratory-frame energy of the precursor ions was about 10 keV. Mainly a- and d-type fragments were observed, both being characteristic of high energy CID [141]. The a-type ions were N-terminus peptide backbone fragments, very useful for unequivocal sequencing of unknown peptides. The d type fragments were not observed with low energy CID or post-source decay instruments. This instrument was particularly successful at collecting a large number of light fragments (below 150 Da), which usually prove problematic for sector instruments due to high scattering. These immonium fragments may be useful for providing positive proof of the existence or otherwise of various specific aminoacids, which may aid the sequencing of unknown peptides.

5.6 Conclusions.

A detailed account of theoretical considerations has been as a prelude and a foundation for an experimental investigation of the feasibility of creating a tandem mass spectrometer by coupling a double-focusing mass spectrometer to a time-of-flight mass analyser. It has been shown that the use of an ion buncher can correct the time-of-flight spread of the precursor ion pack created in the double-focusing mass spectrometer. Beam collimation and steering ion optics have been designed to provide ion transport through the grounded collision cell region and prepare the beam for ejection into a quadratic-field ion mirror, according to its theoretical acceptance characteristics. The design parameters of the quadratic-field ion mirror have been specified through theoretical considerations of resolution and ion transmission. Post-

CID-Spectrum of 0.5 Picomole Substance P



CID-Spectrum of 1 Picomole Substance P

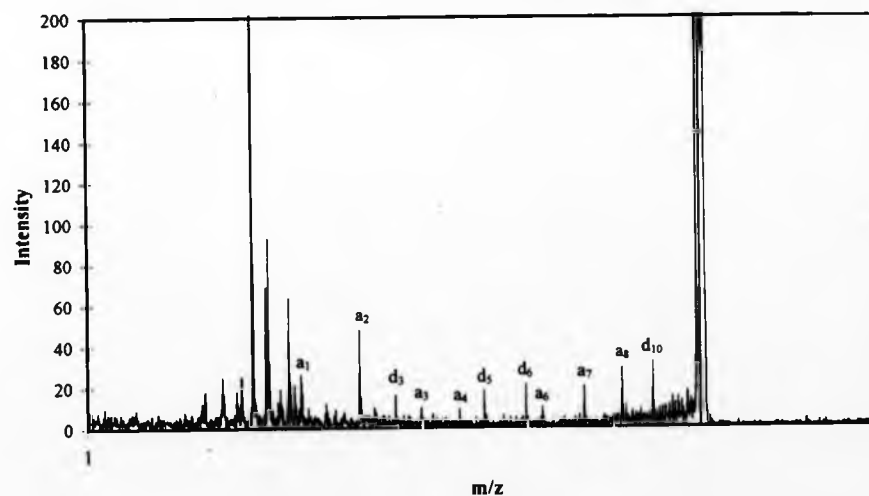


Figure 71. Tandem mass spectra of substance P received with the Mag-TOF prototype tandem mass spectrometer. The amount of sample use has been 1 picomole and 500 femtomole for the upper and lower spectrum respectively.

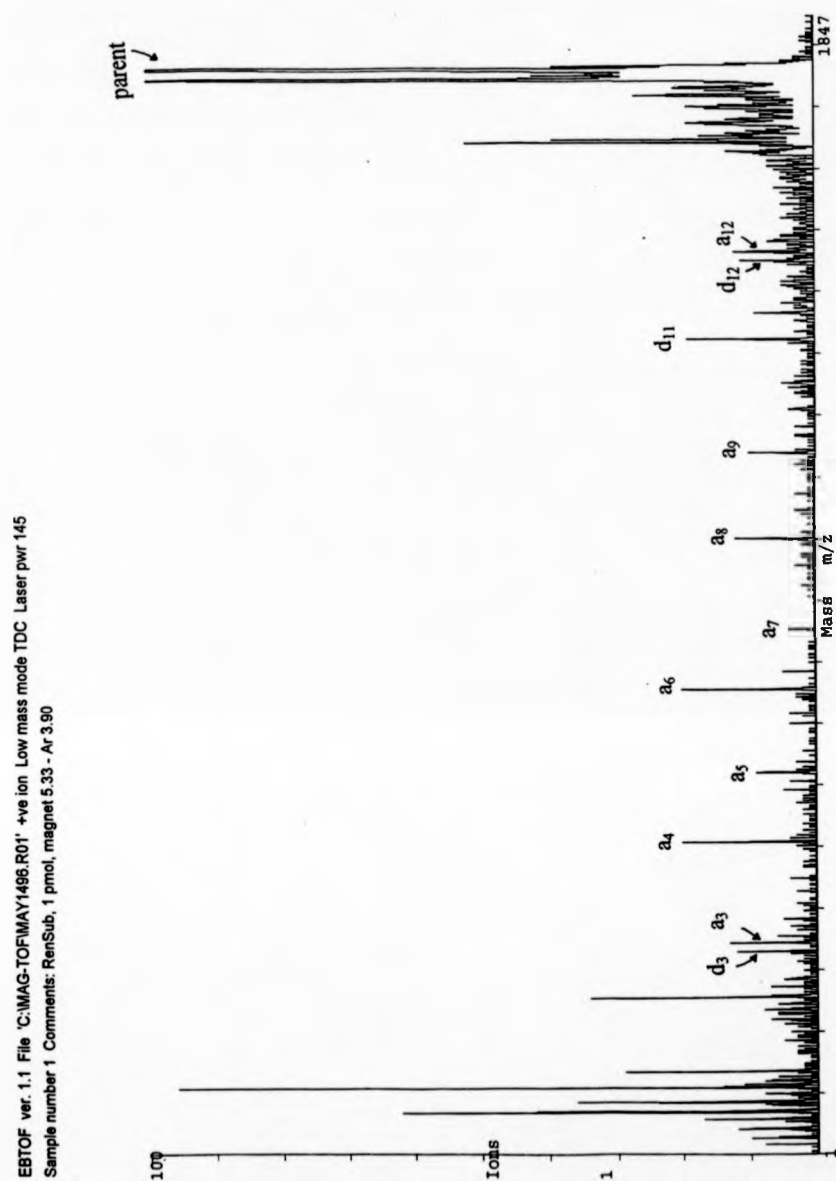


Figure 72. Tandem mass spectra of renin substrate tetradecapeptide received with the Mag-TOF prototype tandem mass spectrometer. The amount of sample used was 1 picomole

acceleration of the ion beam was found to be essential for a number of reasons, including light-fragment detection and light-fragment resolution enhancement. The feasibility of some design compromises were examined for the purpose of simplifying the practical construction of the ion mirror.

The results of the theoretical investigations were the basis for specifying the dimensions and the exact design of the time-of-flight analyser of the Mag-TOF tandem mass spectrometer. The main effort in this study were directed towards the time-of-flight aspects of the instrument, and only absolutely essential modifications were implemented to the double-focusing mass spectrometer. The components of the time-of-flight analyser were designed for ease of manufacturing and assembly, allowing the possibility for quick modifications where necessary during the development process. The Mag-TOF was an advanced prototype where a lot of care has been devoted to high functionality with a partially automated, computer based control and acquisition system, custom-made high- and low-voltage power supplies and purpose-made control and data management/presentation software.

Most importantly, experiments have demonstrated that the combination of an ion buncher with an ideal time-focusing quadratic field can offer high transmission and high resolution for CID-created fragment ions of model ions as well as organic macromolecules. In practical terms, the quadratic-field ion mirror time-of-flight analyser offers simultaneous mass analysis of all fragment ions with unit mass resolution throughout the mass range, fulfilling Fellgett's advantage. The level of sensitivity which has been achieved was already superior to typical values achieved with scanning tandem mass

spectrometers (i.e. four-sector or triple quadrupole instruments). The stability and reproducibility of the mass spectra, as well as the mass accuracy, have been found to be good, although they were primarily a matter of quality of power supplies. Although general mass calibration curves have been established and successfully utilised, further work is necessary to produce more exact calibration correction curves ($\pm 0.1 \text{ m/q}$) to allow unambiguous structural determination of unknown natural samples.

Further instrumental improvements could include the use of higher repetition rate lasers, which would dramatically decrease the time required to acquire a complete mass spectrum. Improvements in the experimental procedure might include computer monitoring of sample spot quality so that the decision to skip a bad spot or acquire a higher number of spectra from a better one would be automatic.

The introduction of a retractable intermediate array detector instead of the post-accelerating detector of the double-focusing mass spectrometer would also enhance tuning capabilities and increase the functionality of the whole device. Although Mag-TOF was operating using a MADLI pulsed ion source, an appropriately modulated continuous source could also be used, making the instrument suitable for analysis of electrospray ions. The use of appropriate electronics could increase the frequency of the data acquisition system, therefore providing a high duty-cycle for such a combination and maintaining a significant advantage over scanning instruments.

Instrument type	Sensitivity *	Resolution *	Complexity	Collision conditions
Four sector instrument with point detector	Medium (100 pmoles)	Very high (>10,000)	Very high	Very versatile
Four sector instrument with array detector	Medium-high (10 pmoles)	Very high (5-10,000)	Very high	Very versatile
Two sector instrument with orthogonal extraction TOF	High (better than 500 femtomoles)	Medium-high (1-2,000)	Medium-Low	Restrictive
Two sector instrument with longitudinal TOF	High (better than 500 femtomoles)	High (2-4,000)	Medium	Very versatile

* Typical Values.

Table V. Comparison of the main characteristics of various types of tandem mass spectrometers. The incorporation of time-of-flight technology in such an instrument can afford sensitivity improvement of the order of 50 to 500 times compared to four-sector instruments with array or point detectors, respectively.

6. Appendix I.

MODELLING OF QUADRUPOLE DOUBLET IN Mag-TOF ION SOURCE

1. Input of data.

$L = 0.3$ m- total length of ion source

$V_0 = 8000$ V- acceleration voltage

$M = 1000$

$TOF = 1218 \cdot 10^{-9}$

$R = 0.004$ m- radius of quadrupole aperture

$w_1 = 0.05$ m- length of th 1st quadrupole

$d = 0.0$

$w_2 = 0.05$ m- length of th 2nd quadrupole

$e_2 = 0.01$

$V_1 = 190$

$V_2 = 72$

Initial beam parameters:

$v_0 = 150$

$X = 0.0002$ m- half-height of beam in x-direction

Final beam parameters:

$X_f = 0.0001$ m- half-height of beam in x-direction

$Y_f = 0.007$ m- half-height of beam in y-direction

2. Matching of variables.

$$v = \sqrt{\frac{10^8 \cdot V_0}{2 \cdot e \cdot M}}$$

$$a = \frac{v_0}{v}$$

$$a = 3.75 \cdot 10^{-3}$$

$$Y = X \quad b = a$$

$$e_1 = v \cdot TOF$$

$$e_1 = 0.049$$

$$k_1 = \sqrt{\frac{V_1}{R^2 \cdot V_0}}$$

$$k_1 = 38.528$$

$$k_2 = \sqrt{\frac{V_2}{R^2 \cdot V_0}}$$

$$k_2 = 23.717$$

4. Direct calculation of matrix

$$M(z) = \begin{pmatrix} 1 & |z| \\ 0 & 1 \end{pmatrix}$$

$$Q1x(k_1) = \begin{pmatrix} \cos(k_1 \cdot w_1) & \frac{1}{k_1} \sin(k_1 \cdot w_1) \\ -k_1 \sin(k_1 \cdot w_1) & \cos(k_1 \cdot w_1) \end{pmatrix}$$

$$Q1y(k_1) = \begin{pmatrix} \cosh(k_1 \cdot w_1) & \frac{1}{k_1} \sinh(k_1 \cdot w_1) \\ k_1 \sinh(k_1 \cdot w_1) & \cosh(k_1 \cdot w_1) \end{pmatrix}$$

$$M_x(k_1, k_2) = \begin{pmatrix} -1.57 & 0 \\ -35.014 & -0.637 \end{pmatrix} \quad M_y(k_1, k_2) = \begin{pmatrix} 3.276 & 0.289 \\ -3.463 & 2.082 \cdot 10^{-15} \end{pmatrix}$$

$$V_1 = k_1^2 \cdot R^2 \cdot V_0$$

$$V_1 = 94.309$$

$$V_2 = k_2^2 \cdot R^2 \cdot V_0$$

$$V_2 = 46.3$$

REFERENCES

1. J. J. Thomson and G. P. Thomson, "Conduction of Electricity through Gases", CUP, Cambridge, 2 (1933) 1, ref. to E. Goldstein, Berl. Monat. (1876) 284.
2. J. H. Beynon, and R. P. Morgan, Int. J. Mass Spectrom. Ion Phys., 27, (1978) 2, ref. to E. Goldstein, Berl. Ber., 39 (1886) 691.
3. J. H. Beynon, and R. P. Morgan, Int. J. Mass Spectrom. Ion Phys., 27 (1978) 2, ref. to W. Wien, Verh. Phys. Gesell., (1898) 17.
4. J. J. Thomson and G. P. Thomson, "Conduction of Electricity through Gases", CUP, Cambridge, 1 (1933) 267.
5. J. J. Thomson and G. P. Thomson, "Conduction of Electricity through Gases", CUP, Cambridge, 1 (1933) 265, ref. to W. Wien, Wied. Ann., 65 (1898) 440.
6. J. J. Thomson and G. P. Thomson, "Conduction of Electricity through Gases", CUP, Cambridge, 1 (1933) 266, ref. to W. Wien, Ann. der Phys., 8 (1902) 241.
7. J. J. Thomson and G. P. Thomson, "Conduction of Electricity through Gases", CUP, Cambridge, 1 (1933) 246, ref. to J. J. Thomson, Phil. Mag., 48 (1899) 547.
8. J. J. Thomson and G. P. Thomson, "Conduction of Electricity through Gases", CUP, Cambridge, 1 (1933) 246.
9. J. H. Beynon, and R. P. Morgan, Int. J. Mass Spectrom. Ion Phys., 27 (1978) 18, ref. to F.W. Aston, Philos. Mag. VI, 38 (1919) 707.

-
10. J. J. Thomson and G. P. Thomson, "Conduction of Electricity through Gases", CUP, Cambridge, 1 (1933) 252, ref. to J. Classen, Z. Phys., 9 (1908) 762.
 11. J. J. Thomson and G. P. Thomson, "Conduction of Electricity through Gases", CUP, Cambridge, 1 (1933) 287, ref. to F.W. Dempster, Phys. Rev., 11 (1918) 316.
 12. J. J. Thomson and G. P. Thomson, "Conduction of Electricity through Gases", CUP, Cambridge, 1 (1933) 276, ref. to F.W. Aston, "Isotopes", Edward Arnold, London (1924).
 13. J. J. Thomson and G. P. Thomson, "Conduction of Electricity through Gases", CUP, Cambridge, 1 (1933) 287, ref. to F.W. Dempster, Phys. Rev., 20 (1922) 631
 14. R. Herzog, Z. Phys., 89 (1934) 447.
 15. J. Mattauch and R. Herzog, Z. Phys., 89 (1934) 786.
 16. C. M. Stevens, J. Terandy, G. Lobell, R. Lewis and N. Beyer, Adv. Mass Spectrom. 2 (1963) 198.
 17. E. G. Johnson and A. O. Nier, Phys. Rev., 91 (1953) 10.
 18. W. E. Stephens, Phys. Rev., 69 (1946) 691.
 19. D. A. Skoog and J. J. Leary "Principles of Instrumental Analysis", fourth edition, Saunders College Publishing, Orlando, USA (1992) 113.
 20. W.C. Wiley and I. H. MacLaren, Rev. Sci. Instr., 26 (1955) 1150.
 21. M. Dole, H.L. Cox, Jr. and J. Gieniec, Adv. Chem. Ser., 125 (1971) 73.
 22. J. Gieniec, L.L. Mack, K. Nakamae, C. Gupta, V. Kumar and M. Dole, Biomed. Mass Spectrom., 11 (1984) 259.

-
23. R. D. Macfarlane, *Anal. Chem.*, 55 (1983) 1247A.
24. R. D. Macfarlane, in A. Benninghoven (Ed.), "Ion Formation from Organic Solids", Springer, Berlin (1983) 32.
25. B. A. Mamyrin, USSR Patent # 198,034, (1966).
26. B. A. Mamyrin, V. I. Karataev, D. V. Shmikk and V. A. Zagulin, *Sov. Phys. JETP*, 37 (1973) 45.
27. V. I. Karataev, B. A. Mamyrin and D. V. Schmikk, *J. Tech. Phys.*, 16 (1971) 1498
28. D.V. Schmikk and B. M. Dubenskii, *J. Tech. Phys.*, 54 (1984) 912.
29. U. Boesl, R. Weinkauff and E.W. Schlag, *Int. J. Mass Spectrom. Ion Proc.*, 112 (1992) 121.
- 30 B. A. Mamyrin, *Int. J. Mass Spectrom. Ion Proc.*, 131 (1994) 1
- 31.L. N. Gall, Y. K. Golikov, M.L. Aleksandrov, Y.E. Pechalina, and N.A. Holin, USSR Inventor's Certificate #1,247,973 (1986).
32. A.A. Makarov, *J.Phys. D: Appl.Phys.*, 24 (1991) 533.
33. P.J. Derrick, A.W. Colburn, A. Giannakopoulos, E.N. Raptakis, D. J. Reynolds, S. C. Davis, A. D. Hoffman and B. Wright, *Proceedings of the 42nd ASMS Conference on Mass Spectrometry and Allied Topics*, Chicago (1994) 1152.
- 34 S. C. Davis, US Patent # 5,077,472 (1991).
35. V. P. Ivanov, A. A. Makarov and A. A. Sysoev, *Proceedings of the 4th International Seminar on the Manufacturing of Scientific Space Instruments*, Frunze, 1990. IKI AN, Moscow, 2 (1990) 65.

-
36. A. L. Rockwood, Proceedings of the 34th ASMS Conference on Mass Spectrometry and Allied Topics (1986) 173.
37. Y. Yoshida, U.S. Patent # 4,625,112 (1986).
38. T. J. Cornish and R. J. Cotter, *Anal. Chem.*, 65 (1993) 1043.
39. D. C. Hamilton, G. Gloeckler, F. M. Ipavich, R. A. Lundgrer, R. B. Sheldon, and D. Hovestadt, *Rev. Sci. Instrum.* 61 (1990) 3104.
40. M. G. Ingram and R. J. Gomer, *J. Chem. Phys.*, 22 (1954) 1279.
41. P. L. Robert and H. R. Schulten, *Anal. Chem.*, 61 (1989) 61.
42. M. S. B. Munson and F. H. Field, *J. Am. Chem. Soc.*, 88 (1966) 2621.
43. M. S. B. Munson, *Anal. Chem.*, 49 (1977) 722A.
44. R. G. Bray, R. M. Hochstrasse and J. E. Wessel, *Chem. Phys. Lett.*, 27 (1974) 167.
45. E. W. Schlag and H. J. Neusser, *Am. Chem. Soc.*, 16 (1983) 16.
46. H. D. Beckey, *Int. J. Mass Spectrom. Ion Phys.*, 2 (1969) 500.
47. L. Prokai (ed.) "Field Desorption Mass Spectrometry", Marcel Dekker, New York (1990).
48. M. L. Vestal, *Int. J. Mass Spectrom. Ion Phys.*, 46 (1983) 193.
49. K. L. Busch and R. G. Cooks, *Science*, 218 (1982) 247.
50. F. Lafortune, R. Beavis, X. Tang, G. Standing and B. T. Chait, *Rapid Comm. Mass Spectrom.*, 1 (1987) 114.

-
51. M Barber, R. S. Bordoli, G. J. Elliot, R. D. Sedgwick and A. N. Tyler, *J. Chem. Soc. Chem. Commun.*, 7 (1981) 325.
52. C. J. McNeal and R. D. Macfarlane, *J. Am. Chem. Soc.*, 103 (1981) 1609.
53. M. Barber, R. S. Bordoli, G. J. Elliot, R. D. Sedgwick and A. N. Tyler, *Anal. Chem.*, 54 (1982) 645A.
54. M. Barber, R. S. Bordoli, G. J. Elliot, R. D. Sedgwick, A. N. Tyler, B. N. Green, V. C. Parr and J. L. Gower, *Biomedical Mass Spectrom.*, 9 (1982) 11.
55. R. D. Macfarlane and D. F. Torgerson, *Science*, 191 (1976) 920.
56. C. J. McNeal, *Anal. Chem.*, 54 (1982) 43A.
57. M. Yamashita and J. B. Fenn, *J. Phys. Chem.*, 88 (1984) 4451.
58. J. Fenn, M. Mann, C. K. Meng and S. F. Wong, *Mass Spectrom. Rev.*, 9 (1990) 37.
59. M. A. Posthumus, P. G. Kstemaker, H. L. C. Meuzelaar, and M. C. Ten Noever de Brauw *Anal. Chem.*, 50 (1978) 985.
60. M. Karas and F. Hillenkamp, A. Benninghoven (ed.) *Ion Formation from Organic Solids*, Springer Series in Chemical Physics, 25, Spingler-Verlag, New York (1983).
61. M. Karas and F. Hillenkamp, *Anal. Chem.*, 60 (1988) 2299.
62. S. Kaur, D. Hollander, R. Haas and A. L. Burlingame, *J. Am. Chem. Soc.*, 107 (1985) 38.
63. P. M. Johnston, M. R. Bergman and D. Zakheim, *J. Chem. Phys.*, 62 (1975) 2500.
64. P. Esherick, J. A. Armstrong, R. W. Dreyfus and J. J. Wyne, *Phys. Rev. Lett.*, 36 (1976) 1296.

-
65. K. Tanaka, H. Waki, Y. Ido, S. Akita, Y. Yoshida and T. Yohida, *Rapid Commun. Mass Spectrom.*, 2 (1988) 151.
66. M. Karas, D. Bachmann and F. Hillenkamp, *Anal. Chem.*, 57 (1985) 2935.
67. M. Karas, D. Bachmann, U. Bahr and F. Hillenkamp, *Int. J. Mass Spectrom. Ion Proc.*, 78 (1987) 53.
68. M. Karas, A. Ingendoh, U. Bahr and F. Hillenkamp, *Biomed. Envir. Mass Spectrom.*, 18 (1989) 841.
69. P. Lecchi and L. K. Pannell, *J. Am. Soc. Mass Spectrom.*, 6 (1995) 972.
70. R. C. Beavis and B. T. Chait, *Rapid Commun. Mass Spectrom.*, 27 (1992) 188.
71. F. Hillenkamp, M. Karas, A. Ingendoh and B. Stahl; in "Biological Mass Spectrometry", A. L. Burlingame and J. A. McCloskey (eds.), Elsevier, Amsterdam (1990) 49.
72. R. C. Beavis and B. T. Chait, *Rapid Commun. Mass Spectrom.*, 3 (1989) 233.
73. P. Y. Yau, PhD Thesis, University of Warwick, UK (1994).
74. T-W. D. Chan, A. W. Colburn and P. J. Derrick, *Org. Mass Spectrom.*, 26 (1991) 342.
75. T-W. D. Chan, A. W. Colburn and P. J. Derrick, *Org. Mass Spectrom.*, 27 (1992) 188.
76. K. Strupat, M. Karas and F. Hillenkamp, *Int. J. Mass Spectrom. Ion Proc.*, 111 (1991) 89.
77. R. C. Beavis, *Org. Mass Spectrom.*, 27 (1992) 653.
78. R. C. Beavis and B.T. Chait, *Rapid Commun. Mass Spectrom.*, 3 (1989) 432.
79. H. Egge, J. Peter-Katalinic, M. Karas and B. Stahl, *Pure Appl. Chem.*, 63 (1991) 491.

-
80. B. Stahl, M. Steup, M Karas and F. Hillenkamp, *Anal. Chem.*, 63 (1991) 1463.
81. P. Juhasz, I. A. Papayannopoulos, C-H. Zeng, V. Papov and K Biemann, *Proceedings of the 40th ASMS Conference on Mass Spectrometry and Allied Topics*, Washington DC, USA, (1992) 1913.
82. M. Karas, F. Hillenkamp, R. C. Beavis and B. T. Chait, *Anal. Chem.*, 63 (1991) 1193A.
83. R. C. Beavis, T Chaudhary and B. T. Chait, *Org. Mass Spectrom.*, 27 (1992) 156.
84. A. E. Giannakopulos, D. J. Reynolds, T-W. D. Chan, A. W. Colburn and P. J. Derrick, *Int. J. Mass Spectrom. Ion Proc.*, 131 (1994) 67.
85. A. E. Giannakopulos, PhD Thesis, University of Warwick, UK (1994).
86. M Vestal, P. Juhasz, C. Blakely and S. Martin, *Proceedings of the 43rd ASMS Conference on Mass Spectrometry and Allied Topics*, Atlanta, USA (1995) 1209.
87. E. Tackach, D. Patterson, W. Hines, P. Juhasz, R. Lee and M Vestal, *Proceedings of the 44th ASMS Conference on Mass Spectrometry and Allied Topics*, Portland, USA (1996).
88. M. Dole, L. L. Mach, R. L. Hines, R. C. Mobley, L. P. Ferguson and M. B. Alice, *J. Chem. Phys.*, 49 (1968) 2240.
89. R. D. Smith, J. A. Loo, C. G. Edmonds, C. J. Barinaga and H. R. Udseth, *Anal. Chem.*, 62 (1990) 882.
90. E. C. Huang, T. Wachs, J J. Conboy and J. D. Henion, *Anal. Chem.*, 62 (1990) 713A.
91. J. V. Iribarne and B. A. Thomson, *J. Chem. Phys.*, 64 (1976) 2287.
92. J. W. S. Rayleigh, *Philos. Mag.*, 14 (1882) 184.

-
93. G. Schemelzeisen-Redeker, L. Buterig and F. W. Rollgen, *Int. J. Mass Spectrom. Ion Proc.*, 90 (1989) 139.
94. J. B. Fenn, M. Mann, C. K. Meng, S. F. Wong and C. M. Whitehouse, *Mass Spectrom. Rev.*, 9 (1990) 37.
95. A. N. Verentchikov, W. Ens and K. G. Standing, *Anal. Chem.*, 66 (1994) 126.
96. P. W. Geno and R. D. Macfarlane, *Int. J. Mass Spectrom. Ion Proc.*, 92 (1989) 195.
97. J. Axelsson, E. S. Parilis, C. T. Reimann, P. Sullivan and B. U. R. Sundqvist, *Nucl. Instr. And Meth. B*, 101 (1995) 343.
98. F. W. Aston, *Proc. Cambridge Philos. Soc.* 19 (1919).
99. J. H. Callahan, F. L. King and M. M. Ross, *Abstr. J. Am. Chem. Soc.*, 200 (1990) 36.
100. K. L. Busch and G. C. DiDonato, *Amer. Lab.*, 8 (1986) 17.
101. D. A. Skoog and J. J. Leary, *Principles of Instrumental Analysis*, Fourth Edition, Saunders College Publishing, Fort Worth, USA (1992).
102. D. R. Jardin, D. S. Alderdice and P. J. Derrick, *Org. Mass Spectrom.*, 26 (1991) 915.
103. R. H. Bateman, R. S. Bordoli, A. J. Gilbert, J. B. Hoyes and H.R. Morris, *Proceedings of the 44th ASMS Conference on Mass Spectrometry and Allied Topics*, Portland, USA, (1996).
104. J. Allison and R. M. Stepnowski, *Anal. Chem.*, 59 (1987) 1072A.
105. A. G. Marshall and P. B. Grosshans, *Anal. Chem.*, 63 (1991) 215A.
106. H. M. Rosenstock and C. E. Melton, *J. Chem. Phys.*, 26 (1957) 314.
107. S. E. Kupriyanov and A. A. Perov, *Russ. J. Phys. Chem.*, 39 (1965) 871.

-
108. W. F. Haddon and F. W. McLafferty, *J. Am. Chem. Soc.*, 90 (1968) 4745.
109. K. R. Jennings, *Int. J. Mass Spectrom. Ion Phys.*, 1 (1968) 227.
110. F. W. McLafferty, P. F. Bente, R. Kornfeld, S.-C. Tsai and I. Howe, *J. Am. Chem. Soc.*, 95 (1973) 2120.
111. F. W. McLafferty, R. Kornfeld, W. F. Haddon, K. Levsen, I. Sakai, P. F. Bente, S.-C. Tsai and H. D. R. Schuddemage, *J. Am. Chem. Soc.*, 95 (1973) 3886.
112. R. A. Yost and C. G. Enke, *Anal. Chem.*, 51 (1979) 1251A.
113. J. H. Beynon, R. G. Cooks, J. W. Amy, W. E. Baitinger and T. Y. Ridley, *Anal. Chem.*, 45 (1973) 1023A.
114. R. G. Cooks, (ed) *Collision Spectroscopy*, R. G. Cooks, Plenum: New York (1979).
115. K. Levsen and H. Schwarz, *Mass Spectrom. Rev.*, 2 (1983) 77.
116. J. Durup in "Recent Developments in Mass Spectrometry", K. Ogata, T. Hayakawa (eds) University Park Press, Baltimore (1970) 921.
117. J. Bricker and D. H. Russell, *J. Am. Chem. Soc.*, 108 (1986) 6174.
118. M. Sheil and P. J. Derrick, *Org. Mass Spectrom.*, 23 (1988) 429.
119. E. Uggerud and P. J. Derrick, *J. Phys. Chem.*, 95 (1991) 1430.
120. C. D. Bradley, J. M. Curtis, P. J. Derrick and M. M. Sheil, *J. Chem. Soc. Faraday Trans.*, 90 (1994) 239.
121. A. Russek, *Physica*, 48 (1970) 165.
122. O. K. Rice and H. C. Ramspeger, *J. Am. Chem. Soc.*, 49 (1927) 1616.

-
123. L. S. Kassel, *J. Phys. Chem.*, 32 (1928) 225.
124. R. A. Marcus, *J. Chem. Phys.*, 20 (1952) 359.
125. D. W. Oxtoby and S. A. Rice, *J. Chem. Phys.*, 65 (1976) 1676.
126. J. Ford, *Adv. Chem. Phys.*, 24 (1973) 155.
127. B. Spengler, D. Kirsch and R. Kaufmann, *Rapid Commun. Mass Spectrom.*, 5 (1991) 198.
128. B. Spengler, D. Kirsch and R. Kaufmann, *J. Phys. Chem.*, 96 (1992) 9678.
129. X. Tang, R. Beavis, W. Ens, F. Lafortune, B. Schueler and K. G. Standing, *Int. J. Mass Spectrom. Ion Proc.*, 3 (1989) 443.
130. S. Della-Negra and Y. Le Beyec, *Anal. Chem.*, 57 (1985) 2035.
131. P. Juhasz, S. Martin and M. Vestal, *Proceedings of the 44th ASMS Conference on Mass Spectrometry and Allied Topics*, Portland, USA (1996).
132. W. Yu, J. E. Vath, M. C. Huberty and S. A. Martin, *Anal. Chem.*, 65 (1993) 3015.
133. T. J. Cornish and R. J. Cotter, *Proceedings of the 43rd ASMS Conference on Mass Spectrometry and Allied Topics*, Atlanta, USA (1995) 133.
134. J. C. Rouse, W. Yu and S. A. Martin, *J. Am. Soc. Mass Spectrom.*, 6 (1995) 822.
135. J. B. Summer, *J. Biolog. Chem.*, 69 (1926) 435.
136. J. H. Northrop, *J. Gen. Physiol.*, 13 (1930) 739.
137. I. A. Papayannopoulos, *Mass Spectrom. Rev.*, 14 (1995) 49.

-
138. K. Biemann in "Biochemical Applications of Mass Spectrometry", G. R. Waller (ed.) John Wiley & Sons, New York (1972) 405.
139. H. D. Niall, *Meth. Enzymol.*, 27 (1973) 942.
140. A. V. Fowler and I. J. Zabin, *I. J. Biol. Chem.*, 253 (1978) 5521.
141. F. Sanger, A. R. Coulson, B. G. Barrel, A. J. H. Smith and B. A. Roe, *J. Mol. Biol.*, 143 (1980) 161.
142. K. Biemann, *Anal. Chem.*, 58 (1986) 1289A.
143. P. Roepstorff and J. Fohlman, *Biomed. Envir Mass Spectrom.*, 11 (1984) 601.
144. K. Biemann, *Biomed. Envir. Mass Spectrom.*, 16 (1988) 99.
145. R. S. Johnson and K. Biemann, *Biochemistry*, 26 (1987) 1209.
146. T-W. D. Chan, I. Thomas, A. W. Colburn and P. J. Derrick, *Chem. Phys. Lett.*, 222 (1994) 579.
147. U. Boesl, R. Weinkauf, C. Weickhardt and E. W. Schlag, *Int. J. Mass Spectrom. Ion Proc.*, 131 (1994) 87.
148. E. K. Zavoiskii and S. D. Fanchenko, *Sov. Phys:Doklady*, 1 (1956) 285.
149. T-W. D. Chan, PhD thesis, University of Warwick, 1993.
150. T. Bergmann, T. P. Martin and H. Schaber, *Rev. Sci. Instrum.*, 61 (1990) 2592.
151. H. Wollnik, *Anal. Instrum.*, 16 (1987) 15.
152. T. Bergmann, T. P. Martin and H. Schaber, *Rev. Sci. Instrum.*, 60 (1989) 347.

-
153. J. Ximen, *Aberration Theory in Electron and Ion Optics*, Academic Press Inc., Orlando (1986) 35.
154. Lambda Physik LPX100 Excimer Laser User Manual.
155. Lambda Physik FL3002 Tunable Dye Laser User Manual.
156. O. Vorm, P. Roepstoff and M. Mann, *Anal. Chem.* 66 (1994) 3281.
157. E. N. Raptakis, F. G. Hopwood, D. J. Reynolds, A. W. Colburn and P. J. Derrick, *Proceedings of the Annual Meeting of the British Mass Spectrometric Society*, St. Adrews, Scotland (1991).
158. J. A. Hill, R. S. Annan and K. Biemann, *Rapid Commun. Mass Spectrom.*, 5 (1991) 395.
159. F. C. Walls, M. A. Baldwin, A.M. Falick, B. W. Gibson, S. Kaur, D. A. Maltby, B. L. Gillece-Castro, K. F. Madsihradzsky, S. Evans and A. L. Burlingame, in "Biological Mass Spectrometry", A. L. Burlingame and J. A. McCloskey eds., Elsevier, Amsterdam (1990).
160. H. Wollnik, "Optics of Charged Particles", Academic Press, Orlando (1987) 225.
161. Kratos Concept IIHH Tandem Mass Spectrometer Operating Manual, page 4.18.
162. H. Wollnik, "Optics of Charged Particles", Academic Press, Orlando, (1987) 110.
163. J. S. Cottrell and S. Evans, *Anal. Chem.*, 59 (1987) 1990.
164. R. S. Annan, H. J. Kochling, J. A. Hill, and K. Biemann, *Rapid Commun. Mass Spectrom.*, 6 (1992) 298.
165. J. A. Hill, J. E. Biller, S. A. Martin, K. Biemann, K. Yoshidome and K. Sato, *Int. J. Mass Spectrom. Ion Proc.*, 92 (1989) 211.

-
166. J. T. Stults, C. G. Enke and J. F. Holland, *Anal. Chem.*, 55 (1983) 1323.
167. F. H. Strobel, T. Solouki, M. A. White and D. H. Russell, *J. Am. Soc. Mass Spectrom.*, 2 (1990) 91.
168. J. D. Pinkston, M. Rabb, J. T. Watson, and J. Allison, *Rev. Sci. Instrum.*, 57 (1986) 583.
169. D. R. Jardine, J. Morgan, D. S. Alderdice and P. J. Derrick, *Org. Mass Spectrom.*, 27 (1992) 1077.
170. T. J. Cornish and R. J. Cotter, *Anal. Chem.*, 65 (1993) 1043.
171. T. Sakurai, H. Ito and T. Matsuo, *Anal. Chem.*, 66 (1994) 2313.
172. A. J. Alexander, P. Thibault, R. K. Boyd, J. M. Curtis and K. L. Rinehart, *Int. J. Mass Spectrom. Ion Proc.*, 98 (1990) 107.
173. C. D. Bradley, J. M. Curtis, P. J. Derrick and B. Wright, *Anal. Chem.*, 64 (1992) 2628.
174. R. H. Bateman, T. Davis and M. R. Green, *Proceedings of the 44th ASMS Conference on Mass Spectrometry and Allied Topics*, Portland, USA (1996).
175. W. P. Poschenrieder, *Int. J. Mass Spectrom. Ion Phys.*, 6 (1971) 413.
176. W. P. Poschenrieder, *Int. J. Mass Spectrom. Ion Phys.*, 9 (1972) 357.
177. D. R. Bandura and A. A. Makarov, *Int. J. Mass Spectrom. Ion Proc.*, 127 (1993) 45.
178. H. Wollnik, "Optics of Charged Particles", Academic Press Inc., Orlando, USA (1987) 17
179. M. Szilagy, "Electron and ion optics", Plenum Press, New York, (1988).

-
180. E. Uggerud, P. J. Derrick, *J. Phys. Chem.*, 95 (1991) 1430.
181. D. Ioanoviciu, *Int. J. Mass Spectrom. Ion Proc.*, 131 (1994) 43.
182. E. K. Zavoiskii, S. D. Fanchenko, *Sov. Phys. Dokl.*, 1 (1956) 285.
183. H. Wollnik, "Optics of Charged Particles", Academic Press, Orlando, USA (1987)
63
184. H. Wollnik, "Optics of Charged Particles", Academic Press, Orlando, USA (1987)
50
185. G.A. Korn and T.M Korn, "Mathematical Handbook for Scientists and Engineers",
McGraw-Hill, New York, 1961.
186. A. A. Makarov, E. N. Raptakis and P. J. Derrick, *Int. J. Mass Spectrom. Ion Proc.*,
146/147 (1995) 165
187. F. Bertein, *Ann. De Radioelectricite*, 2 (1947) 379; 3 (1948) 49
188. A. W. Colburn, A. A. Makarov, E. N. Raptakis, D. J. Reynolds, P. J. Derrick, S. C.
Davis and A. D. Hoffman, to be submitted to *Rev. Sci. Instrum.*

THE BRITISH LIBRARY
BRITISH THESIS SERVICE

TITLE HIGH RESOLUTION, HIGH SENSITIVITY
TANDEM MASS SPECTROMETRY OF
MACROMOLECULES USING
TIME-OF-FLIGHT TECHNIQUES

AUTHOR Emmanuel N
RAPTAKIS

DEGREE Ph.D

**AWARDING
BODY** Warwick University

DATE 1996

**THESIS
NUMBER** DX200744

THIS THESIS HAS BEEN MICROFILMED EXACTLY AS RECEIVED

The quality of this reproduction is dependent upon the quality of the original thesis submitted for microfilming. Every effort has been made to ensure the highest quality of reproduction. Some pages may have indistinct print, especially if the original papers were poorly produced or if the awarding body sent an inferior copy. If pages are missing, please contact the awarding body which granted the degree.

Previously copyrighted materials (journal articles, published texts, etc.) are not filmed.

This copy of the thesis has been supplied on condition that anyone who consults it is understood to recognise that its copyright rests with its author and that no information derived from it may be published without the author's prior written consent.

Reproduction of this thesis, other than as permitted under the United Kingdom Copyright Designs and Patents Act 1988, or under specific agreement with the copyright holder, is prohibited.

DX

200744